6-1-2011

Dynamical processes near the super massive black hole at the galactic center

Fabio Antonini

Dynamical Processes Near the Super Massive Black Hole at the Galactic Center

By

Fabio Antonini

A dissertation submitted for the degree of Ph.D. in Astrophysical Sciences and Technology, in the College of Science, Rochester Institute of Technology

June 2011

Approved by _____

Prof. Andrew Robinson Date
Director, Astrophysical Sciences and Technology

ASTROPHYSICAL SCIENCES AND TECHNOLOGY
COLLEGE OF SCIENCE
ROCHESTER INSTITUTE OF TECHNOLOGY
ROCHESTER, NEW YORK

CERTIFICATE OF APPROVAL

Ph.D. DEGREE DISSERTATION

The Ph.D. Degree Dissertation of Fabio Antonini has been examined and approved by the dissertation committee as satisfactory for the dissertation requirement for the Ph.D. degree in Astrophysical Sciences and Technology.

Dr. David Merritt, Thesis Advisor

Professor George Thurston, Committee Chair

Dr. Joshua Faber, Committee Member

Dr. John T. Whelan, Committee Member

Date: 22/6/2011

Declaration

I, Fabio Antonini ("the Author"), declare that no part of this thesis is substantially the same as any that has been submitted for a degree or diploma at the Rochester Institute of Technology or any other University. I further declare that this work is my own. Those who have contributed scientific and other collaborative insights are fully credited in this thesis, and all prior work upon which this thesis builds is cited appropriately throughout the text.

For illustrative and discussion-oriented purposes, I have reproduced various figures appearing in **Chapter 1** from the work of other authors. These figures are always fully credited in the associated caption.

Modified portions of this thesis have previously been published by the Author in peer-reviewed articles appearing in *The Astrophysical Journal* (ApJ).
Of course, none of the work presented in this thesis would be possible were it not for the unending support and scientific guidance of Dr. David Merritt, my thesis adviser.

F. Antonini
Rochester, June 2011

List of Published Works

1. **Antonini, Fabio**; Capuzzo-Dolcetta, Roberto; Merritt, David: A Counterpart to the Radial-Orbit Instability in Triaxial Stellar Systems, 2009, MNRAS, 399, 671

2. **Antonini, Fabio**; Faber, Joshua; Gualandris, Alessia; Merritt, David, Tidal Breakup of Binary Stars at the Galactic Center and Its Consequences: Tidal Breakup of Binary Stars at the Galactic Center and Its Consequences, 2010, ApJ, 713, 90

3. **Antonini, Fabio**; Montez, Rodolfo, Jr.; Kastner, Joel H.; Bond, Howard E.; Soker, Noam; Tylenda, Romuald; Starrfield, Sumner; Behar, Ehud: XMM-Newton Detection of a Transient X-ray Source in the Vicinity of V838 Monocerotis, 2010, ApJ, 717, 795

4. **Antonini, Fabio**; Lombardi, James C., Jr.; Merritt, David: Tidal Breakup of Binary Stars at the Galactic Center. II. Hydrodynamic Simulations, 2011, ApJ, 731, 128

The papers currently in preparation have been excluded from this list. Conference proceedings have also been excluded.

Abstract

Observations of the stellar environment near the Galactic center provide the strongest empirical evidence for the existence of massive black holes in the Universe. Theoretical models of the Milky Way nuclear star cluster fail to explain numerous properties of such environment, including the presence of very young stars close to the super massive black hole (SMBH) and the more recent discovery of a parsec-scale core in the central distribution of the bright late-type (old) stars. In this thesis we present a theoretical study of dynamical processes near the Galactic center, strongly related to these issues.

Using different numerical techniques we explore the close environment of a SMBH as catalyst for stellar collisions and mergers. We study binary stars that remain bound for several revolutions around the SMBH, finding that in the case of highly inclined binaries the Kozai resonance can lead to large periodic oscillations in the internal binary eccentricity and inclination. Collisions and mergers of the binary elements are found to increase significantly for multiple orbits around the SMBH. In collisions involving a low-mass and a high-mass star, the merger product acquires a high core hydrogen abundance from the smaller star, effectively resetting the nuclear evolution clock to a younger age. This process could serve as an important source of young stars at the Galactic center.

We then show that a core in the old stars can be naturally explained in a scenario in which the Milky Way nuclear star cluster (NSC) is formed via repeated inspiral of globular clusters into the Galactic center. We present results from a set of N-body simulations of this process, which show that the fundamental properties of the NSC, including its mass, outer density profile and velocity structure, are also reproduced. Chandrasekhar's dynamical friction formula predicts no frictional force on a test body in a low-density core, regardless of its density, due to the absence of stars moving more slowly than the local circular velocity. We have tested this prediction using large-scale N-body experiments. The rate of orbital decay never drops precisely to zero, because stars moving faster than the test body also contribute to the frictional force. When the contribution from the fast-moving stars is included in the expression for the dynamical friction force, and the changes induced by the massive body on the stellar distribution are taken into account, Chandrasekhar's theory is found to reproduce the rate of orbital decay remarkably well. However, this rate is still substantially smaller than the rate predicted by Chandrasekhar's formula in its most widely-used forms, implying longer time scales for inspiral. Motivated by recent observations that suggest a parsec-scale core around the Galactic center SMBH, we investigated the evolution of a population of stellar-mass black holes (BHs) as they spiral in to the center of the Galaxy. After ~ 10 Gyr, we find that the density of BHs can remain substantially less than the density in stars at all radii; we conclude that it would be unjustified to assume that the spatial distribution of BHs at the Galactic center is well described by steady-state models.

Contents

List of Figures

List of Tables

Chapter 1

Introduction

The super massive black hole (SMBH) at the Galactic center (GC) was first discovered as a strong radio emission (Sgr A*) in the direction of the inner 1 pc of the Galactic nucleus (Balick & Brown 1974). At the present, we know that Sgr A* is at the dynamical center of the Galaxy and it is associated with a very massive dark object and compact dark mass concentration . Observations together with theoretical arguments have lead to the conclusion that the dark mass is a black hole, providing the strongest empirical evidence for the existence of massive black holes.

Observations show that massive compact objects, with masses in the range $10^6 - 10^9\,\mathrm{M}_\odot$, reside at the center of most nearby galaxies. Understanding the origin and properties of galactic nuclei in external galaxies is however hindered by their small sizes that make them spatially unresolved even under the best ground-based observing conditions. The superior resolution of Advanced Camera for Surveys (ACS) instrument on the Hubble Space Telescope, allows the measurement of half-light radii for nuclei as small as $0''.025$, or 2 pc at the distance of the Virgo Cluster. But, even with the superb imaging capabilities of ACS, the faintest nuclei in Virgo are close to the instrumental resolution limit and also for the near brightest galaxies the environment in the immediate vicinity of central black hole cannot be resolved in single stars.

What makes the GC so special is therefore its proximity. The Milky Way nuclear star cluster (NSC), only 8 kpc away, provides a unique opportunity to study stellar dynamics around super massive black holes (SMBHs) and test modern theories of gravitation. In spite of its proximity, observations of the GC are very challenging due to the strong extinction by interstellar dust, which is opaque to UV-optical wavelengths. Consequently, observations of stars in the GC must be conducted in the infrared (IR), primarily in the K-band (2.2 μm), at which wavelength the visual extinction along the line of sight to the GC is $A_K \sim 3$ mag (Rieke et al. 1989), corresponding to a transmission ratio of 1:15 photons.

In most respects, the center of the MW appears to have properties similar to those of NSCs observed in other galaxies of comparable luminosity and, therefore, it can serve as a template for

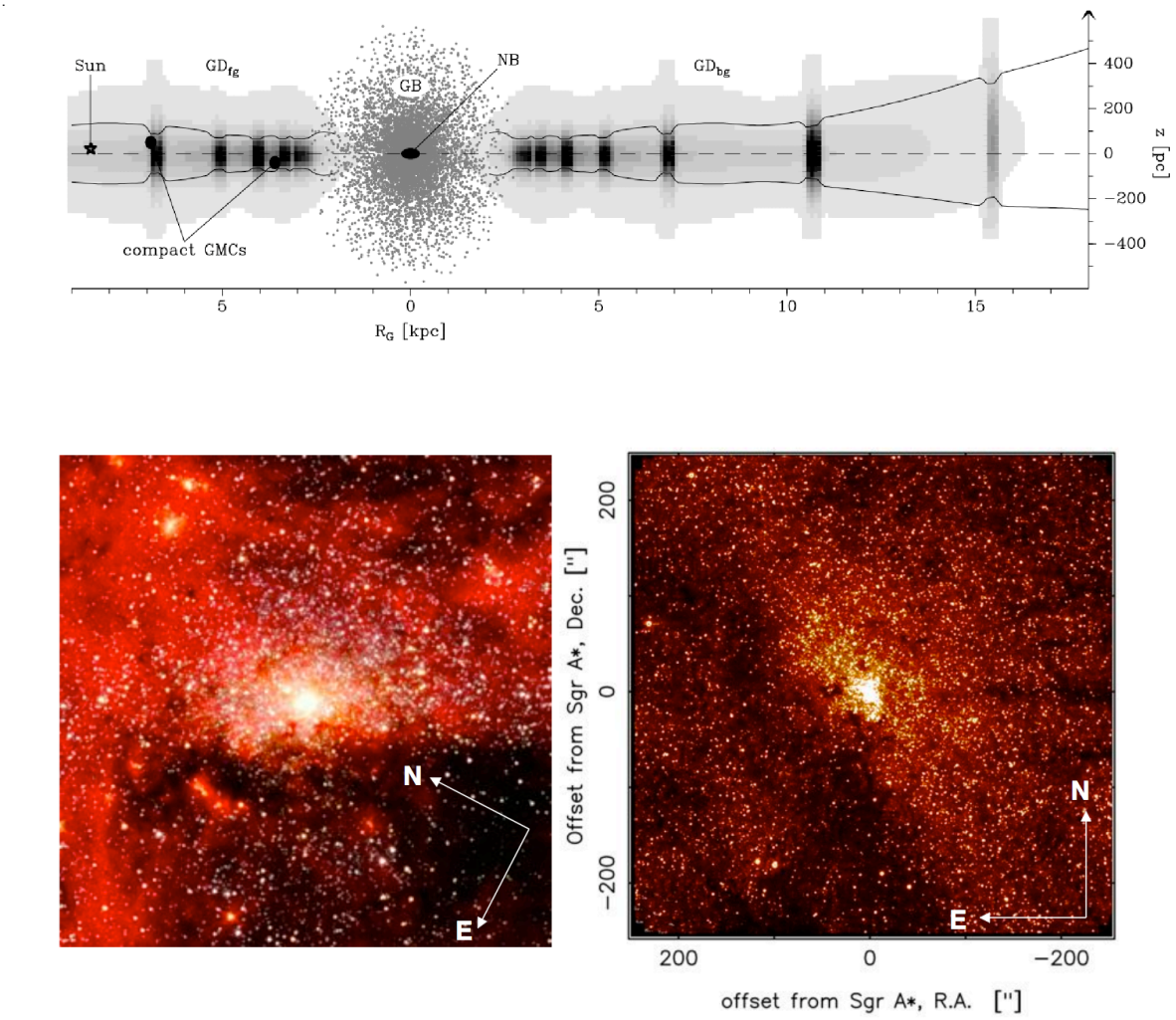

Figure 1.1 Upper panel: schematic representation of the different large scale structures of the Milky Way which contribute to emission and absorption in the direction of the central region. The grey-scale gives the average hydrogen density in the Galactic disk. Dark narrow features correspond to spiral arms which have a 3 to 30 times enhanced average density. Subscripts "fg" and "bg" refer to the foreground and background parts of the Galactic disk with respect to the Galactic center. The dashed line denotes the Galactic mid-plane and solid lines mark the density FWHM thickness of the gaseous disk (H2 + HI + HII). Giant molecular clouds (GMCs) appear as discrete patches of high extinction along the line of sight. Note that the z scale is stretched with respect to the RG scale. The Galactic bulge (GB) is not drawn in its full extent in latitude. The nuclear bulge (NB) is shown on scale (Credit: Launhardt et al. 2002). Lower panels. Left: composite (3.6, 4.5, 5.8, and 8.0 μm) Spitzer (IRAC) image of the Milky Way nuclear star cluster (Credit:NASA/JPL-Caltech/S. Stolovy, SSC/Caltech). The size of the image is approximately $100'' \times 100''$ or 20×20 pc. Right: Ks-band image of the GC with IRSF/SIRIUS (see Nishiyama et al. 2006, 2009).

systems containing similar massive central objects. The primary scientific goal of this thesis is using numerical models of the Galactic center (GC) to study the dynamics of stars and stellar remnants around SMBHs as well as the orbital evolution of secondary black holes in galactic nuclei. Here, we start by introducing the dynamical components of the GC, and discuss the key questions regarding the central few parsecs of our Galaxy.

1.1 The Milky Way Nuclear Bulge

The Nuclear Bulge appears as a distinct, massive disk-like complex of stars and molecular clouds which is, on a large scale, symmetric with respect to the Galactic center. It is distinguished from the Galactic bulge by its flat disk-like morphology, very high density of stars and molecular gas, and ongoing star formation. The Galactic nuclear bulge consists of an r^{-2} nuclear stellar cluster at the centre, a large nuclear stellar disk with radius $\sim$ 200 pc and scale height $\sim$ 45 *pc*, and the nuclear molecular disk of same size. The total stellar mass and luminosity of the nuclear bulge are 1.5×10^9 $M_\odot$ and 2.5 $\sim$ $L_\odot$, respectively. About 70% of the luminosity is due to optical and UV radiation from young massive main-sequence stars which are most abundant inside in the nuclear star cluster (Launhardt et al. 2002). The r^{-2} density distribution holds only for the central $\sim$ 20 pc (i.e., within the nuclear star cluster) and, at larger radii, the mass distribution is dominated by the nuclear stellar disk which has a flat density profile (1.1).

The Milky way nuclear bulge is characterized by a history of continuous star formation (Figer et al. 2004, 2005) and by a current stellar population consisting of a mixture of old low-mass and young massive stars. Massive molecular clumps and star clusters have also been observed in these regions (Figer 2003). Approximately half of the young stars in the GC are observed in three few Myr old, massive clusters: the central cluster around Sgr A*, the Quintuplet cluster ($\sim$ 30 pc in projection, $M \sim 10^4 M_\odot$, $\langle\rho\rangle \sim 10^3 M_\odot/\mathrm{pc}^3$) and the Arches cluster ($\sim$ 30 pc in projection, $M \gtrsim 10^4 M_\odot$, $< \rho > \sim 10^5 M_\odot/\mathrm{pc}^3$). These clusters contain in total hundreds of main-sequence O-stars, tens of Wolf-Rayet stars and a few luminous blue variables. (Wolf-Rayet stars are stars with masses of few $\times 10\,\mathrm{M}_\odot$ undergoing rapid mass loss through stellar wind, which removes the hydrogen-rich outer layer and uncovers the helium-rich core. Luminous blue variables are the progenitors of Wolf-Rayet stars still in the phase of loosing their envelopes.) Within a galctocentric distance of 20 pc, about thousands of X-ray sources are also observed which follow the distribution of stars in the IR. This exotic stellar population consists of magnetically accreting white dwarfs and X-ray pulsars in high mass X-ray binaries. The central few parsecs also contains neutral, ionized, and extremely hot gas (Becklin & Neugebauer 1968, Genzel et al. 1994, Mezger et al. 1996). The inner parsec region is mostly ionized and consists of the HII region Sgr A West, and a concentration of hot (10^6 K) x-ray emitting gas (Baganoff et al. 2001, 2003). This low-density ionized central cavity is pervaded by a set of orbiting ionized filaments (the "minispiral").

The discovery that the radial velocity of the ionized gas (in the 12.8 μm line of [Ne II]) in

the Milky Way increases to few hundred km/s in the central parsec and the application of a virial analysis to the gas velocities represents, historically, the first dynamical evidence for a massive black hole at the GC (Wollman et al. 1977). The minispiral is embedded in the circum-nuclear disk, a complex system of molecular cloud streamers at $1.5-4$ pc. Beyond its outer edge the circum-nuclear disk is bordered by a young supernova remnant, Sgr A Est, and by dense molecular clouds on a scale $5-100$ pc.

Within the central parsec, the stellar spatial distribution outside 0.5 pc is a continuation of the r^{-2} density distribution of stars at larger radii. Inside 0.5 pc, the stellar population is composed of red and blue giants, and lower-mass main-sequence (MS) stars. The faintest MS stars currently observed are B dwarfs but it is assumed that the bulk of the population consists of fainter, yet unobserved lower-mass main sequence stars, as well as stellar remnants, i.e., white dwarfs, neutron stars and stellar black holes.

1.2 Massive young stars in the center of the Galaxy

1.2.1 Disk(s) of young massive stars at the Galactic center

While the red giants and B-dwarfs are isotropically distributed, the large majority of OB giants in the central parsec are found in one, or perhaps two, warped disks which extend inward from ~ 0.5 pc to a sharp inner cut-off at 0.04 pc. Doppler shift measurements of the the radial velocities of the blue giants show that they have a common clockwise motion pattern (on the sky), exactly opposite to the rotation pattern of the Milky-Way and old-stars in the nuclear star cluster (Genzel et al. 1996, 2000, Tanner et al. 2006). This coherent velocity field suggests that the OB giants are part of an inclined disk in Keplerian rotation around the GC (Genzel et al. 2000). However, a single rotating disk cannot describe the motion of all bright stars in these regions as some of them are observed in counterclockwise motion (e.g., IRS 16NE). In order to explain the observations, Genzel et al. (2003) and Paumard et al. (2006) proposed that there are two young rotating stellar disks (or rings) around SgrA*, with large angles with respect to each other and to the Galactic plane. One disk rotates clockwise in projection, the other one counterclockwise. The clockwise disk (CWD) has 2.5 times as many massive stars as the counterclockwise disk (CCWD), it is much better defined than the CCWD and appear to be located inside most of the counterclockwise stars. Two prominent over-density of stars appear in the disks: (i) the IRS16 complex (Lu et al. 2005), located in the CCD, and (ii) IRS13, an over-concentration of stars with common velocities, part of the CCWD (Shödel et al. 2005). Both disks appear to have an outer density profile scaling as $\Sigma \sim R^{-2}$ and they are coeval with an age of ~ 6 Myr. The presence of few Myr old stars in the disks shows that massive star formation has occurred at or near the GC in the last few million years. This is surprising since in-situ star formation should be strongly inhibited by the tidal shear from the SMBH and surrounding cusp. A variety of physical scenarios have been proposed to explain the presence of

the young massive stars outside the central cusp, at $3'' - 10''$ from SgrA*. The two most promising are:

1 The in-situ accretion disk scenario, where the stars formed where they are observed today, very close to the central black hole. However, to overcome the SMBH tidal field, gas clouds have to be much denser ($\simeq 10^{12} R_{1''}^{-3} \mathrm{cm}^3$) than currently observed. Morriss (1993) proposed that star formation occurred few million years ago in gaseous disks and/or streams formed from infalling and/or colliding gaseous clumps. Modern numerical simulations together with analytical computations (Nayakshin & Cuadra 2005; Levin 2007) have shown that stars could form in such fragmenting clumps to form stellar disks in the region where the young O/WR stars are currently observed. This scenario could, in principle, explain the radial distribution of O-stars in the disk and possibly their eccentricities. The robustness of producing star formation in the GC region under a variety of conditions explored makes this scenario the most promising for the origin of the young stellar disk and stellar structures.

2 The cluster infall scenario, in which a young stellar cluster spirals into the GC due to dynamical friction and it is disrupted within ~ 0.5 pc from the SMBH (Gerhard 2001; Fujii et al. 2010). If the dissolving cluster is on a quasi-circular orbit it is likely to form a disk like structure at, approximately, its tidal disruption radius and it would also produce a bias towards more massive stars in the GC since these are the last starts to dissolve from the cluster. However, such more massive stars can be transported in the very center only if the cluster contains an intermediate mass black hole ($M > 10^4$ $\mathrm{M}_\odot$) (Yu & Madau 2007). The existence of such black holes is not supported by observations and detailed N-body simulations of stellar clusters, combined with stellar evolution, do not produce intermediate mass black holes (Glebbeek et al. 2009). In addition, the cluster may not be able to inspiral in the appropriate time window for producing the stellar disk even if ti contains a preexisting IMBH (Kim & Morriss 2003, Kim et al. 2004). The infall cluster scenario is therefore unfavorable given our currents understanding.

1.2.2 The paradox of youth in the S-stars cluster

The S-stars cluster consists of about 20 stars, mainly B dwarfs, orbiting the SMBH within a galactocentric radius of ~ 0.04 pc. From the orbits and radial distributions of the S-stars it is clear that they are not part of the stellar disks. The S-stars are very young with ages in the range $5 - 400$ Myr. The precise determination of the S-stars orbits in the immediate vicinity of Sgr A*, including one complete orbit (S2), provide the strongest empirical evidence for a SMBH at the GC. The presence of such young stars very close to the SMBH is highly unexpected due to the strongly tidal shear from the SMBH. A different mechanism is required to account for the S-stars beyond the scenarios discussed above in the contest of the stellar disks. The most promising mechanism is

the interaction of a massive binary with the SMBH, in which the binary is disrupted, one member captured on a tight orbit and the other ejected at very high velocity (Hills 1998). To account for the number of currently observed stars in the S-stars cluster, there should be a very efficient resupply of *young* binary stars on very eccentric orbits. A possibility is that massive-perturbers, accelerate the rate at which binbary stars interact closely with the central black hole (Perets et al. 2007). Massive-perturbers such as massive molecular clouds, stellar clusters or perhaps intermediate mass black holes, can reduce the relaxation time scale in the inner parsec with respect to the two-body relation by stars alone of many orders of magnitude. Although this model is very promising, it is not clear at which extends it can explain the current mass-function of stars in the central arcsecond. Another plausible mechanism is the migration of binary stars from the stellar disks, perhaps aided by an intermediate mass black hole or due to dynamical instabilities in the eccentric disk (Madigan et al. 2009). But, while the S-stars are primarily B dwarfs, the young stars in the disk are mainly luminous Wolf-Rayet and OB supergiants and giants (Paumard et al. 2001). This limits the connection between the two stellar populations, as O/W-R stars are typically more massive and shorter-lived than B type stars. To overcame this argument it is usually assumed that in the disk-origin scenario the S-stars were formed in a older, now disrupted, stellar disk. It is also important to note that in the Hills process the eccentricity of captured binary members is very high, and the resulting distribution is very different from the only slightly superthermal eccentricity observed distribution of the S-stars. Perets et al. (2009) have shown how perturbations from a dense cluster of $10\,M_{\odot}$ stellar black holes, expected to accumulate around the SMBH due to mass segregation (Hopman & Alexander 2006), tend to randomize orbits with high eccentricity in $\sim$ 20Myr. Alternatively, if the binaries are transported to the center by the inspiral of a massive cluster containing an IMBH, interactions with the same IMBH will thermalize the eccentricities in $\sim$ 1Myr (Merritt et al. 2009). Another plausible explanation for the S-stars is that they are the merger products of lower mass stars. The merger of two stars would create a single more massive star, potentially with a mass larger than that of the progenitor stars. While a star born with a mass larger than that of stars would have already evolved off of the main sequence, a more massive star which formed via merger would not have evolved as quickly and would still be on the main-sequence. The merger product will look much younger than the stars from which it originated. Although the collisional rate in the proximity of SgrA* is too low to explain the ~ 20 B type stars in this region, more exotic processes like Kozai induced collisions near the SMBH can increase the merger rate and account for at least the youngest members of the S-stars cluster (we will come back to this point below).

1.2.3 Hypervelocity stars

Gravitational encounters involving stellar binaries and the SMBH have recently been studied by several authors in the context of hypervelocity stars (HVSs) (Gualandris et al. 2005; Bromley et al. 2006; Ginsburg & Loeb 2006; Sesana et al. 2007). HVSs have such extreme velocities

($500 - 1000$ km s^{-1} as measured in the Galactic halo) with respect to their parent population that they require a dynamical encounter with a massive black hole for their explanation (Hills 1988; Yu & Tremaine 2003). The idea is that stellar binaries on low angular momentum orbits interact with the SMBH and are dissociated by its strong tidal field. As a result, one component is captured by the SMBH into a wide eccentric orbit while the other star is ejected to infinity with large velocity. After the fortunate discovery of the first HVS in the Galactic halo (Brown et al. 2005), a handful have been found escaping the Galaxy at large speeds (Brown et al. 2006). More recent surveys of hypervelocity stars found 16 stars with velocities larger than the Galactic escape velocity (Brown et al. 2007, 2009). Gould & Quillen (2003) first proposed the "Hills" capture mechanism for the origin of the S-stars. In principle the the S-stars cluster properties are compatible with this scenario for several reasons: (i) the youngest S-stars are normal main sequence stars with low rotational velocities (Eisenhauer et al. 2005); (ii) the angular momentum distribution of the S-stars orbits appears to be isotropic (Bartko et al. 2010); (iii) the luminosity function of the S-stars is consistent with a normal (i.e., Galactic-disk) IMF. These findings suggest a field origin for the B stars. Moreover, in the Hills mechanism initial binary semi-major axis and the orbital semi-major axis of the captured stars are proportional to each other, and, therefore, the orbital distribution of the initial binaries should map directly into the semi-major axis distribution of bound stars. The observed semi-major distribution of the S-stars is consistent with an Öpik's (Öpik (1924)) distribution for the internal semi-major axis of the primordial binaries, which in turns approximates the major-axis distribution of massive binaries in the solar neighborhood. This means that the B stars near the GC may originate from a population of binaries with an Öpik distribution of semi-major axes.

The most important question for the HVSs is whether they originated from the GC. Constraining their origin, however, is challenging since precise proper motion measurements are required. Of about 20 HVSs known, for only few of them it has been possible (so far) to constrain their origin: HD 271791 is a massive (11 $M_\odot$), rapidly-rotating B-type star with chemical composition consistent with that of the sun. Its Galactic rest-frame velocity exceeds the Galactic escape velocity. Heber et al. (2008) found that the proper motion of this star and its age (longer then its travel time from the GC), are inconsistent with a GC origin. Tillich et al. (2009) reconstructed the trajectory of SDSS J013655.91+242546.0, a ~ 2.5 $M_\odot$ late B-type star traveling with a Galactic rest frame velocity of 550 km s^{-1} . Even in this case, proper motion measurements excludes a GC origin, indicating, instead that the star originated from the outskirts of the Galaxy. Based on observations with the Hubble Space Telescope, Brown et al. (2010) measured the proper motion of the HVS HE 0437-5439, a 9 $M_\odot$ B-type star located 16 degrees from the Large Magellanic Cloud (LMC) on the sky. It has a heliocentric radial velocity of 723 km s^{-1} and a heliocentric distance of 61 kpc. Brown et al. found that its velocity vector points from the Milky Way. An origin from the center of the Large Magellanic cloud, as first proposed by Edelmann et al. (2005), was then ruled out at 3σ level. However, the travel time of the star from the Milky Way exceeds its main-sequence lifetime, probably excluding a GC origin. An alternative picture is that the star is a blue straggle that was

ejected fro the GC as a binary system that subsequently merged and rejuvenated during its flight.

1.3 The distribution of (old) stars at the Galactic center

1.3.1 The Bahcall-Wolf Solution

Gravitational encounters drive the local velocity distribution toward a Maxwellian distribution. But, a Maxwellian velocity distribution implies an exponentially divergent mass near the SBH and therefore the existence of a inner region where stars are captured and destroyed. The tidal disruption rate is approximately $\dot{N} \approx N/\left[\ln(2/\theta_{lc})\right] T_r$, where $\theta_{lc} \approx \sqrt{r_t/r_{\rm bh}}$ is the angular size subtended by the sphere of radius the tidal disruption radius (r_t) as seen from $r = r_{\rm bh}$, N is the number of stars within the SMBH influence radius $r_{\rm bh}$, and T_r is the relaxation time at $r_{\rm bh}$. Therefore, also in collisional nuclei, where the relaxation time is short, the density of stars drops to zero within r_t. The tidal disruption or capture of stars from the SMBH prevents the nucleus from reaching a state of thermal equilibrium. For luminous galaxies and more massive black holes the SBH Schwarzschild radius is most relevant since it is larger than the the tidal disruption radius. However, these latter systems have relaxation times much grater than the age of the universe implying much lower loss-cone refilling rate than in the case of collisional nuclei.

Assuming spherical symmetry, the evolution of f can be approximated via the isotropic orbit-averaged Fokker Planck equation. Ignoring a possible dependence of the stellar phase space density on orbital angular momentum L, the Fokker Planck equation reads:

$$4\pi^2 p(E)\frac{\partial f}{\partial t} = -\frac{\partial F_E}{\partial E}, \tag{1.1}$$

$$F_E(E,t) = -D_{EE}\frac{\partial f}{\partial E} - D_E f \tag{1.2}$$

(Spitzer 1987). Here $p(E)$ is a phase-space volume element, $p(E) = 2^{-3/2}\pi G^3 M_\bullet^3 |E|^{-5/2}$ near the SBH, F_E is the flux of stars in energy space, and D_E and D_{EE} are diffusion coefficients that describe the effects of small-angle scattering:

$$\begin{aligned} D_{EE}(E) &= 64\pi^4 G^2 m^2 \ln\Lambda \left[q(E)\int_{-\infty}^{E} dE' f(E') + \int_E^0 dE' q(E') f(E') \right], \\ D_E(E) &= -64\pi^4 G^2 m^2 \ln\Lambda \int_E^0 dE' p(E') f(E') \end{aligned} \tag{1.3}$$

with $\ln\Lambda \approx \ln(M_\bullet/m)$ the Coulomb logarithm and $q(E) = (2^{1/2}\pi/6) G^3 M_\bullet^3 |E|^{-3/2}$. The boundary conditions are $f(E_t) = 0$ and $f(0) = f_0$; $E_t = GM_\bullet/r_t$ is the energy at which stars are lost to the SBH and f_0 is the phase space density at $E = 0$ (See Merritt 2006).

Numerical solutions to Equations (1.1, 1.2) show that a steady state is reached after about one relaxation time computed at the SMBH influence radius. If $|E_t| \gg GM_\bullet/r_h$, (i.e. if the disruption radius r_t is much smaller than $r_{\rm bh}$), the steady-state solution is a power law,

$$f(E) = f_0 |E|^{1/4}, \quad \rho(r) = \rho_0 r^{-7/4}, \quad |E| \ll |E_t|, \quad r_t \ll r. \tag{1.4}$$

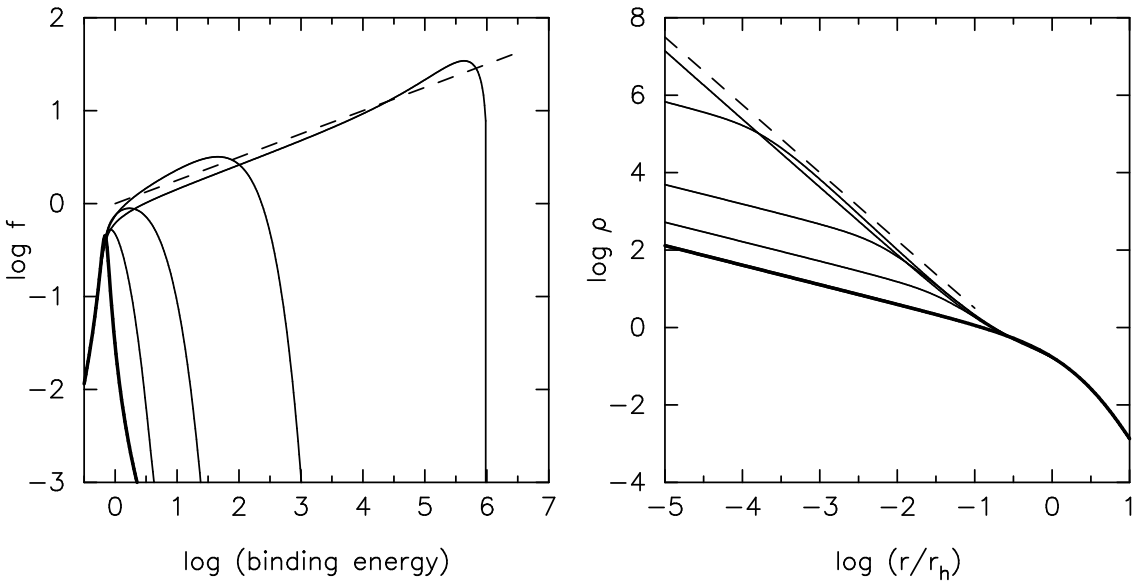

Figure 1.2 Evolution of the stellar distribution around a SBH due to energy exchange between stars. Left panel: Evolution of the phase space density f of a stellar distribution around a SMBH due to energy exchange between stars. Left panel: evolution of the density profile ρ. The tick line gives the initial distribution ($\rho \propto r^{-0.5}$) near the SBH; thin curves show the distribution at times of $(0.2, 0.4, 0.6, 1.0) \times T_{\rm r}$ where $T_{\rm r}$ is the relaxation time at the SBH's initial influence radius (here indicated as $r_{\rm h}$). Dashed lines show the Bahcall-Wolf solution (From Meritt 2006).

However, we stress that Equation (1.4) is a "zero-flux" solution which neglects the diffusion of stars into the disruption sphere, and it is therefore unphysical.

Figure 1.3.1 illustrates the evolution of $f(E,t)$ in the case of a spherical stellar system around a SMBH. The system has initially a shallow density profile at the center which is converted into the Bahcall-Wolf cusp in approximately one relaxation time (at $r_{\rm bh}$), with the cusp rising above the pre-existing density inside a radius $\sim 0.2 r_{\rm bh}$. More recently, the predictions obtained under the Fokker-Planck formalism have been directly verified by N-body simulations (Preto et al. 2004).

When the system is a multi-mass model, $m_l < m < m_u$, due to equipartition of energy, the specific kinetic energy of the high mass stars tends to decrease while that of the low-mass stars increases. As a consequence, the massive stars sink and segregate toward the center on a dynamical friction time scale (Alexander 2005). In this situation the distribution function can be approximated by power laws, $f(E) \propto E^{p_m}$, with $p_m = m/4m_u$. In the vicinity of amassive black hole, this corresponds to power-law density cusps, with $\alpha = 3/2 + p_m$. Bahcall & Wolf (1977) found $\alpha = 7/4$ for the most massive particles and $\alpha = 3/2$ for the lightest stars.

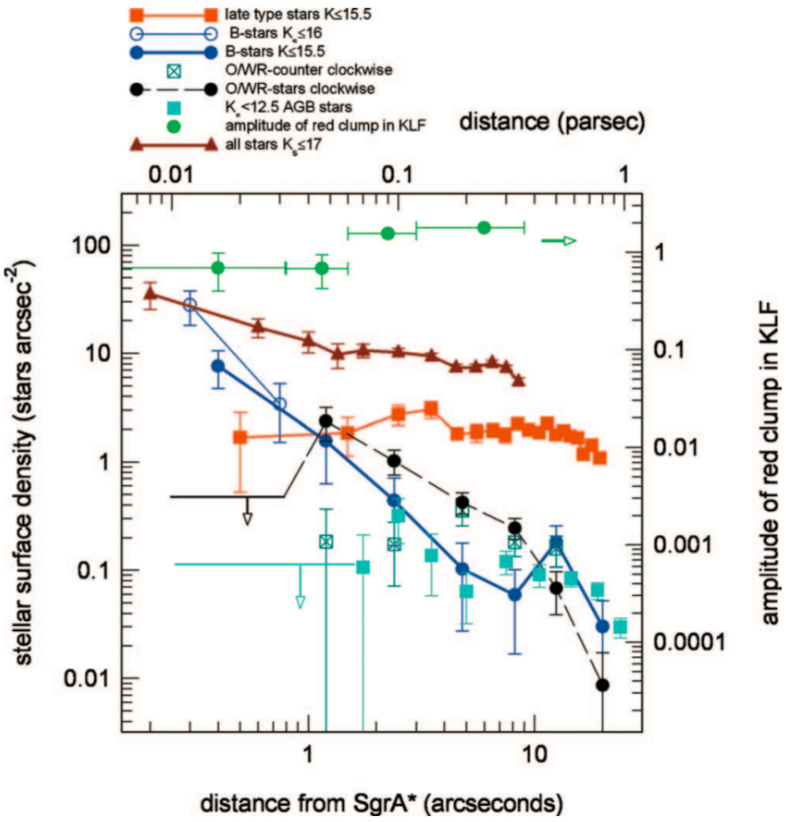

Figure 1.3 Observed radial surface density distribution of different stellar populations as a function of projected distance from SgrA* as described in more detail into the text (from Bartko et al. 2010).

1.3.2 A missing stellar cusp at the Galactic center

At the Galactic center the relaxation time is probably short enough that one would expect the old stars in these regions to follow a Bahcall-Wolf cusp. Number counts of the old giants near the GC, assumed to represent the distribution of the dominant population of main sequence stars, suggest instead a space density that is weakly rising, or falling, toward the SMBH, inside a core of radius ~ 0.5pc (Buchholz et al. 2009; Do et al. 2009; Bartko et al. 2010). Do et al. (2009) found that the intrinsic density distribution of giants and red clumps stars to $K_s \leq 15.5$ has a power law index that flattens to < 1 in the inner 10 arc sec at the 99.7% probability level. In contrast, the density of early type stars, however too young to be relaxed, strongly increases as one approaches the SMBH.

Figure 1.3 gives the radial surface density distribution of different stellar populations at the GC obtained from NACO and SINFONI observations on the VLT (Bartko et al. 2010). Filled red and cyan squares mark spectroscopic late-type stars to $K_s \leq 12.5$, while filled and open blue circles give the density of spectroscopic blue stars with $14.5 \leq K_s \leq 15.5$ and $K_s \leq 16$. The densities of spectroscopic O/WR stars in the CWD and CCWD disk are marked by black circles and dark green

crossed squares respectively. The overall distribution of all stars to $K_s \leq 17$ is given by filled brown triangles. From the figure, It is evident that the mass density distribution of late-type stars is flat within 0.5 pc.

Many different scenarios have been so far proposed to explain the puzzling discovery of a flattened stellar cusp around SgrA*. As discussed above, mass segregation in a multimass system cannot account for density cusps with $\mathrm{dln}\rho/\mathrm{dln}r \leq -1$. A very high density of stellar remnants can be however invoked as a potential solution for the depletion of giants as physical collision between stellar black holes and red giants can remove the stellar envelope and significantly change the population of late-type giants in the vicinity of the SMBH. In this model, the radial distribution of giants would not be representative of the unobserved (dominant) population of low mass main sequence stars since the stellar luminosity function changes inside the core. Dale et al. (2009) found that, for a population of a few 10^4 stellar black holes in the central 0.1 pc, the cumulative effect of such collisions can account for a significant depletion of giants in the $10.5 < K_s < 12$ band. However, it was also found that depleting the brighter objects out to the required galactocentric radius would require a large population of black hole impactors which would in turn deplete the $10.5 < K_s < 12$ giants in a region much extended than is observed. The efficiency of this process is indeed quite uncertain and it is difficult to constrain by observations since it strongly depends on the population of stellar remnants at the GC.

A top-heavy IMF, applicable through the all nuclear star cluster would also lead to a lack of old stars and an overabundance of stellar remnants in the very center. A dependence of the IMF on radius would be however required to account for the observed radial distribution of stars.

Another option is that of the inspiral of an intermediate-mass black hole at the GC. A black hole of $10^3\,\mathrm{M}_\odot$ would destroy a preexisting Bahcall-Wolf cusp generating a core of size $\sim 1 \times 10^{-2}$pc (Baumgardt et al. 2006), which is, evidently, too small to explain the extension of the observed core. The inspiral of a much larger black hole $\gtrsim 10^4\,\mathrm{M}_\odot$ or, alternatively, multiple inspirals of $\sim 10^3\,\mathrm{M}_\odot$ black holes would account for a larger core, but, the lack of evidence for any large scale disturbance together with dynamical constrains from the S-stars orbits strongly limit the parameter space available for second (non-stellar) black holes at the GC (Gualandris & Merritt 2009).

Finally, Merritt (2010) estimated that the relaxation time at the sphere of influence of SgrA* is $20 - 30$ Gyr, suggesting that it is long compared to the age of the Galaxy. In this scenario the nuclear star cluster would not have yet reached a steady state under the influence of gravitational encounters and the observed core may then reflect the initial conditions of the nuclear star cluster at formation. A pre-existing core of radius ~ 2 pc would evolve, due to two-body relaxation, to the size of the GC core (~ 0.5 pc) after 10 Gyr.

1.4 Thesis structure

This thesis is concerned with two distinct, but extremely connected, topics: (i) the origin of the young stars near SgrA* (Chapters 2 and 3) and (ii) the distribution of old star at the GC (Chapters 4 and 5).

As previously discussed, the tidal breakup of binary stars by the SMBH at the Galactic center can explain a number of otherwise puzzling discoveries, including the hypervelocity stars that are observed in the halo of the Milky Way (Brown et al., 2005, 2006, 2007, 2009), and the S-stars, apparently young, main-sequence stars in tight eccentric orbits around the SMBH (Eisenahauer et al. , 2005; Gillessen et al., 2009). If the nite sizes of stars are taken into account, a number of outcomes are possible in addition to simple binary disruption. The two stars can collide, resulting in a merger if the relative velocity is less than stellar escape velocities (Ginsburg & Loeb , 2007). Since the radius of tidal disruption of single stars by the SMBH is comparable to the binary disruption radius, stars can also be tidally disrupted by the SMBH. In Chapter 2 we show that Kozai induced oscillations in the orbital elements of tight binaries at the Galactic center is a promising channel to enhance the rates of mergers/collisions in these regions. In Chapter 3 we use a smoothed particle hydrodynamic code code to study the structure and composition of collision products showing that in mergers involving a low-mass and a high-mass star, the merger product acquires a high core hydrogen abundance from the smaller star, effectively resetting the nuclear evolution clock to a younger age. From this work it appears clear that a merger event would not necessarily leave evidence of its violent history, and that the lack of unusual features in the S-stars spectra does not necessarily constrains their origin.

In Chapters 4 and 5 we study the formation and properites of the Milky Way NSC. In a relaxed nucleus, stars distribute into a cusp around the SMBH. Inside the influence radius ($r_{\rm bh}$) of the SMBH at the Galactic center, the two-body relaxation time is approximately 10 Gyr. This suggests that there may have been enough time for the stars in these regions to have reached a relaxed, quasi-steady-state density profile. On the other hand, as previously discussed, number counts of the dominant (old) stellar population near the Galactic center show a space density that is weakly rising, or falling toward the SMBH (Buchholz et al. 2009; Do et al. 2009; Bartko et al. 2010), inside $r_{\rm bh}$: to the paradox of youth of the S-stars we now add another puzzle arising from the distribution of late-type stars around the SMBH. In Chapters 4 we found that such initial parsec scale core is the natural consequence of the formation process of the Milky Way Nuclear star cluster, if this formed through merger of massive clusters in inner Galactic regions as proposed, for instance, in Capuzzo-Dolcetta & Miocchi (2008). Finally, in Chapter 5, we study the evolution of massive bodies in a shallow density cup around a SMBH showing that dynamical friction in these models can be extremely inefficient. Chapter 6 sums up and explores some future avenues of study.

Chapter 2

Tidal break-up of binary stars at the Galactic center and its consequences

2.1 introduction

The center of the Milky Way can be regarded as a rather unusual galactic nucleus in many respects. The supermassive black hole (SMBH) at the Galactic center has a mass of $M_{\rm MW} \sim 4 \times 10^6\,{\rm M}_\odot$ (Ghez et al. 2008; Gillessen et al. 2009), making it perhaps the smallest SMBH with a well-determined mass (Ferrarese & Ford 2005). Furthermore, while most known galactic nuclei have relaxation times much longer than the Hubble time, the relatively high density at the center of the Milky Way ($\gtrsim 10^6\,{\rm stars\,pc^{-3}}$) and the small mass of the SMBH imply a two-body relaxation time that is as short as a few Gyr inside the SMBH influence radius (Alexander 2005). The combination of high stellar densities, large velocities, and short relaxation time effectively make the inner parsec of the Milky Way a collisional system.

In a collisional environment, otherwise rare dynamical processes can take place at an appreciable rate. These include dynamical encounters between stars, binaries and higher-order systems. If a massive black hole is present, as is believed to be the case for most, if not all, galactic nuclei, stars and binaries can interact with it and be ejected with extreme velocities. Given the high stellar density at the Galactic center, it is plausible that stars interacting with the SMBH will come close enough to each other that finite size effects become important and physical collisions occur. In this case, the SMBH acts as catalyst for their interaction. Ginsburg & Loeb (2007) (hereafter GL07) first noted that the tidal breakup of a stellar binary interacting with the SMBH can lead, at least for some orbital parameters, to a physical collision soon afterwards. If the two stars collide with

a relative impact speed smaller then the escape speed from their surface, coalescence can occur, resulting in the formation of a new, heavier star.

Using Aarseth's direct integration scheme (Aarseth 1999) to investigate the dynamics of the encounter, Ginsburg & Loeb found that the rate of collision events at the Galactic center is about ten times smaller than the rate of formation of hypervelocity stars ($\sim 10^{-5}\mathrm{yr}^{-1}$, Brown et al. 2006), and that among the collision products, stellar coalescence occurs in about twenty percent of the cases. In this chapter we expand on their work and investigate the possibility that stellar encounters with the SMBH are responsible for the production of a population of rejuvenated stars around the SMBH.

If a binary approaches the SMBH within its tidal disruption radius, at the periapsis the stars can reach velocities a few percent of light speed, making relativistic effects potentially important in determining the properties of the unbound population and the rate at which the stars are ejected at hypervelocities. Here, we perform the first N-body simulations of binary-SMBH encounters that include post-Newtonian (PN) terms up to order 2.5, for both star-SMBH and star-star interactions.

In §2.2 and §2.3, we describe the parameters we chose for our N-body evolutions and their physical motivation. In §2.4, we discuss the likelihood of tidal capture of stars by the SMBH during close passages of binary systems. §2.5 and §2.6 consider in greater detail the populations of HVSs and stellar collision/merger products, respectively, including mechanisms like Kozai resonance that are critical in understanding the long-term evolution of binary systems. A systematic comparison between Newtonian and PN integrations is provided throughout. Finally, in §2.6, we provide a summary.

2.2 Initial models and numerical methods

We use N-body simulations to study the evolution of main sequence binaries as they make close passages by the SMBH at the Galactic center. We determine the conditions under which gravitational interactions produce HVSs, and the properties of the resulting distribution of both unbound and bound stars. All the simulations were carried out using the `ARCHAIN` (Mikkola & Merritt 2008) integrator, which includes PN corrections to all pairwise forces up to order PN2.5. The code employs an algorithmically regularized chain structure and the time-transformed leapfrog scheme to accurately trace the motion of tight binaries with arbitrarily large mass ratios (Mikkola & Merritt 2008; Merritt 2006).

Given the significant computational resources per run made necessary by the high precision of our simulations we focus on a simplified set of initial conditions. We consider circular equal-mass binary systems with random initial orientations, initial separations $a_0 = 0.05-0.2\,\mathrm{AU}$, and individual stellar masses $M_* = 3-6\,\mathrm{M}_\odot$. We define M_b to be the total mass of the binary system. Obviously, the choice of equal-mass components limits our work. A treatment of binaries with a spectrum of masses similar for instance to that found in Duquennoy & Mayor (1991) is outside the scope of this

chapter, but could be included in a future work.

We give the binary a tangential initial velocity $v_{\rm in}$ at a distance $d = 0.01 - 0.1$pc from the SMBH of mass $M_\bullet = 4 \times 10^6\,{\rm M}_\odot$, in effect setting the periapsis distance:

$$r_{\rm per} = \frac{(v_{\rm in} d)^2}{2GM_\bullet - v_{\rm in}^2 d} \tag{2.1}$$

for a Newtonian elliptical orbit.

Our initial binary separations are close to the extremes of the interval within which HVSs are produced. Since the ejection velocity increases with the internal binary energy, few stars will be ejected with velocities sufficiently large to escape from the Galaxy for $a_0 > 0.2$AU, unless very large stellar masses are considered (Gualandris et al. 2005). We also note that, for the initial distances d we choose, binaries with $a_0 > 0.2$AU are unlikely to survive for many orbits around the SMBH due to close encounters with field stars (Perets 2009a). The lower limit of 0.05AU is required by the consideration that smaller separations will result in contact binaries. GL07 pointed out that, assuming a constant probability per $\ln(a_0)$ for $0.02 < a_0 < 20$AU, the probability to find a binary with a separation within the considered interval is $\sim 20\%$. We place the binaries on highly elliptical orbits about the SMBH, rather than e.g. on parabolic/hyperbolic orbits (Gould & Quillen 2003).

The origin of the young stars (and binaries) in the Galactic center is still a matter of ongoing research. One possibility is that stars/binaries formed in-situ, i.e. at distances of a few tens of milliparsecs from the SMBH. This model faces severe difficulties since tidal forces from the SMBH inhibit star formation at these distances. Instead, it is typically assumed that the stars need to form further away from the SMBH and then migrate to the center within their lifetimes. Among the various migration models that have been proposed, three produce orbits similar to those considered in this work (i.e. highly eccentric): (i) the eccentric disk instability scenario (Madigan et al. 2008) (ii) the cluster infall scenario aided by an intermediate mass black hole (IMBH) (Gerhard 2001) and (iii) the triple disruption scenario (Perets 2009b). The first model considers a dynamical instability of an eccentric disk as the mechanism that drives the eccentricities of the stars away from their initial values and produces near-radial orbits within a few Myr. The second model assumes stars and binaries form during the collapse of a giant molecular cloud and inspiral due to dynamical friction toward the Galactic center. The cluster, which is subject to tidal disruption, can reach distances of $10 - 50\,$mpc if it harbors an IMBH of mass $\gtrsim 10^3\,{\rm M}_\odot$ at its center. Tidally removed stars can then be scattered onto eccentric orbits by the IMBH (Merritt et al. 2009). Finally, in the triple disruption scenario, young and runaway stars can form by disruptions of triples by the SMBH, which in some cases results in the capture of binaries on close orbits.

At least some of the binary progenitors of observed HVSs were likely to have been part of the young stellar disk observed at the Galactic center, whose inner edge lies at a radius 0.1pc from the SMBH (Löckmann et al. 2008), and this fact motivated our choice for the maximum value of d. The distance 0.01pc adopted as a minimum value for d is comparable to the radii of the smallest observed stellar orbits at the Galactic center (Eckart & Genzel 1997; Genzel et al. 1997).

2.3 Basic relations

Three radii play a fundamental role in our simulations:

- the periapsis separation $r_{\rm per}$ of the initial orbit of the binary with respect to the SMBH;
- the tidal disruption radius $r_{\rm t}$ of a single star due to the SMBH;
- the tidal disruption (i.e. breakup) radius $r_{\rm bt}$ of the binary due to the SMBH.

A binary with initial separation a_0 will be broken apart by tidal forces if its center of mass approaches the massive object within the distance (Miller et al. 2005; Sesana et al. 2009)

$$r_{bt} \sim \left(3\frac{M_\bullet}{M_{\rm b}}\right)^{1/3} a_0. \tag{2.2}$$

As Hills (1988) noted, the tidal disruption of single stars is an important issue in the context of binaries. Because of their low densities, main sequence (MS) stars do not survive close interactions with the SMBH; small initial velocities take the stars too close to the SMBH and no HVSs are produced (compact objects, e.g., neutron stars and white dwarfs, can survive significantly closer approaches). Tidal disruption occurs for stars that approach the SMBH more closely than r_t, where

$$r_{\rm t} \sim \left(\frac{M_\bullet}{M_*}\right)^{1/3} R_*, \tag{2.3}$$

with R_* the stellar radius. We assume a mass-radius relation $R_*/R_\odot = (M_*/M_\odot)^{0.75}$ (Hansen et al. 2004) which yields $R_* = 0.01$ AU for $M_* = 3$ $\rm M_\odot$, and $R_* = 0.016$ AU for $M_* = 6$ $\rm M_\odot$. Stars with orbits meeting the criterion $r_{\rm per} < r_t$ are fully disrupted (Luminet & Carter 1986; Evans & Kochanek 1989; Faber et al. 2005). Note that this condition is stronger than the classical Roche limit formula given by Paczynski (1971) and Eggleton (1983). Even when tidal disruption does not occur, we expect that mass will be stripped from the outer regions of any star passing within the Roche limit, which would have a fundamental impact on the subsequent evolution and orbit of the stars.

For $M_* = 3\,\rm M_\odot$ and $M_\bullet = M_{\rm MW}$, r_t is ~ 1.10 AU, while for $M_* = 6\,\rm M_\odot$ the corresponding value of $r_{\rm t}$ is ~ 1.40 AU (i.e., MS stars with larger masses are disrupted at larger distances).

A comparison of equations (2.2) and (2.3) reveals that for MS binaries we always have $r_{\rm bt} > r_{\rm t}$ (for contact binaries instead it is possible to disrupt a star before ejection occurs). Our numerical simulations demonstrate that for large binary separations where $r_{\rm per} < r_{\rm bt}$, the two stars remain bound to each other up to distances $\sim r_{\rm bt}/2$. This can be understood if the dynamical crossing time of the binary at $r_{\rm bt}$ is of the order of the time scale of tidal breakup of the binary. Furthermore even at later times, after the binary is broken apart, both stars remain close to the original Keplerian orbit of the binary around the SMBH until reaching distances $\sim r_{\rm per}$. We will come back to this point below.

Using equations (2.1) and (2.3) we can roughly estimate the lowest value of $v_{\rm in}$ that avoids tidal disruption of the individual stars. The condition $r_{\rm per} > r_{\rm t}$ yields

$$v_{\rm in} \geq v_1^c \approx \left[\frac{2GM_\bullet}{(d^2/r_{\rm t}+d)}\right]^{1/2}. \tag{2.4}$$

For $d = 0.01(0.1)$pc, this critical velocity is $v_1^c = 44(4.0)\,{\rm km\,s^{-1}}$ for $M_* = 3\,{\rm M}_\odot$ and $50(4.5)\,{\rm km\,s^{-1}}$ for $M_* = 6\,{\rm M}_\odot$. When PN corrections are included the orbits are no longer Keplerian and the periastron distance can be found by including relativistic terms in the expression for the potential (Soffel 1989):

$$V(r) = -\frac{GM_\bullet M_{\rm b}}{r} + \frac{L^2}{2M_{\rm b}r^2} - \frac{GM_\bullet L^2}{c^2 M_{\rm b} r^3}, \tag{2.5}$$

where L is the binary angular momentum and c the speed of light. For a given initial velocity, the net relativistic effect consists of a decrease of $r_{\rm per}$, yielding a higher limit for the initial velocity than for the Newtonian case. This value, in the case $d = 0.01$pc, is $v_1^c \sim 47$ and $53\,{\rm km\,s^{-1}}$ for $M_* = 3$ and $6\,{\rm M}_\odot$ respectively. For $v_{\rm in} < v_1^c$ stars would be tidally disrupted.

We can derive an expression for the maximum initial velocity that should still be able to produce a HVS. The minimum condition is that the binary itself is broken apart. Together with equation (2.2), this gives

$$v_{\rm in} \leq v_2^c \approx \left[\frac{2GM_\bullet}{(d^2/r_{\rm bt}+d)}\right]^{1/2}. \tag{2.6}$$

Very few HVSs are likely to be ejected at $v_{\rm in} > v_2^c$.

In this approximate model, HVSs are produced for $v_1^c < v_{\rm in} < v_2^c$. Between these limits, one member of a binary may be captured by the SMBH and begin to orbit it at large eccentricity, while the other star is ejected with a velocity $v_{\rm ej}$ that is larger than the escape velocity from the Galaxy. An approximate expression for $v_{\rm ej}$ was obtained by Hills (1988) and Yu & Tremaine (2003):

$$v_{\rm ej} \approx 1770\left(\frac{a_0}{0.1AU}\right)^{-1/2}\left(\frac{M_{\rm b}}{2M_\odot}\right)^{1/3}\left(\frac{M_\bullet}{3.5\times10^6 M_\odot}\right)^{1/6} f_{\rm R}\ {\rm km\ s^{-1}} \tag{2.7}$$

with $f_{\rm R}$ a function of the dimensionless closest approach parameter $D = (r_{\rm per}/a_0)[2\,M_\bullet/10^6\,M_{\rm b}]^{-1/3}$. An expression for $f_{\rm R}$ was derived by Bromley et al. (2006):

$$\begin{aligned} f_{\rm R} = 0.774 + (0.0204 + [-6.23\times10^{-4} + \{7.62\times10^{-6} + \\ (-4.24\times10^{-8} + 8.62\times10^{-11}D)D\}D]D)D, \end{aligned} \tag{2.8}$$

which reproduces the spectrum of ejection velocities for binaries initially unbound relative to the SMBH. For bound orbits, the ejection speeds will typically be smaller, unless very large apoapses are adopted.

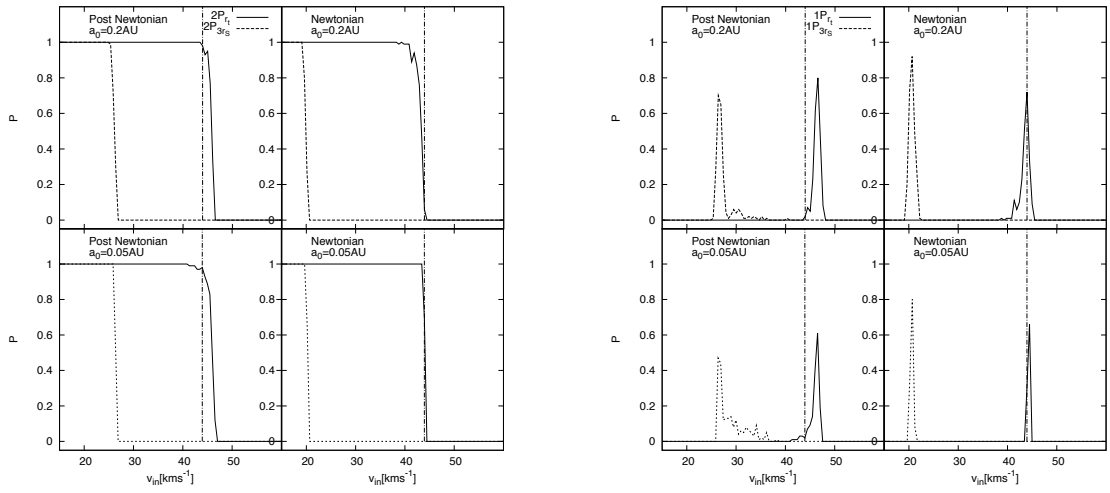

Figure 2.1 Probability that both stars (2P in the left panels) or only one star (1P in the right panels) of the binary fall within the tidal disruption radius $r_{\rm t}$ (solid lines) and the SMBH ISCO $3R_{\rm S}$ (dashed lines) as a function of the initial velocity $v_{\rm in}$. The vertical dot-dashed line represents the value of v_1^c.

2.4 Tidal captures

We first devised a set of simulations to determine the rate at which stars are captured by the SMBH. Here, "capture" means that a star passes either inside the stellar tidal disruption radius $r_{\rm t}$, or inside the innermost stable circular orbit (ISCO) at $3R_{\rm S}$, $R_{\rm S} \equiv 2GM_\bullet/c^2$; $R_{\rm ISCO} \approx 0.25\,{\rm AU}$ for $M_\bullet = 4\times10^6\,{\rm M}_\odot$. Naively, one expects that passage of the binary within either radius would result in both stars being captured. In fact, due to the finite size of the binary, it is possible for one star to be destroyed and the other to escape as a HVS.

We performed ~ 36000 integrations with equal mass $M_* = 3\,{\rm M}_\odot$ binaries, $a_0 = 0.05$ or $0.2\,{\rm AU}$ and $d = 0.01{\rm pc}$, choosing random orientations and initial tangential velocities in the range $4\,{\rm km\,s^{-1}} \le v_{\rm in} \le 85\,{\rm km\,s^{-1}}$. For each of the two binary separations, we considered both Newtonian and PN cases. Stars were treated as point masses, and we recorded all instances when a star fell inside $3R_{\rm S}$ or $r_{\rm t}$. Given the possibility that only one of the two stars is captured during a close passage to the SMBH, it is important to include initial conditions with $r_{\rm per} \lesssim r_{\rm t}$ (or equivalently $v_{\rm in} < v_1^c$).

Figure 2.1 shows the probability that one or both stars will pass inside $3R_{\rm S}$ and/or $r_{\rm t}$ as a function of the initial velocity $v_{\rm in}$. As a rule, passage of one star inside $r_{\rm t}$ or $3R_{\rm S}$ implies that both stars are captured.

The probability that both stars are tidally disrupted rises essentially to one at $v_{\rm in} \lesssim v_1^c \approx 44\,{\rm km\,s^{-1}}$ in the classical case, and at a slightly higher velocity in the relativistic case.

The relativistic shift is well known: for a Keplerian orbit with $r_{\rm per} \sim 1\,{\rm AU}$, the difference in the relativistic periapsis with respect to the Newtonian value is $\sim 0.12\,{\rm AU}$, attributable to the

attractive third term that appears in the relativistic potential in equation (2.5). Thus, when the binary has $v_{\rm in} < 50\,{\rm km\,s^{-1}}$, both stars are likely to be tidally disrupted by the SMBH.

Ginsburg & Loeb (2006) noted that the typical impact parameter that leads to the break-up of the binary by the black hole, is much larger than r_t, the tidal disruption radius for a single star. On this basis, they ignored stellar tidal disruptions. Our initial conditions are essentially the same as theirs; but as shown in Figure 2.1, these initial conditions would result in stellar tidal disruption for a large fraction of the orbits, contrary to the assumption of Ginsburg & Loeb. In their subsequent paper, Ginsburg & Loeb (2007) assumed $v_{in} < 25\,{\rm km\,s^{-1}}$, which *always* leads to stellar disruption. Our study demonstrates that the relevant distance in the problem is the orbital periapsis of the center of mass of the binary (equation 2.1), which is also the distance of the closest approach of the stars to the SMBH. Indeed, for a wide range of initial velocities, the stars penetrate deeply the SMBH's potential well. For $v_{\rm in} \gtrsim 45\,{\rm km\,s^{-1}}$ tidal disruption is avoided but tidal perturbations of the SMBH would still be expected to have a significant influence on the subsequent evolution of the stars.

Figure 2.1 also indicates that it is possible for only one star to be captured. In our calculations this mechanism does not produce a significant number of HVSs since this occurs for a narrow range of initial velocities: $v_{\rm in} \approx v_1^c$ in the classical case, and $v_{\rm in} \gtrsim v_1^c$ in the relativistic case. Between these cases we found that for wider binaries ($a_0 = 0.2$AU) the non-disrupted star is typically still on a bound orbit around the SMBH while for tighter binaries ($a_0 = 0.05$AU) the ejection probability is around $\sim 80\%$ and the mean ejection velocity is $\sim 3000\,{\rm km\,s^{-1}}$.

If $r_{\rm per}$ is slightly larger than $r_{\rm t}$, the binary is usually disrupted at the first encounter with the SMBH. However we found a small fraction of orbits for which the binary survived for longer times. In our simulations, unbinding of the binary ($E_{\rm b} \approx 0$) occurs approximately at 2 AU for $a_0 \approx 0.05$ AU and at ~ 10 AU for $a_0 \approx 0.2$ AU. In the subsequent evolution the separation between the stars does not change appreciably until the periapsis passage. After this point, the stars can either separate or become bound to each other again, continuing to orbit the SMBH as a binary. When this occurs, the minimum separation between the stars can become very small at later times.

An example of the latter situation is illustrated in Figure 2.2, which shows the evolution of the separation between the stars, as well as the orbit of the binary with respect to the SMBH, for an initial separation $a_0 \sim 0.05$ AU and initial velocity $v_{\rm in} = 51\,{\rm km\,s^{-1}}$. After the first encounter with the SMBH, where the internal binary eccentricity suddenly changes, the periapsis separation between the stars is ~ 0.035 AU while the apoapsis separation is ~ 0.08 AU. After the second encounter, the stars orbit each other on an elliptical orbit with periapsis separation ~ 0.028 AU. The third encounter with the massive object results in a very eccentric orbit. Finally, after four encounters with the SMBH the binary is disrupted and the two stars begin to orbit the SMBH on two different high eccentricity orbits.

The previous arguments suggest that the eventual shrinkage of the orbit after the encounter with the SMBH can easily trigger mass transfer and, in extreme cases, a coalescence between the

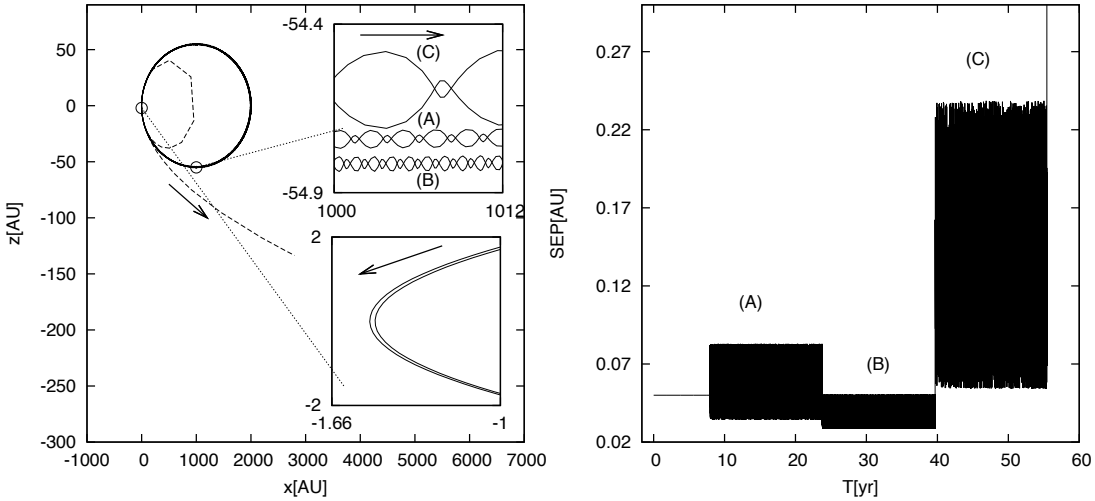

Figure 2.2 Example of an orbit whose periastron separation from the SMBH is $r_{\rm per} \gtrsim r_t$. The binary is initially located at $x = 2000$AU(0.01pc) with a purely tangential initial velocity of $v_z = 51\,{\rm km\,s^{-1}}$. The stellar masses are $M_* = 3\,{\rm M}_\odot$ with initial binary separation $a_0 = 0.05$ AU. The left panel shows the orbit of the stars. The binary makes three revolutions around the SMBH before it is disrupted, after this point the individual stellar orbits are given by dashed lines. The upper inset panel schematically displays the different internal binary orbits during the first (A), second (B), and final loop (C). The lower inset panel shows the stars' orbits with respect to the SMBH during the first encounter. Note that the x and z-axes have very different scales. The right panel displays the change of the separation between the stars with time. The upper and lower limits of each "block" represent apoapsis and periapsis of the internal binary orbit respectively.

stars. The merger remnant would orbit the SMBH on a highly eccentric orbit. In the case displayed in Figure 2.2, the minimum separation between the stars is small enough to allow mass transfer after the second passage close to the SMBH. The Roche limit corresponding to the onset of mass transfer in binary systems of equal-mass stars would be $\sim 2.8R_*$ while the dynamical instability limit in the case of co-rotating equal-mass MS stars is located around $\sim 2.4R_*$ (Rasio & Shapiro 1992, 1995); for the case of eccentric binaries the radius of the Roche lobe is similar to that of circular binaries when calculated at periastron (Regös et al. 2005). We also stress that this scenario would hold for higher values of $r_{\rm per}$, in which case it would not be restricted to small periastron separations, as will be shown below.

From this first set of integrations we deduce that cases in which only a single star is captured are relatively rare, and occur when $r_{\rm per} \approx r_{\rm t}$. Stars ejected from these orbits are expected to contribute weakly to the population of HVSs. This conclusion should hold in general when different values of d and M_* are chosen.

Table 2.1 Initial parameters.

a_0[AU]	M_*[$M_\odot$]	d[pc]	Gravity
0.2	3	0.01	post-Newtonian and Newtonian
0.2	6	0.01	post-Newtonian and Newtonian
0.05	3	0.01	post-Newtonian and Newtonian
0.05	6	0.01	post-Newtonian and Newtonian
0.2	3	0.1	post-Newtonian
0.2	6	0.1	post-Newtonian
0.05	3	0.1	post-Newtonian
0.05	6	0.1	post-Newtonian

Table 2.2 Ejection probabilities for the post-Newtonian (Newtonian) runs described in Table 2.1 for cases where $r_{\rm per} < r_{\rm bt}$.

a_0[AU]	M_*[$M_\odot$]	d[pc]	Escape with $v_{\rm ej} > 800\,{\rm km\,s^{-1}}$	Escape with $v_{\rm ej} > 1000\,{\rm km\,s^{-1}}$	Escape with $v_{\rm ej} > 1400\,{\rm km\,s^{-1}}$	Escape SMBH
0.2	3	0.01	11.0(9.57)	9.71 (7.35)	6.60 (7.02)	28.2 (24.3)
0.2	6	0.01	55.5(56.3)	53.5 (49.7)	27.7 (27.5)	57.3 (60.7)
0.05	3	0.01	68.6(62.0)	66.7 (62.0)	65.6 (62.0)	72.0 (62.0)
0.05	6	0.01	54.2(66.0)	52.5 (65.1)	52.5 (65.1)	65.5 (66.3)
0.2	3	0.1	80.0	74.5	55.5	89.1
0.2	6	0.1	80.9	79.1	71.8	85.5
0.05	3	0.1	69.3	69.3	69.3	71.6
0.05	6	0.1	44.3	44.3	44.3	44.3

2.5 Ejection of HVSs

For the remainder of this chapter, we focus on cases where $r_{\rm per} > r_{\rm t}$. This allows us to neglect possible tidal effects on stars that would require a hydrodynamic treatment.

The tidal disruption of binaries by SgrA* is generally accepted to be the main source of HVSs (stars ejected with $v > 1000\,{\rm km\,s^{-1}}$) in our galaxy. The maximum velocity that can be achieved with the classical binary supernova scenario (Blaauw 1961) is $\lesssim 300\,{\rm km\,s^{-1}}$ for $3\,M_\odot$ stars. Interactions with a massive compact object seem necessary in order to explain the extreme velocities of HVSs.

In this section we explore this mechanism by integrating a set of ~ 10000 orbits featuring binary stars closely interacting with a SMBH. Two different stellar masses were considered: $M_* = 3\,M_\odot$ and $6\,M_\odot$. The runs were performed for initial velocities that correspond to periapsis between $r_{\rm t}$ and $6r_{\rm bt}$. In all the simulations the final integration time was fixed to 60 orbital periods of the initial binary orbit around the SMBH. For the adopted periapsis distances, this integration time is long enough for the perturbations induced by the SMBH on the internal binary's orbit to grow dramatically. Table 2.1 summarizes the initial parameters we chose for the integrations.

Because the binary is initially bound to the SMBH, no HVS is produced when two stars merge (i.e., if the relative velocity is lower than the escape velocity from the stellar surface after a

collision). On the other hand, if the stars collide without merging the ejection of a single star is still possible. Hence, in the following, we assume that a HVS ejection is possible even after the stars collide, unless the final product is a merger.

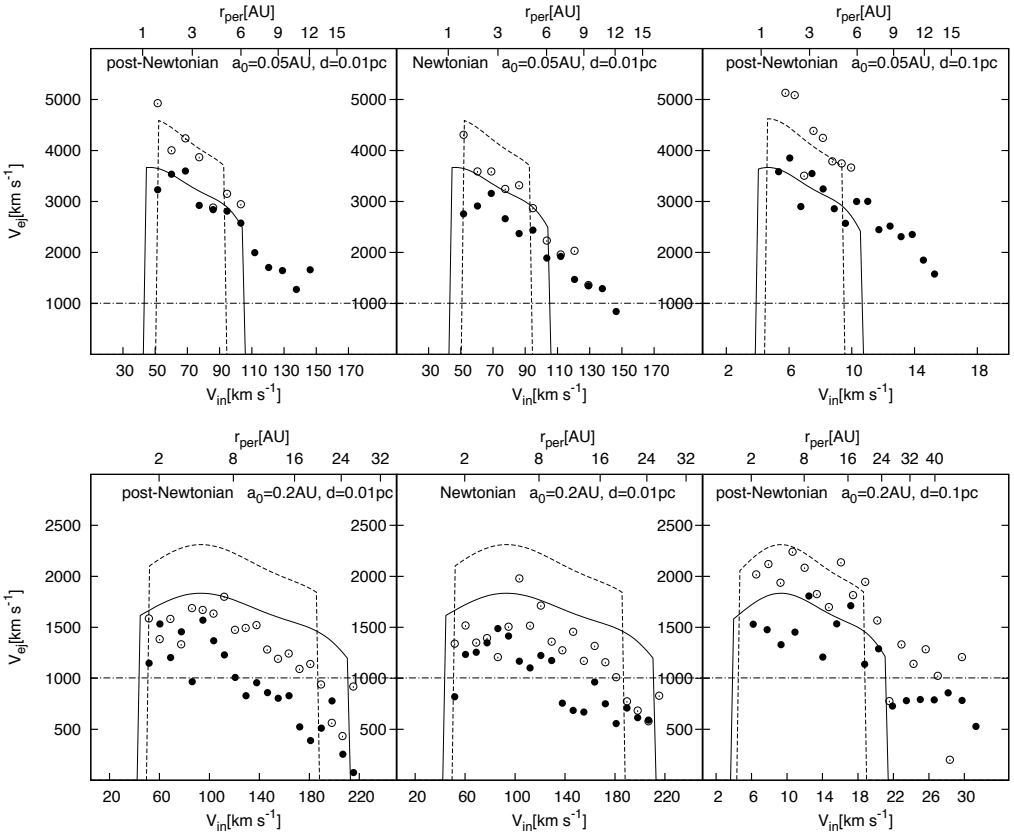

Figure 2.3 Average ejection velocity of the stars unbound to the SMBH for stellar masses 3 $M_\odot$ (filled circles) and 6 $M_\odot$(open circles). The model described in §3 is superposed using dashed lines for 6 $M_\odot$ and solid lines for 3 $M_\odot$. The horizontal dot-dashed line shows the approximate escape velocity from the Milky Way ($\sim 1000\,\mathrm{km\,s^{-1}}$).

2.5.1 Unbound population

Figure 2.3 displays the average asymptotic ejection velocity of the stars unbound from the central object, as well as a comparison with the approximate model described by equations (2.4), (2.6) and (2.7). Our results are in fair agreement with the predicted model, at least for $d = 0.1$pc. When the apoapsis of the initial orbit is reduced to $d = 0.01$pc and $a_0 = 0.2AU$, the ejection speed of the unbound stars can be a factor of 2 smaller than the typical values found for initially unbound stars. For $a_0 = 0.05$AU, on the other hand, the results are in good agreement with the model. The larger discrepancy in the case of wider binaries with respect to the theoretical model (i.e.,

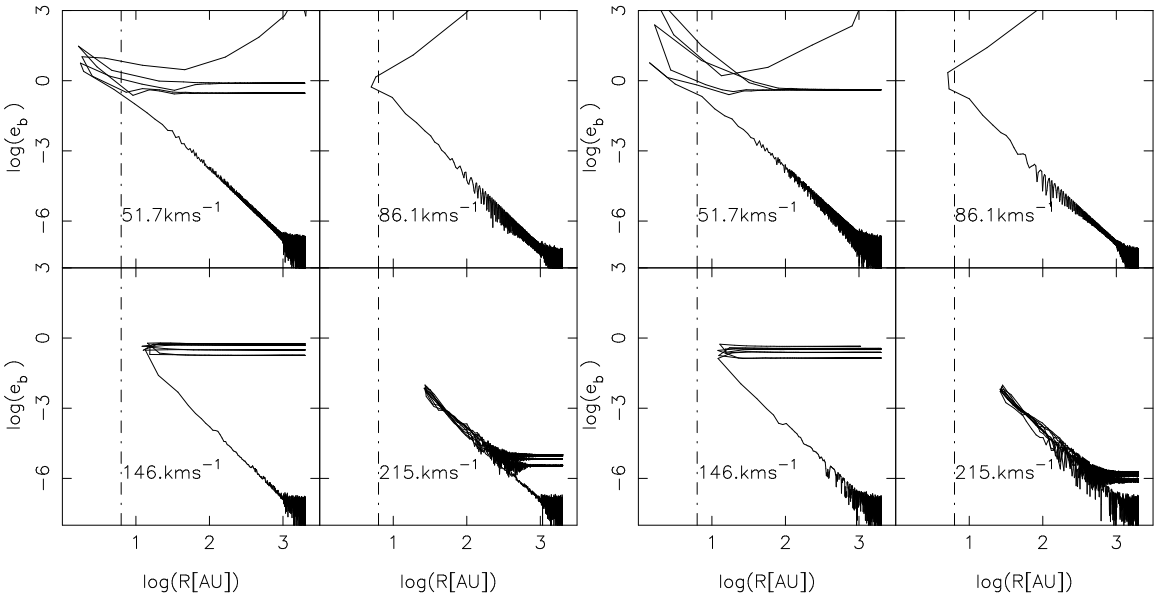

Figure 2.4 Internal binary eccentricity $e_{\rm b}$ as a function of the distance R to the SMBH for different initial velocities (displayed in the panels). The binaries have initial separation $a_0 = 0.05\,{\rm AU}$, stellar masses $3\,{\rm M}_\odot$ and the apoapsis is 0.01pc. Top: Newtonian integrations. Bottom: PN integrations. The vertical dot-dashed line gives the value of $r_{\rm bt}$. For small $v_{\rm in}$, the binary approaches very near the SMBH and the encounter results in the tidal break-up of the binary. In some cases the binary can complete several orbits around the SMBH before its stellar components are finally separated, even though $r_{\rm per} < r_{\rm bt}$. Binaries with larger periapsis separations, or, equivalently, larger initial velocities, are likely to survive for a larger number of orbits. During each periapsis passage, gravitational interactions produce significant changes in the internal eccentricity of the binary.

unbound orbits) is due to their larger value of $r_{\rm bt}$. Since the ejection velocity depends strongly on the Keplerian velocity of the binary when its components start to separate, the contribution of the binary orbital energy to $v_{\rm ej}$ will be more important when the disruption occurs at larger distances from the SMBH. Another source of the observed discrepancy is due to the artificial truncation done at v_2^c, beyond which a number of unbound stars are still produced which represent the tail of the distribution with the lowest values of $v_{\rm ej}$. These cases are mainly due to binaries which are broken apart after few orbits around the central object. At each encounter the internal eccentricity of the binary changes, and there is a new chance for the stars to be separated and for a member to be ejected.

To demonstrate the orbital evolution during an integration, Figure 2.4 shows the change of the internal binary eccentricity $e_{\rm b}$ as a function of the distance to the SMBH for several representative cases with different initial velocities in both PN and Newtonian gravity. The eccentricity was evaluated from the specific angular momentum and binding energy of the binary:

$e = \sqrt{1 + 2EL^2/(GM_{\rm b})^2}$. The initial separations, stellar masses, and apoapses were given respectively by $a_0 = 0.05\,{\rm AU}$, $M_* = 3\,{\rm M}_\odot$ and $d = 0.01{\rm pc}$. The eccentricity behaves similarly for different initial conditions, increasing suddenly at $\sim r_{\rm bt}$, though in some cases the orbits may do several passages within $r_{\rm bt}$ while maintaining a negative internal binary energy. When the binary has a small periapsis, several transitions between $e_{\rm b} > 1$ (unbound) and < 1 (bound) are possible.

Results from our runs whose orbits have periapses within the binary tidal disruption radius (i.e., $r_{\rm per} < r_{\rm bt}$) are described in Table 2.2. In general, we find for wider binaries with $a_0 = 0.2{\rm AU}$, lighter binaries with $M_* = 3\,{\rm M}_\odot$ are less likely to produce HVSs capable of escaping the galaxy than heavier binaries with $M_* = 6\,{\rm M}_\odot$, though they can produce a significant population of stars bound to the galaxy but unbound from the central SMBH. For tighter binaries with $a_0 = 0.05{\rm AU}$ the situation is reversed, and lighter binaries are more likely to eject HVSs from the galaxy. For these tighter binaries, there are very few ejections of stars that unbind from the SMBH but remain bound to the galaxy, regardless of the stellar mass.

A comparison between the velocity distributions of the ejected stars in the Newtonian and PN cases reveals that relativistic effects have a slight influence on the mean properties of the sample. In particular for $a_0 = 0.05{\rm AU}$ and $d = 0.01{\rm pc}$ the mean ejection speed is larger when the relativistic corrections are included. For larger separations, instead, this effect is absent and the simulations show similar results. However, we were not able to identify a clear systematic effect due to the PN corrections in the properties of the ejected stars.

2.5.2 The Bound Population

Each star ejected during a binary-SMBH encounter is associated with a captured companion that loses energy in the process and becomes more tightly bound to the SMBH on a high eccentricity ($e \gtrsim 0.9$) orbit. Bound stars are also produced after the tidal break up of a binary if neither star is ejected. The orbital parameters of the bound stars will be strongly correlated with the amount of energy carried away by the companion. For an initially unbound orbit the apoapsis distance of the bound star is approximately

$$a \sim \frac{GM_\bullet}{v_{\rm ej}^2}, \tag{2.9}$$

and the corresponding orbital period is

$$P \sim \frac{GM_\bullet}{v_{\rm ej}^3}. \tag{2.10}$$

The mean value of the semimajor axis A (with respect to the massive body) for three-body exchanges with equal-mass binaries can be expressed as (Hills 1991)

$$\langle A \rangle \approx 0.56 \left(\frac{M_\bullet}{M_{\rm b}}\right)^{2/3} a_0. \tag{2.11}$$

Bound stars can also be produced when the binary components merge. A coalescence remnant will not be able to escape the SMBH gravitational potential if the initial binary is bound

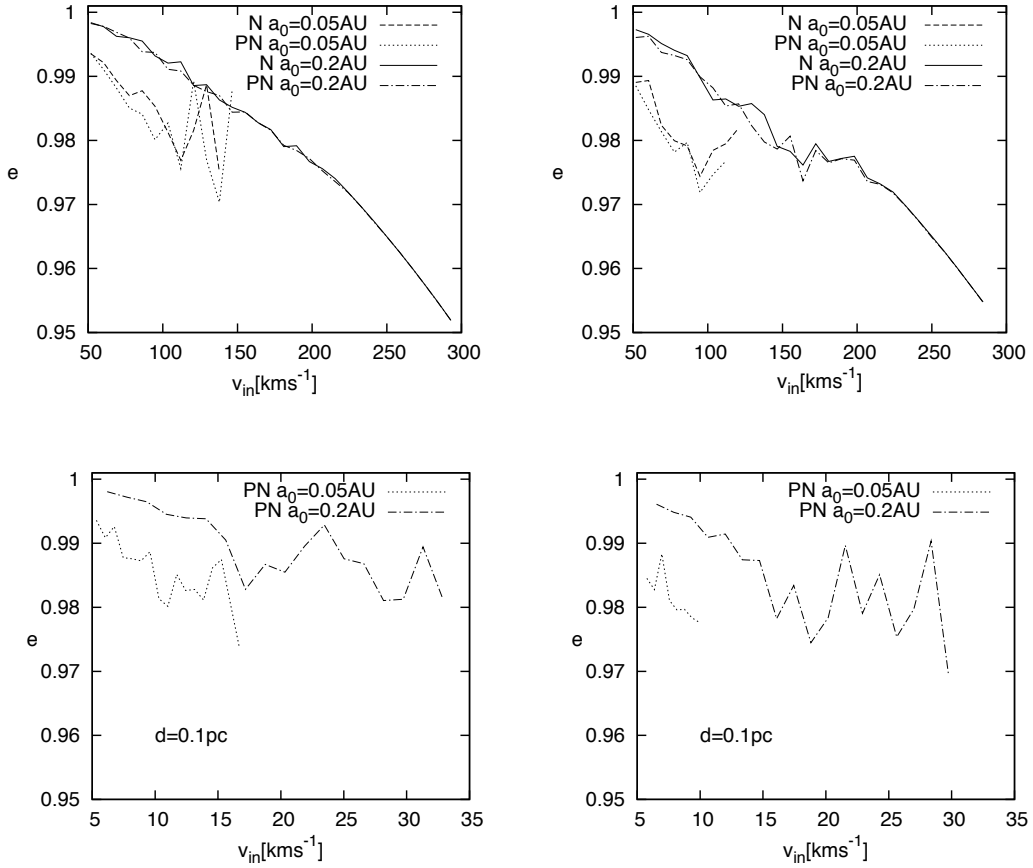

Figure 2.5 eccentricity versus the initial velocity $v_{\rm in}$ of the initial orbit with respect to SMBH, for the orbits of bound stars with masses $3\,{\rm M}_\odot$ (left panels) and $6\,{\rm M}_\odot$ (right panels). The eccentricity is average over initial binary orientation. Higher stellar masses and lower binary separations tend to reduce the orbital eccentricity of the captured stars.

to the SMBH unless significant mass loss occurs during coalescence.

Figure 2.5 shows the dependence of the average final eccentricity of bound stars on $v_{\rm in}$. A decrease in $v_{\rm in}$ (and thus an increase in the eccentricity of the initial orbit) results in a larger final eccentricity for the bound star, while larger stellar masses and initial binary separations decrease the eccentricity of the captured star's orbit. Figure 2.6 displays the eccentricity instead as a function of the orbital period of the stars that remain bound to the SMBH at the end of our PN simulations (the Newtonian calculations look similar). If we neglect the bound stars produced by mergers, three different families can be identified:

1) Bound stars whose companion also orbits the SMBH (grey open circles in Figure 2.6);

2) Bound stars whose companion has been ejected by the SMBH but remains bound to the Galaxy

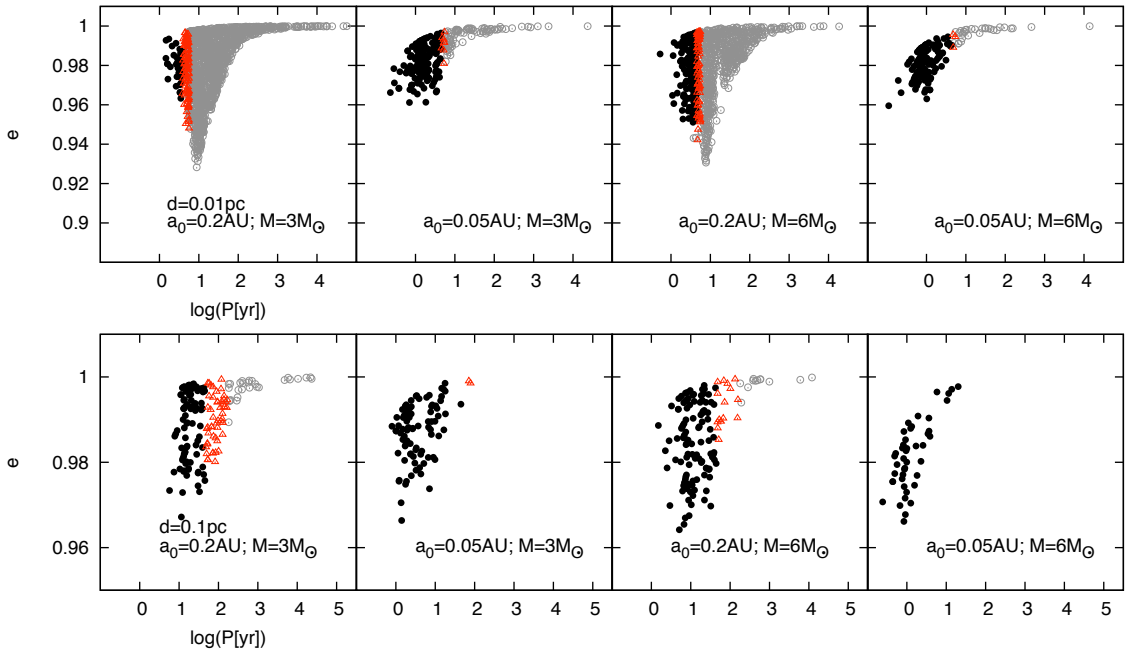

Figure 2.6 Eccentricity versus period for the orbits of the stars that remain bound to the SMBH at the end of the PN integrations. The grey open circles correspond to stars whose companion is also orbiting the SMBH. Stars whose companion has been ejected by the SMBH but remains bound to the Galaxy are represented by red triangles, while stars whose companion escapes as a HVS are indicated by filled circles.

(red triangles in the figure);

3) Bound stars whose companion is a HVS escaping the Galaxy (filled circles in the figure). The approximate escape velocity from the Galaxy was chosen to be $1000\,\mathrm{km\,s^{-1}}$ which corresponds to stars able to reach distances larger than ~ 100kpc from the Galactic center (Kenyon et al. 2008).

Due to the dependence of the apoapsis distance on the ejection velocity (see equation 2.9) the three families occupy distinct regions on the $e-P$ plane. If more kinetic energy is deposited into the ejected star, the apoapsis distance of the bound star is reduced. In the case of equal mass binaries, the range of possible periods for the three populations of bound stars are independent of the stellar mass and the binary separation.

On the other hand, in the case of unequal mass binaries with $q = M_{\rm b}/2M_1$ the apoapsis distance of the bound star can be approximated by

$$a_1 \sim \frac{GM_\bullet}{v_{\rm ej}^2} q, \tag{2.12}$$

where $v_{\rm ej}$ is given by equation 2.7 and for moderate mass ratios, the probability to be captured is almost independent by the stellar mass.

Figure 2.6 shows that the stars with the highest values of P and e have reached velocities close to the escape velocity from the SMBH. Their companions also orbit the SMBH, but with much shorter periods. The region $e = 0.92 - 0.95$, strongly populated for $a_0 = 0.2\,\mathrm{AU}$ and $d = 0.01\mathrm{pc}$, is occupied by stars that were initially part of binaries with the largest values of v_{in}. For $d = 0.1\mathrm{pc}$ bound stars are mainly companions of ejected stars and the comparable region is empty.

Stars whose the companion is escaping the Galaxy have orbital periods $\lesssim 50\mathrm{yr}$. Many cases with orbital periods $\lesssim 10\mathrm{yr}$ are also observed.

Finally, we note that in PN gravity the periapsis distances of bound stars are about 0.1 AU smaller than in the Newtonian regime.

2.6 Collisions and Mergers

In this section, we study the evolution of binaries that are strongly perturbed during close passages to the SMBH, leading to stellar collisions and mergers. Stellar collisions due to either binary evolution or dynamical interactions are thought to be the main mechanism for the production of blue stragglers in star clusters (Collier et al. 1984; Benz & Hills 1987; Leonard 1989; Mateo et al. 1990). Similar processes may occur at the Galactic center, producing a population of "rejuvenated" stars. Genzel et al. (2003) proposed that the S-stars may be "super-blue stragglers" formed by collisions of lower mass stars and/or tidal heating. The apparent normality of their spectra (Eisenahauer et al. 2005) argues against rejuvenation (Figer 2008), but given the uncertainties in the relaxation of merger products and the redistribution of angular momentum, it is difficult to draw firm conclusions as to their history.

It is possible that the S-stars are drawn from the young population observed in the stellar disk that extends inward to within 0.1 pc of the SMBH, but while the S-stars are primarily B dwarfs, the young stars in the disk are mainly luminous Wolf-Rayet and OB supergiants and giants (Paumard et al. 2001). This limits the connection between the two stellar populations, as O/W-R stars are typically more massive and shorter-lived than B types. Löckmann et al. (2008) proposed that binaries scattered from the stellar disk on highly eccentric bound orbits around the SMBH would be disrupted, ejecting one member as a HVS while leaving the other member bound. The inspiral of a cluster hosting an IMBH would generate stars on comparable orbits.

GL07 noted that the production of HVSs at the Galactic center could also result in collisions: the SMBH disrupts a binary, delivering an impulsive kick to one of the two stars at some direction with respect to the orbital plane, and under some circumstances the two stars will collide. We expect a dependence of the collision probability on the initial binary orientation (unless gravitational focusing dominates) and a correlation between the number of HVSs produced and the number of collisions. However, GL07 concluded that the frequency of mergers is so low that no star in the Galactic center is expected to have been produced by binary coalescence.

To investigate the rates of mergers and collisions using N-body techniques, we define the

minimum impact parameter for a collision as $2R_*$, and the two stars are assumed to merge when their relative speed upon collision is lower than the escape velocity from their surfaces.

We find a much higher rate of coalescence than found by GL07, with most close collisions occurring only after repeated encounters of the binary with the SMBH. The mechanism that leads to the majority of the close encounters in our integrations is Kozai oscillations.

Table 2.3 HVSs ($v_{\rm ej} > 1000\,{\rm km\,s^{-1}}$), Collision and Merger frequency(%) for runs with $r_{\rm per} \leq 6r_{\rm bt}$.

post-Newtonian (Newtonian); $d = 0.01$pc									
	1 orbital period			5 orbital periods			60 orbital periods		
a_0[AU], M_*[$M_\odot$]	HVSs	Coll	Merg	HVSs	Coll	Merg	HVSs	Coll	Merg
0.2, 3	3.14 (3.00)	2.54(2.18)	1.50(2.15)	3.65 (3.25)	8.30 (9.10)	5.49 (5.29)	4.31 (3.26)	22.0 (20.5)	17.0(16.6)
0.2, 6	15.2 (15.4)	4.47(2.92)	3.01(2.62)	16.5 (16.7)	18.3 (12.5)	9.11 (9.59)	17.4 (16.8)	30.6 (30.6)	27.5(27.4)
0.05, 3	16.3 (16.8)	8.05(9.74)	5.97(5.45)	21.7 (18.2)	15.7 (23.4)	14.4 (20.6)	22.4 (21.0)	41.0(47.0)	40.1(43.8)
0.05, 6	15.6 (16.2)	13.8(16.2)	13.8(13.3)	15.9 (16.9)	24.3 (30.2)	23.9 (27.9)	20.8 (20.2)	47.5 (55.5)	47.1 (53.2)
post-Newtonian; $d = 0.1$pc									
	1 orbital period			5 orbital periods			60 orbital periods		
a_0[AU], M_*[$M_\odot$]	HVSs	Coll	Merg	HVSs	Coll	Merg	HVSs	Coll	Merg
0.2, 3	29.0	1.66	1.00	30.0	5.00	3.60	30.0	18.6	17.1
0.2, 6	31.6	4.33	3.33	35.6	12.0	9.33	37.0	20.3	16.3
0.05, 3	25.0	8.33	8.05	27.1	21.7	21.0	28.0	30.3	29.6
0.05, 6	13.3	18.3	16.0	14.3	27.0	24.3	14.7	40.0	37.3

2.6.1 Kozai oscillations

The perturbations on the inner binary's orbit caused by the gravitational interaction with the SMBH can result in periodic oscillations (Kozai cycles) of both the internal binary eccentricity $e_{\rm b}$ and the mutual inclination j (Kozai 1962). This occurs when the initial inclination $j_{\rm in}$ is sufficiently large and when the stars approach the SMBH at relatively large periapses ($\gtrsim r_{\rm bt}$) . More precisely, the perturbations from the SMBH on the inner binary must always be weak and $j_{\rm in}$ needs to satisfy the relation $i_{\rm c} \leq j_{\rm in} \leq 180^\circ - i_{\rm c}$, where the critical angle $i_{\rm c}$ can be assumed to be $\sim 40^\circ$ in the case of initially circular binaries and Newtonian gravity. Kozai cycles can result in a reduction of the periapsis separation, allowing the inner bodies to collide. The period of the cycles can be written in terms of the masses of the three bodies, the eccentricity of the outer binary e and their semimajor axis as:

$$\tau = \frac{P_{\rm out}^2}{P_{\rm b}} \left(1-e^2\right)^{3/2} \left(\frac{M_{\rm b}+M_\bullet}{M_\bullet}\right) K(e_{\rm b}, \omega_{\rm b}, j_{\rm in}) \simeq \frac{P_{\rm out}^2}{P_{\rm b}} \left(1-e^2\right)^{3/2} \tag{2.13}$$

where $P_{\rm b}$ is the periods of the inner binary , $P_{\rm out}$ the external period, $e_{\rm b}$ and $\omega_{\rm b}$ the inner binary eccentricity and argument of periapsis, and K is generally of order unity (Ford et al. 2000). Writing

$$P_{\rm b} = 2\pi \left(\frac{a_0^3}{G\ M_{\rm b}}\right)^{1/2} = 4.5\times10^{-3} \left[\left(\frac{a_0}{0.05{\rm AU}}\right)^3 \left(\frac{6M_\odot}{M_{\rm b}}\right)\right]^{1/2} {\rm yr} \tag{2.14}$$

and

$$P_{\rm out} = 2\pi \left(\frac{[d/(1+e)]^3}{G\ M_\bullet}\right)^{1/2} = \frac{44.4}{(1+e)^{3/2}} \left[\left(\frac{d}{0.01{\rm pc}}\right)^3 \left(\frac{4\times10^6 M_\odot}{M_\bullet}\right)\right]^{1/2} {\rm yr} \tag{2.15}$$

the Kozai period becomes

$$\tau \simeq \frac{2\pi}{\sqrt{G}} \frac{M_{\rm b}^{1/2}}{M_\bullet} \left(\frac{d}{a_0^{1/2}}\right)^3 \frac{\left(1-e^2\right)^{3/2}}{\left(1+e\right)^3} = 4.4\times10^5 \left(\frac{a_0}{0.05{\rm AU}}\right)^{-3/2} \left(\frac{M_{\rm b}}{6{\rm M}_\odot}\right)^{1/2} \times \left(\frac{M_\bullet}{4\times10^6{\rm M}_\odot}\right)^{-1} \left(\frac{d}{0.01{\rm pc}}\right)^3 \frac{\left(1-e^2\right)^{3/2}}{\left(1+e\right)^3} {\rm yr}. \tag{2.16}$$

Thus, in our integrations, the Kozai period is between ~ 2 and ~ 120 times longer than the orbital period around the SMBH, and the full effect of the Kozai cycles is only felt after several revolutions.

If the orbit is initially circular, the maximum eccentricity achieved during a Kozai cycle is

$$e_{\rm b,max} = \left[1-(5/3)\cos^2 j_{\rm in}\right]^{1/2} \ , \tag{2.17}$$

the amplitude of the oscillations depending only on the initial inclination of the inner orbit relative to the external perturber. The eccentricity of the outer binary remains roughly constant throughout the evolution, because its variation is caused by octupole interactions, which are weaker than the quadrupole interactions driving the oscillations of the inner binary's eccentricity (Takeda & Rasio 2005).

Kozai resonances can be suppressed by additional sources of apsidal precession such as tides and relativistic precession in the inner binary. The inclusion of PN effects between the two stars damps the oscillations of the inner orbital eccentricity, eventually causing a decrease in the number of observed collisions and mergers (Holman et al. 1997; Blaes et al. 2002).

2.6.2 Results

The results of our runs show, for what we believe to be the first time, that binary break-up is not a prerequisite for physical collisions, and that the collision probability increases strongly with time: increasing the simulation time (and thus the number of revolutions around the SMBH) results in a dramatic increase in the number of collisions. The first point is of particular relevance for binaries with high values of $r_{\rm per}$, for which the SMBH more gradually reduces the internal binary angular momentum. This would allow the two stars to closely interact through mass transfer and eventually merge while they are still bound to each other. We note that the first encounter with separation $\leq 2R_*$ usually occurs just after the closest approach of the binary to the SMBH, when the orbital parameters suddenly change (see Figure 2.2). With regard to the second point: allowing the orbit to make only $2-3$ extra revolutions around the SMBH increases the collision probability by up to three times with respect to shorter integrations (GL07). This is a consequence of the fact that the Kozai period is longer than the period of revolution around the SMBH.

Figure 2.7 gives four representative examples of how the inner binary parameters change when repetitive collisions occur between the stars, with and without PN corrections. These cases are difficult to treat with an N-body approach, but we may safely conclude that the stars are likely to merge after a short time. When relativistic terms are included, the maximum value of the binary eccentricity reached in a Kozai cycle, $e_{\rm b,max}$, decreases. However, we found that the effect of relativistic precession on the likelihood of collisions and mergers observed in our simulations is weak.

In Table 2.3 we list the fraction of observed collisions, mergers, and HVS ejections after the first binary-SMBH encounter, after 5 orbital periods, and after 60 orbital periods. After the first encounter, most of the binaries with small periapsis are broken apart, depositing one star on a tight orbit around the SMBH while ejecting the companion as a HVS. The frequency of HVS ejection is nearly unchanged over time because the orbits with larger periapsis do not get close enough to the SMBH to eject a member. Such orbits, instead, suffer strong perturbations from the SMBH, altering the internal orbital parameters of the binary. The larger the periapsis, the larger the time required for the perturbations to become important, and the collision and merger frequency increase strongly with time. PN terms have important consequences only for initially small binary separations since the relativistic precession period is smallest for these systems. However, as shown in Table 2.3 the fraction of collisions is reduced by no more than 10% for $d = 0.01$pc, since for tight binaries even small eccentricities lead to close stellar encounters.

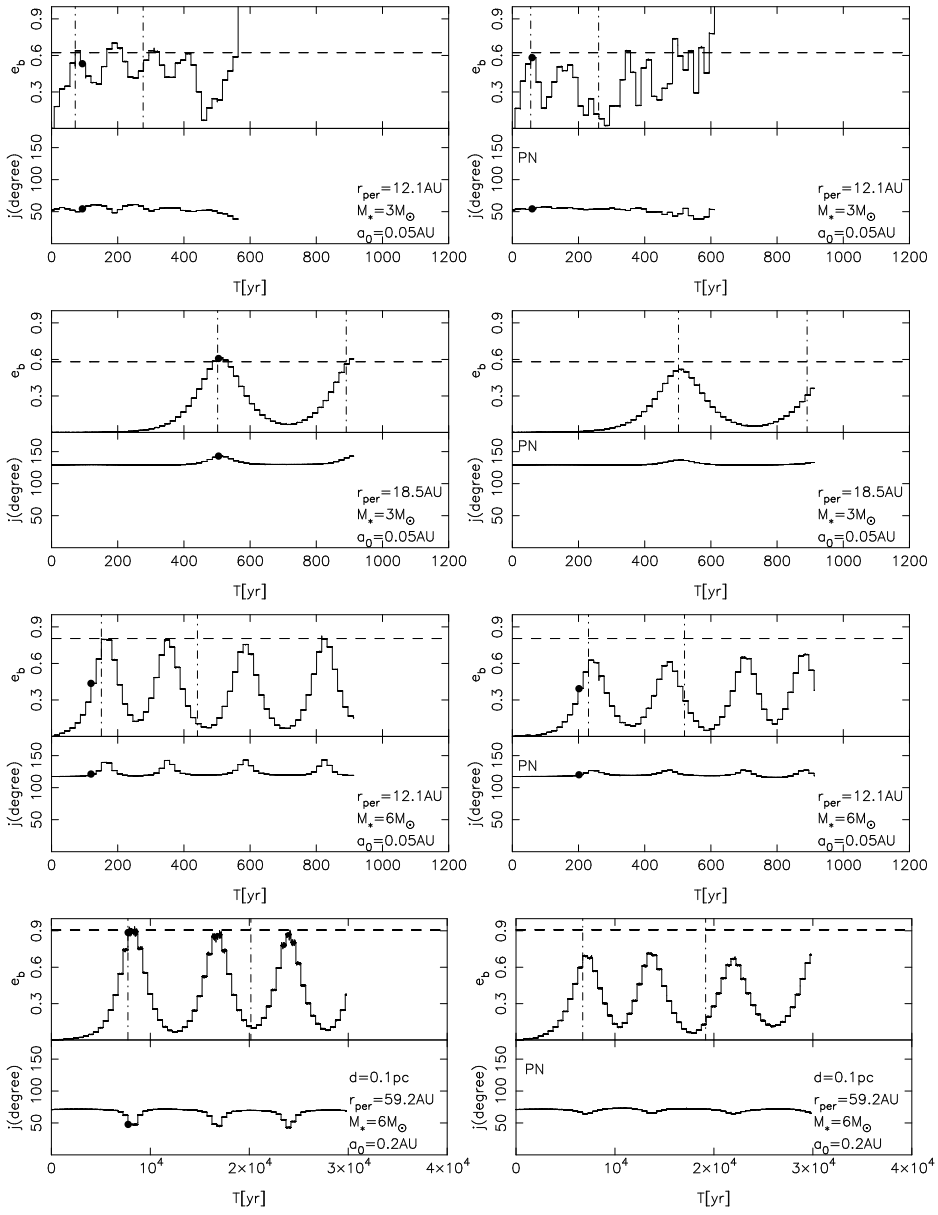

Figure 2.7 Evolution of the internal binary eccentricity and the mutual inclination j for different simulations in Newtonian (left panels) and PN (right panels) runs. In the cases shown, stars experience multiple collisions, and the time at which they finally merge is marked by a filled circle. For each periapsis distance considered , the corresponding Newtonian and PN integrations were started from the same initial conditions. The top three rows have $d = 0.01$pc and the bottom panels have $d = 0.1$ pc. The horizontal dashed lines marks the *classical* value $e_{\rm b,max}$ given in equation (2.17). The vertical dot-dashed lines give the Kozai timescale. When the periapsis is sufficiently large the binary undergoes Kozai resonance, periodically changing both $e_{\rm b}$ and j. When PN terms are included the amplitude of the oscillations decreases, resulting in a larger survival time for the binary and a smaller probability for a collision. The bottom panels show the evolution for systems with $d = 0.1$pc, for which the stars do not merge if PN corrections are included.

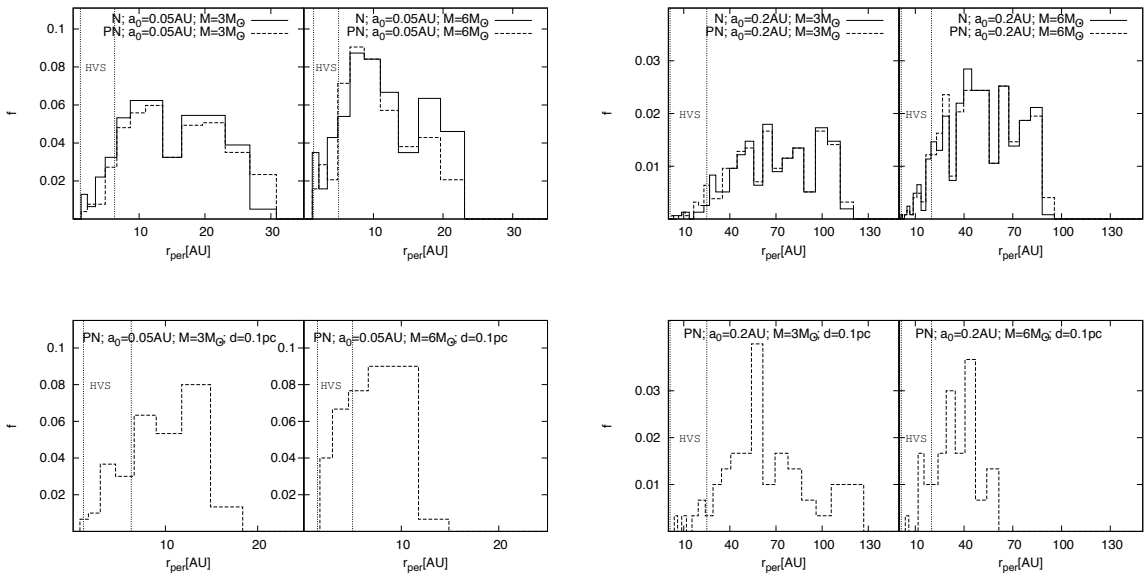

Figure 2.8 Fraction f of orbits leading to stellar mergers as a function of the periapsis distance for PN and Newtonian simulations. The vertical dot-dashed lines bound the region where HVSs are produced.

When the apoapsis is $d = 0.1$pc the ratio between the timescale of relativistic precession in the binary and the period of the Kozai cycles becomes much smaller suppressing the Kozai resonance. Writing the timescale of relativistic precession as:

$$\dot{\omega} = \frac{3G^{3/2}M_{\rm b}^{3/2}}{a_0^{5/2}\ c^2\ (1-e_{\rm b}^2)} = 4.9\times10^{-3}\left(\frac{M_{\rm b}}{6M_\odot}\right)^{3/2}\left(\frac{a_0}{0.05{\rm AU}}\right)^{-5/2}{\rm yr}^{-1} \tag{2.18}$$

with c the speed of light, the product $\dot{\omega}\tau$ of the initial configuration gives the relative strength of relativistic precession to that of the tidal field of the SMBH. For $M = 6M_\odot$ and $r_{\rm per} \gtrsim 12$AU , this product can be as large as 10^2 and the Kozai cycles are completely suppressed (Fabrycky & Tremaine 2007). The ejection probability, instead, increases due to the larger eccentricity of the external orbit. The combination of these effects causes a smaller fraction of collisions/mergers respect to the number of HVSs.

Figure 2.8 displays the fraction of stellar mergers as a function of the periapsis distance $r_{\rm per}$, with most cases occurring for $r_{\rm per} > r_{\rm bt}$ where the Kozai mechanism becomes active. Figure 2.9 shows the cumulative fraction of stellar collisions, mergers and ejected HVSs in our PN integrations. Most of the HVSs are ejected during the first periapsis passage. Collisions and mergers, instead, typically occur later due to Kozai resonance, on a typical time scale $\sim \tau/2$, where τ is given by equation (2.13).

We note that strong mass transfer and/or mergers can lead to the formation of a rejuvenated star (Vanbeveren et al. 1998; Dray & Tout 2007).

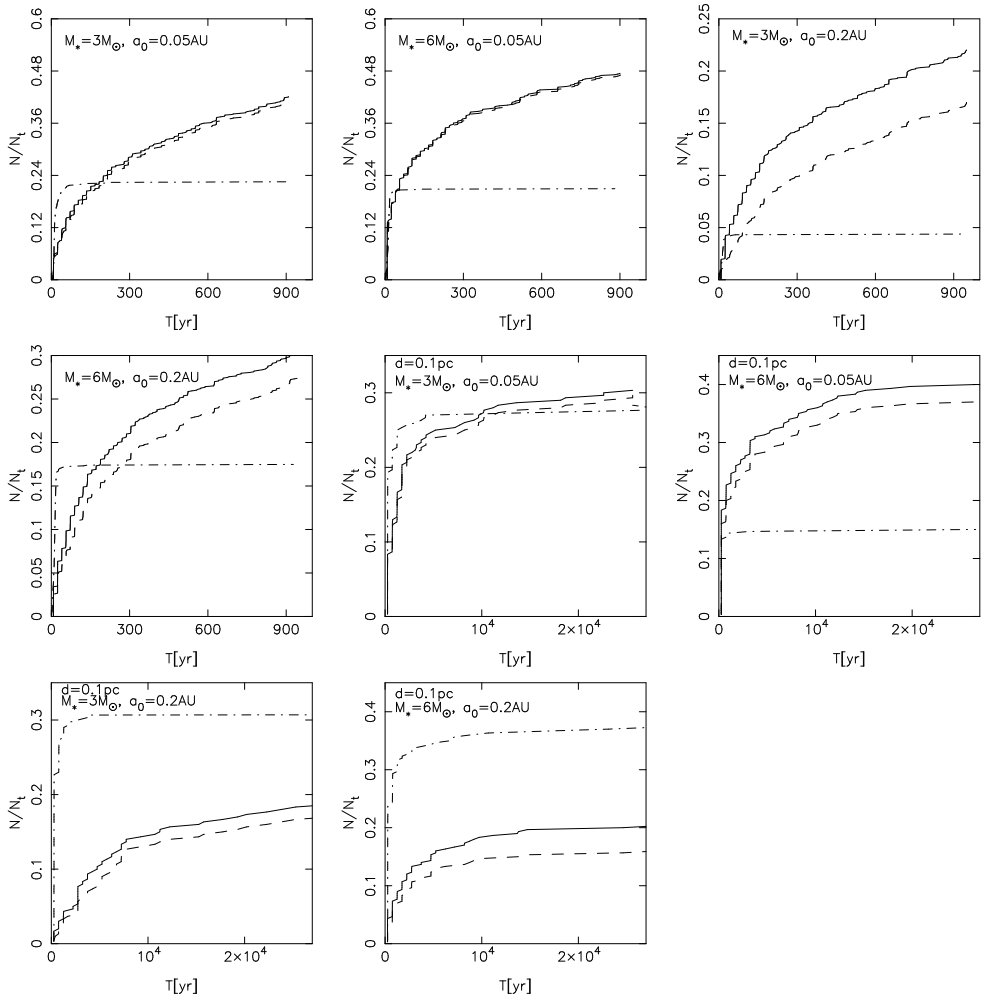

Figure 2.9 Cumulative fraction of stellar collisions (solid lines), mergers (dashed lines) and ejected HVSs (dot-dashed lines) in our PN integrations. Most of the HVSs are ejected during the first encounter with the SMBH; collisions and mergers, on the other hand, occur more frequently later after the inner binary's parameters have evolved due to the gravitational perturbations induced by the SMBH.

The implications of these results for the actual rate of stellar mergers at the center of the Galaxy will depend on the dominant mechanism that drives binaries toward the SMBH. If binaries are scattered inward by "massive perturbers" (Perets et al. 2007), most of their orbits will be weakly bound or unbound with respect to the SMBH, with apoapses of order parsecs, and will only encounter the SMBH once before being scattered onto different orbits. Given the low probability which we find for collisions during the first encounter with the SMBH for $d = 0.1$pc, we do not expect a significant merger rate unless the binary population at the Galactic center is biased toward low values of a_0. Moreover, if the binary is initially unbound, the merger product is likely to be

ejected at low velocities and it will neither remain bound (unless substantial mass loss occurs) nor become a HVS. Alternatively, mergers in this scenario may result from disruption of triples that can leave binaries on bound orbits with small apoapse (Perets 2009b). Obtaining an explicit value for the merger rate would be difficult in this case given the large uncertainties about the population of multiple stellar systems in the Galactic center.

Alternatively, the binaries may form closer to the SMBH, perhaps in a disk, and migrate inward. In this case, the rate of collisions/mergers, as given in Table 3, would be comparable to the ejection rate of HVSs, i.e. $\sim 10^{-5}\mathrm{yr}^{-1}$. However, given the strong dependence of the collision probability on the distance of closest approach to the SMBH, the merger rate will be strongly correlated with the periapse distribution of the infalling binaries. The generation of massive new stars through binary-SMBH encounters in this scenario could possibly explain the presence of the stars that appear to be the youngest among the S-star group at the Galactic center (see also Perets (2009b) and Perets & Fabrycky (2009) for discussion on rejuvanting stars through Kozai-oscillation induced mergers).

In our simulations, the distribution of the semimajor axes and eccentricities of the captured stars are fixed by the initial distance d of the binary we adopt, and therefore is completely arbitrary. Nevertheless, as previously discussed, the apoapses found in our runs are consistent with those predicted assuming the binary progenitors of HVSs were scattered on eccentric orbits bound to the SMBH. The orbital eccentricities we find ($e > 0.95$), it should be noted, are larger than those observed for the S-stars at the Galactic center, which are consistent with a thermal distribution (i.e., $N(e) \propto e$). Perets et al. (2009) have shown how perturbations from a dense cluster of $10\,\mathrm{M}_{\odot}$ stellar black holes, expected to accumulate around the SMBH due to mass segregation (Hopman & Alexander 2006), tend to randomize orbits with high eccentricity in $\sim$ 20Myr. Alternatively, if the binaries are transported to the center by the inspiral of a massive cluster containing an IMBH, interactions with the same IMBH will thermalize the eccentricities in $\sim$ 1Myr (Merritt et al. 2009). These processes of orbital randomization result also in the evolution of the periapsis distance r_{per}, but on a timescale much larger than that required for the binary systems to collide. We note, finally, that the presence of external forces on the inner binary as well as tidal friction between the stars could suppress the Kozai resonances reducing the number of stellar collisions.

2.6.3 Effect of the Initial Binary Orientation

Based on the results of our simulations, we find no strong dependence of the collision and/or merger probability during the first SMBH passage on the initial binary orientation. To quantify our results, we use the Rayleigh (dipole) statistic ζ_{c} (ζ_{m}) defined as the length of the resultant of the unit vectors $l_i,\ i = 1, ..., N$, where l_i is perpendicular to the initial internal orbital plane of the i^{th} binary system whose component stars collide (merge) during the integration and N is the number of collisions or mergers. Here the subscripts c and m refer to 'collision' and 'merger' respectively.

Table 2.4 Raleigh statistics ζ_c and ζ_m and values expected for an isotropic distribution for collisions (EV_c) and mergers(EV_m) after the first binary-SMBH encounter.

	Post-Newtonian(Newtonian); d=0.01pc			
$a_0[AU]$, $M_*[M_\odot]$	ζ_c/N	EV_c	ζ_m/N	EV_m
0.2, 3	0.33 (0.30)	0.18±0.15	0.25 (0.29)	0.23 ± 0.18
0.2, 6	0.19 (0.23)	0.17±0.14	0.21 (0.25)	0.20 ± 0.16
0.05, 3	0.20 (0.18)	0.12±0.10	0.26 (0.21)	0.13 ± 0.11
0.05, 6	0.16 (0.14)	0.10±0.08	0.21 (0.15)	0.11 ± 0.09
	Post-Newtonian; d=0.1pc			
a_0, M_*	ζ_c/N	EV_c	ζ_m/N	EV_m
0.2, 3	0.45	0.38±0.26	0.46	0.43 ± 0.27
0.2, 6	0.14	0.17±0.14	0.30	0.30 ± 0.24
0.05, 3	0.28	0.20±0.16	0.33	0.20 ± 0.17
0.05, 6	0.14	0.14±0.11	0.16	0.15 ± 0.12

For an isotropic distribution $\zeta \sim \sqrt{N}$, while $\zeta \sim N$ if some preferential direction exists (Rayleigh 1919).

In order to test the agreement with an isotropic distribution we used a Monte Carlo approach: for each set of simulation parameters we generated a set of 1000 samples, each containing N randomly oriented orbits. Then, for the whole sample we computed the average of ζ and the corresponding standard deviation and we compared the resulting values with those obtained for the colliding/merging binaries.

Table 2.4 gives the estimated values of ζ after the first binary-SMBH encounter as well as the expected values for an isotropic distribution. Assuming a confidence interval of 90%, most of the values shown in Table 2.4 are consistent with an isotropic distribution.

We find values of ζ_m too large to be consistent with isotropy only for PN integrations where $a_0 = 0.05\,\mathrm{AU}$ and $d = 0.01$pc, though for Newtonian integrations with the same apoapsis and $a_0 = 0.05\,\mathrm{AU}$, the values of ζ_m are quite large as well, possibly indicating some degree of anisotropy. In Figure 2.10, we plot the spatial projection of the angular momentum vectors for the inner binary, showing that when the angular momentum is aligned with the $+y$-axis, the stars are unlikely to merge. These binaries are retrograde and their internal orbital plane coincides the orbital plane of the binary with respect to the SMBH. In all the other cases we conclude that the collision probability does not show any significant dependence on the initial binary orientation during the first encounter with the SMBH.

At later times stellar collisions are mainly produced by the Kozai mechanism which is active only for large initial inclinations $j_{\rm in}$. This corresponds to a low probability of collisions for

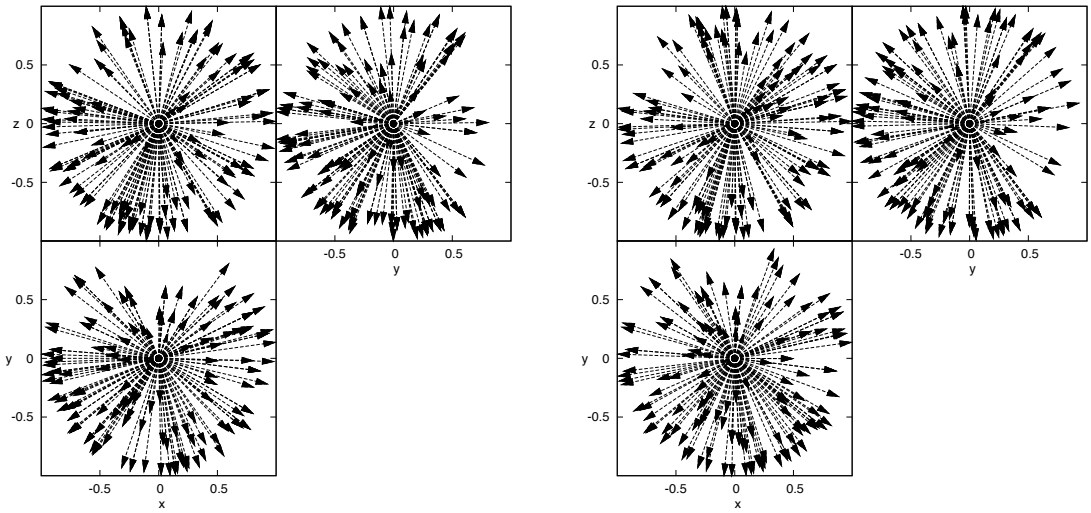

Figure 2.10 Projection of the angular momentum vectors for binaries with $a_0 = 0.05\,\mathrm{AU}$ and $d =$ 0.01pc merging during the first encounter with the SMBH for PN (left panels) and Newtonian (right panels) runs. A slight dependence of the merger likelihood on the initial binary orientation is observed, with a deficit apparent for initial orbits whose angular momentum is aligned with the $+y$-axis. The deficit is less significant in the Newtonian integrations.

binaries with the angular momentum aligned with either the $\pm y$-axis. For these cases our Rayleigh statistic results are still consistent with isotropy, but this is found to be an artifact attributable to the dipole nature of the Rayleigh statistic. A more careful analysis of the orbital distribution of binaries whose components merge at later times shows that, as expected, the population of colliding binaries is strongly biased toward large inclinations of the inner orbit with respect to the external orbital plane. An illustrative example is given in fig 2.11 which shows the projection of the internal angular momentum vectors for binaries with $a_0 = 0.2\,\mathrm{AU}$ and $d = 0.01$pc merging between 10 and 60 orbital periods. Even though the result of our statistical analysis in this case is consistent with isotropy, the distribution of the angular momenta is clearly anisotropic with most of the collisions occurring for large inclinations. The discrepancy is a consequence of the dipole nature of the Rayleigh statistic: the majority of the unit vectors l_i have a quasi-antialigned counterpart giving a net contribution close to zero.

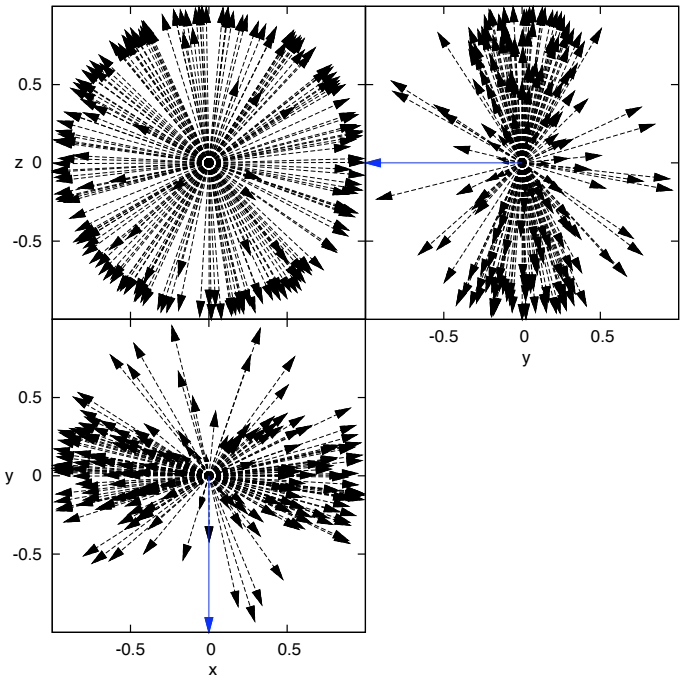

Figure 2.11 Projection of the angular momentum vectors for binaries with $a_0 = 0.2\,\mathrm{AU}$ and $d =$ 0.01pc merging between 10 and 60 orbital periods for Newtonian runs. This shows how the Kozai mechanism selects highly inclined orbits (the external orbital plane lies on the x-z plane and the direction of angular momentum corresponding to the external orbit is given by a blue continue arrow).

2.7 Summary and Discussion

We have carried out post-Newtonian numerical integrations of binary stars on highly elliptical orbits around a supermassive black hole and classified the final fates of both stars. Our main conclusions can be summarized as follows:

1. If the binary orbit passes through the stellar tidal disruption radius $r_{\rm t}$ of the SMBH, both stars are likely to be disrupted during the initial passage, although there is a non-trivial chance that one star may remain outside the tidal disruption radius while the other passes within. We found that after the binary internal energy becomes positive the stellar orbits remain close to the initial trajectory of the disrupted progenitor. This demonstrates that HVSs can suffer strong tidal perturbations and mass loss before ejection.

2. Binaries with periapses in the range $r_{\rm t} < r_{\rm per} < r_{\rm bt}$ with $\sim r_{\rm bt}$ the tidal breakup radius of the binary are the main hypervelocity star progenitors. In these cases the (hypervelocity) ejection

probability is typically larger than 50%, although the combination of wider separations ($a_0 = 0.2$AU) and small apoapses ($d = 0.01$pc) can result in probabilities less than 30%.

3. For tighter binaries (taken here to have separations of 0.05 AU), there is a strong inverse correlation between the periapse distance of the binary and the HVS ejection velocity, while the dependence is present but weaker for wider binaries.

4. While many binaries perform several orbits around the SMBH before merging and/or colliding, the vast majority of HVSs were produced during the first passage by the SMBH. This is due to the strong dependence of HVS production on the periapse distance of the binary orbit: binaries that get sufficiently close to the SMBH are broken apart, while those farther away will typically be unbound or collide.

5. The tidal break-up of equal-mass binaries by the SMBH results in a population of bound stars with periods and eccentricities defined mainly by the fate of the companion star (Fig. 6). Companions to escaping hypervelocity stars remain bound to the SMBH with orbital periods $P \lesssim 50$yr, but also extremely short periods $P < 1$yr are found. A much larger range of periods ($10^2 \lesssim P \lesssim 10^5$) is instead possible for stars whose companion is also left orbiting the SBH.

6. For sufficiently inclined orbits, the Kozai mechanism produces periodic oscillations of the inner binary eccentricity. This reduces the internal binary periapsis allowing for close stellar encounters. We find that the probability for collisions between the components of the binary increases with time, resulting in substantially larger numbers of mergers than in simulations that stop after the first passage.

7. When the external orbital period is large compared to the period of relativistic precession in the inner binary the PN corrections tend to suppress the oscillations reducing the probability of a collision which, however, remains high in our integrations. For initially bound orbits with $r_{\rm per} < 6r_{\rm bt}$ the probability that the two stars collide is similar (for $d = 0.1$pc) or much larger (for $d = 0.01$pc) than that of hypervelocity ejection.

Stars caught on highly eccentric orbits around the SMBH (with periapsis $r_{\rm t} < r < 2r_{\rm t}$) can eventually spiral in as their orbital energy is converted into heat through tidal interactions durisng each periapse passage (e.g. Alexander & Morris 2003). Such stars would have orbital properties generally consistent with the S-star population, but N-body calculations cannot accurately predict the properties of the merger products. Instead, in the next chapter, we will study the evolution of binaries as they orbit the BH and collide or merge using a smoothed particle hydrodynamics (SPH) code, to determine the properties of the resulting stars, including their masses and angular momentum distributions. This will help to clarify whether they would be expected to possess normal spectra or features more commonly associated with blue stragglers.

Finally, our study provides concrete evidence that relativistic effects can have important consequences for the distribution of HVSs and the collision/merger probabilities of HVS progenitors.

Chapter 3

Tidal break-up of binary stars at the Galactic center. Hydrodynamic simulations

3.1 Introduction

Tidal breakup of binary stars by the supermassive black hole (SMBH) at the Galactic center (GC) has been invoked to explain a number of otherwise puzzling discoveries, including the hypervelocity stars (HVSs) that are observed in the halo of the Milky Way (Brown et al. 2005, 2006, 2007, 2009), and the S-stars, apparently young, main-sequence stars in tight eccentric orbits around the SMBH (Eisenahauer et al. 2005; Gillessen et al. 2009). As first pointed out by J. Hills, close passage of a binary star near a SMBH can result in an exchange interaction, such that one component of the binary is ejected with greater than escape velocity while the other star is scattered onto a tightly-bound orbit (Hills 1988; Yu & Tremaine 2003). The predictions of this model are broadly consistent with the observed properties of both the HVSs (Bromley et al. 2006) and the S-stars (Perets et al. 2009; Perets & Gualandris 2010).

The origin of the binary progenitors of the HVSs is not clear. One possibility is that the binaries originated at distances of a few parsecs from the GC and were subsequently scattered inward by "massive-perturbers" (Perets et al. 2007). In this scenario, most of the binaries will lie on either unbound or weakly-bound orbits with respect to the SMBH, and they will encounter it only once before being scattered onto different orbits. Alternatively, the binaries may form closer to the SMBH, perhaps in the young (or an older) stellar disk that is observed between ~ 0.04 pc and ~ 0.5 pc from the SMBH (Nayakshin & Cuadra 2005; Paumard et al. 2006; Nayakshin & Cuadra 2007; Levin 2007). Also, Perets (2009b) suggested that binaries could be left near the GC

through a triple disruption by the SMBH. In these latter cases, the binaries would be bound to the SMBH and would encounter it many times before being disrupted.

If the finite sizes of stars are taken into account, a number of outcomes are possible in addition to simple binary disruption. The two stars can collide, resulting in a merger if the relative velocity is less than stellar escape velocities (Ginsburg & Loeb 2007). Since the radius of tidal disruption of single stars by the SMBH is comparable to the binary disruption radius, stars can also be tidally disrupted by the SMBH, either before or after their close interaction with each other.

In Chapter I (see also Antonini et al. (2010)) we presented the results of a large number of N-body integrations of point-mass binary stars on eccentric orbits around the GC SMBH. In many cases, the trajectories of the two stars were found to imply a physical collision, assuming that the unperturbed stars had radii similar to those of normal main-sequence stars of the same mass. The probability of physical encounters was found to increase significantly if the binaries were allowed to complete many orbits about the SMBH. In some cases, one or both stars also passed close enough to the SMBH that gravitational tides would be expected to significantly affect their internal structure.

In this chapter, we use smoothed-particle hydrodynamics (SPH) simulations to study the binaries from Chapter I that approached closely enough to physically interact. The N-body simulations of Chapter I were first used to identify initial conditions that resulted in close interactions between the two stars. The point-mass stars were then realized as macroscopic, fluid-dynamical models and integrated forward in the gravitational field of the SMBH using an SPH algorithm. As in Chapter I, we followed the trajectories for multiple orbits around the SMBH, allowing us, for the first time, to investigate the consequences of repeated tidal interactions with the SMBH.

In §3.2 we briefly discuss time scales for binary disruption at the GC. Our initial conditions and numerical methods are described in §3.3 and the results in §3.4. Some observable consequences are presented in §3.5. §3.6 sums up.

3.2 The survival time of binaries at the Galactic Center

In a dense environment, binaries may evaporate due to dynamical interactions with field stars if

$$|E|/(M_{\rm b}\sigma^2) \lesssim 1, \tag{3.1}$$

with E the internal orbital energy of the binary, $M_{\rm b}$ the binary mass, and σ the one-dimensional velocity dispersion of the stellar background. In principle, because most of the binaries at the GC are expected to be "soft", $|E| \lesssim M_{\rm b}\sigma^2$, and because the binary evaporation time $t_{\rm ev}$ is a function of the distance from the SMBH, the variation of $t_{\rm ev}$ with galactocentric radius can be used to constrain the origin of the HVSs (Perets 2009a). If the evaporation time at some radius is shorter than the lifetime of a typical main-sequence star, the stellar population in this region would be dominated by isolated (i.e. single) stars.

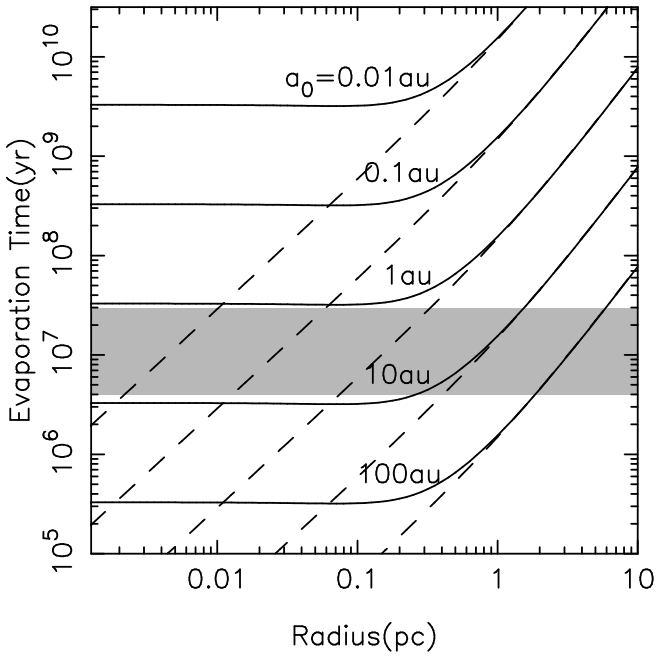

Figure 3.1 Evaporation time of binaries vs. galactocentric radius for different values of the binary semimajor-axis a_0. Solid curves show the evaporation time for the density model of equation (5.14) with $\gamma = 0.5$ while the dashed curves correspond to the coreless model with slope $\gamma = 1.8$. The filled grey region gives the ages of the S-stars (Eisenahauer et al. 2005).

Here we show that the survival time of binaries at galactocentric distances $r < 0.1$pc is likely to be comparable to the typical main-sequence lifetimes of most stars in this region. We also show that, within a radius of $r \sim 0.3$pc, $t_{\rm ev}$ becomes essentially independent of radius.

Beyond $\sim$ 1 pc from Sgr A*, the mass density determined from the stellar kinematics follows $\rho \sim r^{-\beta}$, $1.5 \lesssim \beta \lesssim 2$ (e.g. Oh et al. 2009). At smaller radii, *number counts* of the dominant (old) stellar population near the GC suggest a space density that is weakly rising, or falling, toward the SMBH, inside a core of radius ~ 0.5pc (Buchholz et al. 2009; Do et al. 2009; Bartko et al. 2010). Approximating the mass density as a broken power-law,

$$\rho(r) = \rho_0 \left(\frac{r}{r_0}\right)^{-\gamma} \left[1 + \left(\frac{r}{r_0}\right)^2\right]^{(\gamma-\beta)/2} \tag{3.2}$$

with $r_0 = 0.3$pc and $\beta = 1.8$, and setting $\rho_0 = 1.3 \times 10^6 {\rm M}_\odot {\rm pc}^{-3}$ gives a good fit to the space density outside the core (e.g. Merritt 2010). At smaller radii, the uncertainties in ρ are represented by the poorly determined value of γ.

The evaporation time is given by (Binney & Tremaine 1987) :

$$t_{\rm ev} = \frac{M_{\rm b}\sigma}{M\ 16\sqrt{\pi}\rho a_0 \ln\Lambda}, \tag{3.3}$$

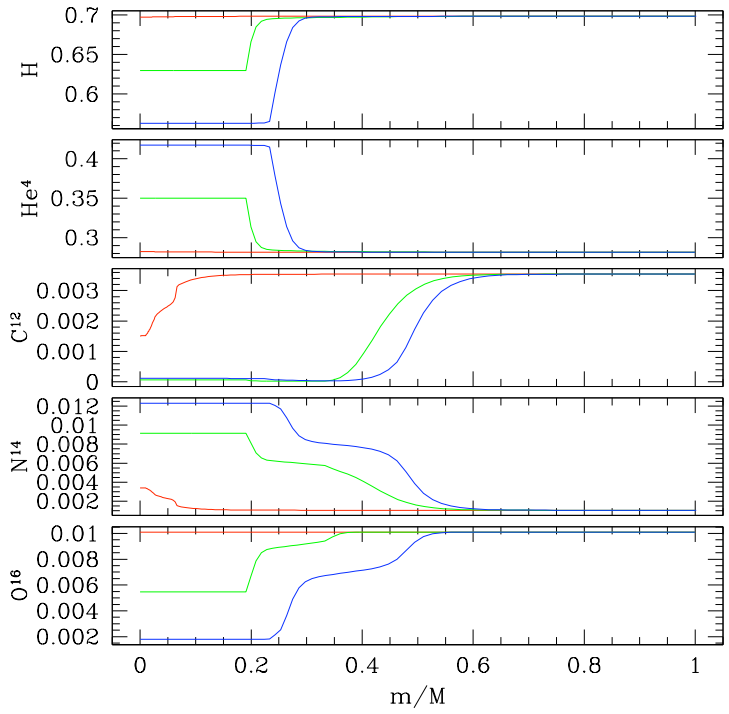

Figure 3.2 Fractional chemical abundances (by mass) versus enclosed mass fraction m/M for our $M = 1\,\mathrm{M}_\odot$ (red curves), $3\,\mathrm{M}_\odot$ (green curves), and $6\,\mathrm{M}_\odot$ (blue curves) stars, as calculated by the TWIN stellar evolution code.

where $\ln\Lambda$ is the Coulomb logarithm, M the mass of the field stars, a_0 the binary semimajor-axis, and σ is calculated from the Jeans equation,

$$\rho(r)\sigma(r)^2 = G\int_r^\infty dr' r'^{-2}\,[M_\bullet + M_\star(<r')]\,\rho(r'), \tag{3.4}$$

with $M_\star(<r)$ the total mass in stars within r, and $M_\bullet$ the mass of the central black hole. Hereafter, we adopt $M_\bullet = 4\times10^6\,\mathrm{M}_\odot$ (Ghez et al. 2008; Gillessen et al. 2009). In Figure 3.1 we plot the evaporation time of binaries in the density model of equation (3.2) as a function of galactocentric radius, assuming $M_\mathrm{b} = 2M$, $\ln\Lambda = 15$ and two different values of the internal slope: $\gamma = 0.5$ representative of the observed distribution and $\gamma = 1.8$ which corresponds approximately to a relaxed system around a SMBH (Bahcall & Wolf 1976).

From the figure it is clear that the survival time of binaries would be greatly increased if the distribution of stars at the GC has a low density core (for comparison, see also Figure 1 in Perets [2009]). The figure also shows that, at any radius, for $a_0 \lesssim 1\,\mathrm{AU}$, this time is larger than the typical lifetime of the the S-stars. Therefore, it cannot be excluded that the S-stars were initially part of binary systems originating at galactocentric distances of few tens of milliparsecs.

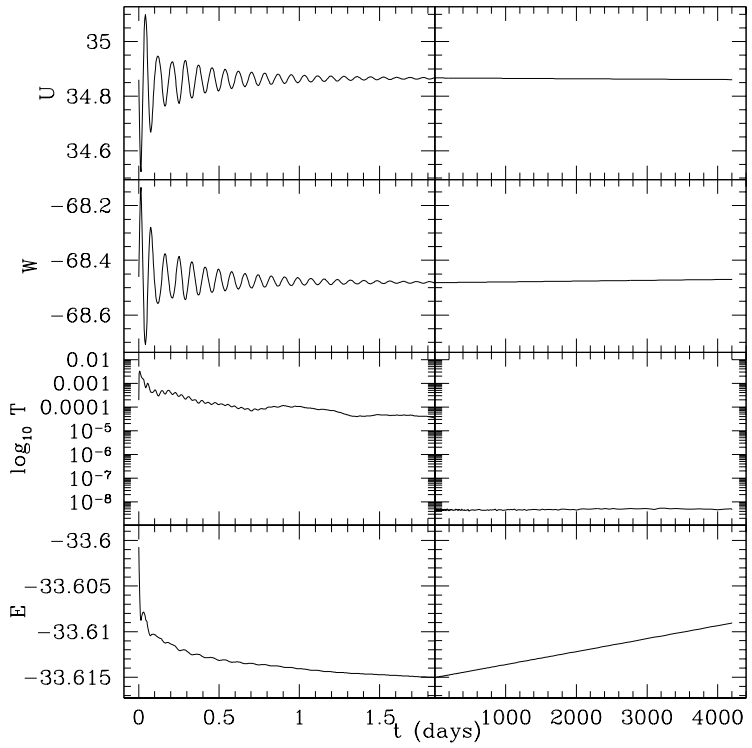

Figure 3.3 Internal energy U, gravitational potential energy W, kinetic energy T, and total energy E versus time t for the relaxation (left panels) and subsequent dynamical evolution in isolation (right panels) of the SPH model for a $6\,M_\odot$ star. Note that the time t is shown on different linear scales for the relaxation and the dynamical evolution. Energies are in units of 10^{48} erg.

We finally note that, in the context of this chapter, it might be more appropriate to compare $t_{\rm ev}$ with the time scale required to drive the eccentricities of the stars away from their initial values to produce quasi-radial orbits. At the GC this time can be of the order of few Myr (Löckmann et al. 2008; Madigan et al. 2008; Merritt et al. 2009; Perets et al. 2009; Fujii et al. 2010), which is much shorter than the typical evaporation time scale of binaries with $a_0 \leq 0.2\,{\rm AU}$.

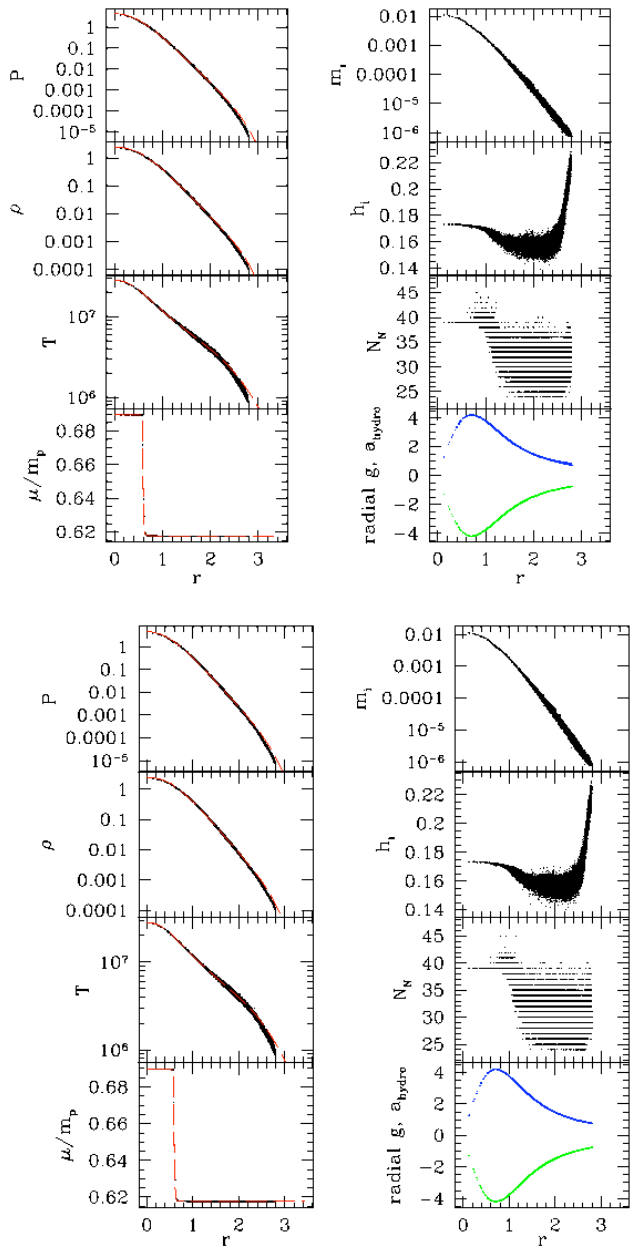

Figure 3.4 Radial profiles of the SPH model for a $6\,M_\odot$ star both at the end of relaxation (upper panels) and after 4200 days of hydrodynamical evolution (lower panels). The frames in the left column show profiles of pressure P, density ρ, temperature T (in Kelvin), and mean molecular weight μ in units of the proton mass m_p, with the dashed curve representing results the TWIN evolution code and dots representing particle data from our SPH model. The right column provides additional SPH particle data: individual SPH particle mass m_i, smoothing length h_i, number of neighbors N_N, and radial component of the hydrodynamic acceleration $a_{\rm hydro}$ (upper data) and gravitational acceleration g (lower data). Unless otherwise stated, quantities are in solar units ($G = M_\odot = R_\odot = 1$).

3.3 Initial conditions and numerical method

3.3.1 Orbital initial conditions

In Chapter I we used the high-accuracy numerical integrator `ARCHAIN` (Mikkola & Merritt 2008; Mikkola & Merritt 2006) to study the dynamics of main-sequence binary stars on highly elliptical orbits whose periapsides lay close to the SMBH. We determined the final orbital properties of both ejected and bound stars. Initial conditions consisted of equal-mass binaries on circular relative orbits with random orientations, initial separations a_0 in the range 0.05 - 0.2 AU, and individual stellar masses M of $3\,\mathrm{M}_\odot - 6\,\mathrm{M}_\odot$. The binaries were given a tangential initial velocity in the range 4 km s^{-1} - 85 km s^{-1} and initial distances of $d = 0.01 - 0.1$ pc from the SMBH. Using the mass-radius relation $R/\mathrm{R}_\odot = (M/\mathrm{M}_\odot)^{0.75}$ (Hansen et al. 2004), we could assign a physical dimension to the particles and investigate the probability of stellar collisions and mergers. In detail, we defined the minimum impact parameter for a collision as $2R$, and the two stars were assumed to coalesce when their relative velocity upon collision was lower than the escape velocity from their surface. The binary separations adopted in this work were close to the extremes of the interval within which HVSs can be produced: small semimajor-axes, $a_0 \lesssim 0.05\,\mathrm{AU}$, result in contact binaries, while for $a_0 > 0.2\,\mathrm{AU}$ few stars would be ejected with velocities sufficient to escape the Galaxy (Gualandris et al. 2005).

In order to treat also the case of unequal-mass binaries, we extended the work of Chapter I to include an additional set of ~ 2000 integrations of binaries with component masses $M_2 = 1 - 3\,\mathrm{M}_\odot$ and $M_1 = 6\,\mathrm{M}_\odot$. Initial conditions and results of these new runs are summarized in Appendix A. In the following, for the case of unequal mass binaries, we distinguish between the primary and secondary stars' quantities using the subscripts 1 and 2 respectively.

The orbital initial conditions that we adopt in the SPH simulations correspond to binaries that enter well within their tidal disruption radius r_{bt}, approximated by the expression (Miller et al. 2005):

$$r_{\mathrm{bt}} \sim \left(\frac{M_\bullet}{M_{\mathrm{b}}}\right)^{1/3} a_0, \tag{3.5}$$

with $M_{\mathrm{b}} = M_1 + M_2$ the total mass of the binary. Therefore, the binaries in all of our simulations are strongly perturbed at the first periapse passage. Moreover, we focus on cases where the tidal perturbations from the SMBH on the single stars are expected to be significant. This corresponds to binaries with periapsides that lie close to the tidal disruption radius of a single star, or

$$r_t \sim \left(\frac{M_\bullet}{M}\right)^{1/3} R. \tag{3.6}$$

We selected three types of initial condition that can be classified according to the final outcome of the SPH simulations.

1. *Stellar collision* (without merger). In some cases, gravitational perturbations from the SMBH can lead to a physical collision between the two stars. If the relative velocity at collision is sufficiently

high, the stars can survive the interaction and avoid a merger. Soon after the collision, one star can be ejected at high velocity.

2. *Stellar merger*. If the two stars collide with a relative velocity at impact smaller than approximately the escape velocity from their surfaces, coalescence occurs, resulting in the formation of a new, more massive star. The merger remnant will remain bound to the SMBH unless extreme mass loss occurs during coalescence.

3. *(Clean) ejection of a HVS*. The tidal breakup of the binary by the SMBH results in the ejection of a star at very high velocity. The former companion of the ejected star loses energy in the process and is deposited onto a tight orbit around the SMBH. Here, "clean" means that the member stars of the binary do not collide with each other during the process of ejection.

For the sake of simplicity, in all the SPH simulations we chose the initial apoapsis of the external binary orbit to be $d = 2000\,\mathrm{AU} \approx 0.01$ pc (except for case H8 which has $d = 1700\,\mathrm{AU}$; see Table 3.1). However, starting the SPH simulations from this distance would greatly increase the required computational time. The stars were therefore initially placed at a point of the orbit corresponding to a much smaller distance from the SMBH: $r_0 = 5r_{\mathrm{bt}}$. This choice for r_0 was motivated by the fact that at these distances, the tidal forces from the SMBH are still too weak to significantly influence the internal structure of the stars. In addition, since r_0 is considerably larger than r_{bt}, at the initial time the internal binary eccentricity is still close to zero ($e \lesssim 10^{-2}$). As in Chapter I, the plane of the binary's orbit about the SMBH is the $x - z$ plane.

Table 3.1 Summary of the SPH simulations.

Run	$M_1(\mathrm{M}_\odot)$	$M_2(\mathrm{M}_\odot)$	a_0(au)	$r_{\rm per}$(au)	λ_1 (λ_2)	$\zeta_1(\zeta_2)$	SPH	N-body
C1	3	3	0.05	1.50	1.36	0.668	Collision+HVS	Collision+HVS
C2	3	3	0.2	2.67	2.43	1.19	Collision+HVS	Collision+HVS
C3	6	6	0.05	1.50	1.07	0.526	Collision+HVS	Merger
C4	6	6	0.2	2.04	1.46	0.716	Collision+HVS	Collision+HVS
C5	6	3	0.1	5.61	4.01 (5.09)	1.96 (2.49)	Collision+HVS (primary)	Collision+HVS (primary)
M1	3	3	0.05	5.05	4.59	2.25	Merger	Merger
M2	3	3	0.05	1.50	1.36	0.668	Merger	Merger
M3	3	3	0.05	4.18	3.79	1.86	Merger	Collision+HVS
M4	3	3	0.2	4.18	3.79	1.86	Merger	Merger
M5	3	3	0.2	38.2	34.7	17.0	Merger	Merger
M6	6	6	0.05	2.67	1.91	0.935	Merger	Collision+HVS
M7	6	6	0.05	2.67	1.91	0.935	Merger	Merger
M8	6	6	0.05	4.18	2.99	1.46	Merger	Merger
M9	6	6	0.05	5.05	3.62	1.77	Merger	Merger
M10	6	6	0.2	2.04	1.46	0.716	Merger	Merger
M11	6	6	0.2	20.4	14.6	7.13	Merger	Merger
M12	6	3	0.1	8.08	5.78 (7.34)	2.83 (3.59)	Merger	Merger
M13	6	1	0.1	3.48	2.49 (5.28)	1.22 (2.59)	Merger	Merger
H1	3	3	0.05	1.50	1.36	0.668	HVS	HVS
H2	3	3	0.05	7.07	6.42	3.14	HVS	HVS
H3	3	3	0.2	2.04	1.86	0.909	HVS	HVS
H4	6	6	0.05	1.50	1.07	0.526	HVS	HVS
H5	6	6	0.2	2.04	1.46	0.716	HVS	HVS
H6	6	6	0.2	0.60	0.429	0.210	HVS	HVS
H7	6	1	0.1	1.44	1.03 (2.19)	0.503 (1.07)	HVS (secondary)	HVS (secondary)
H8	6	1	0.1	0.795	0.569 (1.21)	0.278 (0.592)	HVS (secondary)	HVS (secondary)

3.3.2 SPH numerical techniques and initial conditions

SPH is a Lagrangian method in which the fluid is represented by a finite number of fluid elements or "particles." Associated with each particle i are, for example, its position $\mathbf{r}_i$, velocity $\mathbf{v}_i$, and mass m_i. Each particle also carries a purely numerical smoothing length h_i that determines the local spatial resolution and is used in the calculation of fluid properties such as acceleration and density. For a recent review of SPH, see Rosswog (2009). The SPH code used in this work is presented in Gaburov, Lombardi, & Portegies Zwart (2010), with the augmentation that the analytic solution to the Kepler two-body problem can be used to advance a star bound to the SMBH through those portions of the orbit when hydrodynamic effects are negligible (see §3.4.4). The equation of state is ideal gas plus radiation pressure and radiative cooling and heating is neglected. To calculate the gravitational accelerations and potentials, we use direct summation on NVIDIA graphics cards, softening with the usual SPH kernel as in Hernquist & Katz (1989). Thus, gravity is softened only in interactions between neighbors and it is softened by exactly the SPH kernel of each particle. As the smoothing length of a particle changes, so does its softening. The use of such a softening with finite extent (as opposed, for example, to Plummer softening) increases the accuracy and stability of SPH models, consistent with the studies of Athanassoula et al. (2000) and Dehnen (2001).

In our simulations, the SMBH is a compact object particle that interacts gravitationally, but not hydrodynamically, with the rest of the system. The gravity of the SMBH is softened according to a density profile defined by the standard SPH cubic spline kernel with a constant smoothing length $h_\bullet = 20\mathrm{R}_\odot$. This approach has the advantage that the treatment of gravity is unsoftened for separations $r > 2h_\bullet$. We note that $h_\bullet$ is small compared to the periapsis separation $r_{\rm per}$ in all cases, so our code is able to follow bound stars around the black hole for many orbits without introducing spurious secular effects from gravitational softening. The SMBH is allowed to move in response to gravitational pulls. However, because the $4 \times 10^6\,\mathrm{M}_\odot$ SMBH is much more massive than any of the binaries being considered, the SMBH always remains very near the center of mass of the system, which we take to be the origin.

Before simulating the interaction of a binary with the SMBH, we must first prepare an SPH model for each binary component in isolation. To compute stellar structure and composition profiles, we use the TWIN stellar evolution code (Eggleton 1971; Glebbeek & Pols 2008; Glebbeek 2008) from the MUSE software environment (Portegies Zwart et al. 2009). We evolve main-sequence stars with initial helium abundance $Y = 0.28$ and metallicity $Z = 0.02$. The $3\,\mathrm{M}_\odot$ star is evolved to an age of 50 Myr, yielding the same $2.15\mathrm{R}_\odot$ (0.01 au) radius as in the corresponding models of Chapter I. The 1 and $6\,\mathrm{M}_\odot$ stars are each evolved to 18.2 Myr, yielding stellar radii of 0.891 and $3.44\mathrm{R}_\odot$ respectively. Figure 3.2 shows the resulting composition profiles for our 1, 3, and 6 $\mathrm{M}_\odot$ stars, colored red, green, and blue respectively.

Initially, we place the SPH particles on a hexagonal close packed lattice, with particles extending out to a distance only a few smoothing lengths less than the full stellar radius. After

the initial particle parameters have been assigned according to the desired profiles from TWIN, we allow the SPH fluid to evolve into hydrostatic equilibrium. During the relaxation calculation, the drag force we include is the normal artificial viscosity but in the acceleration equation only.

Figure 3.3 shows energies versus time both during and after the relaxation process. From the internal energy U and potential energy W curves, it is apparent that the star oscillates on a hydrodynamical timescale, specifically with a fundamental period of about 0.08 days. During relaxation, these oscillations are damped by the drag force, which does negative work on the system and decreases the total energy E toward that of a minimum energy equilibrium state. At a time of 1.84 days ($= 100 G^{-1/2}\,\mathrm{M}_\odot^{-1/2}\,\mathrm{R}_\odot^{3/2}$), the drag force is removed and the star is allowed, as a test of stability, to evolve dynamically in isolation. During this dynamical evolution, the internal energy U and gravitational energy W each remain nearly constant. By $t = 9$ days, the kinetic energy T has diminished to nearly 10 orders of magnitude less than the total energy E in magnitude, corresponding to an exceedingly small amount of noise in an otherwise static model. The overall level of energy conservation is excellent: extrapolating forward the drift in total energy E, which is linear in time, we find it would take about 2.4×10^5 days (660 years or 3×10^6 oscillation periods) of hydrodynamical evolution to reach a 1% error in total energy.

Our approach allows the parent stars to be modelled very accurately. As an example, Figure 3.4 plots both desired profiles and SPH particle data for the $6\,\mathrm{M}_\odot$ star. The structure and composition profiles of the SPH model closely follow the desired TWIN profiles. Our relaxed models remain static and stable when left to evolve dynamically in isolation: indeed, the particle data shown in the lower panels of Figure 3.4 are nearly identical to those in the upper panels, demonstrating that there are no significant changes in the model even after more than 4000 days (or equivalently 5×10^4 oscillation periods) of hydrodynamical evolution.

The binaries in our simulations are then created simply by shifting two stellar models, each taken from the end of a relaxation calculation, to the appropriate initial position and velocity provided by the N-body code. We begin with binary components irrotational in the inertial frame, which allows us to more easily study any rotation imparted during the subsequent interaction.

Unless otherwise noted, our simulations employ $N \approx 4 \times 10^4$ SPH particles: such a particle number provides an appropriate balance between resolution and the need sometimes to follow the hydrodynamics for time intervals exceeding 10^5 dynamical timescales (corresponding to hundreds of orbits around the SMBH).

3.3.3 Timescale considerations and orbital advancement

Because of shock heating in collisions and mergers, in addition to tidal heating during the periapse passage, the bound stars are out of thermal equilibrium and larger than a normal main-sequence star of the same mass. The global thermal readjustment of the bound stars proceeds on a thermal timescale $t_{\mathrm{thermal}} \approx U/L$, where U is the total internal energy in the star and L is its

luminosity. The SPH simulations confirm that the internal energy U of the bound star after one periapsis passage is comparable to the total internal energy of the star(s) from which the bound star came and typically $U \approx (2-7) \times 10^{49}$erg, with the larger values generally corresponding to more massive stars. For weak collisions and clean ejections of HVSs, the luminosity of the bound star will be comparable to the value it had in the initial binary: the thermal timescale in such cases is then roughly 10^5 to 10^7 years. Guided by calculations of blue stragglers (Sills et al. 1997), we estimate that the luminosity of a bound star produced by a merger or strong collision may be up to ~ 100 times larger than that of a main-sequence star of the same mass. Thus, the luminosity of our most massive merger products could be briefly as large as $\sim 10^6 \mathrm{L}_\odot \approx 4 \times 10^{39}$erg s^{-1}, so that the global thermal timescale $t_{\rm thermal} \gtrsim 600$ years (although the local thermal timescale in the outer layers of the star could be less). We conclude that thermal adjustment over an orbital period is small and often completely negligible, and we therefore do not attempt to model the thermal relaxation here.

Although the orbital period is small compared to the thermal timescale, it is large compared to the hydrodynamical timescale, which is about an hour. Following the full hydrodynamics of a multiple orbit encounter would therefore not be practical. What we do instead is wait for the star(s) to move sufficiently far away from the black hole and then advance any bound star around most of its Kepler two body orbit. At the same time, we remove from the simulation any HVS, any ejecta, and any gas that has become bound to the SMBH. As long as the periapse passages are treated hydrodynamically, our results are not sensitive to precisely which portion of the orbit is treated in the two body approximation. In practice, we wait at least 8 days after periapse, and at least 8 days after the merger or ionization of a binary, before measuring the orbital elements and implementing the two body analytic solution. The orbital advancement is performed such that the distance from the black hole to the bound star is unchanged but that the objects are now approaching one another. We preserve the orientation of the orbit and spin of the bound star during the orbital advancement.

In order to test the reliability of the method, we run a portion of the first orbit for one of our simulations (C1 in Table 1) without any orbital advancement. We found that, at about 20 days after we would have applied the advancement, their masses had decreased by an additional $0.002\,\mathrm{M}_\odot$. We note that even though we retain too much mass, this "extra" mass is far from the stars, so it doesn't significantly participate in the hydrodynamics and it will get ejected in the next passage. We conclude that neglecting hydrodynamics far from periapsis is a reasonable approximation.

3.4 Results

The first important result of the SPH simulations performed in this work is that their qualitative outcome agrees very well with that of the N-body integrations devised in Chapter I. Among a total of 26 simulations, only in 3 cases did the N-body approach fail to match the results of the hydrodynamic calculations.

Table 3.1 reports the chosen initial conditions as well as a qualitative description of the final

Table 3.2 Ejection velocity $v_{\rm ej}$ of the HVS, orbital semimajor-axis a and eccentricity e of the captured star, and distance of closest approach between the two stars (r_0) in the SPH (N-body) calculations. The quantity $\Delta M_{\rm b}/M_{\rm b}$ gives the fraction of mass lost from the binary, while $\Delta M_\bullet/M_{\rm b}$ is the fraction of the mass lost from the binary that remains bound to the SMBH. All quantities are evaluated after the first periapsis passage, once the stars have retreated far from the SMBH.

Run	$v_{\rm ej}$ (km/s)	a (au)	e	$r_0/(R_1+R_2)$	$\Delta M_{\rm b}/M_{\rm b}$	$\Delta M_\bullet/M_{\rm b}$
C1	4608(5681)	124(101)	0.988(0.985)	0.23(0.32)	-1.33×10^{-2}	7.19×10^{-3}
C2	3878(3964)	159(157)	0.983(0.983)	0.49(0.50)	-2.80×10^{-3}	2.06×10^{-3}
C3	3335(4840)	190(117)	0.991(0.987)	0.38(0.45)	-1.24×10^{-2}	6.73×10^{-3}
C4	1467(1554)	380(377)	0.995(0.995)	0.67(0.87)	-1.29×10^{-3}	7.08×10^{-4}
C5	1764(2367)	212(163)	0.974(0.965)	0.42(0.61)	-2.16×10^{-3}	1.53×10^{-3}

outcome of the SMBH-binary interaction in both SPH and N-body simulations. The strength of the SMBH-stars interaction is parameterized by the dimensionless quantity: $\lambda = r_{\rm per}/r_{\rm t}$. In general, stars on orbits meeting the condition $\lambda < 1$ are tidally disrupted (Luminet & Carter 1986; Evans & Kochanek 1989). However, even when tidal disruption does not occur, we expect that mass will be stripped from the outer regions of any star passing within its Roche limit (Paczynski 1971). In the table, ζ gives the Roche lobe radius (evaluated at periapsis) in units of the stellar radius:

$$\zeta = \frac{0.49q^{2/3}}{0.6q^{2/3}+\ln(1+q^{1/3})}\times\frac{r_{\rm per}}{R} \quad , \tag{3.7}$$

with $q = M/M_\bullet$ (Eggleton 1983). Although this formula was derived under the assumption of circular orbit, it has been shown to work reasonably well even for eccentric binaries, if used at periapsis (Regös et al. 2005). Note that because $q << 1$ in the present work, the approximate relation $\zeta \approx 0.49\lambda$ exists between λ and ζ.

The results of our SPH simulations are presented in what follows. We first describe the product of one binary-SMBH interaction (Sections 3.4.1, 3.4.2 and 3.4.3), and then we successively follow the evolution of the bound stars as they perform several revolutions around the SMBH (Section 3.4.4).

3.4.1 Stellar Collisions

Ginsburg & Loeb (2007) noted that the tidal breakup of stellar binaries interacting with the SMBH can lead, under some circumstances, to a physical collision between the two member stars. In this section we investigate the cases in which the two stars collide with a relative impact speed large enough that they do not merge upon impact. Some results of the SPH simulations are shown in Table 3.4, where we also compare the asymptotic ejection velocity of the HVSs ($v_{\rm ej}$), the semimajor-axis (a) and eccentricity (e) of the captured stars with the same quantities obtained in the N-body simulations.

The agreement between the two methods is remarkably good. However, the SPH simulations systematically produce smaller values of $v_{\rm ej}$ and larger a. This is a consequence of the efficient energy and angular momentum transfer occurring between the stars: the ejected star slows down and the captured star gains speed during the collision.

From Table 2.2, it is clear that the mass-loss from the binary is smaller than a few percent of the total mass, and always below $\sim 0.1\,{\rm M}_\odot$. This is consistent with previous simulations of stellar collisions that often found a small fractional mass-loss (Benz & Hills 1987; Benz & Hills 1992). Our calculations indicate that, after a collision, the mass ejected from the SMBH-stars system is comparable to, although smaller than, the mass that is ejected from the binary but remains bound to the SMBH; this mass-loss has a small but measurable impact on the subsequent evolution of the stars' orbits as demonstrated by comparing the SPH and the N-body quantities in the table. Debris will eventually settle into a torus-like structure about the SMBH, that will subsequently evolve due to viscosity, mass inflow, radiative cooling, and winds.

Spin-up is expected to be one of the main signatures of either a (off-axis) collision (Alexander & Kumar 2001) or a tidal encounter with a massive black hole (Evans & Kochanek 1989). In our simulations the close stellar encounter as well as the SMBH tides at periapsis lead therefore to some degree of rotation in the stars with angular frequency:

$$\Omega_{\rm tot} \approx \sqrt{\Omega_*^2 + \Omega_\bullet^2} \approx \sqrt{\frac{G(M_1+M_2)}{r_0^3} + \frac{GM_\bullet}{r_{\rm per}^3}} \quad , \tag{3.8}$$

where Ω_* and $\Omega_\bullet$ are respectively the angular velocity induced by the interaction with the companion star and that imparted by the SMBH tides; r_0 is the distance of closets approach between the stars. The ratio $\Omega_*/\Omega_\bullet$ in the cases considered here is always grater than 1 and varies from a maximum of ~ 20 (simulation C5) to a minimum of ~ 2 (simulation C4).

Figure 3.5 plots the temporal evolution of the dimensionless spin parameter (Peebles 1971):

$$J = \frac{L|E|^{1/2}}{GM^{5/2}} \quad , \tag{3.9}$$

where L is the spin angular momentum of the star and E its binding energy. In all cases, there is a sharp increase in the stars' spins during the periapsis passage followed by a second gradual decrease toward the final relaxed (spinning) configuration. Note that the captured stars have values of the final spin slightly larger than that of the ejected stars. This finding is consistent with the results of Chapter I (but see Sari et al. (2010) as well), where it is shown that the captured member is always the star with the smallest value of the closest approach distance to the SMBH implying, as we expect from equation (3.8), a larger tidal torque at periapsis.

Figure 3.5 also shows the temporal evolution of the stellar masses near the first periapsis passage. Each star typically loses about 1% of its mass, with captured stars (again, those that pass closer to the SMBH) losing slightly more mass than their ejected counterparts. In the cases with an equal mass binary, both stars lose a comparable amount of mass. The captured star in simulation

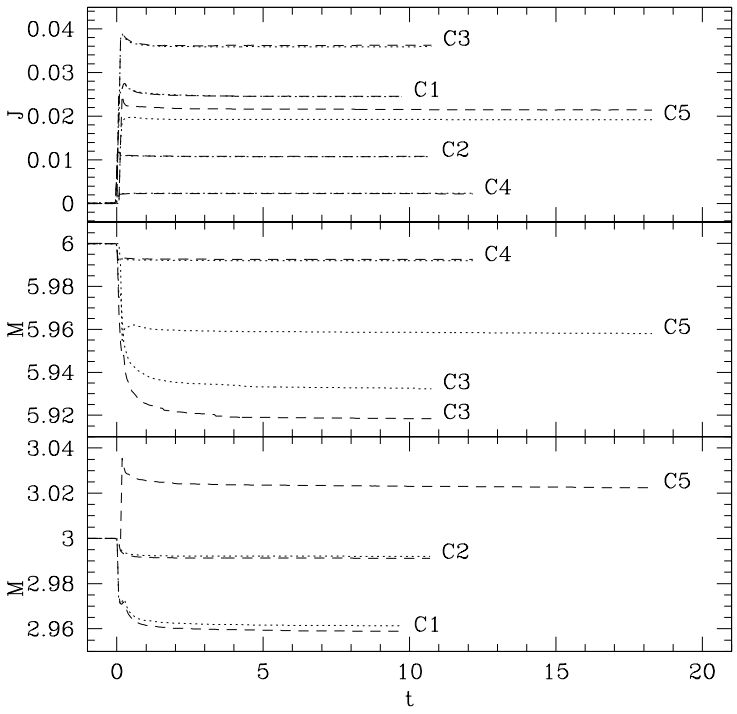

Figure 3.5 Temporal evolution of the dimensionless spin parameter J defined in equation (3.9) and the stellar masses M in solar units at times near the first periapsis passage in simulations with stellar collisions. Dashed curves correspond to the stars captured by the SMBH, while the dotted curves are for the ejected stars. The time coordinate is given in units of days and is shifted in order to have $t = 0$ at the moment of the closest approach of the binary with the SMBH. The curves terminate at the time the orbit is advanced using the analytic two-body solution.

C5 actually gains mass that had been lost from its binary companion, as discussed in more detail below. In all cases, the stellar masses stabilize to an essentially constant value by the time the orbital advancement technique is implemented, which is where the curves terminate.

Figure 3.6 presents column density snapshots for simulation C5. The simulation models a stellar binary with $a_0 = 0.1$ au and with components of masses $M_1 = 6\,\mathrm{M}_\odot$ and $M_2 = 3\,\mathrm{M}_\odot$ (see Table 1). The time indicated on the panels is shifted in order to have $t = 0$ at the moment of the closest approach of the binary with the central black hole. Between $t = 0$ and $t = 0.9$ days the reference frame is the center of mass of the binary while, in the lower-right panels, we switch to the frame in which the center of mass of either the captured (left) or ejected (right) star is at the origin.

The first contact between the stars occurs ~ 0.1 days after the periapsis passage. The interaction leads to an episode of mass transfer between the stars (observed at ~ 0.35 days in

the figure). The smaller star gains mass ($\sim 0.02\,M_\odot$) in the collision, while the larger star loses $\sim 0.04\,M_\odot$. Only $6 \times 10^{-3}\,M_\odot$ becomes ejecta from the entire system (i.e., stars plus SMBH) after the first periapsis passage, while the remainder of the gas lost from the binary remains bound to the black hole. The mass loss from the binary upon impact is therefore of order $\sim 10^{-2}\,M_\odot$. Note that, in this simulation, the penetration factor λ of both stars is large enough that the mass loss from the binary can be completely attributed to the stellar impact rather than to the tidal perturbations from the SMBH.

The two bottom-right panels give column density plots of the captured (left) and ejected (right) stars, both showing a low-density, oblate envelope surrounding a compact spherical nucleus with a central density almost unaltered with respect to that of the parent stars. This particular configuration is common to almost all the other collisional products as shown in Figure 3.7 which

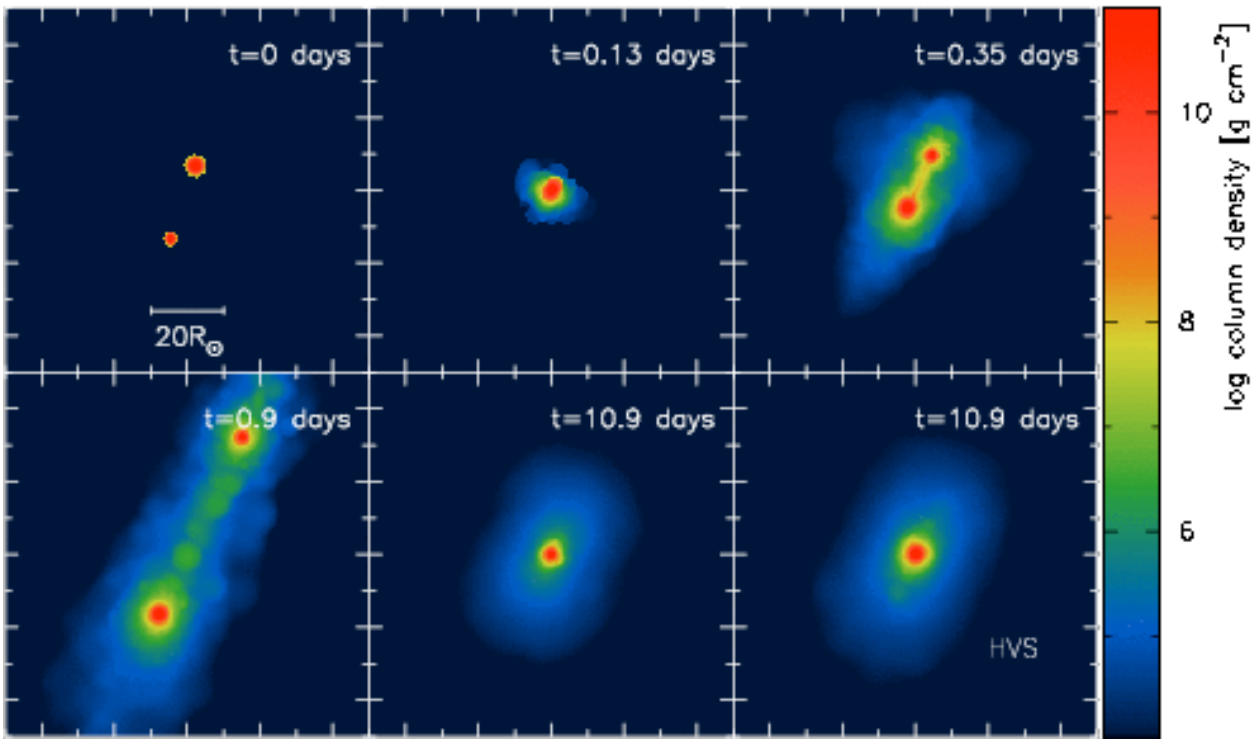

Figure 3.6 Column density plots for simulation C5 on the $X - Z$ plane. In this case the binary has an internal semimajor-axis $a_0 = 0.1$au and its components have masses $M_1 = 6\,M_\odot$ and $M_2 = 3\,M_\odot$. Time $t = 0$ corresponds to the periapsis passage of the binary external orbit. Between $t = 0$ and $t = 0.9$ days the panels are centered on the binary center of mass. The two bottom-right panels are centered on the center of mass of either the captured (left) or ejected (right) star. The black hole is outside the images. At $t = 0.13$ days the stars collide. Subsequently, the $6\,M_\odot$ member is ejected at hypervelocity while the secondary star remains bound to the SMBH.

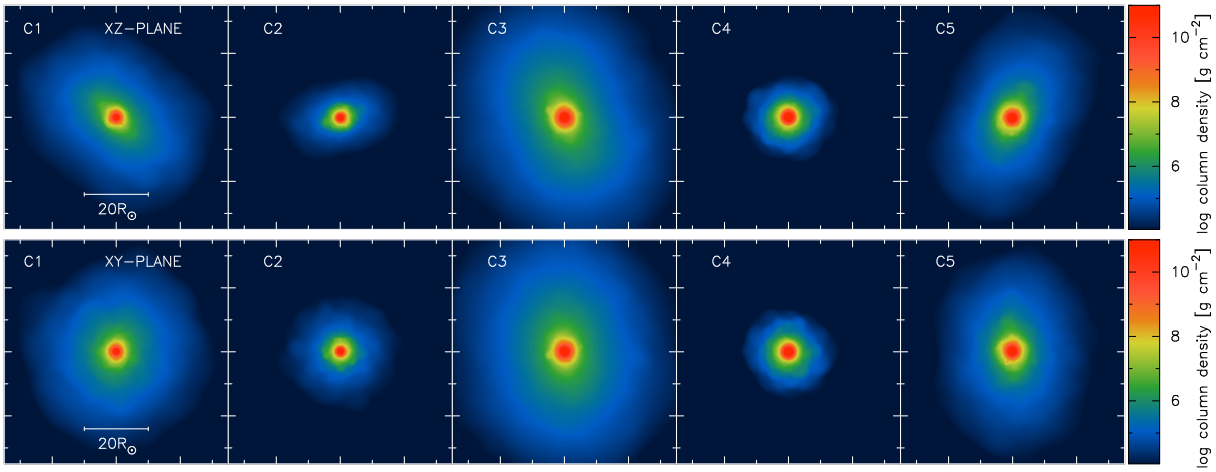

Figure 3.7 Stars ejected in our simulations after a collision with the companion star. The stars show, typically, an oblate envelope surrounding a high density spherical nucleus. Only in simulation C4, where the impact is more "grazing," the collisional product is spherically symmetric even in its outermost envelope.

gives column density plots of the ejected stars. Rotation as well as asymmetric shape can have a fundamental role in the future evolution of the stars and their observable characteristics; a star with a rapidly rotating nucleus can have its main-sequence life-time considerably extended with respect to their non-rotating counterpart (Clement 1994). Only in run C4 the HVS ejected after the collision is slowly spinning and spherical even in its outermost envelope. In this simulation, the stars experience a more grazing collision which leads to some envelope-ejection but leaves the stars' structure essentially unchanged.

3.4.2 Mergers

Stellar collisions due to either binary evolution or dynamical interactions are thought to be the main formation channel of blue stragglers in star clusters (Collier et al. 1984; Leonard 1989; Mateo et al. 1990). Similar processes have been proposed in the past to explain the puzzling presence of the young massive stars observed at galactocentric distances of few mpcs, where star formation is thought to be strongly inhibited by the SMBH tides (Genzel et al. 2003; Eisenahauer et al. 2005). In Chapter I, we showed that gravitational encounters involving stellar binaries and the SMBH lead, for a wide range of orbital parameters, to a stellar collision and that among the collisional products, stellar coalescence occurs in more than 80% of the cases. In this section we study this latter outcome and investigate the properties of the resulting stars to clarify whether they would be expected to posses features commonly associated with the S-star population.

Table 3.4.1 gives the orbital parameters (i.e., eccentricity and semimajor-axis) of the merger

Table 3.3 Same as Table 3.4 but for stellar mergers after the first periapsis passage. Here the quantities in parentheses refer to the initial orbit of the binary center of mass.

Run	a (au)	e	$\Delta M_{\rm b}/M_{\rm b}$	$\Delta M_\bullet/M_{\rm b}$	J
M1	1060(1000)	0.995(0.995)	-2.57×10^{-2}	2.57×10^{-2}	0.153
M2	984(1000)	0.999(0.999)	-1.61×10^{-2}	1.26×10^{-2}	0.167
M3	997(1000)	0.996(0.996)	-5.07×10^{-2}	2.71×10^{-2}	0.103
M4	1010(1000)	0.996(0.996)	-4.26×10^{-2}	4.24×10^{-2}	0.259
M5	1020(1020)	0.958(0.963)	-2.16×10^{-2}	1.86×10^{-2}	0.222
M6	996(1000)	0.997(0.997)	-5.60×10^{-2}	2.93×10^{-2}	0.0666
M7	1180(1000)	0.997(0.997)	-2.50×10^{-2}	2.37×10^{-2}	0.242
M8	1030(1000)	0.996(0.996)	-4.00×10^{-2}	2.06×10^{-2}	0.249
M9	1000(1000)	0.995(0.995)	-2.93×10^{-2}	2.65×10^{-2}	0.238
M10	1020(1000)	0.998(0.998)	-6.09×10^{-2}	5.99×10^{-2}	0.108
M11	1010(1010)	0.980(0.982)	-4.38×10^{-2}	2.51×10^{-2}	0.131
M12	1020(1010)	0.992(0.991)	-1.80×10^{-2}	1.23×10^{-2}	0.181
M13	1060(1000)	0.997(0.994)	-2.20×10^{-2}	1.63×10^{-2}	0.0766

products in our simulations as well as the mass ejected from the binary and the fraction of mass captured by the SMBH after the first periapsis passage. The table shows that the merger remnants lie on a orbit very close to the initial orbit of the center of mass of the binary around the black hole, implying only a small effect of the mass-loss on the dynamical evolution of the stars. The mass ejected from the binary after the first periapsis passage is typically larger than that found in collisions that do not end up with a merger (see Table 3.4) and is of order $\sim 10^{-2}$ times the initial mass of the binary. In many cases most of the mass ejected from the binary during the merger remained bound to the SMBH. This is a quite different situation respect to that found in Section 3.4.1, where approximately half of the mass ejected from the binary remained unbound to the black hole; in these previous runs one of the two stars is always found on an escaping trajectory and, consequently, the debris associated with such a star will also tend to escape the SMBH. The last column in the table gives the dimensionless spin parameter defined in equation (3.9) of the final merger products that show very large spins, some of them close to the "break-up" value (i.e., $J = 1$).

In principle it is possible that, as a consequence of the mass loss occurring near periapsis, the resulting merger product gains orbital energy and escapes the SMBH (see for instance Faber et al. [2005]). Although we do not exclude this outcome for a different set of initial conditions, in our simulations this mechanism does not produce HVSs, and in all cases the merger remnant is still on a bound orbit around the SMBH. Another more important consideration is that, subsequent to the merger, the tidal heating results in some degree of expansion and a weakly bound configuration for the merger product. Because the tidal radius of the newly formed star is much larger than that of its progenitors, the star will successively lose more mass with each periapsis passage and eventually be torn apart by the SMBH tides. And in fact, as it is shown below, this is the final outcome of

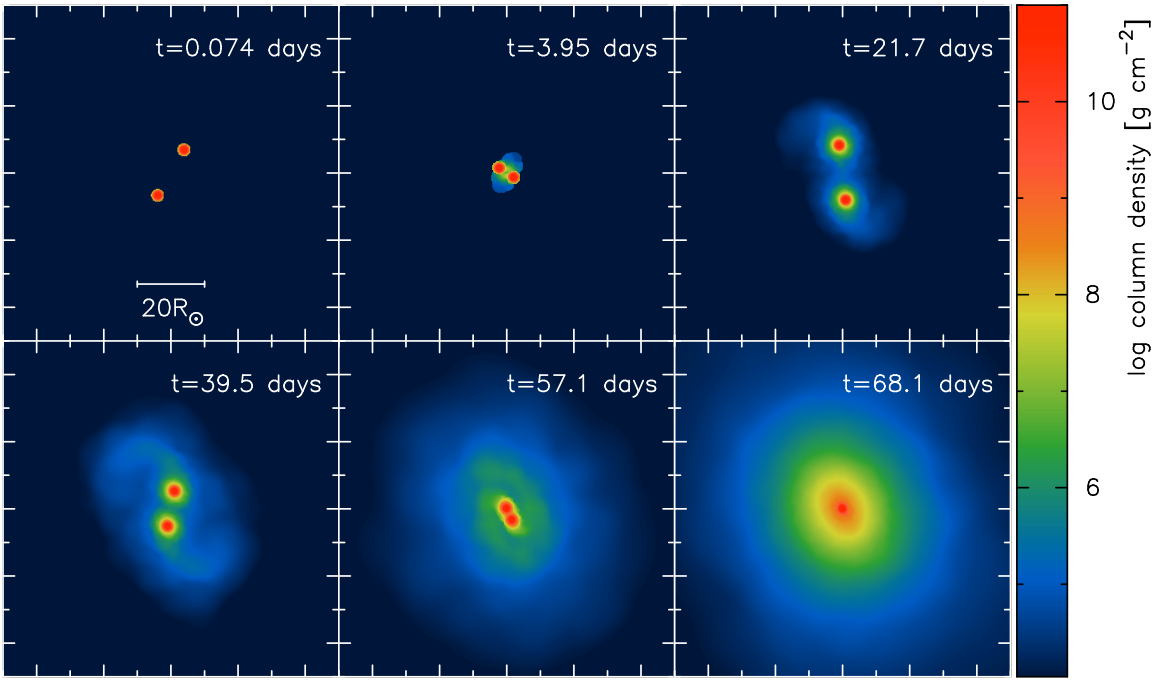

Figure 3.8 Column density plots for simulation M4 on the $X-Z$ plane. The binary has an internal semimajor-axis $a_0 = 0.2$au and its components have masses $M = 3\,\mathrm{M}_\odot$. Time $t = 0$ corresponds to the periapsis passage of the binary external orbit.

some of our simulations.

An example of merger is displayed in Figure 3.8, which involves a binary with $a_0 = 0.2$ au and equal-mass components of masses $M = 3\,\mathrm{M}_\odot$ (run M4). In this run the stars collide for the first time after ~ 4 days from the time corresponding to the periapsis passage; the internal periapsis separation at the first contact is $r_0/(2R) = 0.86$. After the first periapsis passage, as consequence of the SMBH perturbation, the binary star becomes very eccentric. As the stars move through the circum-binary envelope formed during the previous encounters, the orbit gradually circularizes and shrinks. By $t \approx 60$ days, after approximately 30 collisions, the two stellar nuclei merge. The final product has an oblate shape which is a common characteristic of all the merger remnants formed in our simulations.

As another example, Figure 3.9 displays column density plots of simulation M13 where a merger occurs between a 6 and a $1\,\mathrm{M}_\odot$ stars. The stars collide after 1.48 days from the moment of the closest approach to the SMBH, and subsequently merge in the following ~ 1 day. During the merger, the high density core of the lower mass star rapidly sinks to the center of the companion star. The tail-like feature observed at $t = 1.86$ days in the figure, is mostly material coming from the the secondary star that loses part of its outermost envelope while sinking to the center of the merger remnant.

Figure 3.10 shows chemical composition profiles of the merger products for runs M4 and M13, after one periapsis passage. In simulation M4, the remnant has a mass of roughly $5.9\,M_\odot$, its composition profile is very similar to that of the parent stars (see Figure 3.2). Based on how long it would take a normal star of that mass to evolve to that central hydrogen abundance using the TWIN stellar evolution code, we estimate that a "normal" $5.9\,M_\odot$ star would reach a core helium abundance $Y = 0.35$ (assuming $Z = 0.02$) after $\sim$ 2Myr. By colliding two 50 Myr old $3\,M_\odot$ stars, we have effectively made a more massive ($M \sim 6\,M_\odot$), younger (age $\sim$ 2 Myr) star. The merger remnant of run M13 shows a peculiar composition profile when compared to a normal star, but quite normal for merger products. In M13 (and in M12 as well), the low mass star drops to the center of the merger product bringing its fresh hydrogen fuel along and significantly rejuvenating the core. As a result, the maximum He does not occur at the center of the merger product. The main reason of the negligible amount of hydrodynamic mixing is that the cores of the initial stars are very dense and difficult to break even in a head-on collision (Lombardi et al. 1995, 1996). However, we cannot exclude the possibility that other processes occurring on a thermal timescale (as opposed to the hydrodynamic timescale) can produce a significant degree of mixing in the stars as they evolve toward thermal equilibrium (Sills et al. 1997).

Another interesting result, plotted in Figure 3.10, is that a large fraction of the Lithium/Beryllium/Boron

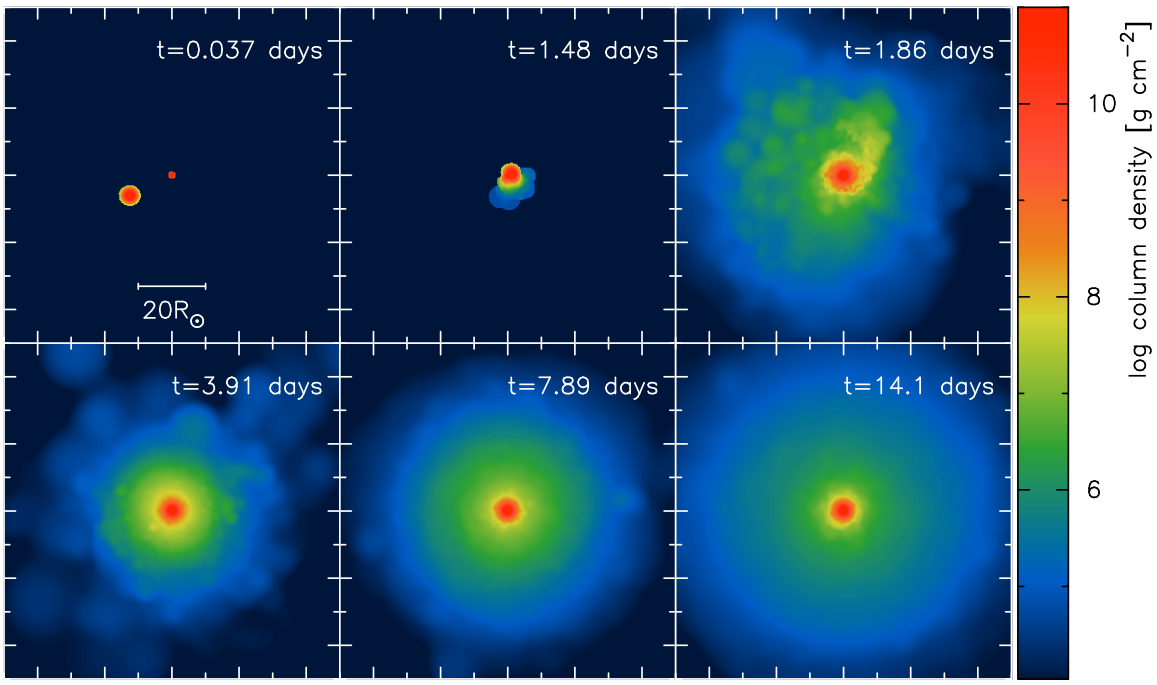

Figure 3.9 Column density plots for simulation M13 on the $X-Y$ plane. The binary has an internal semimajor-axis $a_0 = 0.1$au and its components have masses $M_1 = 6\,M_\odot$ and $M_2 = 1\,M_\odot$. Time $t = 0$ corresponds to the periapsis passage of the binary external orbit.

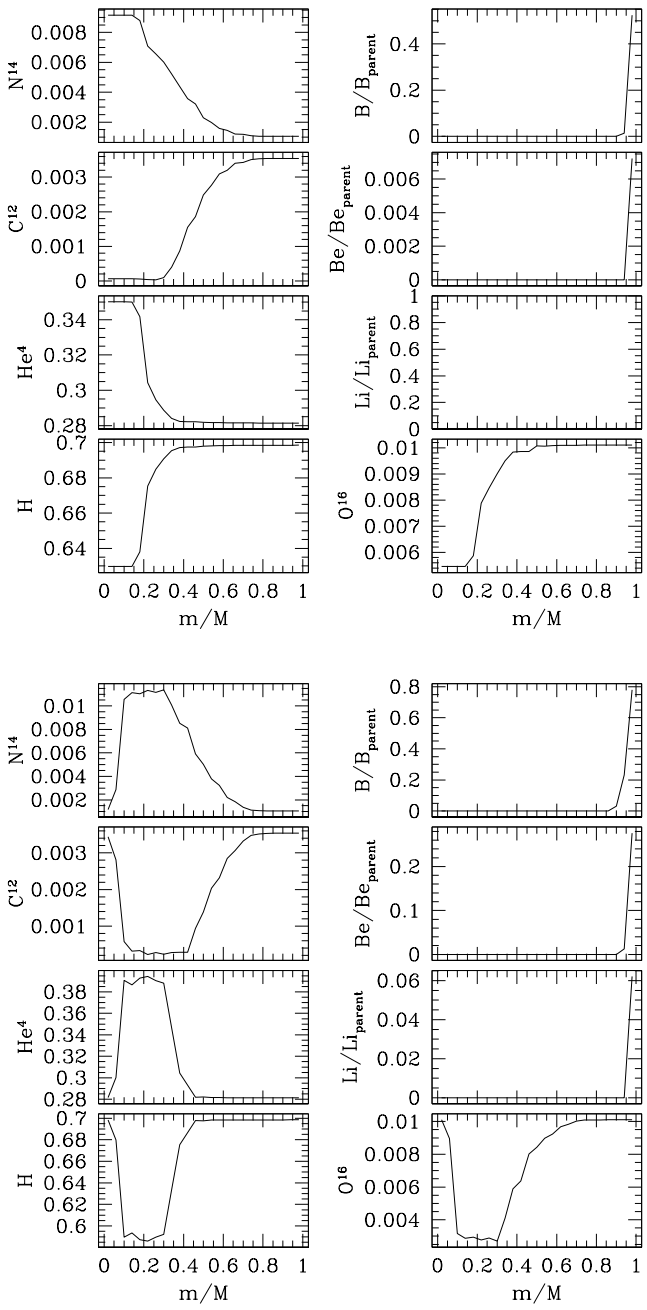

Figure 3.10 Upper panels: composition profile of the merger remnant formed after one periapsis passage in run M4 (see also Figure 3.8). The merger product of two equal mass stars has a composition profile very similar to that of its parent stars. For a $\sim 6\,M_\odot$ star, a final He abundance in the core of $Y = 0.35$ corresponds to an effective age of ~ 2 Myr. Lower panels: composition profile of the merger remnant formed after one periapsis passage in run M13 (see also Figure 3.9). In this case, the merger product has a peculiar profile if compared to a "normal" star. Its core is strongly hydrogen-enriched as a consequence of the low-He fluid transported by the low mass star along with it to the center.

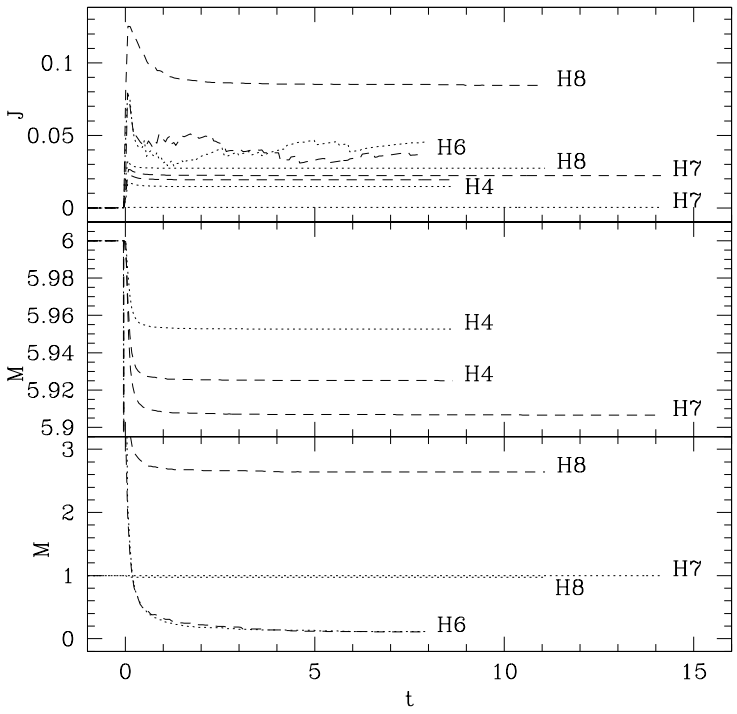

Figure 3.11 Like Fig. 3.5, but for some of the simulations in which there is neither a stellar collision nor a merger.

from the parent stars gets ejected, indicating that a significant gap in the abundances of these elements in the S-star population might be observational evidence of rejuvenation through merger. Reduced atmospheric Lithium abundances are for instance observed in blue stragglers and can also be a strong indicator of mixing (Hobbs & Mathieu 1991; Pritchet & Glaspey 1991).

We finally note that as the stars keep orbiting the SMBH, their chemical profile and their spinning configuration will change in time and therefore the states displayed in Figures 3.8, 3.9 and 3.10 should be intended as not permanent. The evolution will typically lead toward smaller spins and a lower Lithium/Beryllium/Boron abundances in the stars. We will come back to this point below.

3.4.3 Clean Ejection of Hypervelocity Stars

Even when the stars do not collide, tidal torque and mass-loss can occur if the periapsis distance of the binary center of mass initially lies within the Roche limit of its member stars. Similarly to what is done in the previous two subsections, we analyze here the first binary-SMBH interaction, while we discuss the following evolution of the bound stars in the next subsection. Some

of the results of our SPH simulations, for which there is not a direct collision between the stars, are listed in Table 3.4.1. As expected, for $\zeta \gtrsim 1$ there is no mass-loss, and the stars maintain their initial configuration essentially unaltered (runs H2 and H3). Conspicuous mass-loss instead occurs for runs H6 and H8 in which at least one of the stars crosses its tidal radius. Interesting, although the usual condition for tidal disruption is well satisfied (i.e., $\lambda < 1$), in both runs the stars are not fully disrupted by the SMBH's tidal gravity at the first periapsis passage. In the table we also give the final values of the spin parameter J that, in general, are found to be a very small fraction of the breakup value. Figure 3.11 shows the temporal evolution of J and the stellar masses for the cases of Table 3.4.1 that have the highest value of the final spin. The interaction with the SMBH induces a strong rotation only in the stars of runs H6 and H8. We conclude that, unless the stars penetrate deeply their tidal disruption radius, it seems unlikely that the SMBH tides at periapsis alone can produce a significant spin-up of the stars.

As an example, Figure 3.12 gives column density plots of run H8. In this simulation, the primary and secondary stars have masses $1\,\mathrm{M}_\odot$ and $6\,\mathrm{M}_\odot$ respectively. The periapsis of the external orbit ($\sim$ 0.8au) is initially inside the tidal radius of the $6\,\mathrm{M}_\odot$ member but it is still outside the tidal radius of the $1\,\mathrm{M}_\odot$ star. At periapsis, the stars are squeezed by the SMBH's tidal gravity. In the process the primary star losses a large fraction of its initial mass ($\sim 3.4\,\mathrm{M}_\odot$), while the secondary loses only $\sim 0.03\,\mathrm{M}_\odot$. After the interaction with the SMBH the binary is broken apart and the lightest member becomes an HVS. Because of tidal heating during the periapsis passage, the stars are perturbed from their thermal equilibrium state and their radii are somewhat enlarged with respect to a normal main-sequence star of the same mass.

3.4.4 The Bound Population

After the initial encounter between the binary and the SMBH, one star remains in a bound orbit around the SMBH in all of our simulations. Like the orbit of the initial binary about the SMBH, the orbit of such a bound star is highly eccentric: $0.96 < e < 1$. In those cases in which the bound star is a merger product (runs M1 through M13), the semimajor-axis a very nearly equals the semimajor-axis of the initial binary about the SMBH: $a \approx 1000$au, corresponding to an orbital period of about 16 years. We note that these orbital periods are comparable to those of the S-Stars in the GC. In those cases in which a HVS star is ejected (runs C1 through C5 and runs H1 through H8), the ejection energy comes at the expense of the orbital energy of the bound star, which consequently has a somewhat smaller semimajor-axis: 100au $\lesssim a \lesssim$ 700au, corresponding to orbital periods of 0.5 to 9 years.

Tidal Stripping

The most significant hydrodynamic effects occur near the periapsis, where induced collisions and mergers are most likely to occur and where tidal stripping is at its greatest.

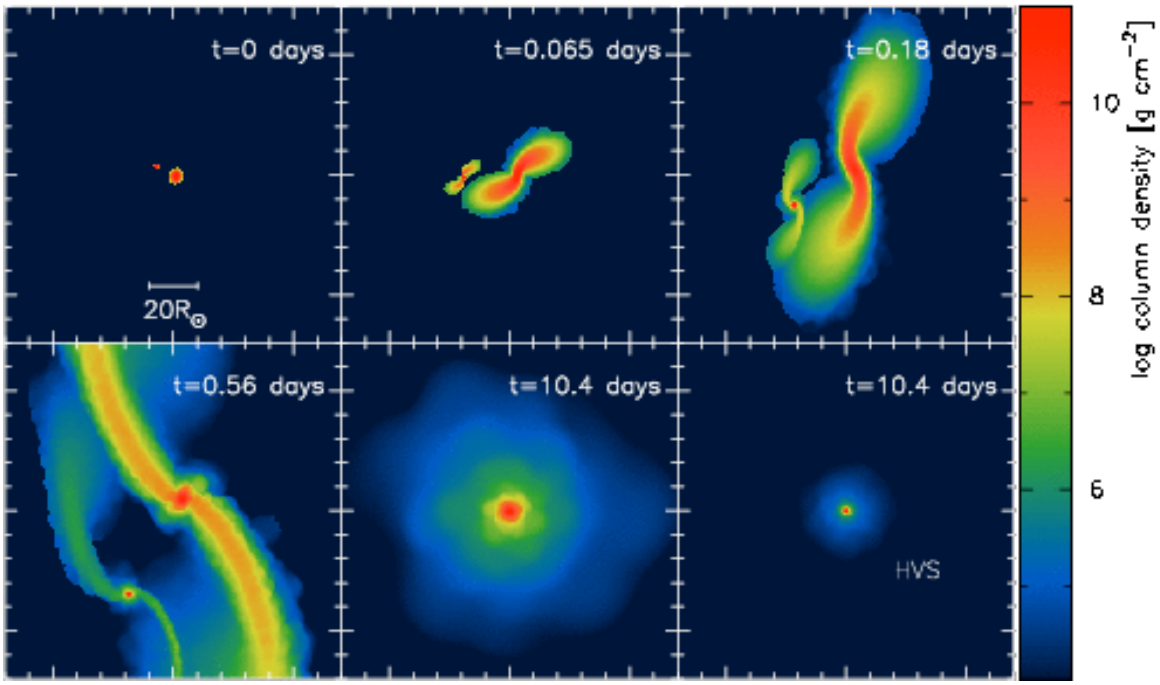

Figure 3.12 Column density plots for simulation H8 on the $X-Z$ plane. The binary has an internal semimajor-axis $a_0 = 0.1$ au and its components have masses $M_1 = 6\,\mathrm{M}_\odot$ and $M_2 = 1\,\mathrm{M}_\odot$. Time $t = 0$ corresponds to the periapsis passage of the binary external orbit. The first four panels are centered to center of mass of the binary, while in the two bottom-right panels the origin is the center of mass of either the captured (left) or ejected star (right).

We find that the periapsis separation of a bound star remains remarkably constant from one orbit to the next, even when there is significant mass loss due to Roche lobe overflow at periapse. As an example, consider the run C1 in which the initial stars have the dimensionless Roche lobe parameter $\zeta = 0.67$. As expected for $\zeta < 1$, the bound star does indeed lose mass each time it sweeps past the black hole. The gradual decrease of the mass M of the bound star can be seen in the top panels of Figure 3.13. The mass δM lost per orbit, shown by the star symbols in the top panel, increases with each orbit, until after 96 periapsis passages the star has been completely disrupted. We note from the bottom panel that the periapsis separation $r_{\rm per} = a(1-e)$ is nearly unchanged during this entire process: in this and other cases, we find the bound star returns to the nearly same relative separation from the black hole regardless of mass loss. The apoapsis separation $d = a(1+e)$ is also somewhat constant, although it decreases at late times when the mass loss is greatest and strong tidal effects remove energy from the orbit.

As another example, the lower panels of Figure 3.13 give the evolution of the merger remnant formed in run M5. In this case most of the mass-loss occurs during the first periapsis passages where very high entropy material is removed from the outer layers of the star that responds

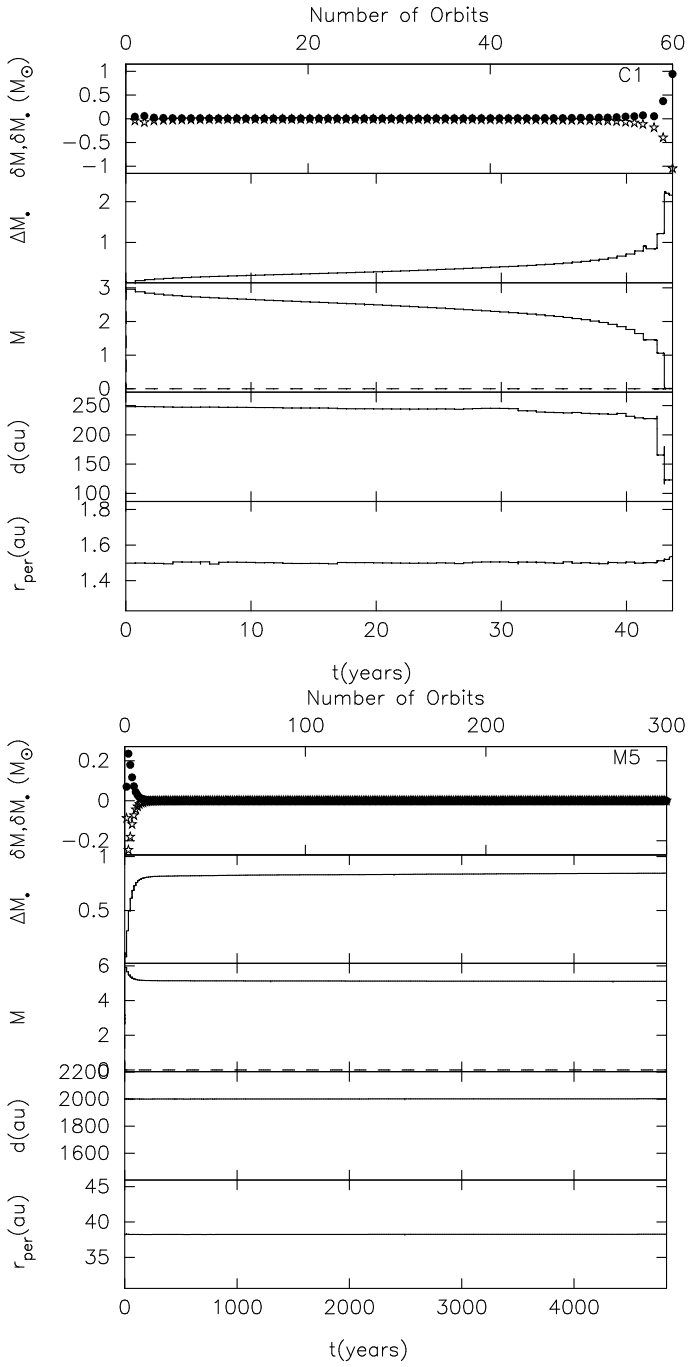

Figure 3.13 Evolution versus time (and number of orbits) in the runs C1 and M5. From the top to the bottom panel: mass $\delta M_\bullet$ gained per orbit by the SMBH (filled circles) and mass δM lost per orbit by the stars (star symbols), cumulative mass $\Delta M_\bullet$ bound to the SMBH, mass M of the bound star, apoapsis d of the bound star, periapsis $r_{\rm per}$ of the bound star.

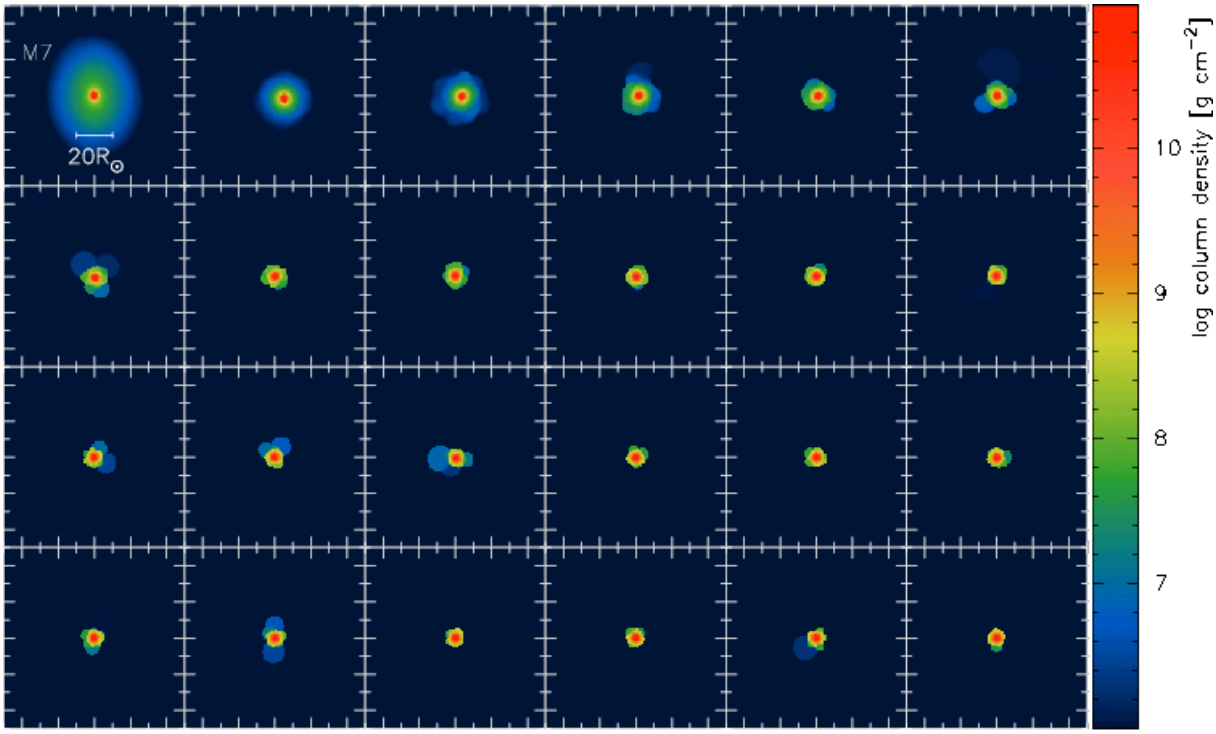

Figure 3.14 Evolution of the merger remnant formed in run M7 after each periapsis passage when the star sets to hydrostatic equilibrium and until mass loss ceases. Time increases from left to right and form top to bottom. Initially the merger remnant has a large low-density envelope that is completely removed after several obits around the SMBH.

by reducing its radius. In the following evolution, mass-loss essentially ceases. We note that merger products have a very non-uniform density profile characterized by a extended low density envelope and a dense central region. Subsequent passages of the star by the SMBH will therefore cause the depletion of the outermost stellar region, unveiling its hot central core. An example of this phenomenon is shown in Figure 3.14, where we plot column density plots for the merger remnant of run M7. After about twenty orbits mass loss stops and the envelope has been completely removed. Similar mechanisms, involving tidal stripping suffered by late-type giants during close passages around a intermediate massive black hole, have been invoked in the past (Miocchi 2007) to explain the extreme horizontal-branch stars observed in some globular clusters (Rich et al. 1997).

We find that the dimensionless parameter ζ is strongly correlated with whether and how quickly a bound star loses mass through Roche lobe overflow. For example in run H2, the bound star has $\zeta > 1$ and does not experience a collision or merger that would change ζ: it consequently continues to orbit the SMBH without ever suffering any mass loss. In all the cases with $\zeta < 1$, the bound star is ultimately destroyed after repeated episodes of Roche lobe overflow, with smaller values

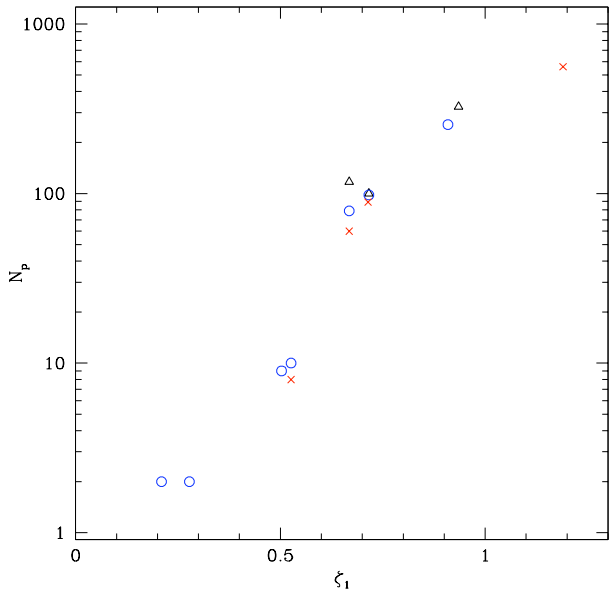

Figure 3.15 The number of periapsis passages past the black hole needed to disrupt the bound star versus the initial dimensionless Roche lobe parameter ζ_1. The different data points represent the scenarios in which the bound star suffers a collision (red crosses: runs C1, C2, C3, and C4), is formed in a merger (black triangles: runs M2, M6, and M10), or is cleanly separated from the HVS (blue circles: runs H1, H3, H4, H5, H6, H7, and H8). Those collision and merger data with $N_p \gtrsim 100$ likely underestimate N_p due to resolution effects and are best considered as lower limits (see text).

of ζ generally corresponding to fewer orbits before disruption. Figure 3.15 shows that the number N_p of periapsis passages before disruption grows exponentially with the initial ζ. In addition, this number of passages depends only weakly on whether the interaction type is a collision (red crosses), merger (black triangles), or clean ejection of a HVS (blue circles).

The rightmost data point in Figure 3.15, corresponding to run C2, deserves some discussion. In this case, $\zeta_1 = \zeta_2 = 1.19 > 1$, so that neither binary component would lose mass if it were not for the collision induced on the first periapsis passage. This collision both increases the radius and slightly decreases the mass of the bound star, effectively decreasing its ζ parameter to a value below 1. Thus, on the subsequent passage past the black hole, the star loses more mass, now due to Roche lobe overflow. The response of this particular star to mass loss is that its radius remains roughly constant. From equation (3.7), the ζ parameter then stays below 1 and slowly decreases as the mass ratio q decreases with each successive passage. Ultimately, after nearly 600 periapsis passages, the star is completely pulled apart.

Similarly to the stars from run C2, the $6\,M_\odot$ star in run M13 has $\zeta = 1.22 > 1$. This

star indeed makes the first periapsis passage without immediately losing any mass; however, while the binary recedes away from the SMBH, the merger causes mass ejection. The resulting $6.84\,M_\odot$ merger product is large enough that ζ drops below 1, and, on the subsequent periapsis passages, mass is lost through Roche lobe overflow. As a result of shedding its high entropy outer layers, the merger product shrinks sufficiently that ζ is pushed back toward $\zeta \approx 1$. By comparing runs C2 and M13, we conclude that the fate of binary stars with $\zeta \gtrsim 1$ depends not simply on the initial values of ζ but also on the type of their interaction and the response of the bound star to mass loss.

In several of our simulations, merger products formed from stars with $\zeta > 1$ are large enough that ζ drops below 1 and at least some mass is lost due to Roche lobe overflow on the second and later periapsis passages (runs M1, M3, M4, M5, M7, M8, M9, M11, M12, and M13). Because shock heating is preferentially distributed to the outer layers of a merger product (Lombardi et al. 2002), this Roche lobe overflow always strips away very high entropy material and the product responds by decreasing its radius. In this way, the ζ parameter gradually approaches a value ≈ 1, corresponding to an eccentric semidetached binary consisting of the bound star and the SMBH. In our SPH simulations of such cases, we typically follow the dynamics for several hundred orbits, without seeing an appreciable decrease in the mass of the bound star: indeed at late times the mass loss typically fluctuates between 0 and 2 SPH particles per periapsis passage. Such situations necessarily challenge the mass resolution limit of our simulations, and it is difficult to say whether such small levels of mass loss are physically meaningful or simply a numerical artifact. In any case, in nature, thermal relaxation in the outermost layers of such a merger product would tend to retract it inside of its Roche lobe and stabilize the star against further mass loss.

To better understand the effects of the numerical resolution, we vary the number of particles used to model several of the scenarios. The results for scenario M7 are summarized in Table 3.5, where we list the mass, eccentricity, and semimajor axis of the bound star after 25 orbits. We find a good agreement of results at all resolutions tested and a convergence of these results as the number of particles N is increased up to the value used in this work ($\approx 4 \times 10^4$). In particular, the final orbital data have converged to within $\sim 0.02\%$.

We also extend our resolution study to cases in which the bound star is ultimately disrupted. We find that, for various particle numbers from $N \approx 5 \times 10^3$ up to 8×10^4, the simulations of the same initial conditions all behave very similarly for at least the first ~ 100 orbits around the SMBH. The top three frames of Figure 3.16, for example, demonstrate this consistency for the mass M, eccentricity e, and semimajor axis a of the bound star after 50 orbits. For situations in which the star orbits the SMBH more than ~ 100 times, the simulations at various resolutions diverge at late times, with higher resolutions simulations in which there is a collision or merger requiring more periapsis passages to disrupt the bound star (see C2 and M6 the bottom frame of Fig. 3.16).

In addition to the scenarios shown in Figure 3.16, we also study resolution effects in simulations of several other cases in which the bound star is ultimately disrupted (specifically C3, H1, H3, H4, H6, and M2), with the particle number N varying from 5×10^3 up to 4×10^4.

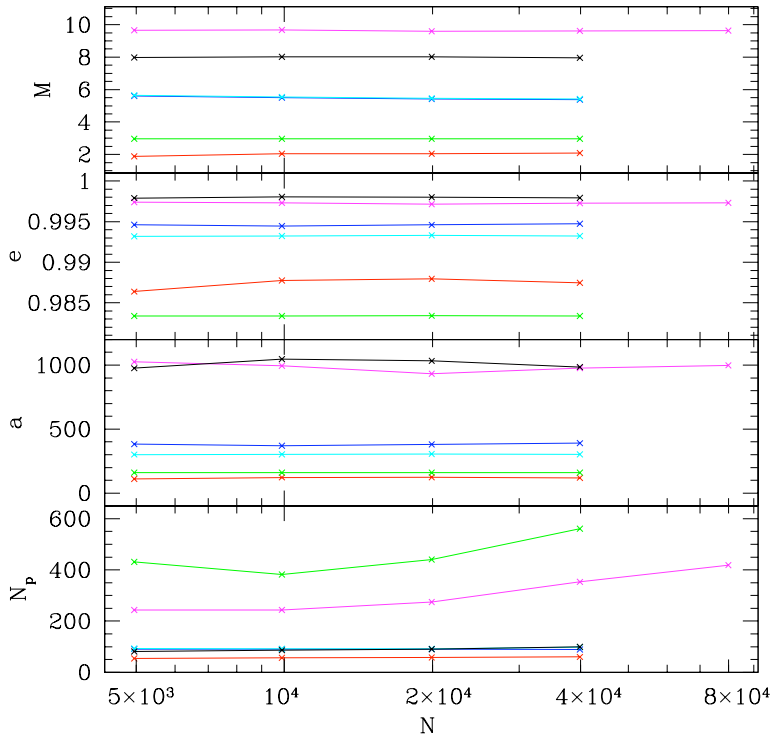

Figure 3.16 The mass M in solar masses, eccentricity e, and semimajor axis a of the bound star, all after 50 periapsis passages, versus total particle number N for several representative scenarios in which the bound star is ultimately disrupted: C1 (red), C2 (green), C4 (blue), H5 (cyan), M6 (magenta), and M10 (black). Also shown, in the bottom frame, is the number N_p of periapsis passages needed to completely disrupt the bound star. For a given scenario, note the consistency of the data for M, a, and e after 50 orbits, as well as for N_p in cases with $N_p \lesssim 100$.

As with the Figure 3.16 data, the consistency of the results is again very good for $N_p \lesssim 100$. For example, for case C4, each of four such simulations predict that it would take somewhere in the range of 89 to 91 periastron passages to completely disrupt the bound star. Furthermore, for case C3 all simulations predict that it takes 8 periastron passages to disrupt the bound star, in case H4 all simulations predict that it takes 10 passages, and in case H6 all simulations predict that it takes 2 passages. We conclude that the particle number employed in this work is sufficient to model accurately the evolution for at least ~ 100 orbits around the SMBH.

Finally, as an illustrative example, Figure 3.17 gives column density plots for run M6 after 50 periapsis passages and for simulations with different number of particles.

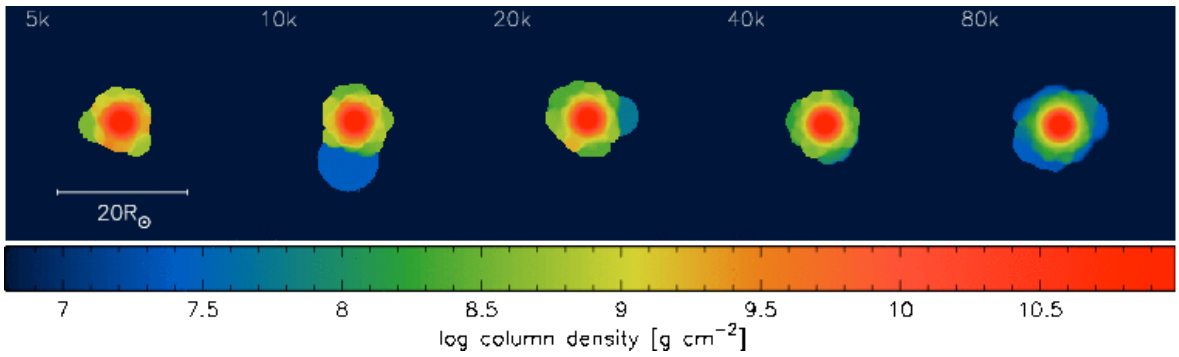

Figure 3.17 Column density plots for run M6 after 50 periapsis passages and using different total number of particles (5k, 10k, ..., 80k).

Internal Structure

Figure 3.18 shows the composition profiles as a function of enclosed mass fraction m/M for the bound star in cases M4 and M13. Here, m is the mass enclosed within an isodensity surface and M is the total bound mass. The dotted curves show the profiles after two periapse passages, while the solid curves show the same profiles once the bound star has effectively reached a steady state. Mass loss experienced during multiple passages removes the outer layers of the star, decreasing the bound mass M and causing the composition profiles to shift slightly to larger enclosed mass fractions m/M.

We note that the helium profile for M13 is qualitatively similar to that of the case G merger product in Sills et al. (1997) (see Fig. 2 in that paper): both have a maximum helium abundance at an intermediate radius inside the star. In both case G and our M13, the strange helium profile is caused by a low mass star sinking to the center of the collision product and displacing the helium rich fluid outward. The stellar track for the case G product is shown in Figures 4 and 6 of Sills et al. (1997). In Figure 6, we see that, on the main sequence, the case G product is somewhat bluer and brighter than a normal main sequence star of the same mass. In Figure 4, we see that the case G product is a little bluer and brighter than a different collision product (case J) with basically the same mass but without the dense hydrogen core. It is the increased helium content in the stellar interior that makes the opacity lower (compared to other main sequence stars of the same mass) and thus bluer and brighter. So, by analogy, our M13 merger product would be a little bluer and brighter than a normal main-sequence star of the same mass.

The elements Li, Be, and B are potentially interesting observational indicators of the history of a star. These elements burn at temperatures of about 2.5×10^6, 3.5×10^6, and 5×10^6 K, respectively, and therefore can exist only in thin outer layers of the parent stars. During a dynamical interaction, these elements can be removed either by ejecting the outer layers of the star or by

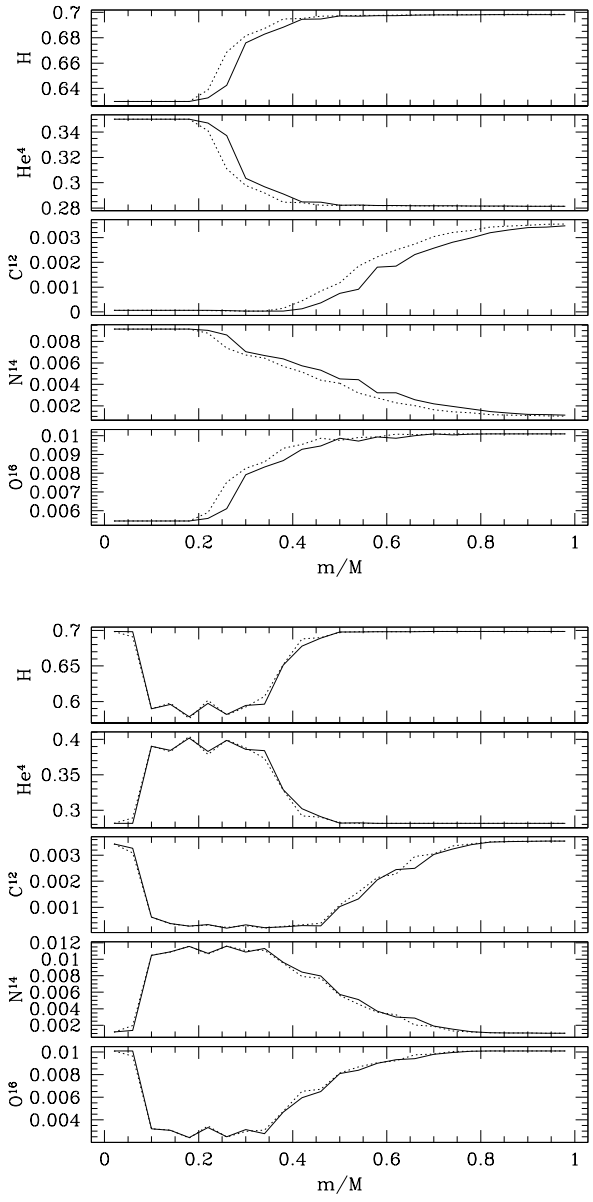

Figure 3.18 Upper panels: composition profile of the merger product in run M4 after two (dotted curves) and eighteen (solid curves) periapsis passages, corresponding to masses $M = 4.75\,\mathrm{M}_\odot$ and $M = 4.27\,\mathrm{M}_\odot$, respectively. Lower panels: composition profile of the merger product in run M13 after two (dotted curve) and 76 (solid curves) periapsis passages, corresponding to masses $M = 6.46\,\mathrm{M}_\odot$ and $M = 6.32\,\mathrm{M}_\odot$, respectively.

redistributing them to an environment too hot for their long term existence. Although Be, B, and Li can exist after the first periapsis passage (see Fig. 3.10), the effect of multiple passages is typically to remove these elements completely. Although there are cases where B still exists in the final bound star, it is always severely depleted. For example, in run M13 the B level at the surface of the final product is only ∼3% of the surface value in the $6\,M_\odot$ parent star from which it originated.

In Table 3.6, we summarize some properties of the bound stars that survive in our SPH simulations (i.e., that are not ultimately disrupted by the SMBH). The "number of passages" represents the number of periapse passages before the mass loss effectively shuts off, which we defined as having 2 or fewer SPH particles ejected. The central hydrogen abundance is given by X_c, which always equals the central hydrogen abundance of the lowest mass parent star. We also list the effective age of the bound star based on its mass and central hydrogen abundance. We evaluate this effective age, based on how long it would take a normal star of that mass to evolve to that central hydrogen abundance using the TWIN stellar evolution code. It is known that the contraction of a merger product to the main-sequence is very similar to the contraction of a pre-main-sequence star to the main-sequence. In the latter case, the most important variable is the mass (for a given hydrogen abundance). In the former case, the two important variables are essentially mass and central hydrogen abundance (Sills & Lombardi 1997). In runs C5 and H2 the bound star is only a slightly perturbed version of one of the binary components, and the ages in these cases is the same 50 Myr as that component. For mergers of two $3\,M_\odot$ stars, the effective age of the merger product is in the range of 14 to 22 Myr. For mergers of two $6\,M_\odot$ stars, the effective age is in the range of 6 to 9 Myr. Mergers of unequal mass stars (M12 and M13) also significantly rejuvenate a star: for example in M13, the sinking of the 1 solar mass star to the center of the merger product essentially resets the nuclear clock to only 0.3Myr after the ZAMS.

In the last three columns of Table 3.6 we list central temperature T_c, internal energy U and thermal timescale $t_{\rm thermal}$ of surviving bound stars. The central temperature is defined as the temperature in the star where the density is highest and therefore is not always the temperature of the highest temperature SPH particle. The central temperature T_c of all the stars is large enough to sustain nuclear burning in the core. The global thermal time scale can be estimated as

$$t_{\rm thermal} = U/\langle L\rangle, \tag{3.10}$$

where $\langle L\rangle$ is a mass weighted average of the luminosity L throughout the entire star.

To calculate L, we take advantage of the fact that the parent stars are massive enough to be fully radiative. In addition, shock heating prevents any convective zones from existing in a newly formed merger product. Thus, we obtain the luminosity L exiting a closed surface by the integral $L = \oint \mathbf{F}\cdot\mathbf{da}$, where $\mathbf{da}$ is an area element on the surface and the diffusive radiative flux $\mathbf{F} = -4acT^3\nabla T/(3\kappa\rho)$. Here a is the radiation constant, c is the speed of light, and κ is the opacity. The surface integral is easily converted to a volume integral by the divergence theorem. The result,

$L = \int \nabla \cdot \mathbf{F} dV$, is straightforward to estimate in SPH:

$$L = \sum_i \frac{m_i}{\rho_i} (\nabla \cdot \mathbf{F})_i, \tag{3.11}$$

where the sum is over only those particles positioned inside the surface under consideration. Because SPH calculations cannot properly resolve the photosphere, equation (3.11) cannot be used to give a reliable total luminosity. However, equation (3.11) does allow us to study the luminosity profile throughout the bulk of the system.

As an example, in Figure 3.19, we show a more detailed look at the interior of the final bound stars in runs M4 and C5. From top to bottom, we give the luminosity L, temperature T, and radius r as a function of enclosed mass m. To evaluate the luminosity profile, we use equation (3.11) on each SPH particle, summing over particles of larger density and calculating the opacity κ from the OPAL tables. Our merger and collision products typically achieve a maximum luminosity in their outermost layers that is comparable to the Eddington luminosity

$$L_{\rm edd} = \frac{4\pi G c}{\kappa} M \sim 3.8 \times 10^4 \mathrm{L}_\odot \frac{M}{\mathrm{M}_\odot} \quad , \tag{3.12}$$

although such a high luminosity would diminish rapidly as the star contracts to the main-sequence in a time $t_{\rm thermal}$ usually of order ~ 0.1Myr.

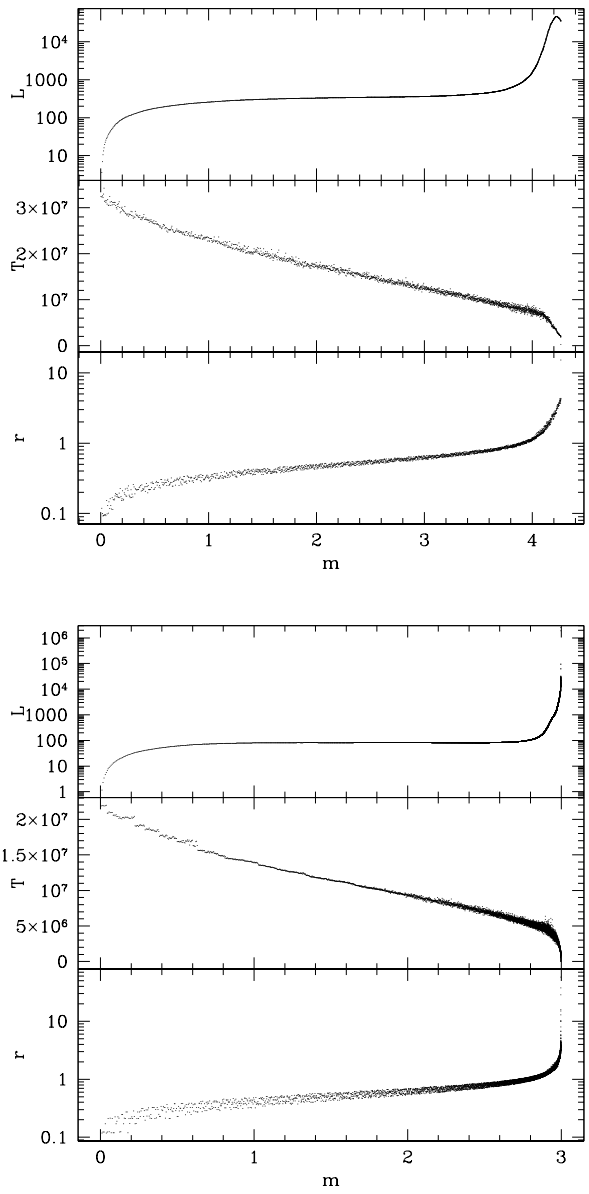

Figure 3.19 From top to bottom: luminosity L, temperature T, and radius r as a function of enclosed mass m for the final bound stars of runs M4 (upper panels) and C5 (lower panels). L, r and m are in solar units, while T is in Kelvin.

3.5 Discussion

The observed rotation rates of HVSs may give important clues to their formational history. Hansen (2007) has proposed that, as a consequence of tidal locking in close binaries, HVSs ejected by the Hills mechanism should rotate systematically slower than field stars of similar spectral type. López-Morales & Bonanos (2008) found that the late B-type star HVS 8 has a rotational velocity of $\sim 260\,\mathrm{km\,s^{-1}}$, more typical of single B-type stars and therefore seemingly contrary to the hypothesis of a binary origin for this star. In order to explain the observations, other ejection mechanisms have been invoked, such as ejection by a close encounter with a massive black hole binary or with a stellar black hole orbiting the galactic center SMBH (Yu & Tremaine 2003; Levin 2006; Sesana et al. 2006; Löckmann, & Baumgardt 2008). However, it has been note that a larger statistic would be certainly required in order for the rotation to be used as a signature for the origin of HVSs and/or S-stars (Perets 2009a). Furthermore, in this chapter we have shown that there are two other potentially important ways with which the stars can somewhat increase their rotation even in the binary disruption scenario: tidal torque by the SMBH at periapsis (if the stars enter within their tidal disruption radius) and/or a collision between the two binary members.

With the help of simplifying approximations, we are able to relate the rotational parameter J calculated in our simulations to the observable rotational velocity v after that star has thermally relaxed back to the main sequence. In particular, we approximate that the star rotates rigidly, that its rotation does not drastically affect its structure, and that the rotational parameter J is conserved during relaxation. Using $L = Iv/R = c_1 MRv$ and $E = -c_2 GM^2/R$ in equation (3.9), we obtain $J = c_1 c_2^{1/2} v (R/(GM))^{1/2}$. Clearly c_1 and c_2 are simply numerical coefficients related to the moment of inertia I and total energy E of a star, respectively. For B-type main sequence stars, we find $c_1 c_2^{1/2} \sim 0.04$ to 0.05 and R/M $\sim$0.5 to 0.8 $\mathrm{R_\odot/M_\odot}$ using models from the TWIN stellar evolution code. Solving for v in terms of J, we find

$$v \sim 1.2 \times 10^4 J\,\mathrm{km\,s^{-1}}, \tag{3.13}$$

accurate to within $\sim 30\%$ for most B-type main sequence stars. Given the J values of ejected stars in our simulations (see Fig. 3.5 and Table 3.5), we estimate from equation (3.13) that the post-relaxation rotational velocity v can be as large as $\sim$400 or 500 km $\mathrm{s^{-1}}$ for HVS stars (consider runs C3 and H6). We therefore conclude that the rotation of the star HVS 8, for example, is completely consistent with a binary origin.

The J values for unmerged stars in our simulations that are bound to the SMBH after the first periapsis passage indicate, via equation (3.13), that the post-relaxation rotational velocity v would be typically $\lesssim$ 400km $\mathrm{s^{-1}}$ but could be as large as $\sim$ 1000km $\mathrm{s^{-1}}$. These large rotation velocities, however, correspond to stars that penetrate deeply within their tidal disruption radius (e.g. runs H6 and H8) and therefore are eventually destroyed after several orbits. Merger products obtain even larger spins after the first periapsis passage (see Table 3.4.1). However, as the merger

Table 3.4 Same as table 3.4 but for simulations in which the stars do not collide and one member becomes a HVS. $J_{\rm captured}$ gives the spin of the stars that remain bound to the SMBH, while $J_{\rm ejected}$ refers to the ejected stars.

Run	$v_{\rm ej}$ (km/s)	a (au)	e	$\Delta M_{\rm b}/M_{\rm b}$	$\Delta M_\bullet/M_{\rm b}$	$J_{\rm captured}(J_{\rm ejected})$
H1	3883(3910)	160(160)	0.991(0.991)	-2.230×10^{-4}	1.221×10^{-4}	$0.211\times10^{-2}(0.188\times10^{-2})$
H2	2026(2160)	309(308)	0.983(0.974)	0	0	$0.268\times10^{-3}(0.238\times10^{-3})$
H3	1082(1100)	423(421)	0.991(0.983)	0	0	$0.153\times10^{-3}(0.729\times10^{-4})$
H4	4221(4252)	142(142)	0.995(0.990)	-1.019×10^{-2}	5.401×10^{-3}	$0.194\times10^{-1}(0.147\times10^{-1})$
H5	2121(2155)	306(307)	0.974(0.993)	-8.454×10^{-5}	4.759×10^{-5}	$0.149\times10^{-2}(0.168\times10^{-2})$
H6	1637(947.6)	174(444)	0.988(0.999)	-0.9914	0.9914	$0.445\times10^{-1}(0.379\times10^{-1})$
H7	2570(2574)	677(674)	0.983(0.978)	-1.335×10^{-2}	6.911×10^{-3}	$0.223\times10^{-1}(0.348\times10^{-3})$
H8	2494(2497)	619(619)	0.991(0.990)	-0.4835	0.2458	$0.845\times10^{-1}(0.274\times10^{-1})$

Table 3.5 Resolution study for scenario M7. The particle number is given by N, while the mass, orbital eccentricity and semimajor-axis of the bound star after 25 orbits around the SMBH are given by M, e, and a respectively.

N	M ($\rm M_\odot$)	e	a (au)
4,957	0.9972	1147.1	8.468
9,889	0.9973	1146.7	8.410
19,933	0.9974	1146.2	8.392
39,877	0.9973	1146.2	8.390

product keeps orbiting the SMBH, J decreases as mass gets pulled off the outside of the star, where the specific angular momentum is greatest. The bound stars that survive to orbit the SMBH end our simulations with $J \lesssim 0.017$ (see Table 3.6), corresponding to post-relaxation rotational velocities $v \lesssim 200\text{km s}^{-1}$. As our simulations began with irrotational stars, the actual final rotational velocity of a (bound) star could be larger or smaller if the parent stars had significant spin, depending on the orientation of the spin axis with respect to the external orbital plane and/or the plane on which the collision occurs. If the spin axis is aligned with the angular momentum of the external orbit, the initial spin will sum up with that acquired due to the tidal torque from the SMBH. A larger spin will also result from a collision, if the angular momentum of the inner binary is initially aligned with the spin axis of the stars. We stress here that, in general, the effect of an initial spin on the final rotation of the stars can be complicated, for this reason we decided to ignore initial rotation and begin with binary components irrotational in the inertial frame, which allows us to more easily measure any rotation imparted during the subsequent interaction.

Deep near-IR observations of the GC show that the S-stars are B0-B9 main-sequence stars with rotational velocities similar to those of field stars of the same spectral type (Alexander 2005). Our final bound stars therefore have properties very similar to those of the S-stars: their masses qualify them as spectral type B main-sequence stars, and their post-relaxation rotational speeds are of the correct general magnitude. For example, the rotational speeds of our fastest rotators are consistent with the 220 ± 40 km s^{-1} value for the S-star SO-2 (Ghez et al. 2003). However, we note that the orbital eccentricities of our bound stars ($0.96 < e < 1$) are larger than that of SO-2 ($e \approx 0.87$), as similarly found in simulations by Ginsburg & Loeb (2006) and Hansen (2007).

For tidal torque from the black hole to have a significant effect on stellar rotation, the stars should enter deep into their disruption zone (i.e., $r_{\rm per} < r_{\rm t}$).

When no collision occurs between the components of a binary, the distance of closest approach of the two stars to the SMBH typically changes little due to the encounter. In such cases, a necessary condition for significant spin-up is that the binary itself be on an orbit that passes within $\sim r_{\rm t}$ of the SMBH. This implies in turn that the fractional change in orbital angular momentum with respect to the SMBH, per orbit, be of order unity. This condition is satisfied in the so-called "full loss cone" regime, which, in a galaxy like the Milky Way, extends inward to ~ 0.2 times the SMBH influence radius, or to $r \approx 0.5$pc (e.g. Wang & Merritt 2004). [1] Inside this region, which is the region of interest for the current study, evolution onto loss-cone orbits is diffusive, and most binaries would be tidally disrupted before finding themselves on orbits that intersect $\sim r_{\rm t}$. We note however that in the "massive-perturber scenario" the apoapsis distance of the binary is of the order of a parsec (i.e., > 0.5pc) and therefore the fractional change in orbital angular momentum with respect to the SMBH, per orbit, can be of sufficient to put the binaries on a trajectory that passes within $r_{\rm t}$ of the SMBH. Even inside 0.5pc, other dynamical processes like resonant relaxation (Rauch & Tremaine

[1] Assuming a $\rho \sim r^{-2}$ density cusp.

Table 3.6 Some properties of the bound stars that survive in our SPH simulations. NP (number of passages) gives the number of SMBH-star encounters before mass-loss ceases. Mass, orbital eccentricity and semimajor-axis of the star are given by M, e and a respectively. The value of J is the final dimensionless spin parameter, while X_c is the central hydrogen abundance. The corresponding effective age is also listed. In the last three columns,we give central temperature T_c (the temperature where the density is highest), internal energy U, and thermal timescale $t_{\rm thermal}$.

Run	NP	M ($\mathrm{M}_\odot$)	e	a (au)	J	X_c	Effective Age (Myr)	T_c $\times 10^6$ (K)	U $\times 10^{50}$ (erg)	$t_{\rm thermal}$ (Myr)
C5	8	2.998	0.974	212	0.009	0.63	50	22	0.141	0.4
H2	2	3.000	0.978	316	0.000	0.63	50	23	0.148	1
M1	30	4.83	0.995	1010	0.009	0.63	16	31	0.326	0.1
M3	30	4.94	0.996	996	0.010	0.63	16	31	0.321	0.2
M4	18	4.27	0.996	1000	0.009	0.63	22	32	0.292	0.2
M5	22	5.15	0.962	1020	0.014	0.63	14	32	0.309	0.05
M7	25	8.39	0.997	973	0.016	0.56	9	39	0.710	0.1
M8	90	10.7	0.996	1030	0.014	0.56	6	39	0.944	0.07
M9	27	8.74	0.995	1010	0.010	0.56	9	39	0.736	0.06
M11	14	10.1	0.980	1010	0.005	0.56	7	36	0.793	0.03
M12	27	7.27	0.992	1020	0.009	0.63	7	32	0.269	0.03
M13	79	6.32	0.997	1060	0.017	0.70	0.3	18	0.391	0.1

1996), scattering from an intermediate mass black hole (Merritt et al. 2009) or perhaps eccentric instability in a disc (Madigan et al. 2008) can produce larger changes in orbital angular momentum than in the case of two-body relaxation alone. On the other hand tidal spin-up is not expected to be very efficient because it is important only for the narrow range of periapses: $\frac{1}{2}r_t \lesssim r \lesssim r_t$ (for $r \lesssim \frac{1}{2}r_t$ the star is fully disrupted; for $r > r_t$ tidal torque is small). As a consequence of the previous condition, the ejected star will lose a large fraction of its mass. An observational indicator of the history of the star would be, even in this case, a deficit in the abundances of light elements (such as Lithium) that can exist only in thin outer layers of the parent star and that are typically removed by the tidal interaction with the SMBH.

One of the main arguments against rejuvenation of the S-stars through merger is the apparent "normality" of their spectra (Figer 2008). We note, however, that the envelope of our merger products will not look significantly different than that of normal stars (compare the right edge of the plots in Figure 3.15 with the right edge of Figure 3.2). In fact, if the parent stars are of equal mass, the merger product will have very normal profiles throughout the star. If the parent stars are of significantly different mass, then the profiles are more peculiar and one should worry about how this affects the stellar evolution. The main effect would probably be to change the opacity and therefore shift slightly the color and luminosity. But, unless significant mixing is induced, the chemical composition of the outermost envelope will remain similar to that of the higher mass star

(with the possible exception of Li, Be, and B levels: see §3.4.2).

The tidal disruption of a star passing close enough by a SMBH to enter its tidal radius, produces a luminous UV/X-ray flare of radiation as the bound stellar gas falls back onto the black hole and is accreted (Rees 1988). Tidal flares are of great interest because they can probe the presence of SMBHs in galaxies with otherwise no evidence of an active nucleus and can be used to measure the mass and spin of the central black hole (Komossa et al. 2004; Gezari et al. 2008, 2009). Computations of the tidal disruption of stars have been performed by several studies in the past, with the aim of understanding the observational signatures of these events (Ulmer 1999; Bogdanović 2004; Gomboc & Čadež 2005; Lodato et al. 2009; Strabbe & Quataert 2009; Guillochon et al. 2009; Kasen & Ramirez-Ruiz 2010). We note that there are many important scenarios in our work that have been so far almost completely ignored: (i) multiple passages by the same star; (ii) merger of two stars resulting in disruption due to the increased size; (iii) partial tidal disruptions.

Predicting the radiative effects of multiple passages of a star by a SMBH is outside the scope of the present work. But, it seems likely that the light curve resulting from these repeated tidal events might show a series of small peaks, separated roughly by the orbital period, before finally producing the large peak that is observed as the "tidal disruption." Assuming the star on a parabolic trajectory, after the star-SMBH encounter, the most bound material moves on a orbit with semi-major axis $a = \frac{1}{2} r_{\rm per}^2/R$ and returns to periapsis after a time

$$t_0 = \frac{2\pi r_{\rm per}^3}{(GM_\bullet)^{1/2}\,(2R)^{3/2}} = 0.22 \times \left(\frac{r_{\rm per}}{r_{\rm t}}\right)^3 \left(\frac{R}{\rm R_\odot}\right)^{3/2} \left(\frac{M}{\rm M_\odot}\right)^{-1} \left(\frac{M_\bullet}{4\times 10^6\,\rm M_\odot}\right)^{1/2} \rm yr\ , \qquad (3.14)$$

that it is also the time when the flare starts, while the peak return rate occurs at $t \sim 1.5 t_0$ (Evans & Kochanek 1989; Li et al. 2002).

As previously discussed, merger products are very large, so it is easy to strip off lots of mass during the early periapsis passages, while at later time the mass loss often ceases. The light curve resulting from these repeated tidal events will eventually show a series of small peaks of declining intensity (see Figure 3.12). The result of the repeated (partial-)tidal disruption of a star with a large envelope (e.g., late-type giants) will show a similar light curve. In collisions without mergers, there is some expansion in size but it is not as dramatic as in a merger. So it is not until late times that there is significant mass overflowing the Roche lobe. The light curve will show peaks of increasing intensity until the last brightest flare produced by the full tidal disruption of the star.

In future work, one could model the material that becomes bound to the black hole more carefully. In particular, it would be interesting to identify possible signatures of interactions between the bound star and the accretion torus left behind from previous periapse passages. Quasi-periodic emission may be detected if X-ray flares arise every time the star crosses the torus plane (Dai et al. 2010).

3.6 Summary

In this chapter, we carried out hydrodynamic simulations of binary stars in orbit about the supermassive black hole (SMBH) at the Galactic center. In the N-body simulations of Chapter I, we assigned physical sizes to stars based on a simple mass-radius relation and predicted which binaries would merge, i.e., undergo a collision with relative velocity less than escape velocity. The fluid simulations presented in this work were found to be quite consistent with the N-body simulations, in the sense that when the latter predicted a stellar merger, the fluid stars typically merged as well. The merger rates presented in Chapter I are therefore confirmed by the present work. Additional results from the fluid simulations presented in this thesis are summarized below.

1 The central temperature of the merged stars in all our simulations is large enough that there would still be nuclear burning in the stellar core. Merger remnants have thermal time scales $\lesssim 0.1$Myr and surface luminosities that are predicted to be a large fraction of the Eddington luminosity (Table 3.6 and Figure 3.19).

2 Assuming an age of 50Myr for our $3\,M_\odot$ stars and 18.2Myr for our $6\,M_\odot$ stars, we found that merger products of two $3\,M_\odot$ stars have effective ages in the range $14 - 22$ Myr, i.e., this is how long it would take a normal star of the same total mass to evolve to have the same central hydrogen abundance. For mergers of two $6\,M_\odot$ stars, the effective age is in the range $6 - 9$ Myr. Mergers of unequal mass stars also significantly "rejuvenate" a star.

3 Mass loss due to a collision or merger is always less than a few percent of the initial mass of the binary. After a collision without merger, the mass associated with the captured star remains bound to the SMBH, while the unbound debris originates mostly from the ejected star. In mergers, because there is no escaping star, most of the ejecta remain bound to the SMBH.

4 Much greater fractional mass loss can occur when one or both stars is tidally perturbed by the SMBH. Even if the initial periapsis of the binary lies beyond the tidal disruption radius of a single star, tidal stripping can still occur, if one star is scattered onto a tighter orbit around the SMBH or if the two stars merge, forming a temporarily more extended object.

5 We performed the first simulations of repeated tidal encounters of a star with a SMBH. In all cases where the star or merger product has a distance of closest approach to the SMBH smaller than the Roche limit ($\zeta < 1$; eq. 6), disruption occurs after repeated periapse passages, with smaller values of ζ corresponding to fewer orbits before disruption. Figure 3.15 shows that the number N_p of periapse passages before complete disruption grows exponentially with ζ. Moreover, the critical number of passages depends weakly on whether the interaction type is a collision, merger, or clean ejection of a HVS.

6 Tidal spin-up of a star that does not suffer a collision is significant only in a narrow range of periapse distances, $r_t/2 \lesssim r_{per} \lesssim r_t$, with r_t the tidal disruption radius of a single star

with respect to the SMBH. For $r \lesssim r_{\rm t}/2$, the stars are fully disrupted at the first encounter with the SMBH, while they typically survive for $r_{\rm per} \approx r_{\rm t}$. If the high rotational velocity of, for instance, HVS 8 is the result of such an encounter, the star would have needed to lose a large fraction of its mass before ejection from the Galactic center. When the stars collide or merge, more efficient spin-up can occur, resulting in an increased rotational velocity for both the ejected and captured stars.

7 In stellar mergers, elements that can exist only in the outermost envelope of the stars such as Li, Be and B are severely depleted, partially due to envelope ejection during the merger but mostly due to tidal truncation by the SMBH in subsequent periapse passages. However, the envelopes of the merger products do not otherwise differ significantly from those of the parent stars. In the case of equal mass stars, composition profiles following a merger are essentially "normal", while for unequal mass binaries the lower mass star sinks to the center of the merger remnant effectively resetting the nuclear clock of the star to the ZAMS.

8 If a bound star has a large low density envelope (as in our merger products), conspicuous mass loss of decreasing amplitude characterizes the first few periapse passages, eventually becoming negligible. The envelope is thereby removed but the denser nucleus survives. More compact stars that enter the tidal disruption sphere lose some fraction of their mass during each periapse passage, with full disruption occurring only after many orbits. Repeated tidal flares, of either increasing or decreasing intensity and separated roughly by the orbital period of the star, are the predicted observational signature of such events.

We finally stress that SPH calculations neglect radiative and heat transport, and therefore can follow the system only over hydrodynamical timescales that are typically of the order of a few hours. For these reasons, in this chapter, we were able to discuss the relaxed structure of merger products only qualitatively and the relaxation time only in order of magnitude. In a subsequent work, we plan to present the results of stellar evolution calculations that can follow the evolution of the SPH merger products over much longer, thermal and nuclear timescales and determine their track in a color-magnitude diagram. These calculations will allow us to compare the observable properties of our models with the properties of stars observed at the galactic center.

Chapter 4

Formation and evolution of the Milky Way Nuclear Cluster

4.1 Introduction

In the previous chapters we focused on the properties of young massive stars observed at the Galactic center and we showed, by means of numerical simulations, how mergers between main sequence stars can be responsible for a population of rejuvenated stars near Sgr A*. In the following we shall focus on the distribution of the dominant population of old stars, studying possible models for the formation and persistence of a low-density core around the SMBH at the Galactic center, and its implications for the distribution of massive remnants. In the current chapter it is shown that a core results naturally from a model in which the nuclear star cluster is formed via repeated infalls of globular clusters into the Galactic center. We present the results from a set of N-body simulations of this process, which show that other properties of the nuclear star cluster, including its mass and outer density profile, are also naturally reproduced.

The formation mechanism of nuclear star clusters (NSCs) is unknown. Two competing models are possible.

In the *gas model*, a NSC can form from the gas that migrates to the center of the galaxy where then forms stars (Schinnerer et al. 2006, 2008). A variety of scenarios have been proposed to account for the required fast radial inflow of gas into the galactic center, including the magneto-rotational instability in a differentially rotating gas disk (Milosavljević 2004), tidal compression in shallow density profiles (Emsellem & van de Ven 2008) or dynamical instabilities (Shlosman & Begelman 1989, Bekki 2007). Because of the inherent complexity of gas dynamics, the gas model is considered more qualitative and difficult to study.

Alternatively, in the *merger model*, massive clusters migrate to the center via dynamical friction and merge to form a dense nucleus (Tremaine et al. 1975, Ostriker 1988, Capuzzo-Dolcetta

1993, Agarwal & Milosavljević 2011). Observations of NSCs in dE galaxies suggest that the majority, but not all dE nuclei, could be the result of packing mass in form of orbitally decayed globular clusters (GCs) (Lotz 2004). Numerical simulations have also shown that the basic properties of NSCs, including their shape, mass density profile, and mass-radius relation are reproduced in the merger model under a variety of explored conditions (Bekki et al. 2004; Capuzzo-Dolcetta & Miocchi 2008a, Capuzzo-Dolcetta & Miocchi 2008b, Hartmann 2011).

NSCs are among the densest star clusters observed, with effective radii of a few pc and central luminosities up to $\sim 10^7$ $L_\odot$. Both these systems, resolved galactic nuclei and NSCs, resemble compact (galactic nuclei) or ultra compact (NSCs) stellar clusters, with a smooth density profile showing a clear similarity to a King profile (King 1966), quite distinct from the underlying stellar galactic distribution (Carollo et al. 1997, Matthews & Gallagher 2002, Böker et al. 2003). Recently, the study of NSCs has raised new interest because of the discovery, in an ever increasing number of galaxies, of compact nuclei in form of stellar resolved systems (see Côté et al. 2006) and/or NSCs which are now known to be present in galaxies across the whole Hubble sequence and not only in the dE, N galaxies (Andersen et al. 2008, Seth et al. 2008b, Bekki & Graham 2010). The evolution of the nuclei is closely linked to the evolution of the entire galaxy, as evidenced by a number of global-to-nucleus scaling relations discovered in the last decade. The existence of such scaling relations seem to indicate a link among large space-time scales and those much smaller typical of the local nuclear environment (Rossa et al. 2006, Wehner & Harris 2006, Ferrarese et al. 2006, Balcells et al. 2007).

NSCs are however difficult to study because they are so compact to be almost unresolved at the diffraction limit of present large telescopes (10m class) and even future 50m class. Consequently, most of the information on NSCs in external galaxies is based on their integrated properties.

A radial profile and velocity structure can be determined only for the Milky Way NSC which is close enough (~ 8 kpc) that it can be resolved into individual stars (Schödel et al. 2007, Schödel et al. 2009). The Milky Way NSC has an estimated mass of $\sim 10^7 M_\odot$ (Launhardt, Zylka & Mezger 2002, Schödel et al. 2008), and it hosts a massive black hole (MBH) whose mass, $\sim 4.3 \times 10^6 M_\odot$ is uniquely well determined (Ghez et al. 2008; Gillessen et al. 2009; Ghez et al. 2005; Eisenhauer et al. 2005).

A handful of other galaxies are also known to contain both a NSC and a MBH (Seth et al. 2008a, Graham & Driver 2007, Graham & Spitler 2009), and the ratio of MBH to NSC mass in these galaxies is of order unity. In models of NSCs, the dynamical influence of a MBH should therefore be considered, at least in bulges brighter than about $10^9 L_\odot$ which are believed to always contain an MBH (Ferrarese & Ford 2005). In a pre-existing NSC, the presence of a MBH inhibits core collapse, causing instead the formation of a Bahcall-Wolf (1976) cusp on the two-body relaxation time scale (Preto et al. 2004), followed by a slow expansion as stars are tidally disrupted (Merritt 2009). At the Galactic center, the relaxation time at SgrA*'s influence radius is robustly estimated to be $20 - 30$ Gyr (Merritt 2010), suggesting that there may not have been enough time for a

Bahcall-Wolf cusp to form. This is consistent with the fact that the late-type stellar population exhibits not a cusp, but rather a space density that is flat or even falling toward SgrA*, inside a core of radius 0.5 pc (Buchholz et al. 2009; Do et al. 2009; Bartko et al. 2010).

In the case of a NSC that forms via repeated inspiral, tidal stresses will disrupt the clusters when they pass within a certain distance from the MBH, effectively limiting the density within that radius (Charlton & Laguna 1995). Disruption occurs at a distance $r = r_{\rm disr}$ from the MBH, where

$$\frac{M_\bullet}{\frac{4}{3}\pi r_{\rm disr}^3} \approx \rho(0) \approx \frac{9}{4\pi G}\frac{\sigma^2(0)}{r_c^2}. \tag{4.1}$$

Here $\rho(0)$ is the central (core) density of the GC, $\sigma(0)$ its central, one-dimensional velocity dispersion, and r_c its core radius; the second relation is the "core-fitting formula" (King 1966). Writing

$$r_{\rm infl} \equiv \frac{GM_\bullet}{\sigma_{\rm NSC}^2} \approx 1.3{\rm pc}\left(\frac{M_\bullet}{4\times10^6 M_\odot}\right)\left(\frac{\sigma_{\rm NSC}}{100{\rm km\ s^{-1}}}\right)^{-2} \tag{4.2}$$

for the gravitational influence radius of the MBH, where $\sigma_{\rm NSC}$ is the stellar velocity dispersion in the NSC, equation (4.1) becomes

$$r_{\rm disr} \approx 2\left(\frac{\sigma_{\rm NSC}}{5\sigma(0)}\right)^{2/3}\left(\frac{r_{\rm infl}}{r_c}\right)^{1/3} r_c. \tag{4.3}$$

Setting $r_c = 0.5$ pc and $\sigma(0) = 20$ km s^{-1}, values characteristic of the most massive GCs, we find $r_{\rm disr} \approx 1$ pc for the Milky Way. This is roughly equal to the radius of the core (~ 0.5 pc) that is observed in the distribution of late-type stars.

In this work, for the first time, we use self-consistent N-body simulations to test the merger model for the formation of the Milky Way NSC. Our simulations are unique in the sense that: (i) they involve the presence of a MBH at the center of the galaxy; (ii) the NSC is build up by consecutive (as opposite to contemporary) infalls (i.e., the clusters start to decay from the same distance but at *different times*); (iii) they explore the (collisional) long-term evolution of the NSC following its formation.

The basic result is that a variety of observed properties of the Milky Way NSC, including its mass and density profile are reproduced in the simulations. In particular, our study demonstrates that a parsec scale core is a natural product of the merger scenario, providing a possible explanation to the depression of late-type stars observed in the vicinity of the black hole at the Galactic center.

The chapter is organized as follows. The details of our initial models are given in §4.2. §4.3 describes our simulations and results. §4.4 is devoted to the study of the collisional evolution of the NSC following its formation. The implications of our results in the contest of Galactic center dynamics are discussed in §4.5. §4.6 sums up.

4.2 Initial conditions

In the following, we perform full N-body simulations to study the consecutive infall and merging of a set of 12 GCs each starting from a galactocentric distance of 20 pc. After the first GC

is disrupted, we wait for the NSC to reach a steady state and we add to the system a second GC. This procedure was iterated until 12 clusters accumulated and merged in the inner regions of the galaxy where we initially placed a central MBH.

We begin in this section by outlining the details of the initial conditions adopted in the simulations.

4.2.1 The Galactic Model

The nuclear bulge is distinguished from the larger Galactic bulge (effective radius ~ 1 kpc) by its flat disk-like morphology, very high stellar densities, and a history of continuous star formation. The nuclear bulge dominates the inner 500 pc of the Milky Way and it appears as a, distinct, massive disk-like complex of stars and molecular clouds which is, on a large scale, symmetric with respect to the Galactic center. It consists of an r^{-2} nuclear stellar cluster within the inner $\sim$ 30 pc, a larger nuclear stellar disk and a nuclear molecular disk of same size (radius $\sim$ 200 pc and scale height $\sim$ 45 pc). The total stellar mass and luminosity of the nuclear bulge are 1.5×10^9 $M_\odot$ and $\sim 2.5 \times 10^9$ $L_\odot$, respectively (Launhardt et al. 2002). The r^{-2} density distribution holds only within the NSC in the central $\sim$ 30 pc, while, at larger radii, the mass distribution is dominated by the nuclear stellar disk which has essentially a flat density profile (Schödel 2010). The initial conditions for the galaxy in our simulations model the nuclear stellar disk and they omit the central NSC. Accordingly, they correspond to a flattened cusp around a MBH, that we also included as a point mass particle of $M_\bullet = 4 \times 10^6 M_\odot$ located at the origin.

We adopted the power law model:

$$\rho_{gx}(r) = \tilde{\rho} \left(\frac{r}{\tilde{r}} \right)^{-\gamma} \mathrm{sech} \left(\frac{r}{r_{\mathrm{cut}}} \right). \tag{4.4}$$

where $\tilde{\rho} = 400 M_\odot/\mathrm{pc}^3$ is the density at $\tilde{r} = 10$pc, and the truncation function is the same used by McMillan & Dehnen (2005): in the most internal region, where $\mathrm{sech}(x) \sim 1 - \frac{x^2}{2}$, the model is essentially the initial power law, while it goes exponentially to zero for $r >> r_{\mathrm{cut}}$. We choose $\gamma = 0.5$, corresponding to the shallowest power law density profile consistent with an isotropic velocity distribution around a dominating point mass potential (Merritt 2006). This choice of normalizing constants gives a mass density at 10 pc similar to what found in the Galaxy outside the NSC ($\sim$ 400 $M_\odot/\mathrm{pc}^3$), where the nuclear bulge turns to an approximately constant mass density profile. We considered initially very massive and quite compact GCs, already sunk in the central region of the galaxy. We chose $r_{\mathrm{cut}} = 22$ pc which gives a total mass of the (truncated) galactic model equal to $9.1 \times 10^7 M_\odot$.

In order to Monte-Carlo sample the distribution function corresponding to the truncated density profile of equation (4.4) we followed the method described in Szell et al. (2005). Using Eddington's formula, it can be shown that the cumulative number of stars at radius r with velocities

less than v is:

$$F(<v,r) = 1 - \frac{1}{\rho}\int_0^E d\phi' \frac{d\rho}{d\phi'} \times \left\{1 + \frac{2}{\pi}\left[\frac{v/\sqrt{2}}{\sqrt{\phi' - E}} - \tan^{-1}\left(\frac{v/\sqrt{2}}{\sqrt{\phi' - E}}\right)\right]\right\}, \tag{4.5}$$

where $E = \frac{1}{2}v^2 + \phi(r)$ and $\phi(r)$ is the total gravitational potential produced by the stars in the galaxy ($\phi_\star$) and the MBH:

$$\phi(r) = -\frac{GM_\bullet}{r} + \phi_\star(r) = -\frac{GM_\bullet}{r} + 4\pi G\left[\frac{1}{r}\int_0^r dr' r'^2 \rho(\mathrm{r}') + \int_r^\infty dr' r' \rho(\mathrm{r}')\right], \tag{4.6}$$

with G the gravitational constant. Once the positions are assigned, equation (4.5) can be numerically solved to distribute the particles in velocity space.

A good compromise between reliability of the results and computational effort is given by $240,000$ particles to represent the galaxy, which means $380\mathrm{M}_\odot$ as the mass of each particle in the system.

4.2.2 The Globular Cluster Model

The GCs were initially placed on circular orbits with radii $r_0 = 20$ pc. In order not to favor any particular direction for the inspiral, the orbital angular momenta were selected in the following way (e.g. Gualandris & Merritt 2009). The surface of a sphere can be tessellated by means of 12 regular pentagons, the centers of which form a regular dodecahedron inscribed in the sphere. The coordinates of the centers of these pentagons were identified with the tips of the 12 orbital angular momentum vectors. In this way, the inclination and longitude of ascending node of each initial orbit were determined. We then selected the argument of periapsis randomly for each orbit.

The choice of circular orbits was motivated by the well-known effect of orbital circularization due to dynamical friction (Casertano et al. 1987, Ibata & Lewis 1998, Hashimoto et al. 2003).

At a distance of 20 pc from the Galactic center, a GC would already have been subject to tidal forces from the galaxy and the MBH, and its total mass and radius would be less than their original values when the GC was far from the center. We assumed that the *central* properties of the GCs were unaffected by tidal forces during the inspiral to 20 pc, and adopted values characteristic of massive clusters: central velocity dispersion $\sigma_\mathrm{K} = 35$ km s^{-1} and core radius $r_\mathrm{K} = 0.5$ pc. If the dimensionless central (King) potential is $W_0 = 8$, the total mass works out to be $m \approx 4 \times 10^6$ M$_\odot$. This value of σ_K is roughly two times the maximum value of ~ 18km s^{-1} listed in Harris's (1996) compilation of Galactic GC properties, while the core radius is roughly equal to the median value in that compilation. Our choice of such a large value for σ_K is justified by the fact that only massive clusters, if they are compact enough, could have arrived in the central regions of the Galaxy in a reasonable time without being destroyed by Galactic tidal forces in the process (Miocchi et al. 2006).

We then needed to generate equilibrium models for GCs with these same central properties, but with total masses and limiting (tidal) radii consistent with the known tidal forces from the Galaxy model at 20 pc. This is not a completely straightforward exercise, since the gravitational force from the GC acting on a star at the cluster's limiting radius, r_T, depends both on r_T and on the cluster mass m_T within r_T, and m_T is a function of r_T.

We proceeded in the following way. We first assumed $r_T \gg r_K$. In this case, a King-like model satisfies the following relation between m_T and r_T:

$$Gm_T \approx \frac{1}{2}\sigma_K^2 r_T. \tag{4.7}$$

Given this relation, the tidal radius can then be related to the Galactic potential ϕ and density ρ by (e.g., King 1962)

$$r_T = \frac{1}{\sqrt{2}}\sigma_K \left[\frac{3}{r_0}\left(\frac{d\phi}{dr}\right) - 4\pi G\rho\right]^{-1/2}. \tag{4.8}$$

Using the galaxy mass distribution of equation (4.4) and considering the presence of the MBH , but ignoring the truncation function, we find

$$\frac{d\phi}{dr} = \frac{8\pi}{5}G\tilde{\rho}\tilde{r}\left(\frac{r}{\tilde{r}}\right)^{\frac{1}{2}} + \frac{GM_\bullet}{r^2}\ , \tag{4.9}$$

giving a limiting radius of

$$r_T = \frac{1}{\sqrt{2}}\sigma_K \left[\frac{4\pi}{5}G\tilde{\rho}\left(\frac{r_0}{\tilde{r}}\right)^{-1/2} + \frac{3GM_\bullet}{r_0^3}\right]^{-1/2} \tag{4.10}$$

and a tidally-truncated mass from equation (4.7). Adopting a distance $r_0 = 20$ pc we find $r_T \approx 8$ pc and $m_T \approx 1.1 \times 10^6$ $M_\odot$; in other words, roughly 3/4 of the GC mass would have been removed in the process of inspiralling to 20 pc.

We then equated this m_T with the mass of a new King model having the same core properties:

$$m_T = m_K \equiv \rho(0) r_K^3 \mu(W_0) \approx \frac{9}{4\pi G}\sigma_K^2 r_K \mu(W_0). \tag{4.11}$$

Here $\mu(W_0)$ is a function of the dimensionless central potential that is tabulated by King (1966). Since all the quantities in equation (4.11) are known except for W_0, we can solve for this variable, and find $W_0 = 5.8$. The three parameters (W_0, r_K, σ_K) then uniquely define the King model that was used to generate the initial conditions of the GCs.

As previously stated, the mass of the single particle in the galaxy was $380M_\odot$. For the particles in the clusters we choose $200M_\odot$, approximately one half of that value. With this choice, the total number of particles in each GC was $5,715$ with 740 particles contained within the cluster core.

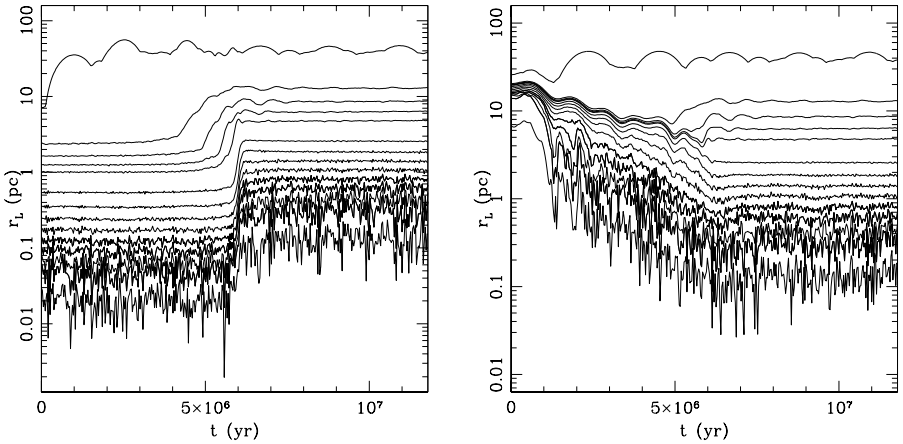

Figure 4.1 Lagrangian radii of the first cluster that arrives at the center of the galaxy. In the upper panel the Lagrangian radii are computed with respect to the center of density of the GC, while in the lower panel with respect to the central MBH. The time for each cluster to settle in a steady state after its disruption is only few Myrs.

4.3 N-body simulations

4.3.1 Numerical technique

Our simulations were performed by using PhiGrape (Harfst et al. 2006), a direct summation code optimized for running on GRAPE clusters. The code implements a fourth-order Hermite integrator with a predictor-corrector scheme and hierarchical time stepping. The accuracy and performance of the code are tuned by the time-step parameter η and the smoothing length ϵ. In what follows, we set $\eta = 0.01$ and $\epsilon = 0.02 r_c$ (10^{-2} pc in our case), this value of the smoothing length being much smaller than the mean first nearest neighbour distance. With this choices, energy conservation was typically $\lesssim 0.01\%$ during each merging event. The simulation was performed using the 32-node GRAPE cluster at the Rochester Institute of Technology and also 2 NVIDIA Tesla C2050 graphics processing units at the Dep. of Physics, Sapienza-Universitá di Roma. In this latter case, PhiGrape was used with SAPPORO, a CUDA library that emulates double-precision force calculations on single precision hardware (Gaburov et al. 2009).

4.3.2 Results

During each infall event, we followed the evolution of the system until the GC reached the center of the galaxy and set there in an approximately steady state. This condition was verified studying the time-evolution of the GC Lagrangian radii that we obtained both with respect to the center of density of the cluster (as defined by Casertano & Hut 1985) and with respect to the central MBH. When the Lagrangian radii of the system flattened to a quasi-stable configuration a

following GC was introduced in the model. An example is illustrate in Figure 4.1 which gives the time evolution of Lagrangian radii for the first infall event. The figure shows that each merging episode lasts approximately 10^7yr and that the time scale for a GC to reach a steady state following its disruption is indeed very short, of the order of Myr.

We verified whether the adopted number of particles had any influence on our results by simulating the first 3 infalls using the same orbital initial conditions but with ten times more particles to represent the clusters. The bulge was the same used in the original simulation. Comparing, after 3 infalls, the density profile of the NSC with that obtained in the original integrations, we did not find any significant difference between the two cases. This suggests that our results are quite robust and they do not strongly depend on the particular choice made for the number of particles in the N-body model.

In addition, we tested the alternative scenario where the 12 clusters, initially located on their respective orbit, start to decay all at the same time. We stress that this "contemporary" infall scenario, adopted in most previously published works, would require a quite special initial state in which all the clusters start their infall at the same radius at a given time. In reality, GCs will arrive at the center at essentially random times, and the interval between these events, which is fixed by dynamical friction time-scale (of the order Gyr), will almost certainly be long compared with the time required for a single GC to reach a steady state following its disruption ($\sim$Myr in Figure 4.1). We also notice that, as long as the simulations respect this separation of timescales, the exact interval between the infall events is essentially irrelevant. In this sense, the "repeated" initial conditions are more generic. For this reason, in what follows, we will focus on this latter scenario, but we will also briefly discuss the results from a "contemporary" infalls simulation.

The density profile

Figure 4.2 shows the spatial profile of the system after the complete merging of 3, 6, 9 and 12 clusters. We fitted the spatial density profile of the final system, within 5 pc around the MBH, using the broken power law model (Saha 1992, Zhao 1996):

$$\rho(r) = \rho_b \left(\frac{r}{r_b}\right)^{-\gamma_i} \left[1 + \left(\frac{r}{r_b}\right)^{\alpha}\right]^{(\gamma_i-\beta)/\alpha}, \tag{4.12}$$

where γ_i is the slope of the inner density profile, β the external slope and α is a parameter that defines the transition strength between inner and outer power laws. The best fit parameters are $\rho_b = 4.1 \times 10^4 \mathrm{M}_\odot/\mathrm{pc}^3$, $r_b = 1.5$pc, $\gamma_i = 0.45$, $\beta = 1.90$ and $\alpha = 3.73$. The model corresponding to this set of parameters is given by the dashed line in Figure 4.2.

The upper panel of Figure 4.3 gives the spatial profile at the end of the simulation for a wider radial range than Figure 4.2 does. We fitted this profile by using two different density laws for the particles in the NSC and for the particles in the galaxy. For the NSC we adopted the modified

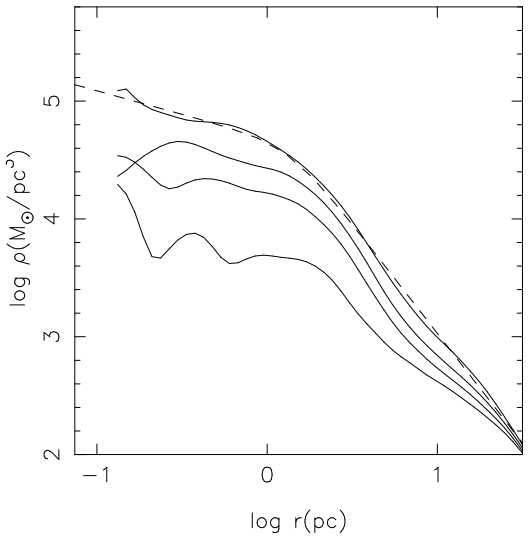

Figure 4.2 Spatial profile of the central NSC after 3, 6, 9 and 12 mergers. The central density grows with time. The dashed line is the fit to the NSC profile obtained at the end of the entire simulation using the broken power law model of equation 4.12.

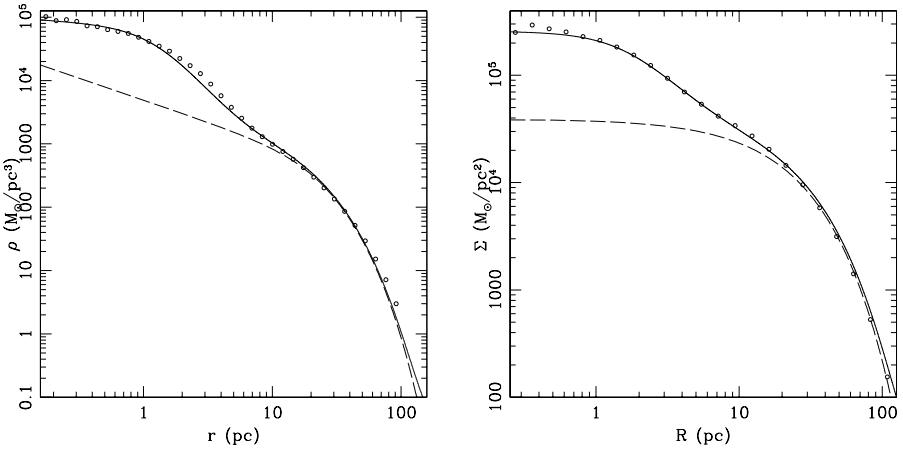

Figure 4.3 Spatial (upper panel) and projected (lower panel) density profiles at the end of the simulation. In each panel, the empty circles give the density profile of the N-body model, the solid lines give the best fitting model to the entire system (galaxy+NSC) and the dashed curves give the fit to the density profile of the galaxy, see text for explanation.

Hubble law (Rood et al. 1972):

$$\rho_{cl}(r) = \frac{\rho_{0,cl}}{\left[1 + \left(\frac{r}{r_{0,cl}}\right)^2\right]^{\frac{3}{2}}}, \tag{4.13}$$

with best fitting parameters $\rho_{0,cl} = 7.46 \times 10^4$ M$_\odot$/ pc^3 and $r_{0,cl} = 1.4$ pc. The galaxy remains well fitted by the initial "truncated" power law of equation (4.1), when $\tilde{\rho} = 9.91 \times 10^2$ M$_\odot$/ pc^3, $\tilde{r} = 10$ pc, $\gamma = 0.69$, and $r_{cut} = 16.3$ pc. The dashed line in the upper panel of Figure 4.3 gives this "best model" for the galaxy density profile, while the solid line was obtained by summing together the fitting density laws of NSC and galaxy.

The lower panel of the figure shows the projected density profile of the N-body model at the end of the simulation. For the NSC we used a modified core model:

$$\Sigma_{cl}(R) = \frac{\Sigma_{0,cl}}{\left[1 + \left(\frac{R}{R_{0,cl}}\right)^2\right]^{\zeta}} , \tag{4.14}$$

while the projected density profile of the galaxy was fitted by a Sérsic law:

$$\Sigma_{gx}(R) = \Sigma_0 \mathrm{e}^{\left[-b\left(\frac{R}{R_e}\right)^{\frac{1}{n}} + b\right]} , \tag{4.15}$$

with

$$b = 2n - \frac{1}{3} + \frac{0.009876}{n}. \tag{4.16}$$

The best fit parameters are: $\Sigma_{0,cl} = 2.18 \times 10^5$ M$_\odot$/pc^2, $R_{0,cl} = 1.99$ pc and $\zeta = 1.03$ for the NSC; $\Sigma_0 = 7.31 \times 10^3$ M$_\odot$/ pc^2, $b = 1.68$, $R_e = 32.3$ pc and $n = 1.003$ for the bulge.

Remarkably, our simulations have reproduced nearly the same slope of the density profile at Galactic center outside ~ 0.5 pc as inferred from observations ($\Sigma(r) \sim r^{-1}$; Becklin & Neugebauer 1968; Haller et al. 1996). In addition, the central region ($r < r_b$) of our model shows a shallow density profile (or a core) near the MBH, also in agreement with observations (Buchholz et al. 2009). The core radius in our model (~ 2 pc) is however more extended than the Galactic center core (of radius ~ 0.5 pc). In §4.4 we show that, as a natural product of two-body relaxation, such initial parsec-scale core shrinks to a core of the size currently observed in a time which is of the order the relaxation time at $r_{\rm infl}$. After this time, the distribution of stars near the SMBH approaches but does not fully reach the quasi-steady-state form described by the Bahcall-Wolf solution (see also Figure 10 in Merritt [2010]).

In the upper panel of Figure 4.4 the half mass radius (r_h) is plotted as a function of the NSC mass (M_{cl}) at the end of each infall. At any time, the NSC mass is given by the sum of the decayed GCs masses. A good fitting scale relation is:

$$r_h = 0.45 \left(\frac{M_{cl}}{M_\odot}\right)^{0.19} \text{ pc} , \tag{4.17}$$

represented by the solid line in the same panel.

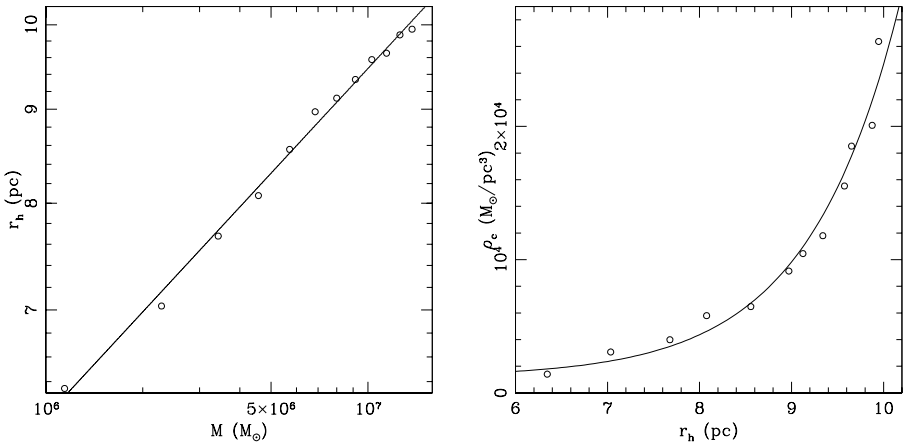

Figure 4.4 Upper panel: empty circles represent the half mass radius of the central NSC as a function of the total mass of the same system. The solid line represents the scaling relation given in equation (4.17). Lower panel: the core density of the cluster versus its half mass radius (empty circles). The solid line shows the $\rho_c - r_h$ relation given by equation (4.18).

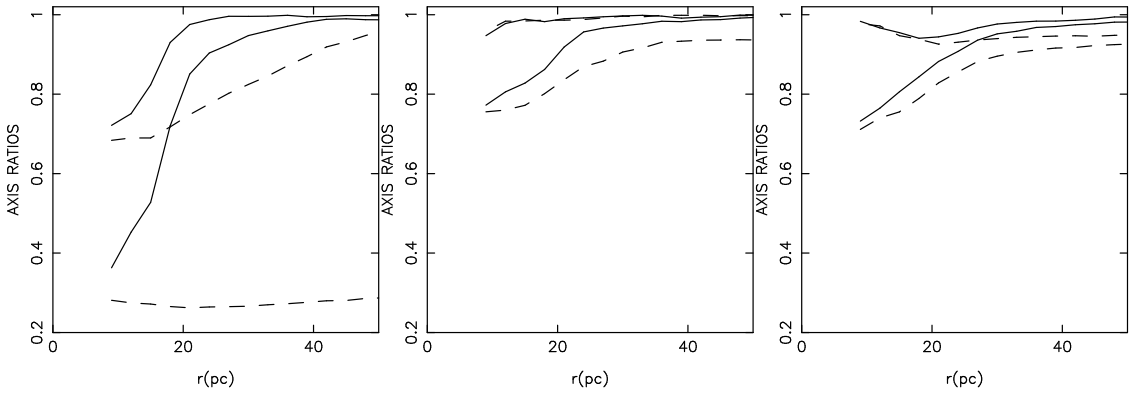

Figure 4.5 Axial ratios of the N-body system as a function of galactocentric radius computed after 1 (left panel), 6 (middle panel) and 12 (right panel) infalls. Solid curves correspond to the entire model (i.e., galaxy plus the NSC), while dashed curves gives the axis ratios of NSC only. After the first infall the NSC is strongly triaxial in the inner regions, but appears nearly oblate at the end of the simulation.

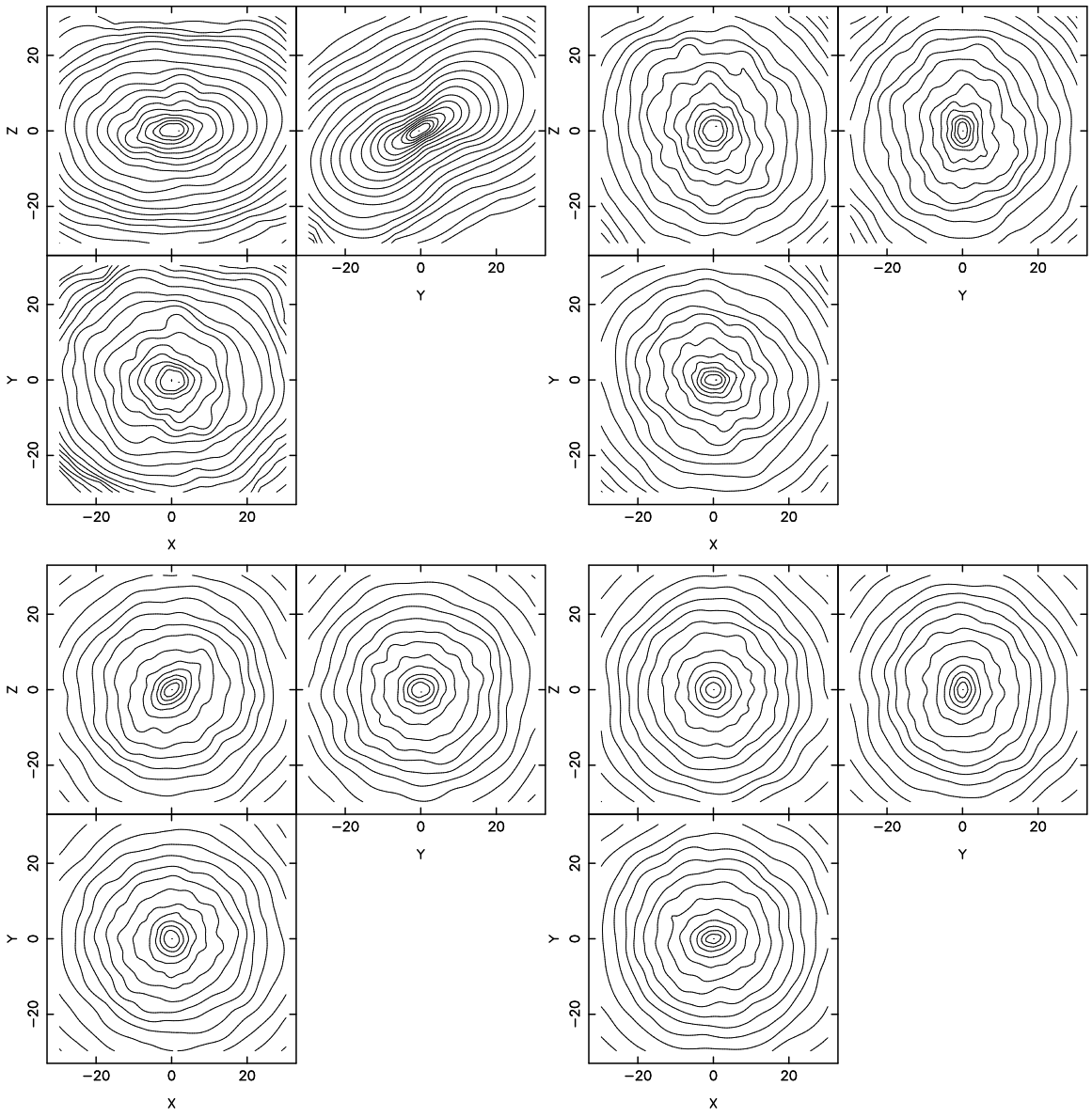

Figure 4.6 Contours of the projected density of the NSC after 1 (upper-left panel), 4 (upper-right panel), 8 (lower-left panel) and 12 (lower-right panel) infalls. As more stellar clusters accumulate to the center, the NSC becomes rounder. However, Its shape, at the end of the simulation (lower-right panel), is still very aspherical especially in the innermost regions.

Assuming for the growing NSC the density law of equation (4.13), the core density can be defined as $\rho_c = \rho_{0,cl}/2^{\frac{3}{2}}$ and the values of ρ_c, obtained after the end of each infall, can be plotted as a function of the half mass radius of the same system (bottom panel of Fig 4.4). These data are well fitted by the power law:

$$\rho_c = \left(1.2 \times 10^3 + 1.1 \times \exp\left[\frac{r_h}{1\ \mathrm{pc}}\right]\right) \mathrm{M}_\odot/\mathrm{pc}^3\ , \tag{4.18}$$

shown as solid line in the bottom panel of Figure 4.4.

Finally, we analyzed the spatial and projected density profile of the system obtained at the end of the simultaneous decay and merging of the 12 GCs. We used the same functions adopted in the previous case to fit the spatial and projected profiles of galaxy and NSC. We fit the cluster density profile using a modified Hubble law (equation [4.13]) with parameters $\rho_{0,cl} = 1.62 \times 10^4$ $\mathrm{M}_\odot/$ pc^3 and $r_{0,cl} = 3.4$ pc. For the galaxy we used the power law density profile of equation (4.1) with $\tilde{\rho} = 7.48 \times 10^2$ $\mathrm{M}_\odot/$ pc^3 and $\gamma = 0.50$, $\tilde{r} = 10$ pc and $r_{cut} = 15.6$ pc. For the total (i.e., galaxy+NSC) projected density profile, we summed the modified core model of equation (4.14) with $\Sigma_{0,cl} = 1.07 \times 10^5$ $\mathrm{M}_\odot/\mathrm{pc}^2$, $R_c = 3.7$ pc and $\zeta = 1.23$, to a Sérsic law (equation [4.15]) with $\Sigma_0 = 7.84 \times 10^3$ $\mathrm{M}_\odot/$ pc^2, $b = 1.65$, $R_e = 30.8$ pc and $n = 0.99$.

In the following we will focus on the repeated infall simulation, that, as previously pointed out, is believed to be more generic. However, it is worth noting the similarity of the NSC in the two different cases of repeated and simultaneous decay, both characterized by an external steep ($d\ln\rho/d\ln r \sim -2$) power law density profile and a flat core within the MBH influence radius. This homogeneity reinforces the idea that our results are robust and not very sensitive to the particular choice made for the initial conditions. We conclude that the basic properties of the Galactic NSC, including its mass and density profile, are the natural product of a model in which this is formed via inspiral of massive clusters into the Galactic center and that such properties can be reproduced under a variety of initial conditions.

The morphology of the NSC

Constraining the morphological structure of galactic nuclei is a fundamental step toward understanding their origin.

Unfortunately, as a consequence of the strong interstellar extinction along the Sun-Galactic center line of sight, our knowledge of the Galactic NSC morphology and size is very limited. Some indications are derived using kinematic modeling of the dominant population of old (few Gyr) stars that can be well described by a uniform, spherical model cluster exhibiting slow solid body rotation (amplitude $\sim 1.4(\mathrm{km\ s}^{-1})$/arcsec; Trippe et al. 2008).

Aspherical NSCs are commonly observed in external galaxies. For instance, in a sample of 9 edge-on nucleated late-type galaxies, Seth et al. (2006) reported that three of these galaxies (IC 5052, NGC 4206, and NGC 4244) have NSCs with significantly flattened isophotes and evidence for

multiple structural components. In addition, one of these galaxies (NGC 4206 may) showed possible indication of AGN activity, suggesting the presence of a black hole within the core of the central cluster. The NSC of the face-one galaxy M33, for which a MBH is instead not detected, is also known to be elongated along an axis parallel to the major axis of the galaxy (Lauer et al. 1998; Matthews et al. 1999). Hartmann et al. (2011) combined integral-field data analysis and N-body simulations to show that the M33 NSC is most likely axisymmetric with an ellipticity of ~ 0.17, consistent with the average observed in the NSCs of edge-on late-type galaxies (Seth et al. 2006). Accordingly, nuclei in the case of formation via clusters inspiral, are expected to be not spherical since mergers tend to destroy spherical symmetry (e.g., Moore et al. 2004).

We quantified the model shape in our simulation by constructing isodensity contours and also by the moment-of-inertia tensor (e.g., Katz 1991, Poon & Merritt 2004, Antonini et al. 2009), as described in what follows: the symmetry axes are calculated as

$$\tau_1 = \sqrt{I_{11}/I_{max}}\ ,\ \tau_2 = \sqrt{I_{22}/I_{max}}\ ,\ \tau_3 = \sqrt{I_{33}/I_{max}}\ , \tag{4.19}$$

where I_{ii} are the principal moments of the inertia tensor and $I_{max} = \max\{I_{11}, I_{22}, I_{33}\}$; particles are then enclosed within the ellipsoid $x^2/{\tau_1}^2 + y^2/{\tau_2}^2 + z^2/{\tau_3}^2 = r^2$. Finally, these previous two steps were iterated until the values of the axial ratios had a percentage change of less than 10^{-3}. Finally, we define $a > b > c$ letting $c/a = min\{\tau_1, \tau_2, \tau_3\}$ and b/a the intermediate value. We also define the triaxiality via the parameter $T \equiv \left(a^2 - b^2\right) / \left(a^2 - c^2\right)$. Oblate and prolate galaxies have $T = 0$ and 1, respectively. The value $T = 0.5$ corresponds to the maximally triaxiality case.

The results are summarized in Figure 4.5 which displays the axial ratios of the NSC as a function of radius and at different times. The model morphology evolves from an initially strong triaxiality (after the first infall) into a more oblate quasi-axisymmetric shape. In particular, notice that the morphological structure of the final product (right panel) is very similar to that after the 6th infall event (middle panel). This shows that the NSC is transformed into a nearly oblate system ($T \lesssim 0.2$ at $r < 20$ pc) after few infalls (~ 4), but its shape remains essentially unchanged from that point on. In the outer regions ($\gtrsim 20$ pc), the system remained instead nearly spherical for the entire course of the simulation.

The shape evolution of the model is more qualitatively illustrated in Figure 4.6 where the contours of the projected density of the NSC are displayed at different times. The morphological transition from a triaxial configuration into a rounder (nearly-oblate) shape can be clearly seen in the figure.

Based on this analysis, a NSC that forms via repeated cluster inspiral will most likely exhibit a nearly oblate shape with $T \sim 0.2$. We note, however, that this result must somewhat depend on the orbital parameters of the progenitor GCs, as a more prolate shape is expected to occur for almost radial mergers (Preto et al. 2011). In addition, two-body relaxation by particle-particle interaction will produce a secular drift of our model towards spherical symmetry (§4.4, Theis & Spurzem 1999).

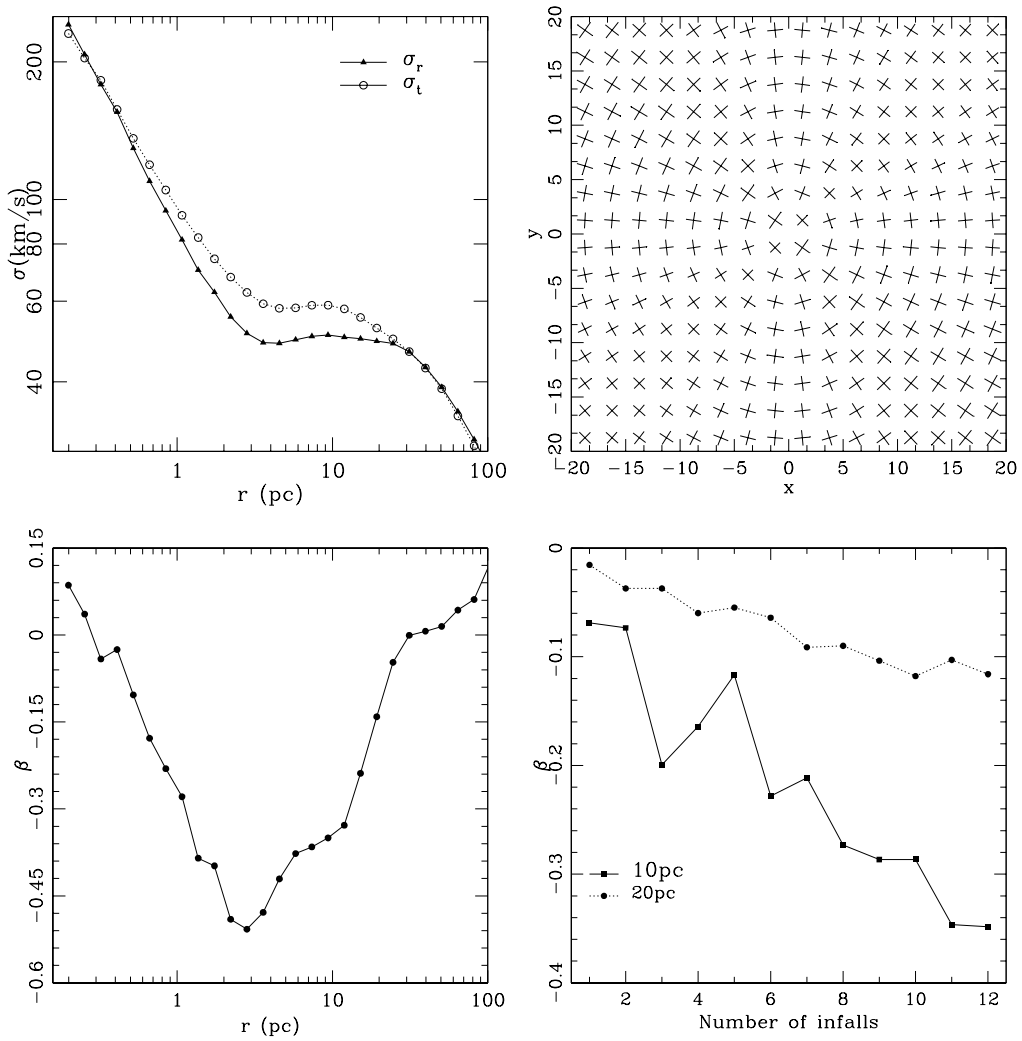

Figure 4.7 Radial (σ_r) and tangential (σ_t) velocity dispersion profiles as a function of distance from the central MBH (upper-left panel). Map of the principal axes of the 2D velocity ellipses of stars in the NSC on the x-y plane(upper-right panel). Anisotropy parameter β of the merging product plotted as a function of radius (lower-left panel). The anisotropy parameter evaluated at 10 and 20 pc versus time (lower-right panel). All profiles refer to the end of the 12th GC inspiral.

Kinematics

The formation mechanism of a NSC strongly influences its kinematical properties.

The Milky Way NSC rotates in the same direction of the whole Galaxy (Trippe et al. 2008). Studying the dynamics of the Galactic center evolved late-type CO absorption line star cluster, Trippe et al. (2008) showed that the 3D stellar velocity distribution is approximately maxwellian, suggesting relaxation of the old stellar component of the NSC. Fitting the observed

velocity dispersion and the rotation curve of the NSC, they found that the NSC is well modelled by a spherical density profile $\rho(R) \propto R^{-2}$. Schödel et al. (2009) investigated the proper motion of more than 6000 old-type stars within 1 pc of SgrA*. Moreover, they analysed the radial and tangential mean velocity of their star sample in circular shells around SgrA*. These authors found evidence for rotation of the NSC parallel to the Galactic plane. This could suggest that the formation mechanism of the NSC may include the accretion of gas and/or star clusters from the Galactic disk (see Seth et al. 2008). In particular it is relevant for our results to mention their Figure 6 where radial and tangential velocity dispersion in circular radial bins is plotted versus the distance from the central MBH. The result is that the NSC is nearly isotropic, even if the global rotation could mimic isotropy for an anisotropic NSC. Future observations are needed to solve this issue. Inside of $R = 8'' \sim 0.3$ pc, from SgrA* data shows a clearly Keplerian increase due to the presence of a MBH of $\sim 4 \times 10^6 M_\odot$, while outside this radius the velocity dispersion seems to set to an almost constant value (~ 100km/s), suggesting the presence of a diffuse mass of $\sim 10^6 M_\odot$ within 1 pc from the central MBH (Schödel et al. 2007 and Schödel et al. 2009). This extended mass can be easily explained by the presence of the NSC. differs from the one by Trippe et al. (2008), in fact in this earlier work the authors did not use a self-consistent

It is worth mentioning the results recently obtained on other galaxies. Geha et al. (2002) analyzed the velocity dispersion of five nucleated Virgo Cluster dE galaxies (VCC 452, VCC 1073, VCC 1577, VCC 1876). They did not find any evidence for rotation along the major axis of any of the observed galaxies. The mean velocity dispersion radial profiles of these galaxies have a quite wide range of shapes. In every case the central nucleus appears to have a kinematics clearly distinguished from that of the underlying galaxy. Four galaxies of the sample are characterized by a velocity dispersion that decreases going toward the galactic center. This result can be explained by the presence of a NSC without a central MBH. Indeed the NSC, which is a non-self-gravitating system with a velocity dispersion lower than that of the host galaxy, dominates the surface density profile (see Capuzzo-Dolcetta & Miocchi 2008). This feature has been reproduced by numerical simulations (see Oh & Lin 2000 and Capuzzo-Dolcetta & Miocchi 2008) of merging GCs in the center of galaxies without central MBH. In the remaining observed nucleated dE galaxy (VCC 1254), Geha et al. (2002) found a central velocity dispersion that, on the contrary, grows going inwards. In this case, a better fit to the data is provided by a model with a MBH of mass $M_{BH} \leq 9 \times 10^6 M_\odot$ (Geha et al. 2002). Another example is M33, which is a nucleated galaxy without a central MBH; the NSC of this galaxy also shows a decreasing trend of the velocity dispersion toward its center (see Gebhardt et al. 2001). A galaxy with a strongly rotating NSC is NGC 4244 (Seth et al. 2008). The radial velocity map shows a rotation of 30 km/s at $\sim 0.4''$ from the nucleus; the rotation is not confined to the younger disk component but it also involves the older and more spheroidal component while the central velocity dispersion is ~ 28 km/s.

To compare our results to the observational data, we studied the velocity dispersion of the stars in the NSC at the end of the 12th merging (for the same analysis repeated after about a

relaxation time see §4.4). The upper-left panel of Figure 4.7 shows the radial (solid line with empty circles) and tangential (dotted line with filled triangles) velocity dispersion versus the distance from the central MBH. In the region close to the MBH, as observationally found by Schödel et al. (2009), we clearly see a Keplerian rapid increase of the velocity dispersion, due to the presence of the MBH. Using radial and tangential velocity dispersion we found that:

- for $r < 0.3$ pc the system is quite isotropic;
- for $0.3 < r < 40$ pc the tangential velocity profile is systematically above the radial velocity dispersion curve;
- for $r > 40$ pc the (almost unchanged) system is isotropic.

In the upper right panel of Fig. 4.7 we show a local measure of the velocity dispersion along radial and tangential directions. We partitioned the $x-y$ plane in boxes and evaluated the aforementioned dispersions in each of them. The length of the plotted axes is proportional to the corresponding value of dispersion. As apparent, the system shows a tangential anisotropy whose value decreases going outwards.

The lower panels of Figure 4.7 show the anisotropy parameter

$$\beta = 1 - \frac{\sigma_t^2(r)}{\sigma_r^2(r)} \ , \tag{4.20}$$

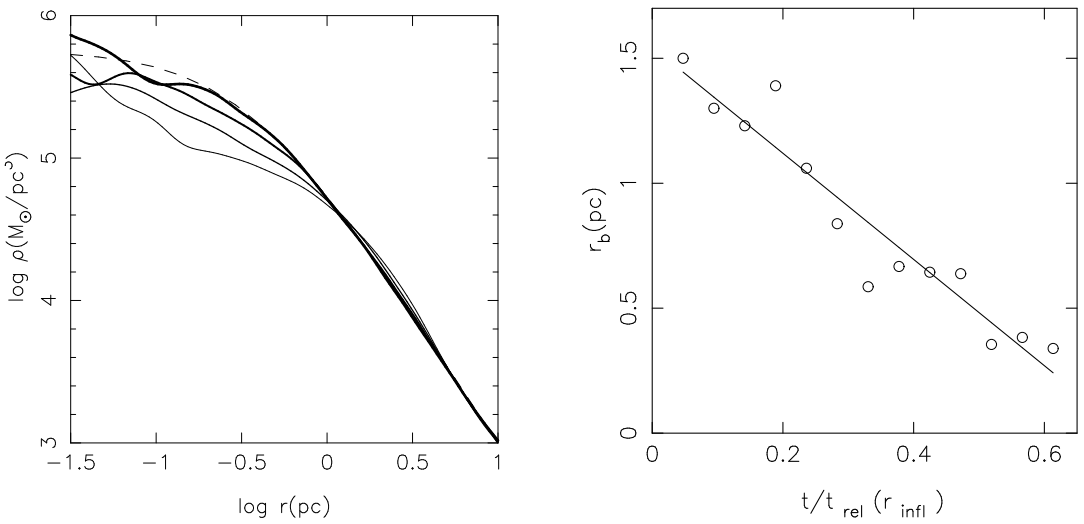

Figure 4.8 Left panel: the spatial profile of the central region of the galaxy at regular intervals of time. Line thickness increases with time. The dashed curve is the best fitting broken power law density profile obtained at the end of the entire simulation. Right panel: core radius as a function of time in the evolving model (empty circles). The continue line represents the relation given in equation (4.22).

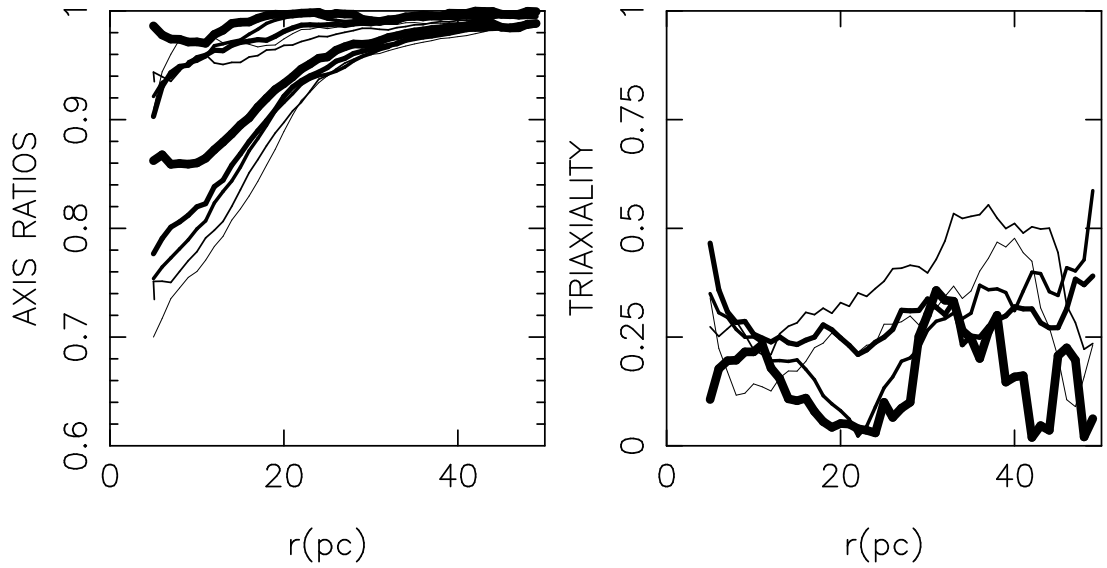

Figure 4.9 Radial profile of the model axial ratios (left panel) and triaxiality parameter (right panel) plotted at regular intervals of time. Line thickness increases with time.

as a function of the radial distance from the MBH (lower left panel) and as a function of time at two different distances, 10 pc and 20 pc, from the center (lower right panel). In the radial range between 0.3 pc and 40 pc, β is negative and the system is tangentially anisotropic. The anisotropy grows with the number of infalls and, as just said, is bigger in the inner region (see bottom right panel of Figure 4.7). This is consistent with the results obtained studying the shape an the axial ratios of the system (see §4.3.2).

4.4 Collisional evolution of the Nuclear Star Cluster

A relaxed quasi-steady-state distribution of stars around a MBH follows a Bahcall-Wolf cusp ($\rho \sim r^{-7/4}$). Number counts of the old stellar population in the inner parsec of the Galaxy seems to indicate instead a low density core near the center.

In our simulations, at the end of the last infall event, we obtained a NSC which is described by a mass density profile which flattens, within the MBH influence radius, inside ~ 2 pc. In this section, we present a new set of N-body integrations that explore the collisional evolution of the NSC following its formation.

It is found that the system undergoes a long-term self-similar evolution during which the core shrinks, while the initial $\rho \sim r^{-2}$ is maintained outside the core. Over approximately half the relaxation time at the sphere of influence of the MBH, the core shrinks to a size compatible with observational data that claims for a core of radius ~ 0.5 pc (Buchholz 2009).

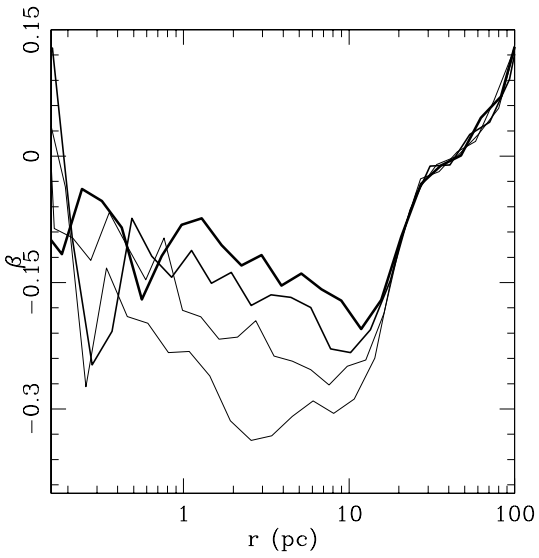

Figure 4.10 Radial profile of the anisotropy parameter β during relaxation displayed at regular interval of times. The anisotropy parameter increases with time and, by the end of the simulation, the NSC is close to isotropy with a small bias toward tangential motion.

For the relaxation time we used the standard expression (Spitzer 1987):

$$t_{rel}(r) = \frac{0.33\sigma(r)^3}{G^2\rho(r)m_* \ln\Lambda} \tag{4.21}$$

where $\ln\Lambda$ is the coulomb logarithm, $m_* = 200$ M$_\odot$ is the mass of the particles in the system, and σ is the one-dimensional velocity dispersion. In our model, setting $\ln\Lambda = \ln(r_{\rm infl}\sigma^2/2Gm_*)$, the relaxation time at the radius of influence of the MBH is $t_{rel}(r_{\rm infl}) \simeq 2.5 \times 10^8$ yr, with $r_{\rm infl}$ given in equation (4.2). This is also the time required to growth a Bahcall & Wolf cusp around the center (Freitag et al. 2006). The adopted expression for $\ln\Lambda$ is equivalent of identifying $r_{\rm infl}$ as the maximum impact parameter for encounters in Chandrasekhar's theory. This choice has been shown to reproduce remarkably well the collisional evolution rates seen in N-body and Fokker-Planck models with central point mass potential (Preto et al. 2004).

In order to study the collisional evolution of the NSC we evolved the system in isolation. The upper panel of Fig. 4.8 gives the mass density profile of the NSC at different times. At the end of the simulation (after $\sim 1.5 \times 10^8$ yr), we fit the density profile thorough the broken power law model of equation (4.12) (dashed line in the figure) with parameters: $\rho_b = 5.75 \times 10^5$ M$_\odot$/pc^3, $r_b = 0.33$ pc, $\gamma_i = 0$, $\beta = 1.82$ and $\alpha = 1.34$. The bottom panel of the same figure gives the time evolution of the NSC core radius that we approximated by the break radius of the best fitting broken power law profile (equation [4.12]). The dependence of the break radius on time is well represented by the linear relation:

$$r_b = \left(-0.085\frac{t}{10^7{\rm yr}} + 1.545\right) {\rm pc} \ . \tag{4.22}$$

A core of the currently observed size ($\sim$ 0.5 pc) is found to form after approximately half the relaxation time as evaluated at the MBH influence radius, or $\sim$ 10 Gyr at the Galactic center (Merritt 2011).

Fig. 4.9 displays the morphological evolution of the NSC during relaxation, showing at regular intervals of time, the radial profile of the system axial ratios (left panel) and triaxiality parameter (right panel). There is essentially no evolution of the intermediate axial ratio that remains close to $\sim$ 0.95 during the entire course of the simulation, while, in the innermost regions of the model, the shortest axis significantly increases with time. Two-body relaxation produces a secular morphological transition toward quasi-spherical symmetry, but at the end of the simulation the model has not yet reached this final state, showing some non-negligible triaxiality. The final model appears indeed nearly oblate with $0.3 \lesssim T \lesssim 0.1$. Such deviations from axisymmetry would be large enough to substantially enhance the rates of stellar capture and disruption by the MBH with respect to the same rate computed in collisionally resupplied loss cone theories (Merritt & Poon 2004).

Figure 4.10 illustrates the NSC evolution toward isotropy by plotting the model anisotropy profile at different times. The core refilling from low-angular momentum orbits increases σ_r at the center and, by the end of the simulation, the NSC appears to have only a small bias toward tangential motion ($\beta \sim -0.15$). This is consistent with proper-motion data from the (projected) inner parsec of the Milky Way that indicate a slight degree of tangential anisotropy. In the radial range $1'' - 10''$, the late type stars have an average anisotropy parameter $\langle B \rangle = 1 - \langle \sigma_T^2/\sigma_R^2 \rangle = -0.124^{0.098}_{-1.05}$, with σ_R and σ_T the radial and tangential velocity dispersions in the plane of the sky and with $\langle\rangle$ denoting number weighted averages over some radial range (Schödel et al. 2009, Merritt 2010).

4.5 discussion

4.5.1 Mass-radius relation

In Figure 4.11 the mean half-mass radius is plotted against total mass for nuclei (filled circles) GCs (open circles) and UCDs (stars). We overplot the track followed by the NSC in our simulation during the infall events (purple continue curve) and during relaxation (continue blue line). The structural properties of the NSC formed in our simulations (blue filled circle) are in good agreement with those of real NSCs.

From the figure we can see that the faintest nuclei have roughly the same mass as a typical globular cluster. The size distributions for the nuclei and globular clusters also overlap, although the clusters in the Galaxy have 3 pc, irrespective of mass, while the nuclei follow a relation of the form $r_h \propto \sqrt{M}$. Fainter than a few million solar masses, the nuclei and globular clusters have comparable sizes (Hşegan et al. 2005).

We now consider the merger model for nucleus formation in the absence of a MBH. In this case simple recursive relations can be derived that give the mass and radius of the NSC during

its formation. The radius of the nucleus increases with increasing total mass, or light, as globular clusters merge. After the merger, its final energy, E_f , equals the energy of the nucleus before the merger, E_i, plus the energy brought in by the globular cluster. This energy has two components: the internal energy or binding energy E_b, and the orbital energy just before the merger, E_o. From conservation of energy:

$$E_f = E_i + E_o + E_b \ . \tag{4.23}$$

Just before the merger, the orbital energy is $E_o = \alpha GmM_i/2Ri_i$, where M_i and R_i are the mass and radius of the nucleus, respectively, m is the mass of the globular cluster, and α is a constant of order unity (Hausman & Ostriker 1978) that depends on the radius of the capture orbit - the radius at which the dominant influence on the trajectory of a globular cluster first comes from the nucleus. After the merger, the nucleus reaches a state of dynamical equilibrium quickly; the virial theorem implies $E_f = -GM_f^2$. The equations above permit expressing the mass, energy, and radius of the nucleus recursively as

$$M_{j+1} = (j+1)M_1, \tag{4.24}$$

$$jE_{j+1} = (j+\alpha)\,E_j + jE_1, \tag{4.25}$$

$$(j+1)^2\,R_{j+1}^{-1} = j\,(j+\alpha)\,R_j^{-1} + R_1^{-1}, j = 1, 2, 3, ... \tag{4.26}$$

where the subscript 1 denotes the initial nucleus, and, by assumption, $M_1 = m$. At the time when a nucleus consists of few merged globular clusters, its mass and that of the next infalling globular cluster are comparable. In this case, equations (4.24,4.26) imply $R \propto M^{0.5}$. However, after many mergers, $M \gg m$, and the relation steepens to $R \propto M$. For $\alpha = 1.2$ and 5(25)100 mergers, equations-(4.24,4.26) imply $R \approx 2(5)10$ and $R \propto M^p$, $p = 0.5(0.6)0.7$. The typical half-mass radius of a globular cluster is about 3 pc (Jordán et al. 2005) so for a nucleus assembled from 25 mergers, $R \sim 15$ pc. This is in reasonable agreement with the measured sizes for the brighter nuclei. For $\alpha = 1.2$, the expected scaling between r_h and mass is shown by the blue dot-dashed curves in Figure 4.11. We show the predicted behavior for two assumptions for the mass, m, of the clusters which merge to form the nucleus: 10^5 and 10^6 $M_\odot$. At least for $m = 10^6$ $M_\odot$, the agreement with the r_h-mass relation for nuclei is remarkably good.

4.5.2 Dynamical friction time scale

For the merger model to be viable, GCs must spiral into the central region of a host galaxy on a time scale shorter than a Hubble time ($\sim 10^{10}$ yr). The time for globular cluster of mass m at an initial radius r_0 to inspiral into the center of a galaxy as a result of dynamical friction is (Binney & Tremaine 1987):

$$\Delta t = \frac{C(\gamma)}{\ln\Lambda}\frac{r_a^3}{m}\left(\frac{\rho}{G}\right)^{1/2}\left(\frac{r_0}{r_a}\right)^{(6-\gamma)/2} \ . \tag{4.27}$$

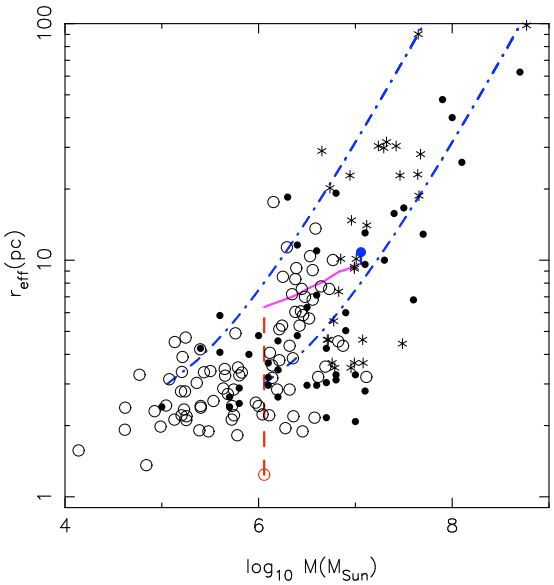

Figure 4.11 The measured mean half-mass radius (or effective radius) plotted against total mass for nuclei (filled circles), GCs (empty circles) and UCDs (stars symbols). Data points are from Forbes et al. (2008) and Côté et al. (2006). Dot-dashed curves show the predicted scaling in the merger model without MBH for two different choices for the mass of merged clusters (see text for details). The red filled circle represents the initial GC model in the N-body simulation. Purple and blue curves are the evolutionary track of the NSC during its formation and during relaxation respectively. The filled blue circle represents the final product of our simulation.

This expression assumes circular orbits, a total mass density of the galaxy that satisfies $\rho(r) = \rho_a(r/r_a)^{-\gamma}$, and a frictional force that is due entirely to stars with velocities less than the orbital velocity of the globular cluster, and a Coulomb logarithm $\ln\Lambda = 6.6$ (Spinnato et al. 2003). The coefficient C in equation (4.27) is a weak function of γ, with $C = (3.9, 3.6, 4.2)$ for $\gamma = (1, 1.5, 2)$. Writing $\tilde{r}_a \equiv r_a/(1\mathrm{kpc})$, $\tilde{\rho}_a \equiv \rho_a/(1M_\odot pc^{-3})$, $\tilde{m} \equiv m/10^6 M_\odot$ and $\tilde{r_0} \equiv r_0/r_a$, the time for a globular cluster to spiral in is:

$$\Delta t \approx 9 \times 10^9 \mathrm{yr} \;\; \tilde{r}_a^3 \tilde{\rho}_a^{1/2} \tilde{m}^{-1} \tilde{r}_0^{(6-\gamma)/2} \; . \tag{4.28}$$

Although the initial distribution of globular clusters is not known, a reasonable assumption is that it follows the distribution of the total baryonic mass predicted by the standard cosmological model (Merritt & Ferrarese 2001).

Let Δt_h be the time for clusters initially within r_h, the half mass radius of the galactic bulge, to spiral to the center. Within Δt_h, the forming nucleus has a luminosity comparable to the luminosities of the surviving clusters. An estimate of r_h is r_e, the observed projected half-light (effective) radius; the stellar density at $r = r_e$ is $\tilde{\rho}_e \approx 14.1 \tilde{r}_e^{-2.519}$, with r_e the half light radius in kpc and $\tilde{\rho}_e$ the stellar density in units of solar masses per cubic parsec. Luminosity profiles for $r < r_e$

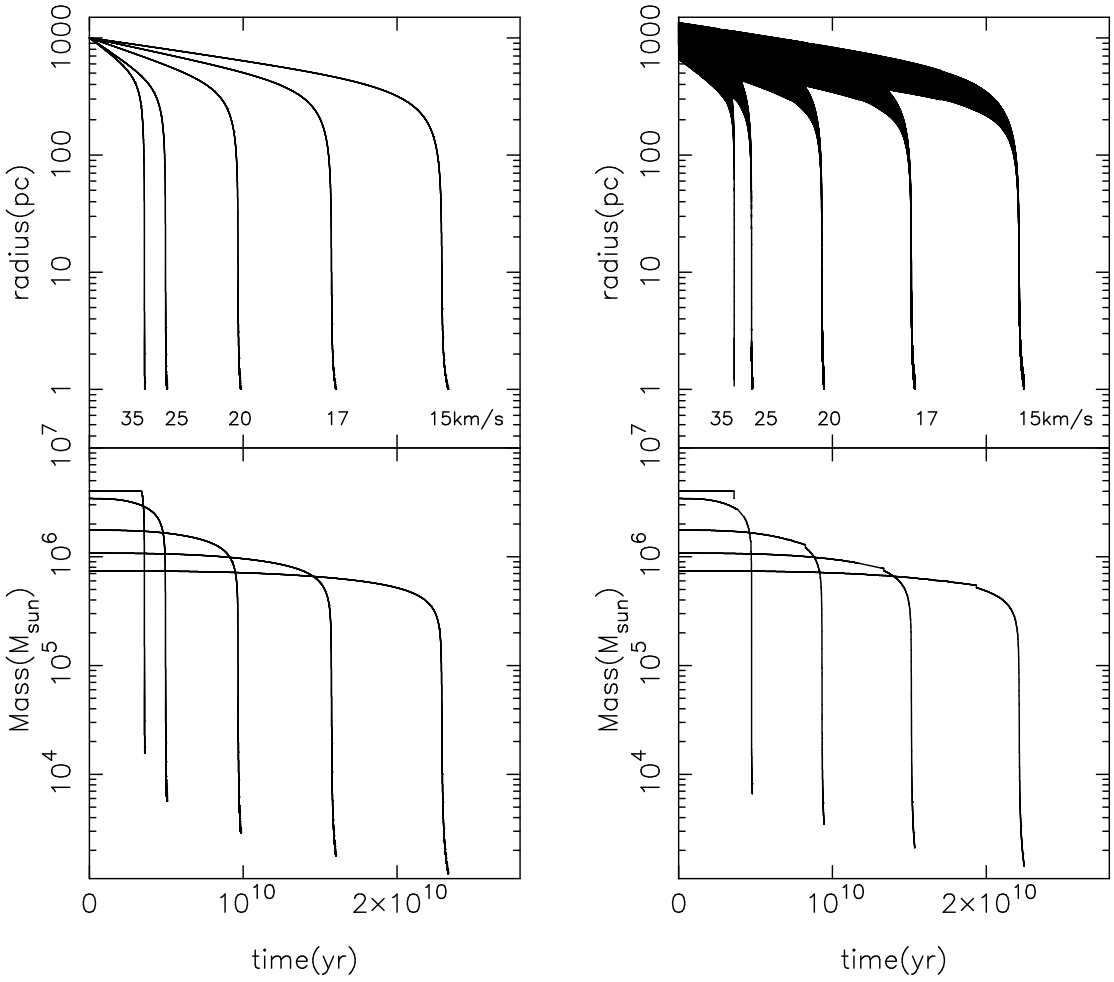

Figure 4.12 Evolution of radius (upper panels) and mass (lower panels) for GCs with different central velocity dispersions starting from an orbital semi-major axis of 1000 pc. In the right panels the orbits have an eccentricity of $e \sim 0.35$. Only GCs with velocity dispersion larger than approximately 20 kms^{-1} would spiral to the center within 10^{10} yr.

are well approximated as power laws with $1 < \gamma < 2$ in the same galaxies (Terzíc & Graham 2005). Thus,

$$\Delta t \approx 3 \times 10^{10}\mathrm{yr}\ \ \tilde{r}_e^{1.75}\tilde{m}^{-1}\ . \tag{4.29}$$

For globular clusters of mass $m = 10^5(10^6)M_\odot$, $\Delta t < 10^{10}$ yr requires $r_e < 140(520)$ pc. For comparison bulges of S0-Sb galaxies and early type galaxies with $-20 < M_B < -16$ have $0.2 \lesssim r_e \lesssim 5$ kpc , albeit with a large scatter (Faber 1997,Ferrarese et al. 2006). Though crude, this calculation implies that a significant fraction of the globular clusters in faint galaxies and bulges would have spiraled to the center in 10^{10} yr.

In order to more quantitatively study the dynamical friction time scale of a massive body

at the Galactic center we numerically integrated the equations of motion of a test particle in a fixed potential including the non-conservative contribution of dynamical friction:

$$\dot{\mathbf{r}} = \mathbf{v}; \quad \dot{\mathbf{v}} = -\nabla\phi + \boldsymbol{f}_{\rm fr}, \tag{4.30}$$

where the frictional force can be approximated as (Chandrasekhar 1943):

$$\boldsymbol{f}_{\mathbf{fr}} \approx -4\pi G^2 m\rho(r)\frac{\boldsymbol{V}}{V^3}F(<v,r)\ \ln\Lambda \tag{4.31}$$

here, V is the orbital velocity of the sinking globular cluster and $F(<v,r)$ is given in equation (4.5). For the background distribution we adopted the density model:

$$\rho(r) = \rho_{\rm NSD} + \rho_{\rm GB} = 400\left(\frac{r}{10{\rm pc}}\right)^{-1}\exp\left[-\frac{r}{250{\rm pc}}\right]\frac{M_\odot}{{\rm pc}^3} \tag{4.32}$$
$$+10\ \exp\left[-\left(\frac{r}{1000{\rm pc}}\right)^2\right]\frac{M_\odot}{{\rm pc}^3}\ ,$$

where $\rho_{\rm NSD}$ is the density of the nuclear stellar disk and the second term ($\rho_{\rm GB}$) represents the contribution of the Galactic bulge which becomes significant for $r \gtrsim 250$ pc (Launhardt et al. 2002). We chose $m = 4\times10^6 M_\odot$ for the mass of the globular cluster. In order to include the effect of tidal stripping, at any time the corresponding tidally-truncated mass (m_T) defined by equation (4.7) was computed and assigned to the infalling GC (i.e., $m = m_T$) if $m_T < m$. The left panels of Figure 4.12 plot the orbital evolution of GCs with different values of the central velocity dispersion and starting on circular orbits of radius $a_{in} = 1000$ pc. In the right panels the orbits have the same orbital radius but a non-zero initial eccentrcity ($e \sim 0.35$). These results show that GCs with central velocity dispersion larger than about 20 kms^{-1} (15 kms^{-1}) would reach the center in less than a Hubble time if they are initially at $a_{in} = 1000$ pc ($a_{in} = 500$ pc). We stress that the sinking times in Figure 4.12 must be interpreted as upper limits on the actual dynamical friction time scales for at lest two reasons: i) the truncated mass m_T is an underestimate of the actual GC mass, since we suppose that mass-loss occurs instantaneously; ii) the background distribution is assumed to be spherical, but in a more realistic triaxial model the sinking time could be greatly reduced (Pesce et al. 1991). This study suggests therefore that a significant fraction of the GC population in the Galactic bulge would have had enough time to spiral in by now.

Chapter 5

Dynamical friction around super massive black holes

5.1 introduction

Dynamical friction is a key process in astrophysics. It drives the formation of massive black hole binaries at the center of merger systems, the orbital inspiral and merger of satellite galaxies with the central galaxy, and it is the fundamental mechanism leading to mass-segregation in dense stellar clusters.

Chandrasekhar formulated the basic principle of dynamical friction under the assumptions of an infinite, homogeneous and isotropic field of stars (Chandrasekhar 1943). Despite these simplifications his theory has been shown to work remarkably well even for more general stellar distributions and it has been extensively used in a variety of astrophysical scenarios including: the decay of satellite galaxy orbits (Murai & Fujimoto 1980; Ibata & Lewis 1998; van den Bosch et al. 1999; Hashimoto 2003); the motion of a massive black hole binary in a see of lighter stars (Merritt 2001; Milosavljević & Merritt 2001; Merritt 2006); the evolution of the globular cluster system in a triaxial galaxy (Pesce et al. 1992; Capuzzo-Dolcetta 1993; Capuzzo-Dolcetta & Miocchi 2008); the motion of a galactic bar inside a dark matter halo (Weinberg 1985); the inspiral of star clusters near the Galactic center (Portegies Zwart & McMillan 2002; Gürkan & Rasio 2005; Fujii et al. 2009).

Dynamical friction can be understood in terms of the drag force produced on the test particle by the overdensity (i.e., the gravitational wake) it raises behind it, along its orbit, in the stellar background (Kalnajs 1972). The surprisingly good agreement between theory and numerical results is then attributed to the fact that the gravitational wake is a local small-scale structure over which the stellar background appears indeed homogeneous (Weinberg 1986). On the other hand, the limits associated with the Chandrasekhar's formula are still unclear and several numerical

studies have demonstrated how the standard theory loses its validity in certain cases of astrophysical interest. Some of these are: the orbital decay of a test object which revolves and rotates through a spherical stellar system (Tremaine & Weinberg 1984); the inspiral of massive bodies in super-resonant potentials (e.g. a constant density core) (Hernandez & Gilmore 1998; Goerdt et al. 2006; Read et al. 2006; Inoue S. 2009); the orbital decay of a kicked super massive black hole in the low density core of a merger system (Gualandris & Merritt 2008).

In this chapter, we present a comprehensive study of dynamical friction in dense stellar systems that are gravitationally dominated by a point mass potential. In particular, we investigate the case of shallow density profiles. Low density cores with central point mass potential are representative of several astrophysical environments. For instance, the density profile of stars near the super massive black hole in luminous early-type galaxies is frequently observed to be very flat (Lauer et al. 1995). Core models are also applicable to dark matter halos in their inner regions, where the galactic potential starts to be dominated by the luminous component (Borriello & Salucci 2001; Binney & Evans 2001; de Blok & Bosma 2002; de Blok et al. 2003; Spekkens et al. 2005). Another remarkable application is the infall of massive objects at the Galactic center, where recent observations (Buchholz et al. 2009; Do et al. 2009; Bartko et al. 2010) have suggested a density of old stars that is weakly rising, or falling toward the massive black hole, inside its influence radius (~ 2 pc).

The orbital evolution of a massive particle can be very sensitive to the detail of the mass distribution of background stars. For instance, the time scale for inspiral is longer in models with a core than in models with a cusp, both because of the lower densities into the core, but also because shallow density cusps around a massive body are described by phase-space densities that fall to zero at low bounding energies. Such a zero-density hole in phase space implies a lack of *slow* moving stars inside the core and therefore a drop of the frictional force. Another major consequence of a flattened cusp is that the frictional drag along an orbit can be most effective at apoapsis, which is necessary condition for an orbit to become more eccentric, while in a homogeneous medium the orbit circularizes since dynamical friction is peaked at periapsis. However, it turns out that friction never drops to zero and that most of the frictional force inside the core comes from stars moving *faster* than the test body. Also, the orbital eccentricity does not rise so steeply as predicted in the standard treatment. We find that including the contribution of "sub-dominant" terms, practically neglected in all previous calculations, and using the self-consistent velocity distribution function instead of the standard Maxwellian more frequently adopted, the Chandrasekhar's theory (without any ad hoc correction) reproduces exceptionally well the orbital decay of massive objects in low density cores around super massive black holes.

The approach adopted in what follows is to scale our numerical models to the Galactic center and consider the inspiral of test objects that are much more massive than a typical star. This includes stellar black holes and intermediate massive black holes, if they exist. Then, farther in the thesis, we show how our simulations can be rescaled and the results re-adapted to describe, as

example, the orbital decay of the super massive black holes after a minor merger between a Milky Way size galaxy and a giant elliptical like M87.

In §5.2 we summarize the steps to derive the dynamical friction and diffusion coefficients for a point mass particle under the same assumptions adopted by Chandrasekhar (1943). In §5.3 we use Chandrasekhar's approximate formulae to integrate the equations of motion of a massive body and follow its inspiral into the Galactic center. In §5.4 we use large scale N-body simulations to test Chandrasekhar's theory and study the dynamical evolution of massive objects in a nuclear star cluster with a flat density profile. §5.5 investigates the formation of the gravitational wake in the self consistent simulations. Applications of our results to a variety of astrophysical problems are discussed in §5.6. §5.7 sums up.

5.2 Dynamical friction

The motivation for the N-body experiments described in this chapter is the existence of physically interesting models of galactic nuclei in which the "standard" dynamical friction formulae predict little, or even zero, frictional force on an orbiting test mass. We begin in this section by deriving those standard formulae, taking care to point out the simplifying approximations that are usually made. We then discuss the consequences of relaxing those assumptions. The results obtained in this section can be used as a baseline for interpreting the N-body results.

5.2.1 Chandrasekhar's treatment

Chandrasekhar (1943) derived the coefficient of dynamical friction by summing the encounters of a test body with passing stars, assuming that the unperturbed motion of the test body was linear and unaccelerated, and that the field star distribution was infinite and homogeneous spatially and isotropic in velocity space.

The velocity change of a test body of mass M in one encounter with a field star of mass $m \ll M$ is

$$\Delta v_{\parallel} = -2V \frac{m}{M} \frac{1}{1 + p^2/p_0^2} \tag{5.1}$$

where V is the relative velocity at infinity, p is the impact parameter, and $p_0 \equiv GM/V^2$. The velocity change in equation (5.1) is parallel to the initial, relative velocity $\boldsymbol{V}$ before the encounter. In order to derive the coefficient of dynamical friction, one sums the velocity changes in the direction of motion of the test mass, per unit interval of time, over all impact parameters and over all values for the relative velocity at infinity. The summation over impact parameters, at fixed V, is achieved by multiplying equation (5.1) by $2\pi pnV\,dp$, with n the number density of field stars, and integrating dp:

$$\overline{(\Delta v_{\parallel})} = -\frac{2\pi G^2 M m n}{V^2} \ln\left(1 + p_{max}^2/p_0^2\right). \tag{5.2}$$

Under the assumption that $\Lambda \equiv p_{\max}/p_0 \gg 1$, this can be written as

$$\overline{(\Delta v_\parallel)} = -\frac{4\pi G^2 M m n}{V^2}\left[\ln\Lambda + \frac{1}{2}\frac{p_0^2}{p_{\max}^2} + ...\right]. \tag{5.3}$$

Terms beyond the first in brackets, the so-called "non-dominant" terms, are usually neglected.

Returning to the more general form (5.2), the dynamical friction coefficient is obtained by a second integration over field star velocities $\boldsymbol{v}_\star$. The relative velocity is $\boldsymbol{V} = \boldsymbol{v} - \boldsymbol{v}_\star$, with $\boldsymbol{v}$ the velocity of the test star. Since equation (5.2) gives the velocity change in the direction of the initial relative motion, it must be multiplied by

$$\frac{\boldsymbol{V}\cdot\boldsymbol{v}}{Vv} = \frac{v - v_\star}{V} \tag{5.4}$$

to convert it into a velocity change in the direction of the test star's motion, assumed here to be along the x axis. Let $f(\boldsymbol{v}_\star)\boldsymbol{dv}_\star$ be the number density of field stars in velocity increment $\boldsymbol{v}_\star, \boldsymbol{v}_\star + \boldsymbol{dv}_\star$, normalized to unit total number. The dynamical friction coefficient is

$$\begin{aligned}\langle\Delta v_\parallel\rangle &= \int f(\mathbf{v}_\star)\,\overline{(\Delta v_\parallel)}\,\frac{v - v_{\star x}}{V}\boldsymbol{dv}_\star \qquad (5.5)\\ &= -2\pi G^2 M\rho\int f(\mathbf{v}_\star)\frac{v - v_{\star,x}}{V^3}\ln\left(1 + \frac{p_{max}^2 V^4}{G^2M^2}\right)\boldsymbol{dv}_\star\end{aligned}$$

where $\rho = mn$.

Henceforth we assume that the field star distribution is isotropic in velocity space. Following Chandrasekhar (1943), we represent the velocity-space volume element in terms of $v_\star$ and V, using

$$v - v_{\star x} = \frac{V^2 + v^2 - v_\star^2}{2v}.$$

The result is

$$\langle\Delta v_\parallel\rangle = -\frac{2\pi^2 G^2 M\rho}{v^2}\int_0^\infty dv_\star\, v_\star\, f(v_\star) H\left(v, v_\star, p_{\max}\right), \tag{5.6a}$$

$$H(v, v_\star, p_{max}) = \frac{1}{8v_\star}\int_{|v-v_\star|}^{v+v_\star} dV\left(1 + \frac{v^2 - v_\star^2}{V^2}\right)\ln\left(1 + \frac{p_{max}^2 V^4}{G^2M^2}\right). \tag{5.6b}$$

(The quantity J defined in equation (26) of Chandrasekhar (1943) is equal to $8v_\star H$.) The integral that defines H turns out to have an analytic solution; however the expression is long and we do not give it here. Chandrasekhar (1943) gave several approximate forms for H valid for $p_{\max}/p_0 \gg 1$, e.g. his equation (30):

$$H \approx \begin{cases} \ln\frac{p_{max}}{GM}(v^2 - v_\star^2) & \text{if } v > v_\star, \\ \frac{1}{2}\ln\left(4\frac{p_{max}}{GM}v_\star^2\right) - 1 & \text{if } v = v_\star, \\ \ln\left(\frac{v_\star + v}{v_\star - v}\right) - 2\frac{v}{v_\star} & \text{if } v < v_\star\ . \end{cases} \tag{5.7}$$

In the standard approximation (e.g. Binney & Tremaine 1990), the non-dominant terms are set to zero, and the velocity dependence of the logarithmic term in the integrand of equation (5.6) is ignored. Instead, one writes

$$\ln\left(1+\frac{p_{max}^2V^4}{G^2M^2}\right)=2\ln\Lambda\equiv 2\ln\left(\frac{p_{max}}{p_{min}}\right) \tag{5.8}$$

and the lower bound $p_{\rm min}$ is set to $GM/v_{\star,rms}^2$. The weighting function H then takes on the simple form

$$H=\begin{cases}\ln\Lambda & \text{if } v>v_\star,\\ 0 & \text{if } v<v_\star\end{cases} \tag{5.9}$$

and the coefficient of dynamical friction is

$$\langle\Delta v_\parallel\rangle=-4\pi G^2M\rho\times 4\pi\int_0^v dv_\star\left(\frac{v_\star}{v}\right)^2 f(v_\star). \tag{5.10}$$

Equation (5.10) reproduces the well-known result that only field stars with $v_\star<v$ contribute to the frictional force.

In this chapter, we consider models for galactic nuclei in which the number of stars moving more slowly than the test body can be vanishingly small. In such models, one expects that a significant fraction of the frictional force might come from stars with $v_f>v$.

The distribution of field-star velocities in our models has the following form near the central SMBH:

$$f(v_\star)=\begin{cases}f_0\left(2v_c^2-v_\star^2\right)^{\gamma-3/2} & \text{if } v_\star<2^{\frac{1}{2}}v_c,\\ 0 & \text{if } v_\star>2^{\frac{1}{2}}v_c\end{cases} \tag{5.11}$$

where the normalizing constant

$$f_0=\frac{\Gamma(\gamma+1)}{\Gamma(\gamma-\frac{1}{2})}\frac{1}{2^\gamma\pi^{3/2}v_c^{2\gamma}} \tag{5.12}$$

corresponds to unit total number. This expression is equivalent to equation (5.5); it gives the local distribution of velocities near a SMBH at a radius where the circular velocity is $v_c=(GM_\bullet/r)^{1/2}$, assuming that the gravitational potential is due entirely to the SMBH, and that the density of field stars follows $r^{-\gamma}$. The phase space density is zero for $v_\star\geq v_{\rm esc}=2^{1/2}v_c$, the escape velocity from the SMBH.

Of more interest here is the behavior of f at small values of $v_\star$, when $\gamma<3/2$; for such values of γ the phase space density diverges at $v_\star=2^{1/2}v_c$. As $\gamma\to 1/2$, the velocity distribution becomes progressively narrower, and in the limit, $f(v_\star)$ is a delta-function at $v_\star=2^{1/2}v_c$; in other words, all stars have zero energy. It follows that $\rho\propto r^{-0.5}$ is the shallowest power law density profile consistent with an isotropic velocity distribution in a point-mass potential.

In the case of a test body moving in a circular orbit with $v=v_c$, the number of field stars with $v_\star<v$ will drop as γ approaches 1/2, and will equal zero in the limiting case $\gamma=1/2$. The standard dynamical friction coefficient, equation (5.10), predicts zero frictional force in this limit.

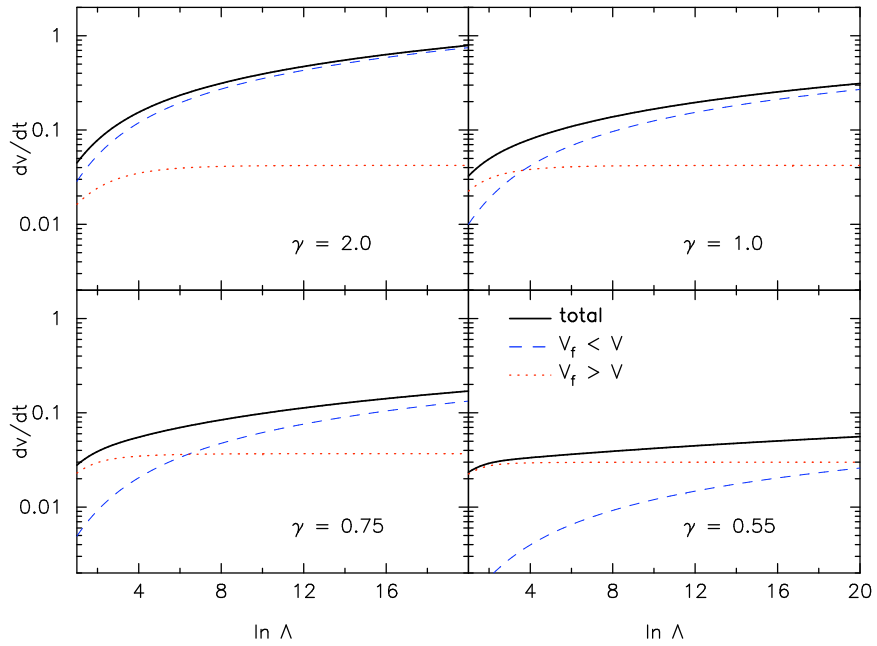

Figure 5.1 Contribution to the total dynamical friction force from stars moving faster, or more slowly, at infinity than the test body, assuming the velocity distribution of equation (5.11). The test body is assumed to be moving at the local circular velocity v_c. In these plots, the configuration-space density ρ remains fixed as γ is varied.

In this situation, it is clearly of interest to compute the contribution of the fast-moving stars to the total frictional force. We did this by evaluating H in its "exact" form, equation (5.6b). Figure 5.1 shows the results. In addition to γ, the results depend on the parameter

$$\ln\Lambda \equiv \ln\left(\frac{p_{\max}v_c^2}{GM_\bullet}\right) \tag{5.13}$$

which plays the role of "Coulomb logarithm". We observe the following:

- For $\gamma \gtrsim 3/2$, the contribution to the frictional force from the fast-moving stars is negligible, particularly when $\ln\Lambda$ is also large.
- For $\gamma \lesssim 3/2$, the fast-moving stars contribute a progressively larger fraction of the total frictional force, particularly when $\ln\Lambda$ is small.
- When $\gamma = 0.55$, near the limiting value, the total frictional force is small, and almost all of it comes from stars with $v_\star > v$.
- Whereas the contribution to the force from the slow-moving stars depends strongly on γ, the contribution from the fast-moving stars is almost independent of γ. The latter contribution is roughly an order of magnitude smaller than the total frictional force under the standard approximation.

According to the approximate formulae (5.7), the contribution of the fast stars must tend to zero as $\ln\Lambda$ is made sufficiently large. This is consistent with Figure 5.1; however, for $\gamma \approx 0.5$, the value of $\ln\Lambda$ required for the slow stars to dominate is far greater than any physically reasonable value.

5.2.2 Mulder's treatment

The foregoing treatment highlights the contribution of the fast-moving stars, $v_\star > v$, to the total frictional force. However it does not provide much physical insight into why the two populations contribute in such a different way to the force. Of course, the N-body experiments described in this chapter include both populations of stars. In the simulations, the field stars quickly establish a nearly steady-state distribution in a frame moving with the test mass – a "dynamical-friction wake." The over-density in the wake is responsible for the decelerating force that acts on the test body. A large fraction of the mass in the wake must be contributed by the fast stars, particularly in the case that the fast stars dominate the density at large distances. Why then do these stars contribute relatively little to the frictional force?

One way to address this question is via the technique of Mulder (1983). Mulder computed the steady-state distributions of stars around a moving test mass, making essentially the same assumptions as made by Chandrasekhar (1943). He did this by invoking Jeans's theorem in a frame moving with the test mass, and showing that an isotropic $f(v_\star)$ at infinity could be expressed in terms of two of the integrals of motion in the Kepler problem. This then allowed him to compute the steady-state density, in the moving frame, at all locations around the test mass. The dynamical friction force followed from a second integration of the density over space; Mulder showed that the results for the frictional force so obtained were consistent with Chandrasekhar's predictions, if $p_{\max}$ were associated with the maximum dimension of the spatial grid used to carry out the force integration.

Mulder's technique can be modified, to compute the separate contributions to the dynamical friction *wake* of the fast ($v_\star > v$) and slow ($v_\star < v$) stars; here, as above, $v_\star$ refers to the field-star velocity at infinity. The results are shown in Figure 5.2, for $\gamma = 5/4$. For this choice of γ, the fast stars dominate the total density at infinity. The density that they generate near the test body is also higher, everywhere along the symmetry axis, than the density due to the slow stars. However the shapes of the two density wakes are very different: in the case of the fast stars, the wake is elongated counter to the direction of the test body's motion, while in the direction parallel to the motion, the change in density between the upstream and downstream sides of the test mass is much less than in the case of the wake produced by the slow stars. These two differences are responsible for the small contribution of the fast stars to the total frictional force (Figure 5.1), in spite of the higher density of those stars at infinity and in the wake.

Comparison of the upstream and downstream densities in Figure 5.2 also suggests why

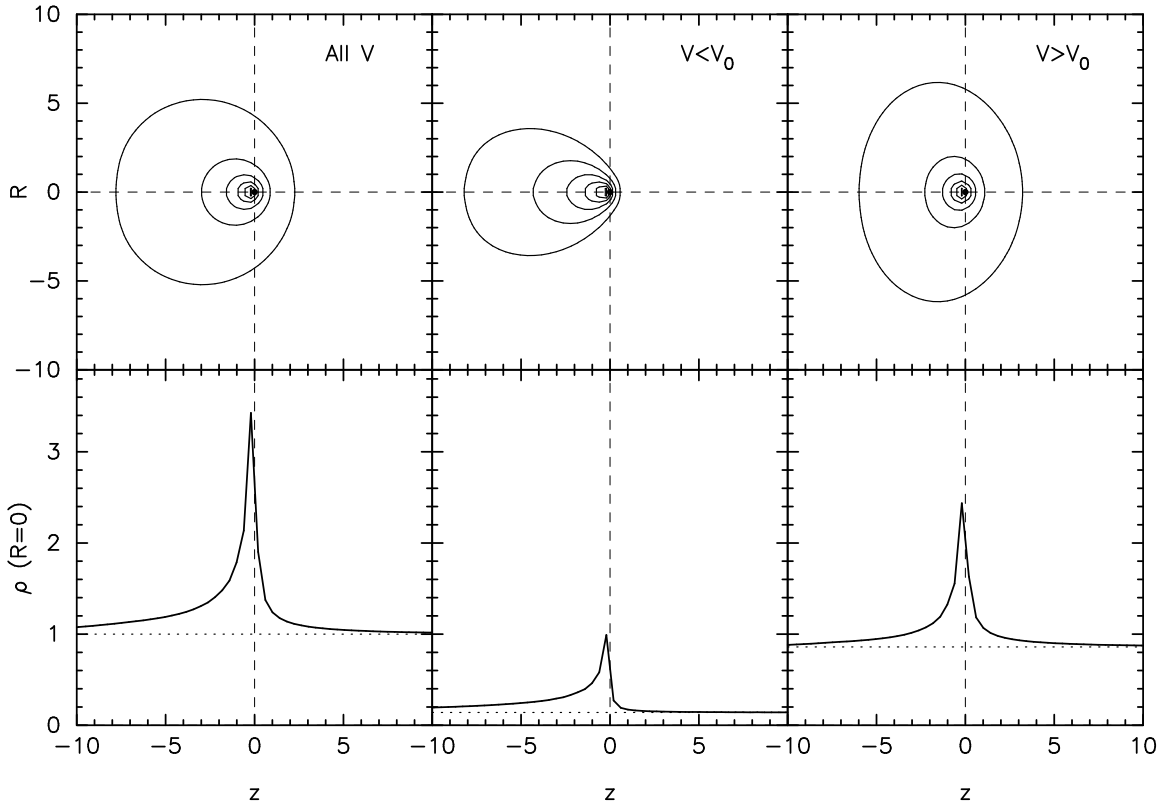

Figure 5.2 Dynamical friction wakes, computed via Mulder's (1983) technique, assuming equation (5.5) with $\gamma = 5/4$ for the velocity distribution at infinity; the test mass is located at the origin and is assumed to be moving at constant velocity $v = v_c$, the local circular velocity, as in Figure 5.1. The top panels show contours of the density, in a plane that contains the test body's velocity vector; the left panel shows the total density, the middle panel shows the density contributed by the stars with $v_\star < v$ at infinity, and the right panel shows the contribution from stars with $v_\star > v$ at infinity. The contours are spaced logarithmically in density and the contour spacing is different in the three panels. The lower panels show the density along the symmetry axis, i.e. a line through the test body in the direction of its motion. Units are $G = m = v_c = 1$.

the relative contribution of the fast stars to the frictional force drops off with increasing $\ln \Lambda$ in Chandrasekhar's treatment (Figure 5.1). At large distances from the test body, the wake produced by the fast stars is nearly symmetric; the greatest asymmetry is in the region near the test mass. The wake generated by the slow stars, on the other hand, maintains its asymmetry much farther from the test body. Roughly speaking, the density far from the origin in Figure 5.2 is produced by stars with large impact parameters, and so increasing $p_{\max}$ in Chandrasekhar's treatment corresponds to more heavily weighting the contribution from the slow-moving stars.

5.3 Orbital Evolution based on Chandrasekhar's Formulae

We are interested in the orbital evolution of a massive black hole as it spirals in toward the center of a galaxy that contains a second, supermassive black hole (SMBH). Below we present results from direct, large-scale N-body simulations. As a basis for comparison, we present in this section the predictions of of Chandrasekhar's approximate formulae. We represent the stars via a smooth, fixed potential and integrate the equations of motion of the massive body in the fixed analytic potential including a term that represents the non-conservative contribution of dynamical friction.

We base our model for the stellar density on the observed distribution of old stars at the Galactic center (GC). Number counts (Buchholz et al. 2009; Do et al. 2009; Bartko et al. 2010) are consistent with a density that follows a broken power-law:

$$\rho(r) = \rho_0 \left(\frac{r}{r_0}\right)^{-\gamma} \left[1 + \left(\frac{r}{r_0}\right)^{\alpha}\right]^{(\gamma-\gamma_e)/\alpha} , \tag{5.14}$$

where α is a parameter that defines the transition strength between inner and outer power laws and r_0 is the scale radius. Following Merritt (2010), we adopt $r_0 = 0.3$pc , $\alpha = 4$ and $\gamma_e = 1.8$ as fiducial values. The central slope γ was left as a free parameter. The normalization factor ρ_0 was chosen in such a way that for each value of γ , the corresponding density profile reproduces the coreless density model:

$$\rho(r) = 1.5 \times 10^5 \left(\frac{r}{1\mathrm{pc}}\right)^{-1.8} \mathrm{M}_\odot \mathrm{pc}^{-3} , \tag{5.15}$$

outside the core. This choice of normalizing constant gives a mass density at 1pc similar to what various authors have inferred (**?**Schödel et al. 2007) and implies a total mass in stars within this radius of $\sim 1.6 \times 10^6 \mathrm{M}_\odot \mathrm{pc}^{-3}$.

Assuming equal-mass stars of mass m and an isotropic velocity distribution, the local two-body relaxation time is defined as (Spitzer 1987) :

$$t_\mathrm{r} = \frac{0.33\sigma^3}{\rho m G \ln\Lambda} , \tag{5.16}$$

where $\ln\Lambda$ is the Coulomb logarithm and σ is the isotropic velocity dispersion; the latter can be computed from Jeans's equation,

$$\rho(r)\sigma(r)^2 = G \int_r^\infty dr' r'^{-2} \left[M_\bullet + M_\star(< r')\right] \rho(r'). \tag{5.17}$$

Here $M_\bullet$ is the mass of the central SMBH that we take to be $4 \times 10^6 \mathrm{M}_\odot$ (Ghez et al. 2008; Gillessen et al. 2009) and $M_\star(< r)$ is the total mass in stars within r. The total stellar mass contained within the SMBH influence radius ($r_\mathrm{bh} \approx 2.5$pc) is $M_\star(< r_\mathrm{bh}) \approx 10^7 \mathrm{M}_\odot$; assuming solar-mass stars, the two-body relaxation time at r_bh is $t_\mathrm{r}(r_\mathrm{bh}) \approx 2 \times 10^{10}$yr.

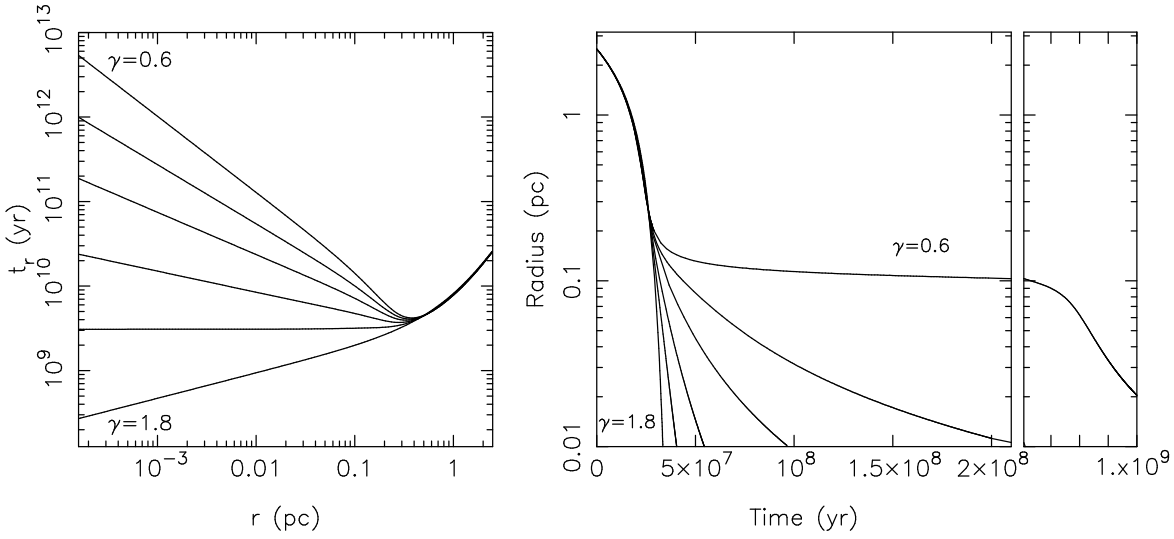

Figure 5.3 Left panel: relaxation time $t_{\rm r}$ versus radius for models based on the density law of equation (5.14). Right panel: Orbital decay of a $10^3 {\rm M}_\odot$ black hole starting from a radius of 2.5pc. In both panels, various values of the inner density slope γ were considered: $(0.6, 0.8, 1, 1.25, 1.5, 1.8)$.

5.3.1 Circular Orbits

The frictional acceleration on a point particle of mass M and velocity $\boldsymbol{v}$ is (Chandrasekhar 1943)

$$\boldsymbol{f_{\rm fr}} = -\frac{4\pi G^2 M \rho(r) F(<v,r) \ln\Lambda}{v^3}\boldsymbol{v}, \tag{5.18}$$

where $F(<v,r)$ is the fraction of stars at r that are moving more slowly than v. This is the standard expression, derived by ignoring the velocity dependence of $\ln\Lambda$ when integrating over the field-star velocity distribution and setting the non-dominant terms to zero. As a result of these approximations, the frictional force is produced only by field stars with velocities less than v. Although equation (5.18) was derived under the assumptions of an infinite and homogeneous background of stars, it has been shown to work reasonably well even for more general stellar distributions (White 1983; Lin & Tremaine 1983; Weinberg 1986; Cora et al. 1997; Merritt 2006; Just et al. 2010).

For a massive particle initially located at $r_{\rm bh}$ on a circular orbit, the inspiral time in the power-law density profile of equation (5.14) with $\gamma = 1.8$ (i.e., the coreless model) is

$$t_{\rm fr} \approx 1.1\times 10^7 {\rm yr}\left(\frac{r}{2.5{\rm pc}}\right)^2 \left(\frac{\sigma}{100{\rm kms}^{-1}}\right) \times \left(\frac{10^3{\rm M}_\odot}{M}\right)\left(\frac{15}{\ln\Lambda}\right) \tag{5.19}$$

independent of the mass of the field stars if $M >> m$.

Figure 5.3 plots the relaxation time as a function of radius for the same model, assuming $\ln\Lambda = 15$, $m = {\rm M}_\odot$ and adopting different values for the inner density slope γ. It turns out that the isotropic distribution function corresponding to the adopted density law (5.14) becomes negative

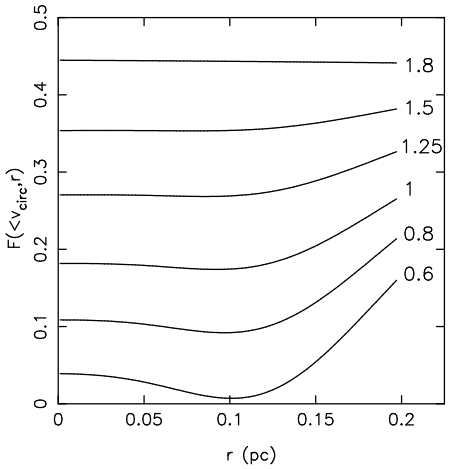

Figure 5.4 Fraction of stars $F(< v_{\rm circ}, r)$ moving more slowly than the local circular velocity as a function of radius for $\gamma = (0.6, 0.8, 1, 1.25, 1.5, 1.8)$. When $\gamma = 0.6$, F is close to zero for $r \approx 0.1$pc . Hence, the frictional force acting on a massive particle which moves on a circular orbit drops essentially to zero at this radius.

at certain energies for $\gamma \lesssim 0.6$. For this reason, we consider in the following only models with $\gamma \geq 0.6$. Figure 5.3 also shows the evolution of a $10^3 \mathrm{M}_\odot$ black hole on a circular orbit starting from a galactocentric distance of 2.5pc. The orbit was numerically integrated by solving the system of first-order differential equations

$$\dot{\mathbf{r}} = \mathbf{v}, \quad \dot{\mathbf{v}} = -\nabla\phi + \mathbf{f}_{\rm fr} \tag{5.20}$$

with $\phi(r)$ the total gravitational potential produced by the stars and the SMBH:

$$\phi(r) = -\frac{GM_\bullet}{r} + \phi_\star(r) = -\frac{GM_\bullet}{r} + 4\pi G\left[\frac{1}{r}\int_0^r dr' r'^2 \rho(\mathrm{r}') + \int_r^\infty dr' r' \rho(\mathrm{r}')\right] . \tag{5.21}$$

The numerical integration was performed using a 7/8 order Runge-Kutta algorithm with a variable time-step (Fehlberg 1968) in order to keep the relative error per step in energy, in the absence of dynamical friction, less than a specified value (10^{-8}). When dynamical friction was included, we checked the integration accuracy through the quantity $E + E_{\rm df}$ with E the energy per unit mass and $E_{\rm df}$ the work done by dynamical friction along the trajectory. The accuracy in this case was of the same order of that found in integrations without dynamical friction. The function $F(< v, r)$ was evaluated using the expression (Szell et al. 2005):

$$F(< v, r) = 1 - \frac{1}{\rho}\int_0^E d\phi' \frac{d\rho}{d\phi'} \times \left\{1 + \frac{2}{\pi}\left[\frac{v/\sqrt{2}}{\sqrt{\phi' - E}} - \tan^{-1}\left(\frac{v/\sqrt{2}}{\sqrt{\phi' - E}}\right)\right]\right\}, \tag{5.22}$$

where $E = \frac{1}{2}v^2 + \phi(r)$.

At all radii, the relaxation time is much longer than the time required for the massive

particle to reach the core. What happens next depends on γ: the orbital decay can essentially stall when γ is small (i.e., ~ 0.6), or continue rapidly if γ is larger.

The explanation of this behavior can be found in Figure 5.4 which plots the fraction of stars moving more slowly than the local circular velocity $v_{\rm circ}(r)$ as a function of radius, for various values of γ. When $\gamma = 0.6$, $F(< v_{\rm circ}, r)$ approaches zero at $r_{\rm st} \sim 0.1$pc and consequently the dynamical friction force drops drastically at this radius (see equation [5.18]). The stalling observed in the orbital evolution for this value of γ is therefore a consequence of the lack of slowly-moving stars in the core. When $\gamma \geq 0.6$, the inspiral continues into the very center since $F(< v_{\rm circ}, r) > 0$ everywhere.

For $\gamma \geq 0.6$, the time required for dynamical friction to bring a $10^3 {\rm M}_\odot$ black hole into the center, starting from a galactocentric distance of a few parsecs, is shorter than the two-body relaxation time evaluated at the SMBH influence radius $t_{\rm r}(r_{\rm bh})$. On the other hand, the efficiency of dynamical friction decreases with the mass of the inspiraling object, and for $M \lesssim 10^2 {\rm M}_\odot$ the infall timescale can significantly exceed a Hubble time. Freitag et al. (2006) found that $t_{\rm r}(r_{\rm bh})$ is also approximately the timescale over which gravitational encounters change an initial density profile into the Bahcall-Wolf Bahcall & Wolf (1976) form, i.e., $\rho \propto r^{-1.75}$. We conclude that for a black hole of mass $M \geq 10^3 {\rm M}_\odot$, inspiral will occur in a mass profile that is almost independent of time. However, for $\gamma \sim 0.6$, the time required to reach a distance ~ 0.01pc, is still comparable with the local relaxation time. This will result in a substantial evolution of the stellar background during the orbital decay.

5.3.2 Eccentric Orbits

In the case of an isotropic distribution function $f(E)$ describing a power law density profile around a SMBH, if the gravitational potential produced by the stars is ignored (i.e., $E << -GM_\bullet/r_{\rm bh}$), then

$$f(E) = \frac{3-\gamma}{8}\sqrt{\frac{2}{\pi^5}}\frac{\Gamma(\gamma+1)}{\Gamma(\gamma-1/2)} \times \frac{M_\bullet}{m}\frac{\phi_0^{3/2}}{(GM_\bullet^{\rm SM})^3}\left(\frac{|E|}{\phi_0}\right)^{\gamma-3/2}, \tag{5.23}$$

with $\phi_0 = GM_\bullet^{\rm SM}/r_{\rm bh}$. For $\gamma \leq 0.5$, $f(E)$ is undefined and so $\gamma \approx 0.5$ is the shallowest density profile consistent with an isotropic velocity distribution around a SMBH. In the case $\gamma = 1.5$, equation (5.23) shows that the distribution function is a constant ($f(E) \equiv f_0$). If one writes

$$\rho(r)F(< v, r) = \rho(r) \times \frac{1}{\rho(r)} 4\pi \int_0^v dv_\star v_\star^2 f_0 = \frac{4}{3}\pi\ f_0 v^3 \tag{5.24}$$

it can be immediately seen that the product $\rho(r)F(< v, r)$ in equation (5.18) will be a function of v only. Under these circumstances, the coefficient of dynamical friction will have only a weak dependence on radius through the Coulomb logarithm. It can be shown that, in this case, the eccentricity of a massive body will remain unchanged during its motion, while dynamical friction

will either circularize the orbit for $\gamma > 1.5$ or make it more eccentric for $\gamma < 1.5$ (Quinlan 1996; Gould & Quillen 2003).

To evaluate the eccentricity evolution of a massive particle in response to Chandrasekhar's dynamical friction formula, a numerical treatment is necessary. We therefore carried out numerical integrations of the set of differential equations (5.20) as described above, adopting as before equations (5.14) and (5.21) for the (fixed) stellar potential.

Figure 5.5 shows the results for $M = 10^3 \mathrm{M}_\odot$. The massive particle was initially placed at $r = 2.5$pc with a tangential velocity of $\sim 0.36 v_{\rm circ}$. With this initial configuration the body penetrates the inner core after few obits. Different values of the internal slope γ, ranging from 1.8 to 0.6 were adopted. As a proxy for the instantaneous orbital elements, we computed over each radial period the largest and the smallest distance from the origin (i.e. the SMBH) and defined these as the apoapsis $r_{\rm ap}$ and periapsis $r_{\rm per}$ respectively. The eccentricity and semimajor axis were then computed using the Keplerian expressions

$$e = \frac{r_{\rm ap} - r_{\rm per}}{r_{\rm ap} + r_{\rm per}}, \qquad a = \frac{r_{\rm ap}}{1+e}. \tag{5.25}$$

The figure reveals a complex behavior of eccentricity on time. For $\gamma \leq 1.5$ we distinguish three regimes. In phase I, the eccentricity decreases (even for $\gamma \geq 1.5$). The duration of this phase is shorter for shallower profiles. After reaching a minimum, the eccentricity then increase rapidly with time (phase II). Finally, in phase III, the eccentricity either continues to increase, but more slowly than in phase II, or remains constant for $\gamma = 1.5$.

This evolution can be understood by considering the changes of $r_{\rm ap}$ and $r_{\rm per}$ with time. In phase I, the black hole periapsis is close to the core radius where the difference between the density models is small. As a consequence, the eccentricity evolution is nearly independent of γ and the orbits circularize. In phase II, $r_{\rm per}$ is well inside the core where the smaller dynamical friction results in a rapid eccentricity increase. Finally, in phase III, the orbit lies entirely inside the core. As a consequence of the declining dynamical friction at $r_{\rm ap}$ the eccentricity growth slows down. As predicted, for $\gamma = 1.5$, the eccentricity remains unchanged in this phase.

These results show that, in the presence of a flat ($\gamma \lesssim 1$) density profile, a second black hole found initially on an eccentric orbit can acquire very large eccentricities ($\lesssim 1$) before entering the regime where relativistic effects become important. In Section 5.6.2 we discuss in more detail how very large eccentricities may modify the expectations for the GW signal from massive black hole binaries for experiments like LISA.

In the first phase, when the periapsis is still outside the core, the orbit evolves completely in the outer cusp ($\gamma_e = 1.8$). Evolution in this regime could lead to a rapid circularization before the black hole reaches the inner ~ 0.3pc. To quantify the amount of circularization in this phase we computed a further orbit in the model with $\gamma = 0.6$, adopting initially a larger semimajor-axis ($a = 12$pc) and a smaller eccentricity ($e = 0.2$). The results of this integration (Figure 5.6) show that the eccentricity reaches a minimum value, $e \approx 0.08$, and then increases rapidly reaching $e \approx 0.2$

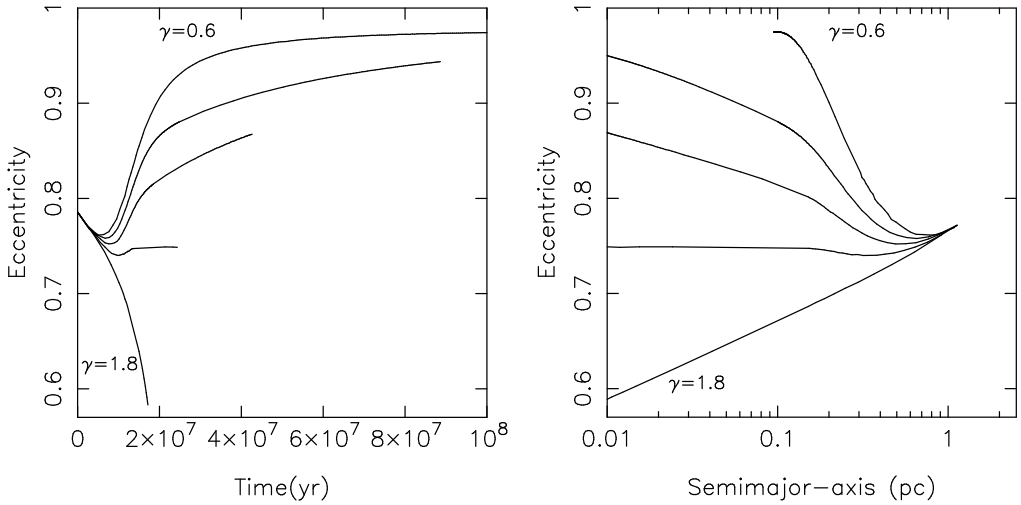

Figure 5.5 Left panel shows the time dependence of the orbital eccentricity of a $M = 10^3 M_\odot$ black hole. In the right panel the orbital evolution is shown in the eccentricity-semimajor axis plane. The inner cusp slopes are $\gamma = (0.6, 1, 1.25, 1.5, 1.8)$. Initial apoapsis and periapsis distances were 2.5 and 0.35pc respectively and initial semimajor axis was $a = 1.4$pc. The integrations terminated either when the semimajor axis of the black hole was 0.01pc or at 10^8yr for $\gamma = 0.6$.

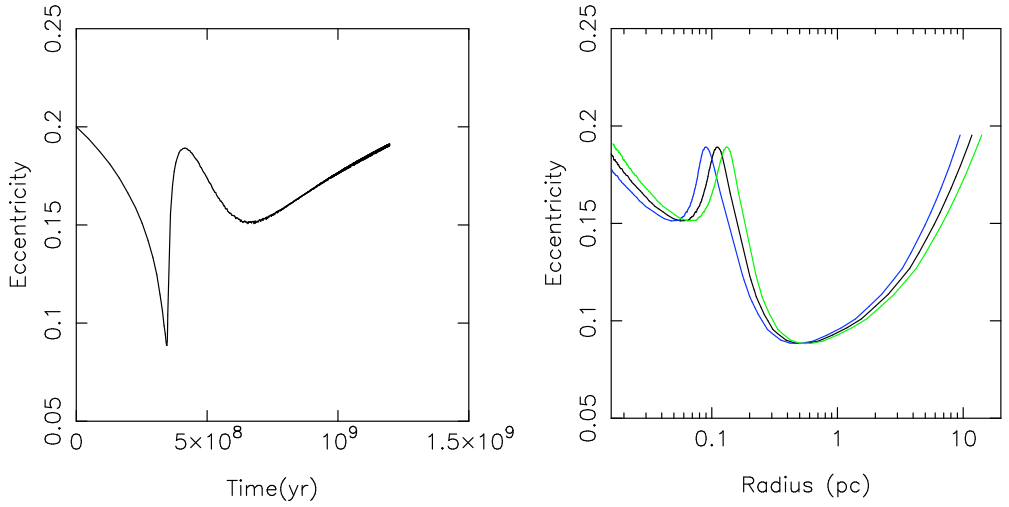

Figure 5.6 Left panel : eccentricity evolution for a $10^3 M_\odot$ black hole. The initial apoapsis and periapsis of the orbit are 15 and 10pc respectively which give a semimajor axis $a \approx 12$pc. Right panel: eccentricity versus semimajor-axis (black line), apoapsis (green line) and periapsis (blue line).

when $r_{\rm per} = 0.1$pc. After this point there is a second phase in which the eccentricity of the orbit decreases. This is an effect of the increasing fraction of slow moving stars close to the SMBH (bottom curve of Figure 5.4). Therefore, for a short interval of time, when $r_{\rm ap} \sim 0.1$pc, the frictional force at apoapsis becomes smaller than that at periapsis and, consequently, the eccentricity decreases. At the end of the integration the orbit retains a substantial eccentricity (~ 0.2), even though it was almost circularized at the beginning of phase II.

5.4 N-body simulations

The numerical integrations of equation (5.18) presented above predict that a massive body that spirals in to the center of a galaxy containing a SMBH, and a nuclear star cluster with flat ($\gamma \lesssim 0.6$) density profile, will stall, at a radius that is roughly the core radius. Moreover, its eccentricity is expected to increase steeply once the orbital periapsis lies inside the core. Here we use N-body simulations to test these predictions.

5.4.1 Initial Conditions and Numerical Method

In order to generate equilibrium N-body models of the GC region that extend self-consistently to the Sgr A* influence radius ($r_{\rm bh} \approx 2.5$pc) we used the truncated mass model

$$\rho(r) = \rho_0 \left(\frac{r}{r_0}\right)^{-\gamma} \left[1 + \left(\frac{r}{r_0}\right)^{\alpha}\right]^{(\gamma-\gamma_e)/\alpha} \zeta(r/r_{\rm t}), \tag{5.26}$$

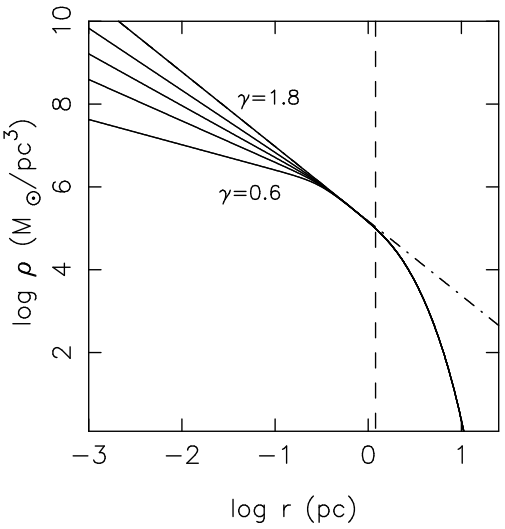

Figure 5.7 Density profiles of equation (5.26) with $\gamma = (0.6, 1, 1.25, 1.5, 1.8)$, $r_0 = 0.3$pc, $\alpha = 4$ and truncation radius $r_{\rm t} = 1.2$pc (vertical dashed line). The dash-dotted line gives the coreless model of equation (5.15).

Table 5.1 Initial conditions.

Model	γ	N k	$r_{\rm t}$ (pc)	M ($10^3 {\rm M}_\odot$)	m (${\rm M}_\odot$)	$e_{\rm in}$	$r_{\rm in}$ (pc)	r^* (pc)	$\ln\Lambda$
A1	0.6	230	1.2	5	22	0	1	0.07	6.7
A2	0.6	130	1.2	5	38	0	1	0.07	6.6
B1	0.8	230	1.2	5	22	0	1	0.06	6.9
B2	0.8	130	1.2	5	38	0	1	0.06	6.9
C	0.6	80	0.6	5	26	0	0.5	0.07	6.3
D	0.6	130	1.2	2	38	0	0.3	0.05	...
E	0.6	130	1.2	10	38	0	1	0.10	6.4
F	0.6	130	1.2	50	38	0	1	0.18	4.8
G1	0.6	200	1.2	5	25	0.54	1	0.07	6.9
G2	0.6	100	1.2	5	50	0.54	1	0.07	6.9

with truncation function

$$\zeta(x) = \frac{2}{{\rm sech}(x) + \cosh(x)}. \tag{5.27}$$

With this choice, the density falls off exponentially at large radii (i.e., $r > r_{\rm t}$) while for $r \ll r_{\rm t}$, where $\zeta(x) \approx 1 - x^4/8$, the model reproduces almost exactly the density of equation (5.14). As above, we chose $r_0 = 0.3$pc, $\alpha = 4$, $\gamma_e = 1.8$ and $\rho_0 = 1.3 \times 10^6 {\rm M}_\odot$. Monte-Carlo initial positions and velocities were then generated by numerically solving equation (5.22); we stress that the equilibrium models so produced include self-consistently the effects of the gravitational force from the stars. Figure 5.7 shows the truncated density profiles for different values of γ and $r_{\rm t} = 1.2$pc.

The initial conditions were evolved using the direct-summation code ϕGRAPE (Harfst et al. 2007) which uses a fourth-order Hermite integrator with a predictor-corrector scheme and hierarchical time steps. The performance and accuracy of the code depend both on the time-step parameter η and on the smoothing length ϵ. In what follows, we set $\eta = 0.01$ and $\epsilon = 5 \times 10^{-4}$pc. With these choices, energy conservation was typically of order 0.1% over the entire length of the integration. Most of the N-body integrations were carried out on the 32-node GRAPE cluster at the Rochester Institute of Technology. In addition, a few were carried out in serial mode using a TESLA C870 graphics processing unit with SAPPORO, a CUDA library that emulates double-precision force calculations on single precision hardware (Gaburov et. al. 2009).

Table 1 gives the parameters of the N-body models. The initial distance of the secondary black hole is given by $r_{\rm in}$ while its initial orbital eccentricity is $e_{\rm in}$. The quantity r^* is the radius at which the initial mass in stars equals M, the mass of the second black hole. All of our N-body models had $r_{\rm in} < r_t$, so that the orbital evolution is expected to be very similar to that in the corresponding non-truncated models. In order to study the dependence of the results on the secondary black hole mass we run simulations with a range of masses, $M = (2000, 5000, 10000, 50000){\rm M}_\odot$. Two cases with nonzero initial eccentricities (runs G1 and G2, with $e_1 = 0.54$) were also considered.

5.4.2 The Coulomb Logarithm

In Table 1 we report the values of the Coulomb logarithm extracted from each N-body integration. The value of $\ln\Lambda$ was obtained by minimizing the quantity:

$$\sum_{i=1}^{n} \left[r_i(t) - r'(t, \ln\Lambda) \right]^2 , \tag{5.28}$$

outside a galactocentric radius of 0.3pc. Here, n is the number of N-body data points, $r_i(t)$ is the position of the black hole in the N-body simulation at time t, and $r'(t)$ is its position at the same time evaluated by means of the Chandrasekhar's formula (5.18). Since analytical expressions are not available for the trajectory of an inspiraling black hole, in order to obtain the expected position $r'(t)$ at any given time, we first solved numerically the equations of motion (5.20) and then built a spline interpolant from the results of the integration. This procedure was applied only in the part of the orbit outside the core, where equation (5.18) is able to describe accurately the black hole orbit. In this way, unlike in most previous studies, we could obtain an estimate of the Coulomb logarithm without any assumptions about the velocity distribution of the field stars (e.g., that it followed a Maxwellian distribution).

Our simulations do not show any obvious dependence of $\ln\Lambda$ on either the number of particles or on the initial eccentricity. We found an average value of $\ln\Lambda = 6.5 \pm 0.2$, in essentially perfect agreement with the value reported by Spinnato et al. (2003): $\ln\Lambda = 6.6 \pm 0.6$.

5.4.3 Results

Circular Orbits

The first simulations we performed consisted in evolving the massive body on a circular orbit with initial radius 0.1pc (i.e., smaller than the stalling radius when $\gamma \lesssim 0.6$) and for a time corresponding approximately to 300 orbits (i.e., $\sim 4\times10^5$yr at this distance). We used $N = 130,000$, $M = 5000\mathrm{M}_\odot$ and $\gamma = (0.6,\ 1,\ 1.5,\ 1.8)$. We also implemented a high-resolution simulation with $N = 500,000$ for the model with $\gamma = 0.6$. As in most of the longer simulations of Table 1, the truncation radius was $r_\mathrm{t} = 1.2$pc. These shorter integrations allowed us to study dynamical friction, while limiting the deviations of the models from their initial configuration that was found to occur on longer timescales as a result of two-body relaxation (see below). The eccentricity of the orbit remained small during these integrations ($e \lesssim 0.1$).

Figure 5.8 shows the time evolution of the semimajor-axis of the orbits and the rate of orbital decay $s = -da/dt$ as a function of γ, evaluated by a linear fit over the full interval of time shown on the left panel of the figure. The agreement with the decay rate computed using Chandrasekhar's formula (5.18) (open squares) is good. For $\gamma = 0.6$, there is not any significant evolution of the orbit in the considered interval of time and, consequently, $s \approx 0$.

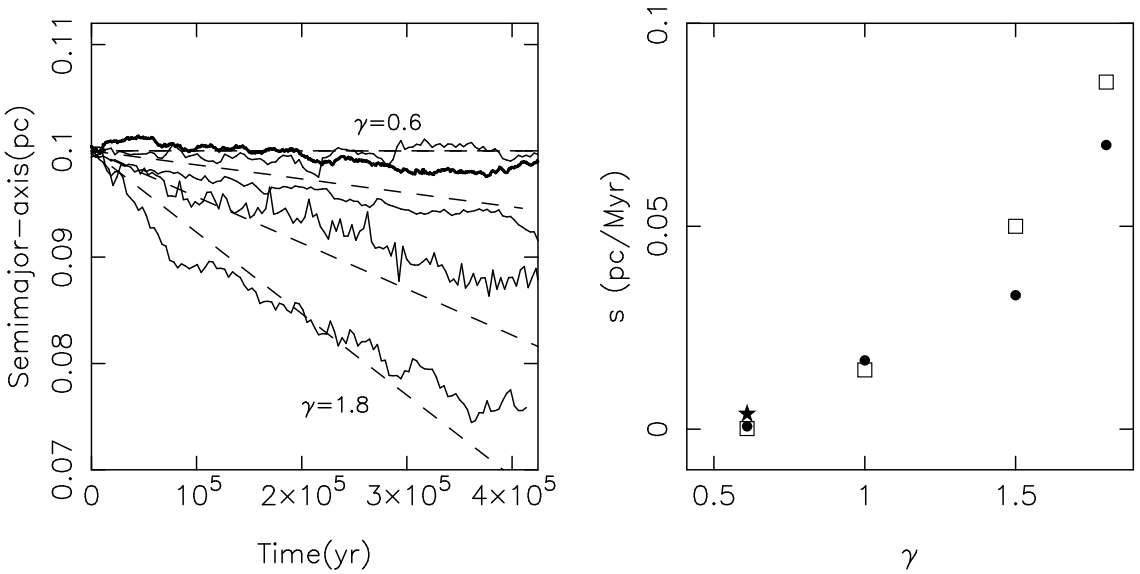

Figure 5.8 Left panel: evolution of the semimajor axis for a $5000M_\odot$ black hole in the short N-body integrations, for different values of the central density slope (from top to bottom, $\gamma = 0.6,\ 1,\ 1.5,\ 1.8$). The thicker line is from the high-N integration, with $N = 500,000$ and $\gamma = 0.6$. Dashed lines are predictions from Chandrasekhar's formula (5.18) using $\ln\Lambda = 6.6$. For $\gamma = 0.6$ there is no significant evolution of the orbit in the considered interval of time. Right panel: orbital inspiral rates $s = -da/dt$ computed for the simulations displayed on the left panel as a function of γ (filled circles). Open squares give the predictions from Chandrasekhar's formula. The star symbol is the decay rate computed from the high resolution run ($N = 500,000$ and $\gamma = 0.6$).

A similar conclusion is implied by Figure 5.9 which shows the trajectory of a $2000M_\odot$ black hole in model D, a longer integration with $N = 130000$ and $\gamma = 0.6$. Initially, the black hole sinks rapidly to the center, reaching $\sim r_{\rm st}$ in ~ 3Myr. As the inspiral progresses, the orbit becomes more eccentric ($e \approx 0.3$ at 4Myr). At later times ($\gtrsim$ 4Myr), the orbit shows no sign of further decay, oscillating in radius between ~ 0.1 and ~ 0.2pc. The orbital eccentricity remains almost constant in this phase.

These findings, obtained for a flattened density cusp around a SMBH, seem to confirm the theoretical predictions made above: i) dynamical friction "vanishes" within ≈ 0.15pc; ii) the orbital eccentricity of an infalling body increases with time.

However, in any N-body simulation, stars are continuously scattered by gravitational encounters with other stars, with the result that the initially empty phase space region responsible for the vanishing dynamical friction force will gradually be refilled. In addition, due in part to the low central density of our GC models when γ is small, the radius at which the cumulative mass in stars becomes comparable to that of the inspiraling black hole can be of order $r_{\rm st}$, even for relatively small M (see table 1). N-body simulations have shown that, in these circumstances, the orbit deviates

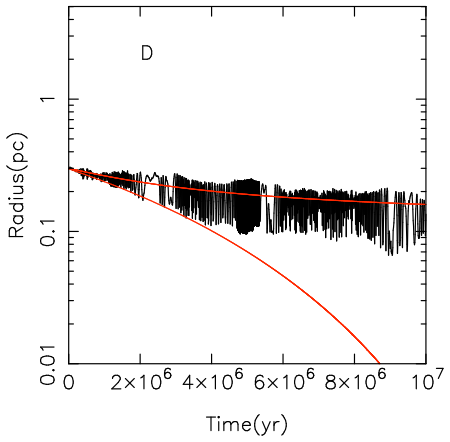

Figure 5.9 Trajectory of a 2000$M_\odot$ black hole into a core with $\gamma = 0.6$ (model D). The top, solid red line is the theoretical prediction obtained from Chandrasekhar's formula (5.18) using $\ln\Lambda = 6.6$. The bottom red curve shows the predicted inspiral in a $\gamma = 1.8$ cusp.

from the theoretical prediction of the Chandrasekhar's formula as a consequence of perturbations induced by the infalling black hole on the inner cusp (Baumgardt et al. 2006; Löckmann, & Baumgardt 2008). Finally, it is not clear whether the approximations made in deriving equation (5.18), which was the basis for the red lines plotted in Figure 5.10, are reasonable, or how large might be the frictional force from fast moving stars that populate the low density core. In fact, as we now demonstrate, these additional effects have a substantial influence on the long-term evolution of the black hole orbit.

Figure 5.10 shows the trajectory of the black hole for some of the N-body integrations from Table 1 and compares them to the evolution predicted by Chandrasekhar's formula (5.18) (upper green curves). (In the upper panels, the comparison is displayed only for the higher resolution runs, i.e., models $A1$ and $B1$.) Although the agreement with the theoretical prediction appears fairly good, at least for $M = 5000M_\odot$, when $\gamma = 0.6$, the N-body integrations reveal a faster decay than predicted. Either some the frictional force must come from stars with velocities $v_\star > v$, or the background stellar distribution is changing during the inspiral (or both). These two possibilities are investigated in what follows.

Dynamical friction from fast-moving stars. Equation (5.18) was derived under standard approximations that ignore the contribution from non-dominant terms and the velocity dependence of $\ln\Lambda$. Although these approximations are reasonable when there is even a small fraction of stars with low velocities (i.e., $v_\star < v$), it is unclear whether they can be applied to a region populated mostly by stars moving faster than the black hole.

Without these assumptions, the instantaneous dynamical friction acceleration becomes

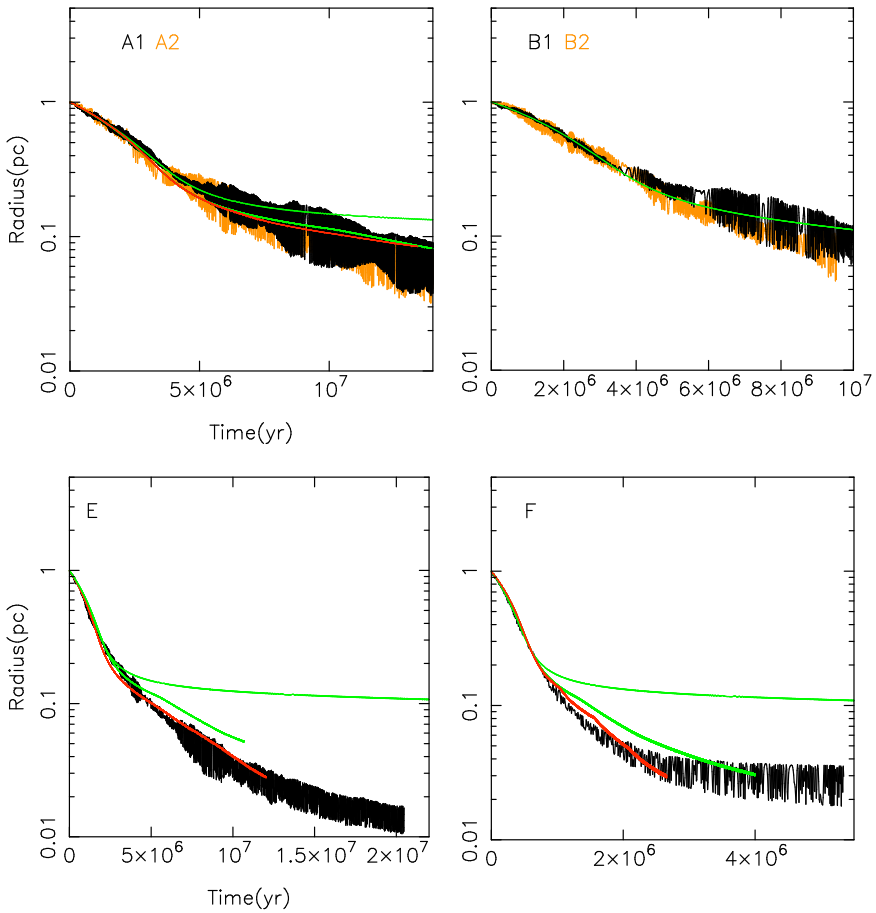

Figure 5.10 Orbital evolution of the second black hole in models A1, A2, B1, B2, E and F. Solid green lines show predictions assuming a fixed background of stars. Upper green curves are obtained by using the standard Chandrasekhar's formula (i.e., equation (5.18)), while lower green curves give the orbital decay computed using equation (5.29) with $p_{max} = 0.5$ pc. Red lines were obtained with equation (5.29) but allowing $f(v_\star)$ and $\rho(r)$ to change according to the evolution of the N-body system.

(Chandrasekhar 1943):

$$\boldsymbol{f}_{\rm fr} = -4\pi G^2 M \rho(r) \frac{\boldsymbol{v}}{v^3} \int_0^{\sqrt{-2\phi(r)}} dv_\star 4\pi f(v_\star) v_\star^2 \frac{1}{8v_\star} \int_{|v-v_\star|}^{v+v_\star} dV \left(1 + \frac{v^2 - v_\star^2}{V^2}\right) \ln\left(1 + \frac{p_{\rm max}^2 V^4}{G^2 M^2}\right) , \tag{5.29}$$

where $f(v_\star)$ is the velocity distribution of field stars, and $p_{\rm max}$ is the effective, maximum value of the impact parameter. In this more accurate treatment, some of the dynamical friction force is due to stars moving more rapidly than the massive particle (Chandrasekhar 1943; White 1949; Merritt 2001). If the condition $p_{\rm max} V^2/GM \gg 1$ is satisfied, the frictional force can be approximated

as (Chandrasekhar 1943)

$$\boldsymbol{f_{\rm fr}} \approx \boldsymbol{f_{\rm fr}^{(v_\star<v)}} + \boldsymbol{f_{\rm fr}^{(v_\star>v)}} = -4\pi G^2 M\rho(r)\frac{\boldsymbol{v}}{v^3}\Big(\int_0^v dv_\star 4\pi f(v_\star)v_\star^2 \ln\left[\frac{p_{\rm max}}{GM}\left(v^2-v_\star^2\right)\right] + \int_v^{\sqrt{-2\phi(r)}} dv_\star 4\pi f(v_\star)v_\star^2\left[\ln\left(\frac{v_\star+v}{v_\star-v}\right)-2\frac{v}{v_\star}\right]\Big). \quad (5.30)$$

Inside $r_{\rm st}$, dynamical friction is produced mostly by stars with $v_\star > v$ and the first term in the integral becomes negligible. This shows the weak dependence of the frictional deceleration inside the core on $p_{\rm max}$.

Adopting equation (5.29), with $p_{\rm max} = 0.5$pc, for the frictional force that appears in the equations of motion (5.20), we obtained the lower green curves in Figure 5.10, which show much better agreement with the N-body results. Evidently, the standard expression for dynamical friction, equation (5.18) , is inadequate to describe the orbital evolution of a massive body at the GC in the case that the density profile of the nuclear star cluster is shallow. This is apparently a consequence of neglecting the non-dominant terms, and not, for instance, of the assumed independence of the Coulomb logarithm on the field star velocity distribution. For models A1 and A2, Lagrangian radii showed essentially no evolution, indicating the absence of any significant change in the stellar distribution induced by the second black hole. We conclude that (at least) some of the drag within $r_{\rm st}$ is due to field stars with $v_\star > v$. A comparable amount of friction was found to be produced by a small fraction of low velocity stars that, due to two-body relaxation, migrated into the low density core. The red lines in Figure 5.10 were derived from equation (5.29) but using a time dependent distribution function $f(v_\star, t)$ extracted (at time t) from the N-body models (see below). For models A1 and A2 the red curves agree exceptionally well with the N-body results and they essentially match the results of the semi-analytical integration that takes into account the friction from fast moving stars. We conclude that for these runs it would be appropriate to ignore the influence of the second black hole on the stellar distribution.

In the left panel of Figure 5.11 we plot the fraction of the dynamical friction force that is predicted, by equation (5.29) , to come from stars with $v_\star > v$, for different values of the inner cusp slope and at different radii. In the right panel of the figure, the total frictional deceleration in our models is given in units of the frictional force computed under the assumption of a Maxwellian distribution of velocities:

$$\boldsymbol{f'_{\rm fr}} = \frac{-4\pi G^2 M\rho(r)\ln\Lambda}{v^3}\boldsymbol{v}\left[{\rm erf}(X) - \frac{2X}{\sqrt{\pi}}e^{-X^2}\right], \quad (5.31)$$

with $X = v_{circ}/\sqrt{2}\sigma$. Clearly, this equation, often used in the past to describe the orbital evolution of a massive object into the GC, overestimates the frictional drag within $r \lesssim 0.2$pc for $\gamma \lesssim 1$.

Influence of the second black hole on the field-star distribution. For larger masses of the infalling body, i.e. $M \gtrsim 10000{\rm M}_\odot$, the perturbations which it induces in the background system introduce a complex time dependence of the phase-space distribution. During the orbital inspiral,

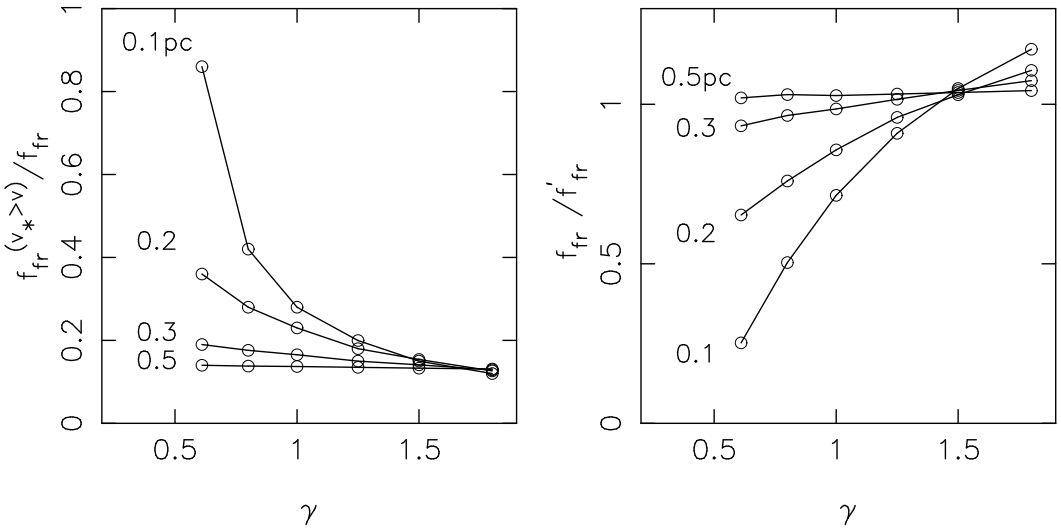

Figure 5.11 Left panel: fraction of the dynamical friction force that is predicted to come from stars with $v_\star > v$ as a function of γ, at different galactocentric radii: $r = 0.1, 0.2, 0.3$ and 0.6 pc. Equation (5.29) was used to compute these curves. When $\gamma = 0.6$, dynamical friction at small radii comes only from stars with $v_\star > v$. As either γ or r increase, the contribution from fast moving stars decreases. Right panel: total dynamical friction force in units of the frictional deceleration computed assuming a Maxwellian distribution of velocities. The frictional force produced by stars with $v_\star > v$, in the flattened cusp (i.e., $\gamma = 0.6$ and $r \lesssim 0.2$pc) is much smaller than that obtained under the simple assumption of thermal distribution of velocities. In both panels we adopted $p_{\rm max} = 0.5$pc and $M = 1000 {\rm M}_\odot$. In the right panel, we used $\ln\Lambda = 6.6$ to solve equation (5.31).

the black hole scatters stars into the inner cusp; consequently, once it reaches $\sim r_{\rm st}$, it will "see" stars with $v_\star < v$ that contribute to the frictional acceleration from that point on.

In order to test Chandrasekhar's formulae under these circumstances, the black hole equations of motion were integrated in a time-varying potential whose properties were varied over time in a way designed to mimic the evolving N-body models. In more detail, the density of the N-body model was computed at fixed intervals of time by binning particles in concentric logarithmically-spaced shells. At the same time the velocity distribution of field stars was obtained directly from the N-body model. Finally, the black hole equations of motion were numerically integrated as described in section (5.3.1) using expression (5.29). In this way, we were able to approximately account for the back-reaction of the second black hole on the stellar distribution. It is worth noting that, even with this more sophisticated approach, two relevant assumptions are retained: i) any induced deviation of the models from isotropy is neglected; ii) the black hole is assumed to move always on a circular orbit, while the N-body simulations clearly show an increase of the orbital eccentricity with time. The red curves of Figure 5.10, obtained through this numerical procedure, show that even when the galactic nucleus is rapidly deviating from its initial configuration, Chandrasekhar's theory can

still accurately reproduce the N-body results if the changes in the stellar distribution are taken into account and the fast moving stars are included when computing the frictional force.

In Figure 5.12 we show the evolution induced by the second black hole in the velocity distribution of the model, by plotting the function $F(< v_{\rm circ}, r)$ at the same time (3×10^6yr) for different masses (left panel). In addition, we show how $F(< v_{\rm circ}, r)$, for $M = 5000{\rm M}_\odot$, evolves as a function of time (right panel). As a consequence of the diffusion of stars at low velocities, the stalling radius is shifted from the initial ≈ 0.1pc to ≈ 0.05pc by the end of the simulation. We note that – in a real galaxy with much larger N – this effect would be essentially absent.

Figure 5.13 illustrates the changes in the configuration-space density for models E and F via the time evolution of their Lagrange radii. The time evolution of models E and F is remarkable: in model F, the perturbations on the stellar distribution are initially so large that the core fills up during the first $\sim 2 \times 10^6$yr. At this point, the black hole, at a galactocentric distance of ~ 0.05pc, starts to carve out the inner region, destroying the cusp that it created before. The final model has a core of size ~ 0.2pc and the internal slope is $\gamma \lesssim 0.5$. However its density, everywhere within 1pc, smaller than that of the initial model as a consequence of displacement of stars from the cusp. A qualitatively similar evolution was found in model E. Figure 5.14 shows the induced evolution of the density profile for runs E and F as well as the time variation of the anisotropy parameter, defined as

$$\beta = 1 - \sigma_t^2/\sigma_r^2 \ , \tag{5.32}$$

with σ_t and σ_r tangential and radial velocity dispersions respectively.

In summary, a straightforward interpretation of our N-body results is that equation (5.18) reproduces remarkably well the real decay rate of a massive object into the GC only until it reaches the stalling radius. In the subsequent evolution, the orbital decay slows down as a consequence of the lack of slow moving stars in the inner galactic nucleus (see Figures 5.8 and 5.9), but it never drops to zero, due apparently to the frictional force generated by stars moving faster than the inspiraling black hole (Figures 5.10 and 5.11).

A massive body of mass $M \approx 1000{\rm M}_\odot$, starting from distances of order $r_{\rm bh}$, will reach a galactocentric radius ~ 0.01pc in $\sim 10^8$yr after which dynamical friction will cease (since the mass in stars becomes comparable to that of the black hole) and the orbit stalls. Note that this distance is about ten times larger than the stalling radius found in previous works that assumed a collisionally-relaxed, steeply-rising density profile around the central black hole (Baumgardt et al. 2006; Löckmann, & Baumgardt 2008).

For larger masses (i.e., $M \gtrsim 10000{\rm M}_\odot$), during the inspiral, the black hole enhances the diffusion of stars into the phase-space region that was initially nearly empty (Figures 5.12 and 5.13). During the stalling phase a low density core is rapidly regenerated by the second black hole as it displaced stars from the cusp.

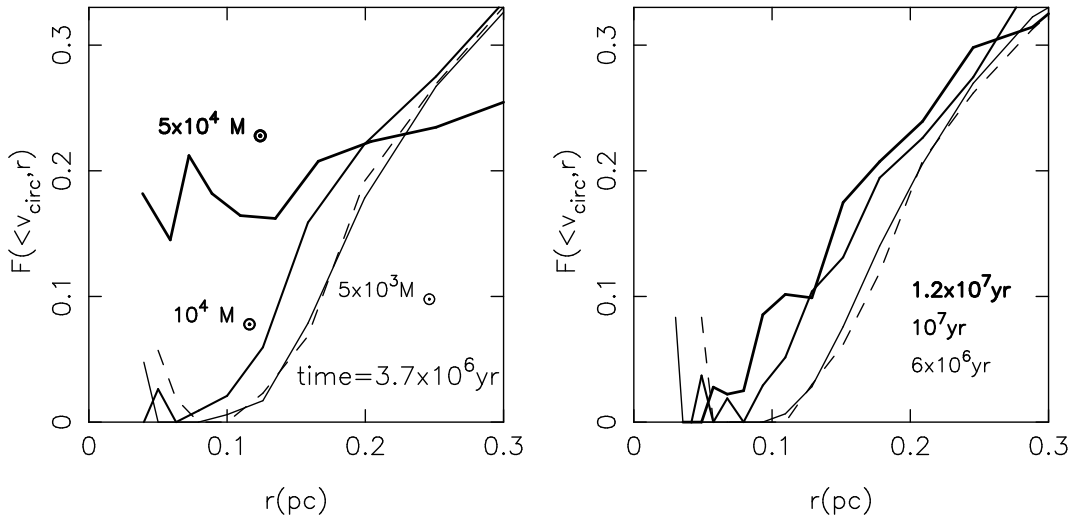

Figure 5.12 Left panel: Fraction of stars with velocities less than the local circular velocity $F(< v_{\rm circ}, r)$ as a function of radius, at the same time (3×10^6yr) for models A2 ($M = 5000\mathrm{M}_\odot$), E ($10000\mathrm{M}_\odot$) and F ($50000\mathrm{M}_\odot$) . The dashed curve corresponds to the initial configuration. The larger the mass of the black hole the faster the changes of the model in velocity space. Right panel: $F(< v_{\rm circ}, r)$ as a function of radius for model A1 at different times. Due to two-body relaxation, stars are scattered toward low velocities and the hole in phase space that characterized the initial configuration is gradually filled up.

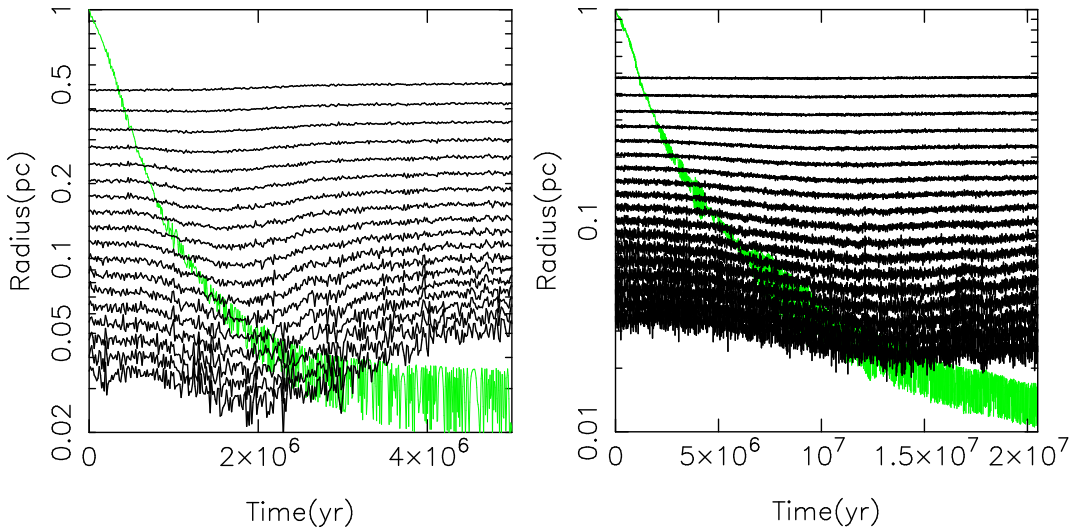

Figure 5.13 Lagrangian radii evolution of models F (left panel) and E (right panel). Green curves show the position of the massive body.

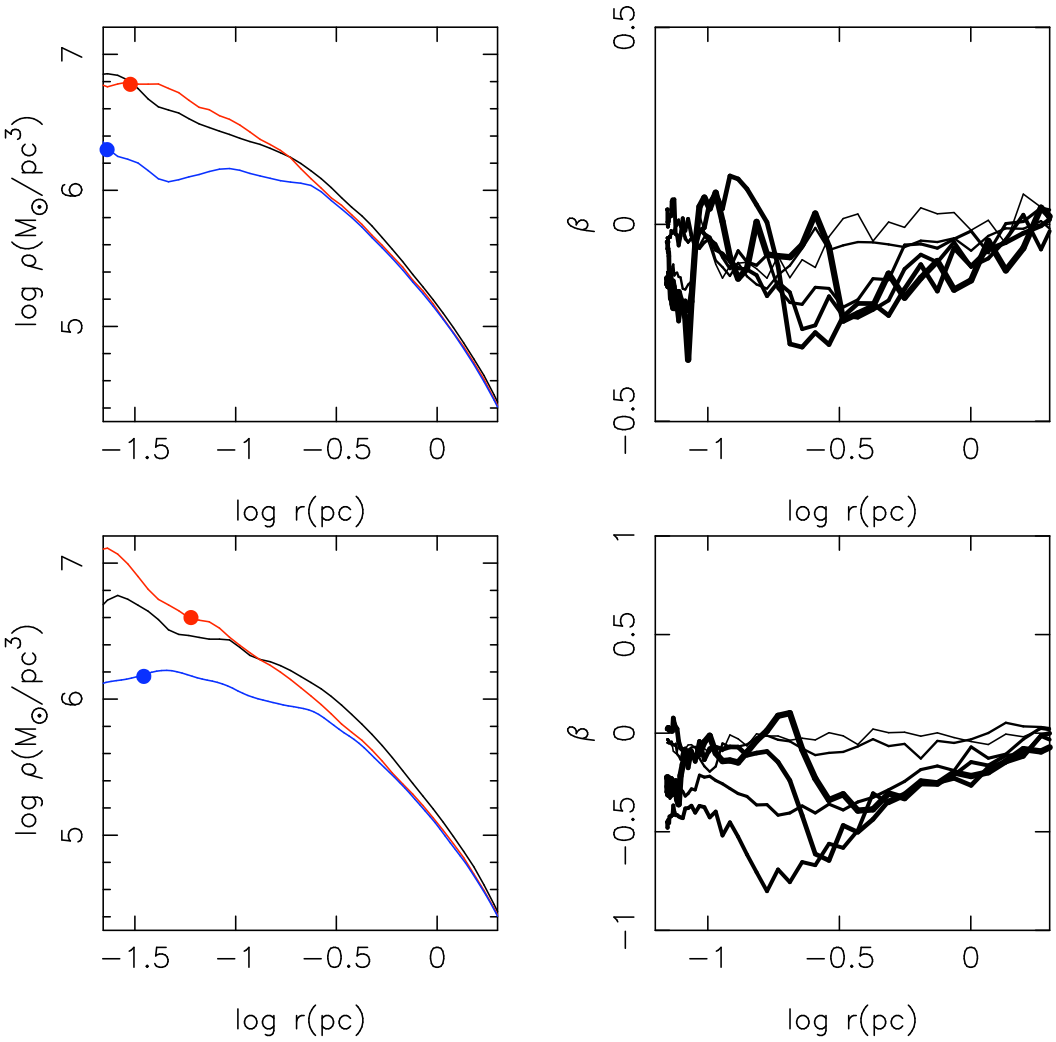

Figure 5.14 Left panels: density profile evolution in run E (upper panel) and F (lower panel). The black curve corresponds to the initial model; the red line is obtained at time 10^7yr for run E and at 2×10^6yr for run F, while the blue lines are the density profile of the final models, after the secondary black hole has stalled carving out a deficiency of stars in the inner regions. Filled circles indicate the position of the inspiraling . Right panels: Evolution of the anisotropy parameter in the models. Line thickness increases with time. As the black hole spirals in, it induces tangential anisotropy in the background system.

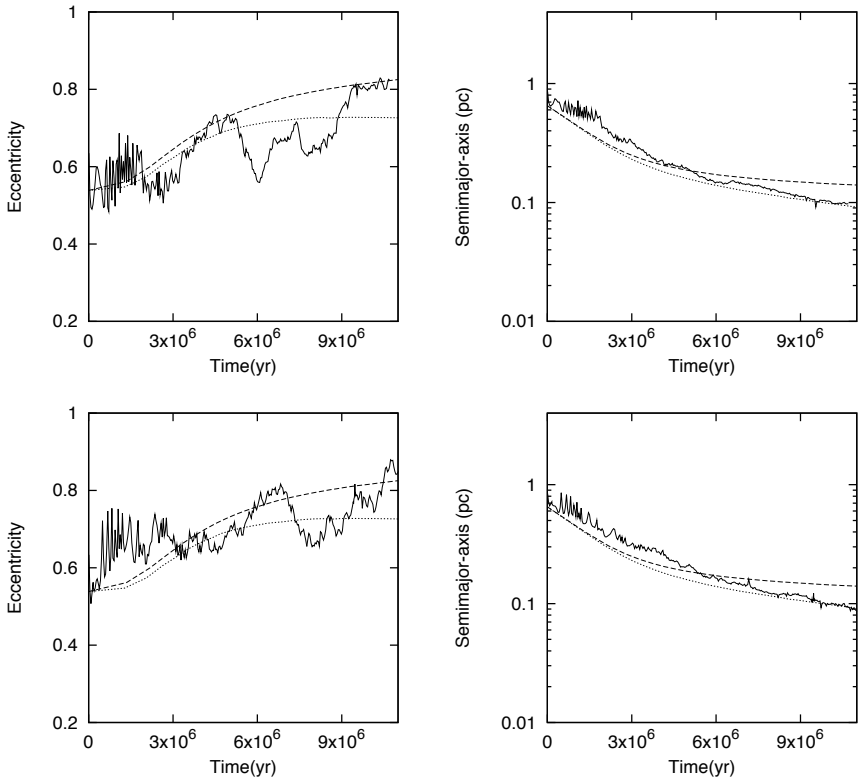

Figure 5.15 Evolution of eccentricity and semimajor axis for models G1 (upper panel) and G2 (lower panel) that differ only in the number of field particles: N=200,000 and 100,000 for models G1 and G2 respectively. Dashed lines are the theoretical predictions from equation (5.18). Dotted lines were obtained with equation (5.29) (i.e., including the frictional drag from stars with $v_\star > v$), where we used $p_{\max} = 0.5$pc. As the black hole spirals in, its orbital eccentricity increases. This conclusion is quite robust, showing essentially no dependence on the number of background particles.

Eccentric Orbits

In this section, we investigate the rate of change of the orbital eccentricity as a consequence of dynamical friction. We devised two simulations that differ only in the number of particles: 200,000 and 100,000. We refer to these simulations as runs G1 and G2 respectively (see Table 1); both have $\gamma = 0.6$. The black hole was initially placed at a radius of $r_{\rm in} = 1$pc on an eccentric orbit with $e_{\rm in} = 0.54$. As discussed earlier (Section 5.3.2), when the orbital periapsis lies within the core, the orbit is expected to become more eccentric as a consequence of the declining frictional force in this region.

Figure 5.15, shows the evolution of the eccentricity and semimajor axis of the orbit as a function of time, demonstrating that, at least qualitatively, Chandrasekhar's theory reproduces the evolution. Although the eccentricity undergoes significant fluctuations, it evidently drifts toward

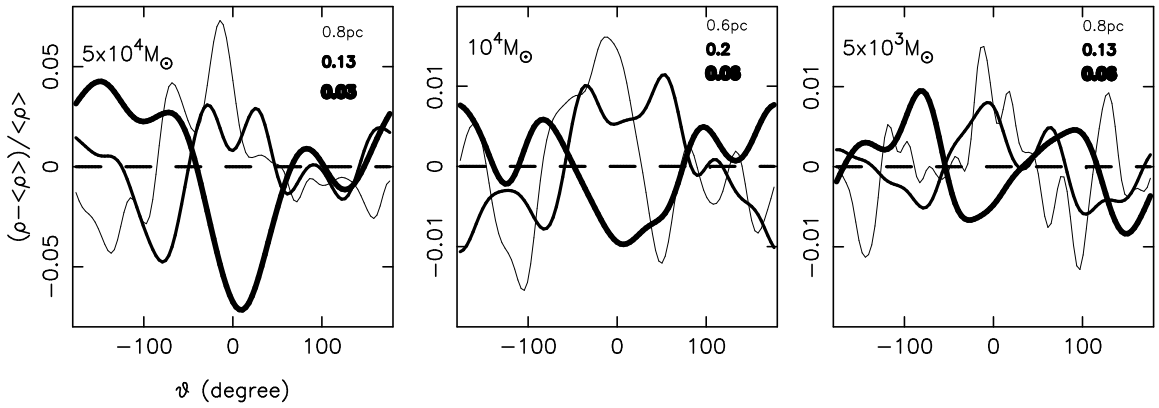

Figure 5.16 Relative overdensity in the N-body models for runs A1, E and F along the black hole orbit. Line thickness decreases with increasing galactocentric distance. In the plots, the second black hole is always located at $\theta = 0$ with $\dot{\theta} > 0$.

larger values with time. This behavior is quite robust showing a negligible N-dependence.

It is generally assumed that dynamical friction, in power-law density models with an isotropic velocity distribution, would circularize the orbit of an infalling body (see for instance Baumgardt et al. (2006)). Our N-body simulations demonstrate that in models characterized by a flat density profile and a central SMBH, the eccentricity can instead be an increasing function of time.

5.5 Gravitational Wake

An alternate way to look at dynamical friction is in terms of the acceleration produced by the overdensity of stars that accumulate behind the massive body – the "gravitational wake" (Danby & Camm 1957; Marochnik 1968; Mulder 1983). The expression for the response wake in a homogeneous medium is given for arbitrary spherical density distribution in Weinberg (1986). The existence of a wake has rarely been confirmed in N-body simulations; an isolated example is provided by Weinberg & Katz (2002) (see also Weinberg & Katz (2007)) who show the wake induced in a dark-matter halo by a stellar bar.

We searched for the wake in our N-body simulations by computing the relative overdensity at each radius along the orbit of the second black hole. The N-body models were first rotated in such a way that the second black hole was situated at $y = z = 0$ with $v_z = 0$ and $v_y > 0$. The density at any position was then estimated using a Gaussian kernel with radially-varying smoothing length. Figure 5.16 shows the results in runs A1, E and F as a function of the azimuthal angle θ at different radii and for different values of M. In the figure, the black hole lies at $\theta = 0$ with $\dot{\theta} > 0$

and the average density is defined as $(1/2\pi)\int_{-\pi}^{\pi} d\theta\ \rho(\theta)$.

Outside the core ($r \gtrsim 0.3$ pc), the peak in the overdensity lies at $-20 < \theta \lesssim 0°$, independent of M, and the amplitude of the overdensity increases with black hole mass, as expected. When $r \lesssim 0.3$ pc, for $M = 5000\mathrm{M}_\odot$, the density enhancement is reduced but its position remains essentially unchanged. For larger masses, the angular dependence of the overdensity in this phase becomes more complex, revealing, in some cases, two distinct peaks. During this phase, the mass distribution is also being affected by gravitational scattering from the massive body. When the black hole is well inside the core, the density maximum is seen to lie at large angular separations ($\theta \lesssim -100°$) from the black hole. This is consistent with the fact that the frictional drag is greatly reduced. Indeed, a density "hole", with amplitude approximately proportional to M, is apparently induced by the black hole at roughly its position during the stalling phase.

Figure 5.17 shows two-dimensional contour maps of the overdensity for run E ($M = 5\times10^4$). The radial extension of the wake (with respect to the galaxy center) does not change greatly over time, but one can clearly see how the location of the density maximum shifts.

To more clearly illustrate how the location of the gravitational wake with respect to the second black hole evolves, we plot in Fig 5.18 the angular position of the maximum as a function

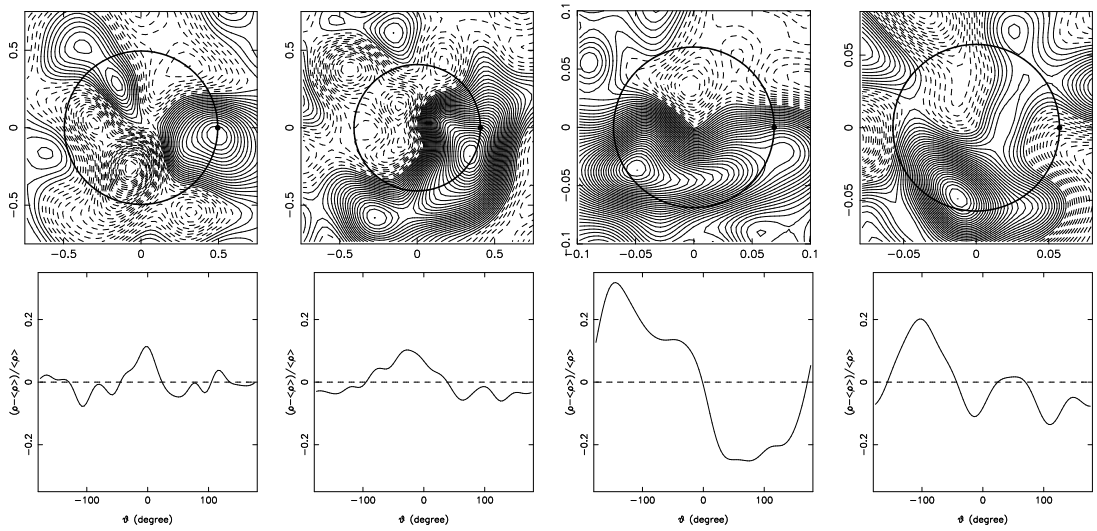

Figure 5.17 The density response (i.e., gravitational wake) induced by the massive body in run E is shown by plotting density contour maps of background stars in the upper panels, and the corresponding relative overdensity along the black hole orbit in the bottom panels. The isodensity contours were obtained by subtracting at any radius the mean density and selecting only particles that were close to the orbital plane. Negative contours (underdensities) are shown by dashed curves. Circular regions show the path over which the density was computed to obtain the plots in the bottom panels.

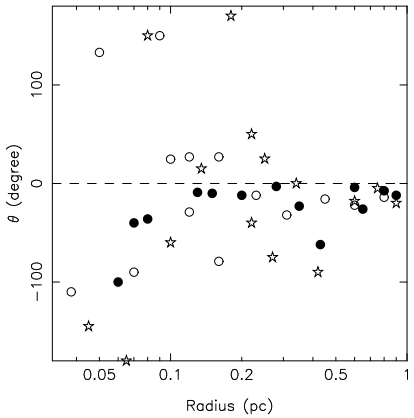

Figure 5.18 Position of the relative density maximum as a function of the black hole galactocentric radius in runs A1 (filled circles), E (open circles) and F (stars symbols). As in Figure 5.16, the N-body models were rotated such that the second black hole is located at $\theta = 0$ with $\dot{\theta} > 0$.

of the black hole galactocentric radius. Outside the core (i.e., $r > 0.3$ pc) the wake is located at small (negative) angles, and therefore it is always just behind the black hole ($\theta = 0$), causing the initial rapid inspiral. The relative position of the wake at the final time is $\lesssim -100°$, such that its gravitational pull on the massive body is much reduced and the orbital decay slows down.

5.6 Discussion

In this final chapter we presented N-body simulations of the inspiral of a massive body into the Galactic center (GC). Our models of the GC nuclear star cluster were motivated by recent observations that suggest a relatively low density of stars inside the SMBH influence radius. Such models are characterized by a zero or near-zero phase-space density at low energies. Under the standard approximation, in which the frictional force from fast-moving stars is ignored, a second black hole that sinks toward the center under the influence of dynamical friction would stall at a distance of roughly 1/2 the core radius, or $\sim$ 0.25pc, from the SMBH. If the smaller black hole moves initially on a non-circular orbit, its orbital eccentricity is predicted to increase with time due to the lower dynamical friction force near periapse.

Using N-body simulations, we found that the frictional force never falls precisely to zero. As noted also by Chandrasekhar, stars moving faster than the test body contribute to the drag. When this contribution is included in the expression for the dynamical friction, Chandrasekhar's formula reproduces quite well the decay observed in N-body simulations of the inspiral of a $\sim 1000 M_\odot$ black hole. The eccentricity increase predicted by Chandrasekhar's theory is also confirmed. When the inspiralling object is more massive, a second mechanism contributes to the frictional force: the second black hole induces evolution of the background system, which tends to refill the initially

empty regions of phase space.

In what follows we discuss the implications of these results for a number of astrophysical problems related to the dynamics of massive bodies near the centers of galaxies. But first, we comment on how our N-body results can be approximately scaled to systems with different masses and densities.

The rate of inspiral of a massive body of mass M is independent of the mass of field stars if $M \gg m$. Chandrasekhar's formula also predicts a linear dependence of the frictional force on M[1], and our simulations (as well as many others) confirm that prediction. If the density response of the background is ignored, it follows that the unit of time in our simulations scales as $\sim \rho M$. The condition that the background not evolve is satisfied in our simulations when $M \lesssim 10^4 \mathrm{M}_\odot$ and at early times in run E.

We apply this approximate scaling to run A1, for which $M = 5000\mathrm{M}_\odot$ and the total integration time is $\sim 1.5 \times 10^7$ yr. Assuming no change in the stellar density, replacing the massive body by a ~ 10 $\mathrm{M}_\odot$ black hole increases the effective integration time by a factor ~ 500, to $\sim 7.5 \times 10^9$ yr (at which time the galactocentric radius is ~ 0.06 pc). This result illustrates how – in the absence of a steep central density cusp – the time for stellar-mass black holes to reach the center of the Galaxy from a starting radius of ~ 1 pc can easily exceed ~ 10Gyr (a point we return to in Section 5.6.1).

Alternatively, we can identify our models with the center of a galaxy like M87, a luminous elliptical galaxy with a flat central density profile. We adopt $M_\bullet = 3 \times 10^9$ $\mathrm{M}_\odot$ for the mass of the SMBH and we use the cumulative mass distribution given in Vesperini et al. (2003),

$$M(r) = (8.1 \times 10^{11} \mathrm{M}_\odot) \left[\frac{(r/5.1\mathrm{kpc})}{1 + r/5.1\mathrm{kpc}} \right]^{1.67} , \tag{5.33}$$

to obtain the length normalization factor. This was done by finding the radius at which the ratio of mass in stars to that of the SMBH is the same as in our models at 0.2 pc. With this choice, the N-body simulations can be approximately scaled via

$$t \to \tau \times t, \; r \to \chi \times r, \; M \to \mu \times M \; , \tag{5.34}$$

with $\tau = 30$, $\chi = 90$ and $\mu = 750$. Using these relations, run E corresponds to the inspiral of a $\sim 7 \times 10^6$ $\mathrm{M}_\odot$ black hole starting from a distance of 90 pc, and a total integration time $\sim 6 \times 10^8$yr. In the case of run F, the inspiraling black hole would have a mass $\sim 4 \times 10^7$ $\mathrm{M}_\odot$; it penetrates the inner ~ 2 pc in $\sim 1.5 \times 10^8$ yr after which it effectively stalls.

5.6.1 Segregation of massive remnants at the Galactic center

About 1% of the total mass of the old population at the GC should be in the form of stellar-mass ($m \approx 10 - 20 M_\odot$) black holes (Alexander 2005). Since stellar black holes are significantly more

[1] In its more general form (**??**), the dynamical friction formula predicts an additional, approximately logarithmic dependence of force on M.

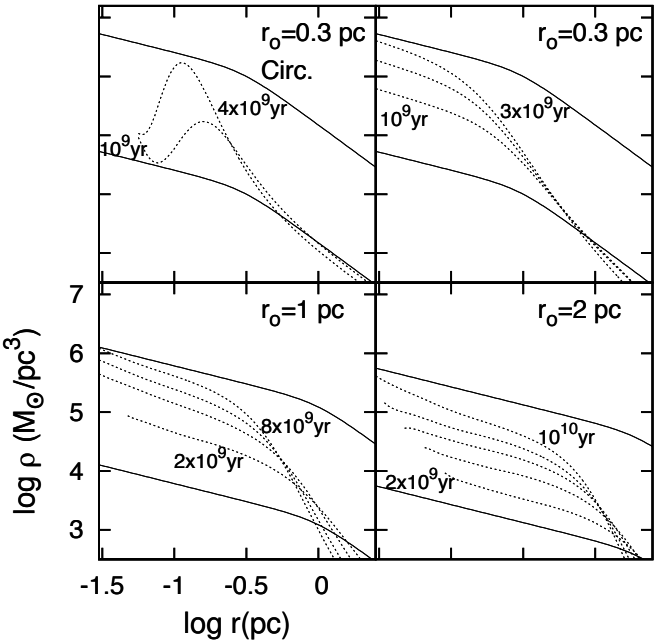

Figure 5.19 Evolution of the number density of a population of 10 $M_\odot$ black holes (dotted curves) assuming that their fraction is 10^{-2} of the total mass density initially. Results are displayed for three choices of the core parameter r_0 =(0.3, 1, 2) pc. Lower (upper) solid lines show the initial density profile of stellar black holes (stars). In the upper-left panel the black holes lie on circular orbits while in the other cases we assume an isotropic initial distribution of velocities. Density profiles are shown at time intervals of $\Delta t = 2\text{x}10^9$Gyr in the lower panels, while $\Delta t = 10^9$Gyr in the upper-right panel.

massive than the mean stellar mass ($\sim 1M_\odot$) expected for an evolved population, they would spiral in to the center and segregate around the SMBH (Morriss 1993). The time evolution of the remnant population depends sensitively on its initial distribution and also on the properties of the background distribution of lighter stars. In the case of a flat core in the stars, and a similar initial distribution in the black holes, the time for the latter to reach a steady state density profile can exceed a Hubble time, since the dynamical friction force essentially ceases inside the core (Merritt 2010). On the other hand, if the stars follow a steep central density cusp, the mass density of the stellar black holes after $\sim$ 10 Gyr can reach or exceed that of the other populations within $\sim 10^{-2}$ pc, leading to a quasi-steady-state density profile $n \simeq r^{-2}$ at small radii (e.g. Hopman & Alexander 2006; Alexander & Hopman 2009).

Understanding the distribution of stellar black holes at the centers of galaxies like the Milky Way is crucial for making predictions about the expected event rate for low-frequency graviational wave detectors (Hughes 2003). Since the stellar black holes at the GC are not directly detected, time-dependent inspiral calculations like the ones presented here provide the best hope of understanding

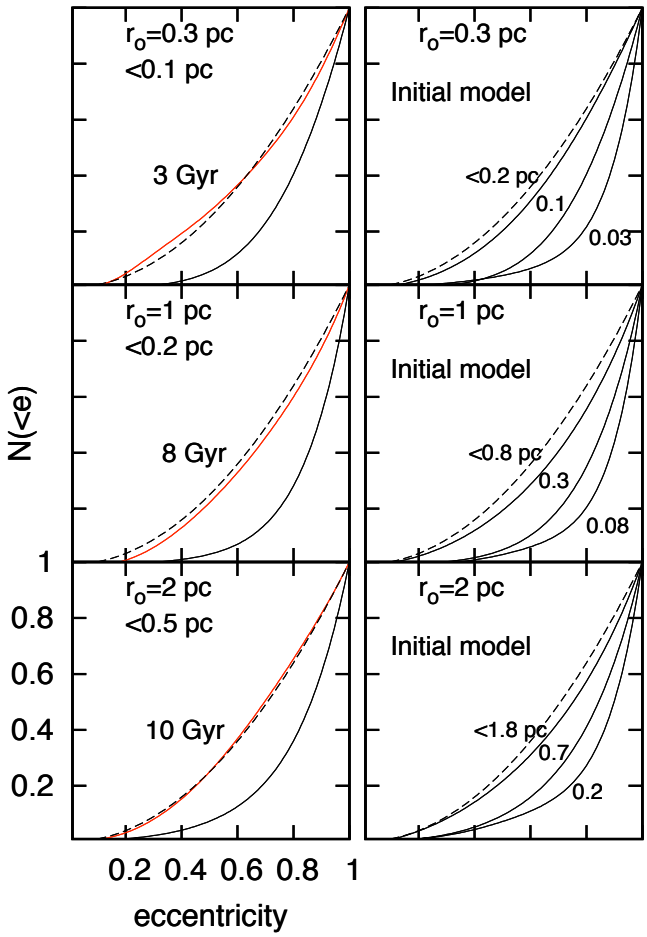

Figure 5.20 Left panels: final cumulative eccentricity distribution of stellar black holes for the integrations displayed in Figure 5.19 (red curves), that would be measured inside the core within some fiducial radius. Solid curves give the initial distributions.. Right panels: cumulative eccentricity distributions of the initial models (solid curves) evaluated within different radii. At small galactocentric radii, the distribution is dominated by high eccentricity orbits, in spite of the fact that the velocity distribution is isotropic. Dashed curves show for comparison a "thermal" eccentricity distribution, $N \sim e^2$.

their distribution. However, if the background stellar distribution is a flat core, our results show that a straightforward application of Chandrasekhar's formula can give misleading results.

Accordingly, we computed the evolution of a population of stellar black holes as they spiralled in to the center of a galaxy with a flat stellar core, including the frictional force from the fast-moving stars. We began by generating random samples of positions and velocities from the isotropic distribution function corresponding to the density model of equation (5.14) assuming $\gamma = 0.6$; cores of various sizes, $r_0 = (0.3, 1, 2)$ pc; and selecting only particles within 5 pc of the

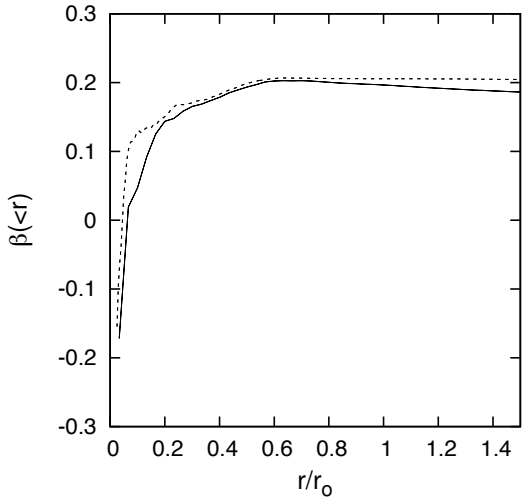

Figure 5.21 Anisotropy parameter β for all stellar black holes within a given radius for $r_0 = 0.3$pc (dotted line) after 3 Gyr, and for $r_0 = 2$pc (solid line) after 10 Gyr; these are the respective times when the mass density in black holes has reached the stellar density at small radii.

SMBH. In each of these models, a total of 800 orbits (representing the stellar BHs) were then integrated by solving the system of equations (5.20), with dynamical friction force given by

$$\boldsymbol{f}_{\mathbf{fr}} = -4\pi G^2 M \rho(r) \frac{\boldsymbol{v}}{v^3} F(< v, r) \ln\Lambda + \boldsymbol{f}^{(\boldsymbol{v}_\star > \boldsymbol{v})}, \tag{5.35}$$

with $\ln\Lambda = 15$, $M = 10$ M$_\odot$ and with $\boldsymbol{f}^{(\boldsymbol{v}_\star > \boldsymbol{v})}$ given by equation (5.30). At each time, the density profile and eccentricity distribution of the inspiralling objects were computed by sampling each orbit over time intervals of 0.3 Gyr. We also considered one model with core parameter $r_0 = 0.3$ pc in which all black holes were initially on circular orbits.

All of the calculations presented in this section assume that the mass density due to the stellar black holes remains small compared with the mass density in stars, and that the stellar distribution is unchanging. Because the two-body relaxation time for 1 M$_\odot$ stars is so long in these models, and ~ 10 times longer than the black hole inspiral time, ignoring the evolution of the stellar distribution due to star-star encounters is reasonable. However, once the density in stellar black holes begins to approach that in the stars, our calculations are no longer valid.

In Figure 5.19 we plot the density profile of stellar black holes at different times, assuming that their fraction is initially 10^{-2} of the total mass density. The upper panels give the results for the model with $r_0 = 0.3$ pc. In these integrations the core is very small and after only ~ 1 Gyr the density of black hole rises very steeply going into the stellar core. After ~ 4 Gyr the black holes accumulate at radii near the core, matching the density in stars at ~ 0.01 pc. In the circular-orbit model, the density profile at 1 Gyr shows a maximum at ~ 0.2 pc, that grows and migrate inward due to the friction produced by fast moving stars inside these radii. The evolution for the isotropic

run is comparably rapid, and after ~ 3 Gyr the density of black holes reaches that in stars at ~ 0.01 pc.

Merritt (2010) showed that a core of the size currently observed is a natural consequence of two-body relaxation acting over 10 Gyr, starting from a core of radius ~ 1 pc. It is therefore of interest to study the evolution of the black hole distribution in models with parsec-scale cores. This is shown in the lower panels of Figure 5.19. In these cases the evolution is slower as a consequence of the increased size of the stellar core, and even after 10 Gyr the density of black holes can remain substantially lower than that in stars at all radii. We conclude that it would be unjustified to assume that the massive remnants have yet reached a steady-state density profile at the GC. As discussed in Merritt (2010), one consequence is that rates of capture of stellar black holes by the SMBH at the GC may be much lower than in standard models that postulate a collisionally-relaxed nucleus.

The left panels of Figure 5.20 plot the cumulative distribution of eccentricities of the stellar black holes inside various radii. Since the final eccentricity of each orbit is larger than its initial value (see Section 2.2), one might naively expect the eccentricity distributions to evolve toward a form that is increasingly strongly peaked near $e \approx 1$. This would be the case if one plotted $N(e)$ for a *fixed* subset of objects. However, when restricting the sample to a given *radial* range, the result is very different. The reason (e.g. Merritt 2010, Appendix) is illustrated in the right-hand panels of Figure 5.20: given a flat density profile, even an isotropic distribution of objects around a SMBH will have an eccentricity distribution that is strongly peaked near $e = 1$, since the only objects that can approach closely to to the SMBH are on highly eccentric orbits. As the distribution of stellar black holes evolves away from this initial configuration, the regions of low-energy phase space that were initially empty are gradually refilled, and the eccentricity distribution begins to approach more closely to a "thermal" form, $N(< e) \propto e^2$. In addition, (i) the eccentricity of individual orbits inside the core grows only very slowly since they are in a region where the dynamical friction force is small (see Figure 5.3); (ii) the orbital eccentricity of black holes initially beyond the core decreases initially since they lie in a $\gamma \approx 1.8$ cusp; their eccentricities subsequently increase as the orbital periapsis enters the core, but in most cases this second phase is too short (see Figure 5.4) to produce final eccentricities significantly different from the initial values.

Figure 5.21 plots the anisotropy parameter (5.32) computed for all black holes within a certain radius as a function of galactocentric distance, for $r_0 = 0.3$pc and 2pc, at the final integration time, defined as the time when the mass density in black holes reaches that in stars at small radii. The plot confirms that the departures from isotropy remain small at all radii.

5.6.2 Dynamical Friction in the Context of the EMRI Problem.

Extreme-mass-ratio inspirals (EMRIs) are a potential source of low-frequency space-based gravitational wave interferometers (Hughes 2003; Barack & Cutler 2004; Amaro-Seoane et al. 2007). In steady-state models of the Galactic center, the distributed mass within 10^{-2} pc of the SMBH is

dominated by stellar black holes. At these radii, dynamical friction is therefore typically ignored and it is assumed that captures for EMRIs are driven by gravitational scattering from other stellar black holes (e.g., Merritt et al. 2011). On the other hand, if the background stellar distribution has a flat core, the density of black holes can remain small, compared with the mass density of other populations (e.g., §6.1, Gualandris & Merritt 2011). Under these circumstances, at any radius, massive remnants would see a background of lighter stars and dynamical friction becomes a competing mechanism in driving capture of EMRIs as we now show.

A way to follow the orbital inspiral of a massive body at the GC, due to both dynamical friction and gravitational radiation, is to couple the Chandrasekhar's expression (18) for the frictional drag with the 2.5 post-Newtonian equations of motion representing the non conservative contribution of GW energy loss. Close to the SMBH ($r << r_{\rm bh}$) and in the limit $M/M_\bullet << 1$, the total acceleration can be approximated by:

$$\boldsymbol{f} = -\frac{4\pi G^2 M \rho(r) F(<v,r) \ln\Lambda}{v^3}\boldsymbol{v} - \frac{GM_\bullet}{r^2}\left[(1+A)\,\boldsymbol{n} + B\boldsymbol{v}\right] \ , \tag{5.36}$$

where $\boldsymbol{n} = \boldsymbol{r}/r$ and

$$A = \frac{1}{c^5}\left[-\frac{24 v_r M v^2 G}{5\ r} - \frac{136 v_r M G^2 M_\bullet}{15\ r^2}\right] \ ; \ \ B = \frac{1}{c^5}\left[\frac{8 M v^2 G}{5\ r} + \frac{24 M G^2 M_\bullet}{5\ r^2}\right] \ , \tag{5.37}$$

with v_r the radial component of the velocity vector. Evidently, both the frictional force and the 2.5 post-Newtonian correction are dissipative terms, but, while the latter term always drives to lower eccentricities, the effect of dynamical friction on the orbital eccentricity has a strong dependence on the phase-space distribution associated with the stellar background (see § 5.3.2). For the sake of simplicity, in equation (5.36), the contribution of the non-dominant terms to the frictional force was neglected. With this choice, the orbit of the massive body can be accurately studied only in models with steep or moderately flat density profiles ($\gamma \gtrsim 1$) in which the friction contributed by fast stars is small (see Figure 5.11). Notice also that, in equation (5.36), both the frictional term and the Post-Newtonian terms depend linearly on M implying that the time evolution of the orbital elements can be trivially rescaled to any M as long as the condition $M/M_\bullet << 1$ holds.

Using equation (5.36) we computed the trajectory of the test mass under a variety of assumptions for the background system. Results of these integrations are displayed in Figure 5.22. We considered orbits of different initial eccentricities ($e = 0.3, 0.5, 0.75$), starting from a semi-major axis $a_0 \approx 0.2$ pc. Our main goal is to explore the conditions under which the frictional force brings the massive body to a galactocentric distance at which the merger time with the central black hole becomes much shorter than a Hubble time. For an eccentric orbit in a flattened cusp, dynamical friction at apoapsis dominates the evolution causing a rapid increase of the orbital eccentricity. In the simplified picture in which the frictional force at periapsis is vanishing small, the apoapsis distance remains unchanged in time, while the periapsis shifts toward the center; at some point, the minimum distance from the SMBH is short enough that the 2.5 post-Newtonian terms start to

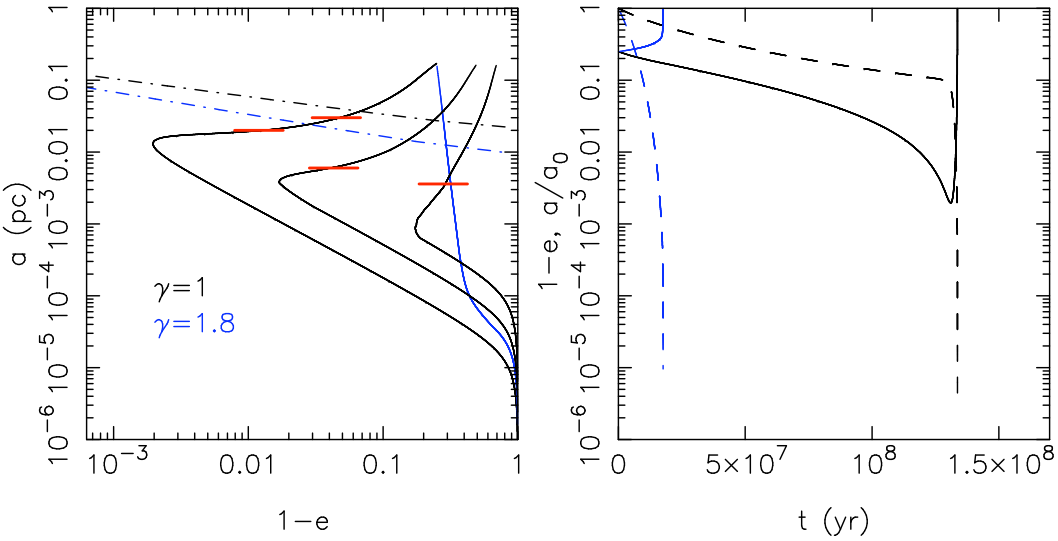

Figure 5.22 Evolutionary tracks of a massive object in the Galactic center starting from various eccentricities (e=0.3, 0.5, 0.7), from an initial semi-major axis $a \approx 0.2$ pc and adopting two different inner slopes of the mass-density profile ($\gamma = 1, 1.8$). The right panel displays the time evolution of eccentricity and semi-major axis for a 10^3 $M_\odot$ secondary black hole. Dot-dashed lines in the left panel give the Schwarzschild barrier, Equation (5.40), beyond which resonant relaxation is suppressed by strong relativistic precession and gravitational scattering is dominated by classical non-resonant relaxation. Red marks give the radii at which the two-body relaxation time scale for changes in angular momentum ($t_{\rm r}$) equals that computed in our integrations in the dynamical friction dominated phase, assuming 10 $M_\odot$ for the mass of the inspiraling black hole (or 17 $M_\odot$ for the lower mark of the left most curve). Below these lines, for $M \leq 10$ $M_\odot$, our integrations are not longer valid since two-body scattering, rather than dynamical friction, would dominate the evolution. For larger masses ($\gtrsim 20$ $M_\odot$), however, we found that at any radius the time for dynamical friction to change L is always shorter then $t_{\rm r}$.

dominate the evolution. The drag at periapsis circularizes the orbit, and causes the merger of the two black holes.

Dynamical friction can be very inefficient if the mass of the inspiraling object becomes comparable of that in stars. In the $\gamma = 1$ cusp for a $\sim 1000(10)$ $M_\odot$, this happens at $\sim 0.02(0.002)$ pc, suggesting that particular caution should be taken in interpreting these results for large inspiraling black hole masses and for initially small eccentricities. For this reason in what follows we discuss these results only for the case of small masses of the test particle for which the perturbations on the background system can be reasonably ignored.

Near a SMBH, as long as the relativistic precession time scale is much longer than the orbital period, the mechanism that dominates the scattering of stars onto high-eccentrcity orbits is resonant

relaxation. Because in the potential of a point-mass the orbits are fixed ellipses, perturbations on a test particle are not random but correlated (Rauch & Tremaine 1996). The residual torque $|\mathbf{T}| \approx \sqrt{N}Gm/r$, exerted by the N randomly oriented, orbit-averaged mass distributions of the surrounding stars, induces coherent changes in angular momentum $\Delta\mathbf{L} = \mathbf{T}t$ on times $t \lesssim t_{coh}$. Where the coherent time t_{coh} is fixed by the mechanism that most rapidly causes the orbits to precess (e.g, mass precession, relativistic precession). The angular momentum relaxation time associated with resonant relaxation is:

$$t_{rr} = \left(\frac{L_c}{\Delta L_{coh}}\right)^2 t_{coh} \ , \tag{5.38}$$

where $L_c \equiv \sqrt{GM_\bullet a}$ is the angular momentum of a orbit with radius $r \approx a$ and $|\Delta L_{coh}| \sim |\mathbf{T}t_{coh}|$ is the accumulated change over the coherence time. Assuming that the precession is determined by the mean field of stars, the angular momentum relaxation time becomes:

$$t_{rr} \approx 2.9 \times 10^7 \mathrm{yr} \left(\frac{M_\bullet}{4 \times 10^6 \mathrm{M}_\odot}\right)^{1/2} \left(\frac{a}{0.01\mathrm{pc}}\right)^{3/2} \left(\frac{m}{\mathrm{M}_\odot}\right)^{-1} \ . \tag{5.39}$$

Dash-dotted lines in the upper-left panel of Figure 5.22 gives the Schwarzschild barrier (SB). Above these lines, resonant-relaxation is the most rapid mechanism to change the orbital angular momentum; below the curves, relativistic precession becomes efficient in suppressing resonant relaxation and the gravitational perturbations are dominated by classical "two-body" relaxation. The value of the angular momentum that defines the Schwarzschild barrier is (Merritt et al. 2011):

$$(1-e^2)_{\mathrm{SB}} \approx 5.9 \times 10^2 \left(\frac{C_{\mathrm{SB}}}{0.7}\right)^2 \left(\frac{a}{\mathrm{mpc}}\right)^{-2} \left(\frac{M_\bullet}{4 \times 10^6 \mathrm{M}_\odot}\right)^{-4} \left(\frac{m}{\mathrm{M}_\odot}\right)^{-2} \left(\frac{N}{10}\right)^{-1} \ , \tag{5.40}$$

where N is the number of stars within radius a and C_{SB} is a constant of order of unity. Passed the barrier, the time for encounters to change the orbital angular momentum L by of order itself is $2(1-e)t_{\mathrm{r}}$, where for the non-resonant relaxation time scale we adopt the approximate expression:

$$t_{\mathrm{r}} = 4.8 \times 10^8 \mathrm{yr} \left(\frac{a}{\mathrm{mpc}}\right)^{3/2} \left(\frac{M_\bullet}{4 \times 10^6 \mathrm{M}_\odot}\right)^{3/2} \left(\frac{m}{\mathrm{M}_\odot}\right)^{-2} \left(\frac{N}{10}\right)^{-1} \ . \tag{5.41}$$

Horizontal red marks in the upper-left panel of Figure 5.22 give the semi-major axes at which t_{r} equals the time scale over which L changes in our integrations (t_{evol}) assuming either 10 $M_\odot$ or 17 $M_\odot$ (lower mark in the left most curve) for the mass of the inspiraling black hole. Below these lines, two-body relaxation cannot be neglected. In the case of a 17 $M_\odot$ black hole, t_{evol} was always shorter than t_{r} for initial eccentricities smaller than ~ 0.7. We conclude that two-body scattering effects from field stars could be ignored for relatively small masses of the sinking black hole.

Within the Schwarzschild barrier, gravitational scattering on the inspiraling black hole can be dominated by other stellar black holes if their density is comparable of that in stars at small radii. In an unsegregated model the number of stellar black holes (of mass 10 $M_\odot$) is predicted to be 10^{-3} times that in stars. From equations (5.40) and (5.41) it follows that in this case the scattering from black holes can be ignored with respect to the perturbations from the stellar population.

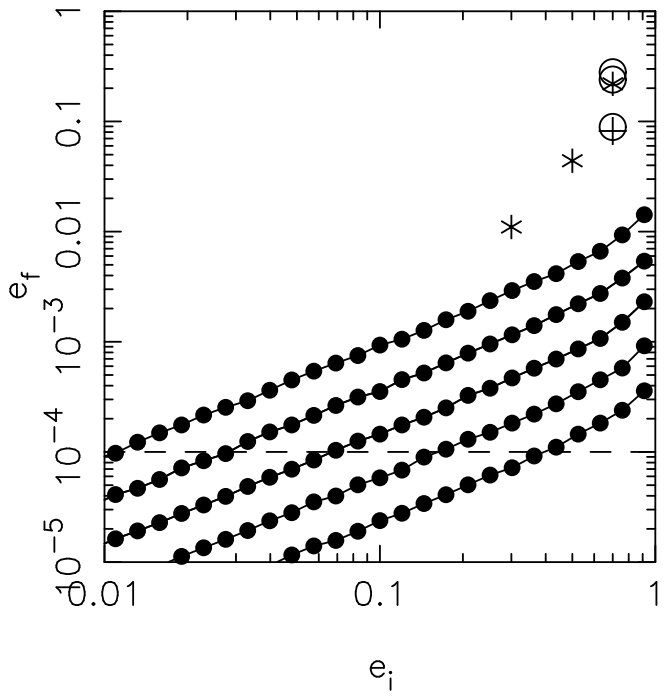

Figure 5.23 Eccentricity at the moment the binary enters the sensitivity window of planned space-based interferometers (e_f) as a function of the initial orbital eccentricity (e_i) for the integrations displayed in Figure 5.22. Stars symbols are for $\gamma = 1$ (continue black curves in Figure 5.22), plus symbol for $\gamma = 1.8$ (continue blue curve in Figure 5.22), and empty circles for the orbits shown in the lower panel of Figure 5.22. In all these cases e_f results significantly different from zero. The continue black lines with filled circles give e_f for a set of integrations with no dynamical friction term. For a given initial eccentricity and secondary black hole mass we fixed the merger time by using equation (5.43). If we assume a 10 $M_\odot$ (1000 $M_\odot$) this corresponds to mergers time of $10^{14},\ 10^{13}, ...10^{10}$ yr ($10^{12},\ 10^{11}, ...10^{8}$ yr) from the bottom to the top line respectively. Horizontal-dashed line represents approximately the lowest value of e_f that would require non circular templates for data analysis ($e \sim 10^{-4}$, Porter & Sesana 2010).

Gravitational scattering from black holes start to compete with that from stars when their number at small radii (~ 1 mpc) is $10^{-2} \times N$, similar to the found at later times in Figure 5.19 for $r_0 \sim 2$pc. In relaxed mass-segregated models, instead, the number of black holes would be approximately N, and they will dominate the orbital evolution of the test mass at any radius inside the Schwarzschild barrier.

Detectability

In order for an extra-galactic source to be observable by proposed space-based interferometers, it must have an orbital frequency $\gtrsim 10^{-4}$Hz, or

$$a \lesssim 1.3 \times 10^{-2}\mathrm{mpc}\left(\frac{M_\bullet}{4\times 10^6 \mathrm{M}_\odot}\right)^{1/3} . \tag{5.42}$$

We explored whether the computed orbits would retain some degree of eccentricity by the time the black hole binary enters the instrumental sensitivity window, by evaluating the eccentricity, e_f, at the time at which the condition (5.42) is satisfied and we compare this value with the minimum eccentricity that would require non-circular templates for data analysis ($e \sim 10^{-4}$, Porter & Sesana 2010). Figure 5.23 plots e_f as a function of the initial eccentricity for the orbits displayed in Figure 5.22. In addition, we computed a set of orbits with different initial eccentricities by removing from equation (5.36) the dynamical friction term. Each curve corresponds to a fixed value for the coalescence time scale that was computed by (Peters 1964):

$$t_m \simeq 3.6\times 10^{12}\mathrm{yr}\left(\frac{10M_\odot}{M}\right)\left(\frac{4\times 10^6 M_\odot}{M_\bullet}\right)^2\left(\frac{a}{\mathrm{mpc}}\right)^4 (1-e^2)^{7/2} . \tag{5.43}$$

Taking $M = 10\ M_\odot$ ($1000\ M_\odot$) this corresponds to $t_m = 10^{14},\ 10^{13}, ...10^{10}$ yr ($10^{12},\ 10^{11}, ...10^{8}$ yr) from the bottom to the top line respectively. It is evident that even for relatively low initial eccentricities and large merger times the binary will have a value of e_f significantly different from zero. This study, while very preliminary, suggests that secondary black holes typically reach the GW radiation regime on wide orbits that are very eccentric. In conclusion, orbital templates with non-vanishing eccentricity should be mandatory for low-frequency GW data analysis.

In future work, one could follow the secondary black hole orbit until coalescence with the SMBH, using post-Newtonian N-body simulations. This will help to understand at which extends the conclusions made here can be applied.

5.7 Conclusions

In this article we explored the orbital evolution of massive objects in shallow density profiles around supermassive black holes. Results from the numerical simulations presented in this chapter are summarized below.

1 The evolution of the orbit of a black hole that spirals in toward the center of a galaxy containing a second SMBH is very sensitive to the detail of the mass distribution of background stars. In models with a low density core the dynamical friction time-scale becomes much longer than in models with a steep cusp, because the phase space densities fall to zero at very low (bounding) energies. The standard Chandrasekhar's formula predicts that, in the presence of a core, the inspiraling black hole will stall at a radius that is roughly the core radius.

2 In low density cusps ($\gamma \sim 0.5$), the eccentricity of a massive body increases because the frictional force is most peaked at apoapsis. In our models, the eccentricity increases very rapidly when the orbital periapsis falls inside the core radius. If the black hole is initially at $r_{\rm bh}$ with $e_{\rm in} \sim 0.7$, its orbital eccentricity, by the time the orbit lies entirely inside the core, is very large ($\gtrsim 0.9$).

3 Using N-body simulations, we found that the frictional force never falls precisely to zero because stars moving faster than the test body contribute to the drag inside the core. When this contribution is included in the expression for the dynamical friction and the changes induced by the massive body on the stellar distribution are taken into account, Chandrasekhar's theory reproduces the decay observed in the N-body simulations. We conclude that, if the background stellar distribution is a flat core, a straightforward application of the standard Chandrasekhar's formula will give misleading results.

4 During the inspiral, for large masses, the black hole enhances the diffusion of stars into the phase-space region that was initially nearly empty and, consequently, the core fills-up. A low density core is rapidly regenerated after the black hole stalls as it displaces stars from the center.

5 We derived an estimate of the Coulomb logarithm without any particular assumptions about the velocity distribution of field stars (e.g., that it follows a Maxwellian distribution), and in the region outside the core, where the standard Chandrasekhar's formula (5.18) reproduces the black hole orbit. We obtained $\ln\Lambda \approx 6.5$, consistent with previous works.

6 We studied the location and evolution of the gravitational wake that the second black hole rises behind it during the inspiral in the N-body simulations. Outside the core, the peak in the overdensity lies close to the massive body at $-20 < \theta \lesssim 0°$, independent of M, and the amplitude of the overdensity increases with black hole mass. After the massive body enters the core, the density maximum is seen to lie at large angular separations from the black hole. This is consistent with the fact that the frictional drag is greatly reduced inside the shallow cusp.

7 In the absence of a steep central density cusp the time for stellar-mass black holes to reach the center of the Galaxy from a starting radius of order ~ 1 pc can easily exceed ~ 10Gyr. We computed the evolution of a population of stellar black holes as they segregate to the Galactic center, including the frictional force from the fast-moving stars. We found that, in models with parsec-scale cores, even after 10 Gyr, the density of black holes can remain substantially lower than that in stars at all radii. We conclude that it would be unjustifieded to assume that the massive remnants have yet reached a steady-state density profile at the Galactic center. As the distribution of stellar black holes evolves away from their initial configuration, the regions

of phase space that were initially nearly empty are gradually refilled, and the eccentricity distribution of the black holes begins to approach a thermal form ($N(< e) \propto e^2$).

8 Secondary black holes reach the gravitational radiation dominated regime on orbits that are typically very eccentric. However, we found that even initially moderate eccentricities would result on non-neglegible eccentricities at the moment the binary black hole enters the sensitivity window of planned space-based interferometers. This in turn would require non-cicular templates for gravitational wave data analysis.

Chapter 6

Summary and Conclusions

In the work presented in this thesis we have investigated the consequences and possible solutions of two of the most puzzling discoveries of the last decade in Galactic astronomy: the presence of young stars close to Sgr A* and the flat distribution of late-type stars near the Galactic center. The main results of this study are summarized below.

In Chapter 2 we used a post-Newtonian N-body code to study the dynamics of main-sequence binaries on highly elliptical bound orbits whose periapses lie close to the SMBH, determining the properties of ejected and bound stars as well as collision products. Unlike previous studies, we followed binaries that remain bound for several revolutions around the SMBH, finding that, in the case of relatively large periapses and highly inclined binaries, the Kozai resonance can lead to large periodic oscillations in the internal binary eccentricity and inclination. Collisions and mergers of the binary elements were found to increase significantly for multiple orbits around the SMBH, while hypervelocity stars are primarily produced during a binary's first passage. We concluded that this process can lead to stellar coalescence and eventually serve as an important source of young stars at the Galactic center. Stellar collisions may play a fundamental role in determining the present mass function near the SMBH.

N-body simulations cannot accurately predict the properties of collision/merger products. For this reason, in Chapter 3, we replaced the point-mass stars by fluid realizations, and used a smoothed-particle hydrodynamics code to follow the close interactions. This allows to study the internal structure of the merger products including their masses and angular momentum distribution. We model the binary components as main-sequence stars with initial masses of 1, 3 and 6 Solar masses, and with chemical composition profiles taken from stellar evolution codes. Outcomes of the close interactions included mergers, collisions that leave both stars intact, and ejection of one star at high velocity accompanied by capture of the other star into a tight orbit around the SMBH. For the first time, we followed the evolution of the collision products for many ($\gtrsim 100$) orbits around the SMBH. Stars that are initially too small to be tidally disrupted by the SMBH can be puffed up

by close encounters or collisions, with the result that tidal stripping occurs in subsequent periapse passages. In these cases, mass loss occurs episodically, sometimes for hundreds of orbits before the star is completely disrupted. Repeated tidal flares, of either increasing or decreasing intensity, are a predicted consequence. In collisions involving a low-mass and a high-mass star, the merger product acquires a high core hydrogen abundance from the smaller star, effectively resetting the nuclear evolution "clock" to a younger age. Elements like Li, Be and B that can exist only in the outermost envelope of a star are severely depleted due to envelope ejection during collisions and due to tidal forces from the SMBH. Tidal spin-up can occur due to either a collision or tidal torque by the SMBH at periapsis. However, in the absence of collisions, tidal spin-up of stars is only important in a narrow range of periapse distances, $r_{\rm t}/2 \lesssim r_{\rm per} \lesssim r_{\rm t}$ with $r_{\rm t}$ the tidal disruption radius. We finally discussed the implications of these results for the formation of the S-stars and the hypervelocity stars.

In the second part of this work we studied the formation history and properties of the Milky Way nucleus. The distribution of stars near the supermassive black hole at the Galactic center is observed to be very different than predicted by theoretical models: instead of a Bahcall-Wolf cusp, there is a parsec-scale core. In Chapter 3 and 4 we focussed on possible models for the formation and persistence of such a low-density core, and its implications for the distribution of massive remnants. A core results naturally from a model in which the nuclear star cluster is formed via repeated inspiral of globular clusters into the Galactic center. We presented results from a set of N-body simulations of this process, which show that other properties of the nuclear star cluster, including its mass and outer density profile, are also naturally reproduced.

Chandrasekhar's dynamical friction formula predicts that the frictional force effectively vanishes for a massive body inspiraling into a flat core around a SMBH. This prediction has been tested in Chapter 4 using large-scale N-body simulations; one finds that the rate of orbital decay never drops precisely to zero, because stars moving faster than the test body contribute to the frictional force inside the core. When this contribution is included in the expression for the dynamical friction and the changes induced by the massive body on the stellar distribution are taken into account, Chandrasekhar's theory reproduces the rate of orbital decay remarkably well. However, this rate is still substantially smaller than the rate predicted by a naive application of Chandrasekhar's formula. To investigate the implications of this slower decay rate for the Galactic center, we evolved a population of stellar black holes in models with a stellar core. After 10 Gyr the density of stellar black holes can remain substantially less than that in stars, contrary to models that assume a density cusp in the stars. One consequence is that rates of capture of stellar BHs by the SMBH at the Galactic center (EMRIs) may be much lower than in standard models.

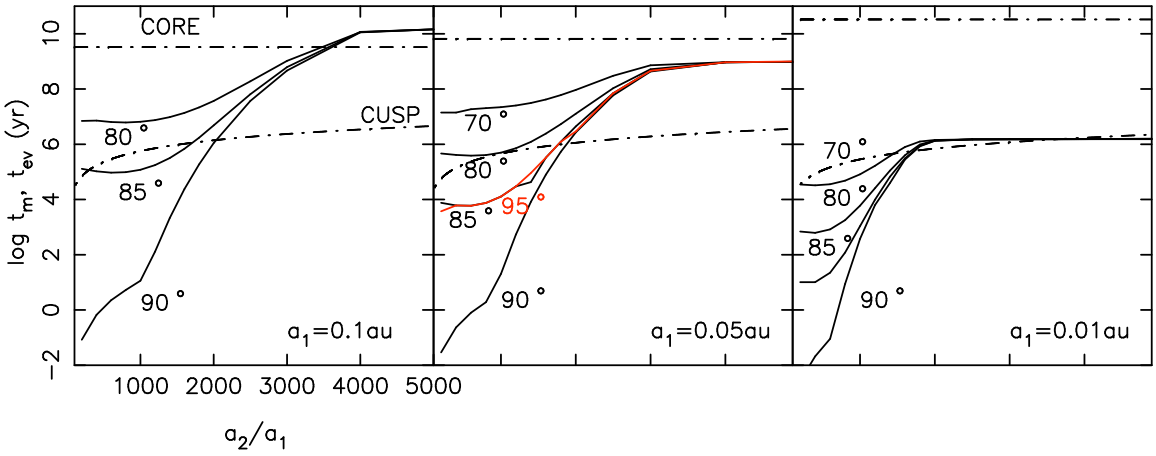

Figure 6.1 Merger time ($t_{\rm m}$) and evaporation time for stellar black hole binaries at the GC ($t_{\rm m}$)). These systems merge in a time typically much shorter than a Hubble time and shorter than the timescale over which the binaries would evaporate due to close encounters with field stars.

6.1 Future work

As a natural continuation of the work presented in Chapter 2 we will further study the effect of the Kozai resonance on the evolution of binary systems near a SMBH. These systems could include binary stars with a realistic and comprehensive spectrum of orbital parameters, but also compact binaries of massive remnants such as stellar black holes and neutron stars. The close environment of massive black holes (MBHs) may in fact contain a large number of stellar compact objects. Some of these compact objects are likely to be members of binaries. The dynamical evolution of such binaries, can be affected by the perturbation from the SMBH. During pericenter approach, at the highest eccentricities during the Kozai-cycles, gravitational wave emission from the binaries become highly efficient, and the binaries are expected to inspiral and coalesce on timescales much shorter than a Hubble time (and much shorter than similar binaries which do not reside near a SMBH). We therefore could explore the close environment of SMBHs as catalysts for the inspiral and merger of compact binaries, these in turn could be detected as GW sources by the next generation of GW detecors (e.g. advanced-LIGO). As an example, Figure 6.1 gives the timescale for merger and evaporation for stellar black hole binaries with components of mass 10 $M_\odot$ orbiting a SMBH of $4 \times 10^6\, M_\odot$ and assuming either a stellar cusp or a core in the density distribution of stars.

In the contest of the SPH simulations presented in Chapter 3, one could model the material that stripped away from the stars remains bound to the central black hole more carefully and indentify possible signatures of the interaction between the bound star and the accretion torus left behind during previous periapsis passages. Periodic X-ray emission may be arise every time the star is at periapsis and hits the accretion torus.

In this contest we also notice that SPH calculations neglect radiative and heat transport,

and therefore can follow the system only over hydrodynamics timescales that are typically in the order of few hours. For these reasons, in Chapter 3, we were able to discuss the relaxed structure of merger products loosely and the relaxation time only in magnitude. Stellar evolution calculations can instead provide the evolution of merger products and determine their track in a color magnitude diagram. The timescales for evolution codes range from thermal to nuclear timescales. By studying the collision products of Antonini et al. (2010b), it would be possible to say more than we did about the relation between the SPH stars, and their expected structure after the collision/merger, when thermal equilibrium has been established again. Based on the technique outlined in Sills et al. (1997) we would be able to evolve the collision products of Antonini et al. (2010b) to the main sequence and beyond to the giant branch, which will help to compare our models to the observed properties of GC stars.

As a possible continuation of the work presented in Chapter 3 it would be of great interest to perform a new set of simulations to better explore the role of the central black hole in determining the properties of the final NSC. This will help to extend our conclusions to external galaxies giving important insights on the origin of their compact stellar nuclei. The goal is to consider at least four different masses for the SMBH, spanning the range between 10^7 10^{10} $M_\odot$, and including a spectrum of masses in the clusters. This in turn would allow us to derive the distribution of stars and stellar remnants in the final NSC and the expected EMRI rate in galactic nuclei.

Another outstanding question is how the presence of a low density core around the SMBH affects the inspiral of massive objects at the Galactic center. As shown in Chapter 4, Chandrasekhar's dynamical friction theory predicts that a secondary black hole that spirals into a low-density core will stall at a radius that is roughly the core radius. A self-consistent study of this scenario would require to follow the inspiral of secondary black hole orbits until they eventually coalesce with the SMBH, using post-Newtonian N-body simulations. This will help to understand whether the orbit can retain some degree of eccentricity by the time relativistic effects become predominant and gravitational radiation enters the instrumental sensitivity window. Finally, N-body results will show how secondary inspirals modify the ambient stellar distribution around SMBHs, including the stellar density distribution and the degree of velocity anisotropy in galactic nuclei.

Bibliography

Agarwal & Milosavljevic, Agarwal 2011, ApJ, 729, 35

Aarseth, S. J. 1999, PASP, 111, 1333

Alexander, T. 2005, Phys. Rep., 419, 65

Alexander, T., & Hopman, C. 2009, ApJ, 697, 1861

Alexander, T., & Kumar, P., 2001, ApJ, 549, 948

Alexander, T., & Morris, M. 2003, ApJ, 590, L28

Amaro-Seoane, P., Gair, J. R., Freitag, M. , Miller M. C., Mandel, I, Cutler, C. J., & Babak, S. 2007 Classical and Quantum Gravity 24, 113

Andersen, D. R. et al. 2008, ApJ, 688, 990

Antonini, F., Capuzzo-Dolcetta, R., & Merritt, D., 2009, MNRAS, 399, 671

Antonini, F., Faber, J., Gualandris, A., & Merritt, D. 2010a, ApJ, 713, 90

Antonini, F., Lombardi, J., & Merritt, D. 2011 ApJ, 731, 128

Athanassoula, E., Fady, E., Lambert, J. C., & Bosma, A. 2000, MNRAS, 314, 475

Baganoff, F. K., et al. 2001, Nature, 413, 45

Baganoff, F. K., et al. 2003, AJ, 591, 891

Bahcall, J. N., & Wolf, R. A. 1976, ApJ, 209, 214

Bahcall, J. N., & Wolf, R. A. 1977, ApJ, 216, 883

Balcells, M., Graham, A. W., & Peletier, R. F. 2007, ApJ, 665, 1104

Balick, B., Brown, R. L., 1974 ApJ 194, 265270

Barack, L., & Cutler, C. Phys. Rev. D 69, 082005 2004, arXiv:gr-qc/0310125.

Bartko et al. 2010, ApJ, 708, 834

Baumgardt, H., Gualandris, A., & Portegies Zwart, S. 2006, MNRAS, 372, 174

Becklin, E. E., and Neugebauer, G 1968, AJ, 151, 145

Bekki, K. 2007, PASA, 24, 77B

Bekki, K. & Graham, A. W. 2010, ApJ, 714, 313

Benz, W., & Hills, J. G. 1987, ApJ, 323, 614

Benz, W., & Hills, J. G. 1992, ApJ, 389, 546

Berentzen, I., Preto, M., Berczik, P., Merritt, D., & Spurzem, R. 2009, ApJ, 695, 455

Binney, J. J., & Evans, N. W. 2001, MNRAS, 327, L27

Binney, J. & Tremaine, S. 1987, Galactic Dynamics (Princeton, NJ:Princeton University Press)

Blaauw, A., 1961, BAN, 15, 265

Blaes, O., Lee, M. H., & Socrates, A. 2002, ApJ, 578, 775

Bogdanović, T., Eracleous, M., Mahadevan, S., Sigurdsson, S., & Laguna, P. 2004, ApJ, 610, 707

Böker, T., Stanek, R., & van der Marel, R. P. 2003, AJ, 125, 1073

Borriello, A., & Salucci, P. 2001, MNRAS, 323, 285

Bromley, B. C., Kenyon, S. J., Geller, M. J., Barcikowski, E., Brown, W. R., & Kurtz, M. J. 2006, ApJ, 653, 1194

Brown, W. R., Geller, M. J., Kenyon, S. J., & Kurtz, M. J. 2005, ApJ, 622, L33

Brown, W. R., Geller, M. J., Kenyon, S. J., & Kurtz, M. J. 2006, ApJ, 647, 303

Brown, W. R., Geller, M. J., Kenyon, S. J., Kurtz, M. J., & Bromley, B. C. 2007, ApJ, 671, 1708

Brown, W. R., Geller, M. J., & Kenyon, S. J. 2009, ApJ, 690, 1639

Brown, W. R., Anderson, J., Gnedin, O. Y.; Bond, H. E., Geller, M. J., Kenyon, S. J., & Livio, M. 2010, ApJ, 719, L23

Buchholz, R. M., Schödel, R., & Eckart, A. 2009, A&A, 499, 483

Capuzzo-Dolcetta, R., Pesce, E., Vietri, M., 1991, ASP Conference Series, 13, 370

Capuzzo-Dolcetta, R. 1993, ApJ, 415, 616

Capuzzo-Dolcetta, R., 1993, ApJ, 415, 616

Capuzzo-Dolcetta, R., Vicari, 2005, MNRAS, 356, 899

Capuzzo-Dolcetta R., & Miocchi, P. 2008, MNRAS, 388, L69

Capuzzo-Dolcetta, R., Miocchi, P., 2008b,ApJ, 681, 1136

Capuzzo-Dolcetta, R., Mastrobuono-Battisti, A., Maschietti, D., 2010, NewAstron, 16, 284

Carollo, C. M., Stiavelli, M., de Zeeuw, P. T., & Mack, J. 1997, AJ, 114, 2366

Casertano, S., Hut, P., 1985, ApJ, 298, 80

Casertano, S., Phinney, E. S., & Villumsen, J. V., 1987, IAU Symp. 127, Structure and Dynamics of Elliptical Galaxies, ed. T. de Zeeuw (Dordrecht: Reidel), 475

Chandrasekhar, S. 1943, ApJ, 97, 255

Charlton, & Laguna 1995, ApJ, 444, 193

Cora, S. A., Muzzio, J. C., & Vergne, M. M., 1997, MNRAS, 289, 253

Cement, M. J., 1994, ApJ, 420, 797

Collier, A. C., & Jenkins, C. R. 1984, MNRAS, 211, 391

Côté et al. 2006 ApJS, 165, 57

Dai, L. J., Fuerst, S. V., & Blandford, R. 2010, MNRAS, 402, 1614

Dale, J. E., Davies, M. B., Church, R. P., & Freitag, M. 2009, MNRAS, 393, 1016

de Blok, W. J. G., & Bosma A. 2002, A&A, 385, 816

de Blok, W. J. G., Bosma, A., & McGaugh, S. 2003, MNRAS, 340, 657

Danby, J. J. A., & Camm, G. L. 1957, MNRAS, 117, 50

Dehnen W., 1993, MNRAS, 265, 250

Dehnen, W. 2001, MNRAS, 324, 273

Do, T., Ghez, A. M., Morris, M. R., Lu, J. R., Matthews, K., Yelda, S., & Larkin, J. 2009, ApJ, 703, 1323

Dray, L. M., & Tout, C. A. 2007, MNRAS, 376, 61

Dubinski J., & Carlberg R. G., 1991, ApJ, 378, 496

Duquennoy , A., & Mayor , M. 1991, A&A, 248, 485

Eckart, A., & Genzel, R. 1997, MNRAS, 284, 576

Eggleton P. P., 1971, MNRAS, 151, 351

Eisenhauer, F. et al. 2005, ApJ, 628, 246

Eggleton, P. P. 1983 ApJ, 268, 368

Emsellem, E. & van de Ven, G. 2008, ApJ, 674, 653

Evans, C. R., & Kochanek, C. S. 1989 ApJ, 346, 13

Faber, J. A., Rasio, F, A., & Willems, B. 2005 Icar., 175, 248

Fabrycky, D., & Tremaine, S. 2007, ApJ, 669, 1298

Fehlberg, E. 1968, NASA Tech Rep, TR T-287

Ferrarese, L., & Ford, H. 2005, Space Science Reviews, 116, 523

Ferrarese, L. et al. 2006, ApJ, 644, L21

Forbes, D. A., Lasky, P., Graham, A. W., & Spitler, L. 2008, MNRAS, 389, 1924

Figer, D. F., 2003. Massive Stars and The Creation of our Galactic Center. Astronomische Nachrichten Supplement 324, 255

Figer, D. F., Rich, R.M., Kim, S. S.,Morris, M., & Serabyn, E. 2004 ApJ 601, 319

Figer, D. F. 2008, *in Massive Stars: From PopIII and GRBs to the Milky Way (in press)*; preprint at http://arxiv.org/abs/0803.1619

Ford, E. B., Kozinsky, B., & Rasio, F. A. 2000, ApJ, 535, 385

Freitag, M., Amaro-Seoane, P., & Kalogera, V. 2006a, ApJ, 649, 91

Freitag, M., Grkan, M. A., & Rasio, F. A. 2006b, MNRAS, 368, 141

Freitag, M., Amaro-Seoane, P., & Kalogera, V. 2006a, ApJ, 649, 91

Fukushige, T., Ebisuzaki, T., & Makino, J. 1992, PASJ, 44, 281

Fujii, M., Iwasawa, M., Funato, Y., & Makino, J. 2009, ApJ, 695, 1421

Fujii, M., Iwasawa, M., Funato, Y., & Makino, J. 2010, ApJ, 716, L80

Gaburov, E., Harfst, S., & Portegies Zwart, S. 2009, New Astronomy, 14, 630

Gaburov E., Lombardi J. C., Jr., Portegies Zwart S., 2010, MNRAS, 402, 105

Gebhardt, K., et al. 2001, AJ, 122, 2469

Geha M., Guhathakurta P., van der Marel R.P., 2002, AJ, 124, 3073

Genzel, R., et al. 1994, The nucleus of our Galaxy, Rep. Prog. Phys. 57, 417

Genzel, R., et al. 1996, ApJ, 472, 153

Genzel, R., Eckart, A., Ott, T., & Eisenhauer, F. 1997, MNRAS, 291, 219

Genzel, R., et al. 2000, ApJ, 317, 348

Genzel, R., Schödel, R., Ott, T., Eisenhauer, F., Hofmann, R., & Lehnert, M. et al. 2003, ApJ, 594, 812

Gerhard, O. 2001, ApJ, 546L, 39

Gezari, S., et al. 2008, ApJ, 676, 944

Gezari, S., et al. 2009, ApJ, 698, 1367

Gerhard, O., 2001, ApJ, 546, L39

Ghez, A. M., et al. 2003, ApJ, 586, L127

Ghez, A. M., Salim, S., Hornstein, S. D., Tanner, A., Lu, J. R., Morris, M., Becklin, E. E., Duchne, G., 2005, ApJ, 620, 744

Ghez, A. M., et al. 2008, ApJ, 689, 1044

Gillessen, S., Eisenhauer, F., Trippe, S., Alexander, T., Genzel, R., Martins, F., & Ott, T. 2009, ApJ, 692, 1075

Ginsburg, I., & Loeb, A. 2006 MNRAS, 368, 221

Ginsburg, I., & Loeb, A. 2007 MNRAS, 376, 492

Glebbeek E., 2008, PhD thesis, Utrecht University

Glebbeek E., Pols O. R., 2008, A&A, 488, 1017

Glebbekk, E., et al. 2009, A & A, 497, 255

Goerdt, T., Moore, B.; Read, J. I., Stadel, J., & Zemp, M. 2006, MNRAS, 368, 1073

Gomboc, A., & Čadež, A. 2005, ApJ, 625, 278

Gould, A., & Quillen, A. C. 2003, ApJ, 592, 935

Graham, A. W., & Driver, S. P. 2007, ApJ, 655, 77

Graham, A. W. & Spitler, L. R. 2009, MNRAS, 397, 2148

Gualandris, A. & Merritt, D. 2008, ApJ, 678, 780

Gualandris, A., & Merritt, D. 2009, ApJ, 705, 361

Gualandris, A., Portegies Zwart, S., & Sipior, M. S., 2005, MNRAS, 363, 223

Gualandris, A. & Merritt, D. 2011, in preparation

Guillochon, J., Ramirez-Ruiz, E., Rosswog, S., & Kasen, D. 2009, ApJ, 705, 844

Gürkan, M. A.; Rasio, F. A. 2005, ApJ, 628, 236

Haller, J. W., Rieke, M. J., Rieke, G. H., Tamblyn, P., Close, L., & Melia, F. 1996, ApJ, 456, 194

Hansen, C. J., Kawaler, S. D., & Trimble, W. 2004, Stellar Interiors, Springer-Verlag New York, Inc.

Hansen, B. M. S., 2007, ApJ, 671, L133

Harfst, S., Gualandris, A., Merritt, D., Spurzem, R., Portegies Zwart, S. & Berczik, P. 2007, New Astronomy, 12, 357

Harris, W. E., 1996, AJ, 112, 1487

Harris, W. E., & van den Bergh, S. 1981, AJ, 86, 1627

Haşegan et al. 2005, ApJ, 627, 203

Hausman, M. A. & Ostriker, J. P 1978, ApJ, 224, 320

Hartmann, H., Debattista, V. P., Seth, A., Cappellari, M., & Quinn, T. R., 2011, arxiv:1103.5464

Hashimoto, Y., Funato, Y., & Makino, J. 2003, ApJ, 582, 196

Heber, U., Edelmann, H., Napiwotzki, R., Altmann, M., & Scholz, R. D. 2008, A&A, 483, L21

Hernandez, X., & Gilmore, G. 1998, MNRAS, 297, 517

Hernquist, L., & Katz, N. 1989, ApJS, 70, 419

Hernquist, L. 1990, ApJ, 356, 359

Hills, J. G. 1988, MNRAS, 368, 221

Hills, J. G. 1991, AJ, 102, 704

Hobbs, L. M.& Mathieu, R. D. 1991, PASP, 103, 431

Holman, M., Touma, J., & Tremaine, S. 1997, Nature, 386, 254

Hopman, C., & Alexander, T. 2006, ApJ, 645, L133

Hughes, S. A. 2003, Annals of Physics, 303, 142

Hughes, S. A. 2003, Annals of Physics, 303, 142

Ibata, R. A., & Lewis, G. F. 1998, ApJ, 500, 575

Inoue, S. 2009, MNRAS, 397, 709

Jordán, A. et al., 2005, ApJ, 634,1002

Just, A., Khan, F. M., Berczik, P., Ernst, A., & Spurzem, R. 2010, MNRAS, tmp.1687

Kalnajs, A. J., 1972, in Gravitational N-body problems, ed. M. Lecar (Dordrecht:Reidel), p. 13

Kasen, D., & Ramirez-Ruiz, E. 2010, ApJ, 714, 155

Katz, N., 1991, ApJ, 368, 325

Khan, F., Just, A., & Merritt, D. 2011, arXiv:1103.0272

King, I. R., 1966, AJ, 71, 64

Kenyon, S. J., Bromley, B. C., Geller, M. J., & Brown, W. R. 2008, ApJ, 680, 312

Kim, S. S., & Morriss, M. 2003, ApJ, 597, 312

Kim, S. S., Figer, D. F. , & Morriss, M. 2004, ApJ, 617, L123

Komossa, S., Halpern, J., Schartel, N., Hasinger, G, Santos-Lleo, M., Predehl, P. 2004, ApJ, 603, L17

Kozai, Y. 1962, AJ, 67, 591

Lauer, T. R., et al. 1995, AJ, 110, 2622

Lauer, T. R., Faber, S. M., Ajhar, E. A., Grillmair, C. J., & Scowen, P. A. 1998, AJ, 116, 2263

Launhardt, R., Zylka, R., & Mezger, P. G. 2002, A&A, 384, 112

Leonard, P. J. T. 1989, AJ, 98, 217

Levin, Y. 2006, ApJ, 653, 1203

Levin, Y. 2007, MNRAS, 374, L515

Li, L., Narayan, R., & Menou, K. 2002, ApJ, 576, L753

Lin, D. N. C. & Tremaine, S. 1983, ApJ, 264, 364L

Löckmann, U. & Baumgardt, H. 2008, MNRAS, 384, 323

Löckmann, U., Baumgardt, H., & Kroupa, P. 2008, ApJ, 683, L151

Lombardi Jr. J. C., Rasio F. A., & Shapiro S. L. 1995, ApJL, 445, L117

Lombardi, J. C., Jr., Rasio, F. A., & Shapiro, S. L. 1996, ApJ, 468, 797

Lombardi J. C., Jr., Warren J. S., Rasio F. A., Sills A., & Warren A. R. 2002, ApJ, 568, 939

López-Morales, M., Bonanos, A. Z., 2008, ApJ, 685, L47

Lotz J. M., Miller B. W., Ferguson H. C., 2004, ApJ, 613, 262

Lu, J. R., Ghez, A. M., Hornstein, S. D., Morris, M., & Becklin, E. E. 2005, ApJ, 625, L51

Luminet, J. P., & Carter, B. 1986, ApJS, 61, 219

Lodato, G., King, A. R., & Pringle, J. E. 2009, MNRAS, 392, 332

Madigan, A., Levin, Y., & Hopman, C. 2009, ApJ, 697, L44

Matthews, L. D., et al. 1999, 118, 208

Matthews, L. D., & Gallagher, J. S. 2002, ApJS, 141, 429

Marochnik, L. S. 1968, Soviet Astr., 11, 873

McMillan, P. J., Dehnen, W., 2005, MNRAS, 363, 1205

Merritt, D., 1984, ApJ, 276, 26

Merritt, D. 2001, ApJ, 556, 245

Merritt, D. 2006a, ApJ, 648, 976

Merritt, D. 2006b, Reports of Progress in Physics, 69, 2513

Merritt, D., Gualandris, A., & Mikkola, S. 2009, ApJ, 693L, 35

Merritt, D. 2009, ApJ, 694, 959

Merritt, D. 2010, ApJ, 718, 739

Merritt, D. & Poon, M. Y. 2004, ApJ, 606, 788

Merritt, D., & Szell, A. 2006, ApJ, 648, 890

Merritt, D., Alexander, T., Mikkola, S., & Will, C. 2011, arXiv:1102.3180

Mezger, P. G., et al. 1996, Astron. Astrophys. Rev., 7, 289

Mikkola, S., & Merritt, D. 2008, AJ, 135, 2398

Mateo, M., Harris, H. C., Nemec, J., & Olszewski, E. W. 1990, AJ, 100, 469

Matsubayashi, T. Makino, J., & Ebisuzaki, T. 2007, ApJ, 656, 879

Mikkola, S., & Merritt, D. 2006, MNRAS, 372, 219

Mikkola, S., & Merritt, D. 2008, AJ, 135, 2398

Miller, M. C., Freitag, M., Hamilton, D. P., & Lauburg, V. M. 2005, ApJ, 631, 117

Milosavljević, M. & Merritt, D. 2001, ApJ, 563, 34

Milosavljević, M. 2004, ApJ, 605, L13

Miocchi, P., Capuzzo-Dolcetta, R., Di Matteo, P., & Vicari, A., 2006, ApJ, 644, 940

Miocchi P. 2007, MNRAS, 381, 103

Moore, B., Kazantzidis, S., Diemand, J., Stadel, J. 2004, MNRAS, 354, 522

Morriss, M. 1993, ApJ, 408, 496

Mulder W. A. 1983, A&A, 117, 9

Murai, T., & Fujimoto, M. 1980, PASJ, 32, 581

Nayakshin, S. & Cuadra, J. 2005, A&A, 437, 437

Nayakshin, S. & Cuadra, J. 2007, MNRAS, 379, 21

Nishiyama, S., Nagata, T., Kusakabe, N., et al. 2006, ApJ, 638, 839

Nishiyama, S., Tamura, M., Hatano, H., et al. 2009, ApJ, 696, 1407

Oh K. S., Lin D. N. C., 2000, ApJ, 543, 620

Oh, S., Kim, S. S., & Figer, D. F. 2009, Journal of Korean Astronomical Society, 42, 17

Öpik, E. 1924, Statistical studies of double stars: On the distribution of relative luminosities and distances of double stars in the Harvard revised photometry north of declination 30°, Publ. Obs. Astron. Univ. Tartu 25, 1.

Ostriker, J. P. 1988, IAUS, 126, 271

Paczynski, H.B. 1971, ARA&A, 9, 183

Paumard, T., Maillard, J. P., Morris, M., & Rigaut, F. 2001, A&A, 366, 466

Paumard, T. et al. 2006, ApJ, 643, 1011

Peebles, P. J. E. 1971, A&A, 11, 377

Perets, H. B., Hopman, C., & Alexander, T. 2007, ApJ, 656, 709

Perets, H. B. 2009a, ApJ, 690, 795

Perets, H. B. 2009b, ApJ, 698, 1330

Perets, H. B., Gualandris, A., Kupi, G., Merritt, D., & Alexander, T. 2009, arXiv:0903.2912

Perets, H. B., & Fabrycky, D. C. 2009, ApJ, 697, 1048

Perets, H. B. &Gualandris, A. 2010, ApJ, 719, 220

Pesce, E., Capuzzo-Dolcetta, R., & Vietri, M. 1992, MNRAS, 256, 368

Peters, P. C. 1964, PhRv, 136, 1224

Portegies Zwart, S. F. & McMillan, S. L. W. 2002, ApJ, 576, 899

Portegies Zwart S., McMillan S., Harfst S. e. a., 2009, New Astronomy, 14, 369

Polnarev, A. G. & Rees, M. J. 1994, A&A, 283, 301

Porter, E. & Sesana, A. 2010, arXiv:1005.5296

Preto, Miguel, Merritt, David, & Spurzem, Rainer 2004, ApJ, 613, L109

Preto, M., Berentzen, I., Berczik, P., Spurzem, R. 2011, ApJ, 732, L26

Price D. J. 2007, Publications of the Astronomical Society of Australia, 24, 159

Pritchet, C. J., & Glaspey, J. W. 1991, ApJ, 373, 105

Quinlan, G. D. 1996, 1996, New Astronomy, 1, 35

Rayleigh, L. 1919, Phil. Mag., 37, 321

Rasio, F. A., & Shapiro, S. L. 1992, ApJ, 401, 226

Rasio, F. A., & Shapiro, S. L. 1995, ApJ, 438, 887

Rauch, K. P., & Tremaine, S. 1996, New Astronomy, 1, 149

Read, J. I., Goerdt, T., Moore, B., Pontzen, A. P., Stadel, J., Lake, G. 2006, MNRAS, 373, 1451

Rees, M. J. 1988, Nature, 333, 523

Regös, E., Bailey, V. C., & Mardling, R. 2005, MNRAS, 358, 544

Rich, R. M., et al. 1997, ApJ, 484, L25

Rood, H. J., Page, T. L., Kintner, E. C., & King, I. R. 1972, ApJ, 175, 627

Rosenbluth, M. N., MacDonald, W. M., & Judd, D. L., 1957, PhRv, 107, 1

Rossa, J. et al. 2006, AJ, 132, 1074

Rosswog S., 2009, NewAR, 53, 78

Saha, P. 1992 MNRAS, 254, 132

Sari, R., Kobayashi, S., & Rossi, E. M. 2010, ApJ, 708, 605

Schinnerer, E. et al. 2006, ApJ, 649, 181

Schinnerer E., Böker T., Meier D. S., & Calzetti D. 2008, ApJL, 684, L21

Schödel, R., Eckart, A., Iserlohe, C., Genzel, R., & Ott, T. 2005, ApJ, 625L, 111

Schödel, R., Eckart, A., Alexander, T., et al. 2007, A&A, 469, 125

Schödel, R., Merritt, D., & Eckart, A. 2008, Journal of Physics Conference Series, 131, 012044

Schödel, R., Merritt, D., & Eckart, A., 2009, A&A, 502, 91

Schödel, R. 2010, arXiv1001.4238

Sesana, A., Haardt, F., & Madau, P. 2006, ApJ, 651, 392

Sesana, A., Haardt, F., & Madau, P. 2007, MNRAS, 379L, 45

Sesana, A., Madau, P., & Haardt, F. 2009, MNRAS, 392, 31

Seth A. C., Dalcanton J. J., Hodge P. W., Debattista V. P., 2006, AJ, 132, 2539

Seth, A. et al. 2008a, ApJ, 678, 116

Seth, A. C., Blum, R. D., Bastian, N., Caldwell, N., & Debattista, V. P. 2008b, ApJ, 687, 997

Shlosman I., & Begelman M. C. 1989, ApJ, 341, 685

Sills, A., & Lombardi, J. C., Jr. 1997, ApJ, 484, L51

Sills, A., Lombardi, J. C., Jr., Bailyn, C. D., Demarque, P., Rasio, F. A., & Shapiro, S. L., 1997, ApJ, 487, 290

Soffel, M. H. 1989, Relativity in Astrometry, Celestial Mechanics and Geodesy (Springer-Verlag: Berlin)

Spekkens, K., Giovanelli, R., & Haynes, M. P. 2005, AJ, 129, 2119

Spinnato, P. F., Fellhauer, M., & Portegies Zwart, S. F. 2003, MNRAS, 344, 22

Spitzer, L. 1987, Princeton, NJ, Princeton University Press, 1987, 191 p.

Szell, A., Merritt, D., & Kevrekidis, I. G. 2005, Physical Review Letters, 95, 081102

Strabbe, L. E., & Quataert, E. 2009, MNRAS, 400, 2070

Takeda, G., & Rasio, F. A. 2005, ApJ, 627, 1001

Tanner, A. M., et al. 2006, ApJ, 641, 891

Teuben, P. 1995, in Astronomical Data Analysis Software and Systems IV, ed. R. Shaw, H. Payne, & J. Hayes (San Francisco: ASP), ASP Conf. Ser., 77, 398

Tillich, A., Przybilla, N., Scholz, R.-D., & Heber, U. 2009, A&A, 507, L37

Tremaine, S. D., Ostriker, J. P., & Spitzer, L., Jr. 1975, ApJ, 196, 407

Tremaine, S., & Weinberg, M. D. 1984, MNRAS, 209, 729

Trippe et al. 2008, A&A, 492, 419

Ulmer, P. 1999, ApJ, 514, 180

Vanbeveren, D., De Loore, C., & Van Rensbergen, W. 1998, A&A Rev, 9, 63

van den Bosch, F. C., Lewis, G. F., Lake, G., & Stadel, J. 1999, ApJ, 515, 50

Vesperini, E., Zepf, S. E., Kundu, A., & Ashman, K. M. 2003, ApJ, 593, 760

Wang, J., & Merritt, D. 2004, ApJ, 600, 149

Wehner, E. H. & Harris, W. E. 2006, ApJ, 644, L17

Weinberg, M. D. 1985, MNRAS, 213, 451

Weinberg, M. D. 1986, ApJ, 300, 93

Weinberg, M. D., & Katz N., 2002, ApJ, 580, 627

Weinberg, M. D., & Katz N., 2007, MNRAS, 375, 425

White, M. L 1949, ApJ, 109, 159

White, S. D. M. 1983, ApJ, 274, 53

Wollman, E. R., et al. 1977, ApJL, 218, L103.

Yu, Q. & Madau, P. 2007, MNRAS, 379, 1293

Yu, Q., & Tremaine, S. 2003, ApJ, 599, 1129

Zhao, H. 1996, MNRAS, 278, 488